

UC Berkeley

UC Berkeley Electronic Theses and Dissertations

Title

Hydrogen Storage and Gas Separations in Metal-Organic Frameworks

Permalink

<https://escholarship.org/uc/item/9637c2n8>

Author

Kapelewski, Matthew Thomas

Publication Date

2018

Peer reviewed|Thesis/dissertation

Hydrogen Storage and Gas Separations in Metal-Organic Frameworks

by

Matthew Thomas Kapelewski

A dissertation submitted in partial satisfaction of the

requirements for the degree of

Doctor of Philosophy

in

Chemistry

in the

Graduate Division

of the

University of California, Berkeley

Committee in charge:

Professor Jeffrey R. Long, Chair

Professor Omar M. Yaghi

Professor Jeffrey A. Reimer

Spring 2018

Hydrogen Storage and Gas Separations in Metal-Organic Frameworks

© 2018

by

Matthew Thomas Kapelewski

Abstract

Hydrogen Storage and Gas Separations in Metal-Organic Frameworks

By

Matthew Thomas Kapelewski

Doctor of Philosophy in Chemistry

University of California, Berkeley

Professor Jeffrey R. Long, Chair

The work presented in this dissertation outlines the design, synthesis, characterization, and use of metal-organic framework materials for applications in gas storage and separations. The materials herein are studied for use in hydrogen storage for mobile applications, such as light-duty vehicles, and for hydrocarbon separations relevant to the chemical industry. The common theme is that all of the studied materials focus on controlling adsorption within the pores of the metal-organic frameworks by taking advantage of the high level of structural design, synthetic control, and porosity, as well as the unique structural motifs present in these materials to engender them with properties suitable for the desired applications. A variety of techniques are used to gain an understanding of the materials and applications presented herein, including gas adsorption, infrared spectroscopy, powder X-ray and neutron diffraction, single crystal X-ray diffraction, multicomponent gas- and liquid-phase adsorption experiments, and electronic structure calculations.

Chapter One provides an introduction to the field of metal-organic frameworks and some of the relevant design principles which are important in the subsequent chapters. The logical extension of traditional inorganic cluster chemistry to extended three-dimensional metal-organic framework solids is discussed. Furthermore, open metal coordination sites are introduced, which are used in the subsequent work in this dissertation. The potential of using metal-organic frameworks for hydrogen storage, olefin/paraffin separations, xylene isomer separations, and acetylene/ethylene separations is introduced, with previous work in each of these fields being reviewed.

Chapter Two describes the synthesis of a new metal-organic framework, $M_2(m\text{-dobdc})$ ($M^{2+} = \text{Mg, Mn, Fe, Co, Ni}$; $m\text{-dobdc}^{4-} = 4,6\text{-dioxido-1,3-benzenedicarboxylate}$), which is a structural isomer of the previously known $M_2(\text{dobdc})$ ($\text{dobdc}^{4-} = 2,5\text{-dioxido-1,4-benzenedicarboxylate}$). While structurally similar, the altered connectivity of this $M_2(m\text{-dobdc})$ material leads to an increased charge density at the open metal coordination sites, which are the key binding site for guests within the pores. This principle was studied in the context of hydrogen storage, with the Ni analog of this material possessing one of the highest physisorptive H_2 binding enthalpies of any known adsorbent. A variety of techniques, including powder neutron diffraction, *in situ* H_2 -dosed infrared spectroscopy, and electronic structure calculations are used to better understand how and where hydrogen is binding in this class of materials. Importantly, this material was also

designed to be produced at scale, with a relatively low cost of synthesis compared to other high-performing MOFs.

Chapter Three extends the work of the previous chapter. The $M_2(m\text{-dobdc})$ series of MOFs that previously showed strong binding of H_2 within its pores is now studied under conditions relevant to on-board hydrogen storage in fuel cell vehicles. Adsorption isotherms up to 100 bar show that $Ni_2(m\text{-dobdc})$ is the top performing porous adsorbent for hydrogen storage of any yet reported, possessing a volumetric H_2 capacity of 11.9 g/L at 25 °C and capacities approaching the U.S. Department of Energy targets at lower temperatures. *In situ* techniques such as powder neutron diffraction and infrared spectroscopy are again used to understand hydrogen binding, revealing that at near-ambient temperatures, the open metal sites control nearly all hydrogen binding and lead to the exhibited high H_2 capacity.

In *Chapter Four*, the utility of the $M_2(m\text{-dobdc})$ series is expanded to gas separations. Adsorptive-based olefin/paraffin separations of C_2 (ethylene/ethane) and C_3 (propylene/propane) hydrocarbon mixtures are studied. Due to the high charge density in these materials at the open metal coordination sites, the olefin is bound more strongly than the paraffin, leading to record adsorptive-based selectivities for each of these separations in the $Fe_2(m\text{-dobdc})$ analog and strong performance from other metals in this structure. High capacity and fast kinetics of adsorption are also demonstrated in this class of materials. Finally, multicomponent gas adsorption experiments demonstrate the applicability of this MOF to real gas separations. The combination of high selectivity and capacity, fast adsorption kinetics, easy desorption, and low raw materials cost make this material the best material for adsorptive-based olefin/paraffin separations.

Chapter 5 examines the separation of xylene isomers (*o*-, *m*-, *p*-xylene and ethylbenzene) in the metal-organic frameworks $Co_2(dobdc)$ and $Co_2(m\text{-dobdc})$ by taking advantage of their open metal coordination sites in a unique way. Rather than having a single guest bind to each open metal site, as in the previous chapters, each xylene molecule interacts with two adjacent metal centers, leading to selectivity based on the ability of each isomer to approach the two-metal binding pocket and pack within the pores. Separation was shown in single-component gas phase isotherms as well as multi-component gas- and liquid-phase adsorption experiments. Furthermore, $Co_2(dobdc)$ was shown to separate all four components. Single crystal X-ray diffraction was key in identifying that each xylene interacts with multiple metal centers and was able to corroborate the adsorption data in identifying how strongly each xylene interacted with the two-metal pocket. Interestingly, the $Co_2(dobdc)$ material undergoes significant structural distortion upon adsorbing *o*-xylene and ethylbenzene at lower temperatures, which was surprising given the previously-assumed rigidity of the structure. Lastly, the different symmetries of the $Co_2(dobdc)$ and $Co_2(m\text{-dobdc})$ isomers of these materials displayed different separation properties and xylene packing, highlighting the structural tunability of metal-organic frameworks.

In *Chapter Six*, the metal-organic framework $Cu[Ni(pdt)_2]$ is used in the separation of acetylene from ethylene. By taking advantage of the small pores and unique structure of this material, it was discovered to have the highest adsorptive selectivity of any known adsorbent for this challenging separation. Through powder X-ray diffraction experiments, the primary binding site was revealed to be a square tetrapyrzine cage in the pores, which can likely interact more strongly with acetylene than ethylene through multiple pi-pi interactions. This material takes advantage of the unique square tetrapyrzine cage this material possesses in order to effect the separation of acetylene and ethylene without the need for open metal coordination sites.

*To my parents,
Tom and Gina Kapelewski*

Table of Contents

Table of Figures	iv
Table of Tables	v
Acknowledgements	vi
Chapter 1: Gas Storage and Separations in Metal-Organic Frameworks	1
Section 1.1. Introduction to Metal-Organic Frameworks	1
Section 1.2 Metal-Organic Frameworks with Open Metal Coordination Sites	3
Section 1.3. Hydrogen Storage in Metal-Organic Frameworks.....	4
Section 1.4. Gas Separations in Metal-Organic Frameworks	6
Section 1.5. References	8
Chapter 2: $M_2(m\text{-dobdc})$ (M = Mg, Mn, Fe, Co Ni) Metal-Organic Frameworks Exhibiting Increased Charge Density and Enhanced H_2 Binding at the Open Metal Sites	12
Section 2.1. Introduction	12
Section 2.2. Experimental	13
Section 2.3. Results and Discussion	18
Section 2.4. Outlook and Conclusions	29
Section 2.5. Acknowledgements	29
Section 2.6. References and Supplementary Data	29
Chapter 3: Record High Hydrogen Storage Capacity in the Metal-Organic Framework $Ni_2(m\text{-dobdc})$ at Near-Ambient Temperatures.....	79
Section 3.1. Introduction	79
Section 3.2. Experimental	81
Section 3.3. Results and Discussion	85
Section 3.4. Outlook and Conclusions	95
Section 3.5. Acknowledgements	96
Section 3.6. References and Supplementary Data	96
Chapter 4: $M_2(m\text{-dobdc})$ (M = Mn, Fe, Co, Ni) Metal-Organic Frameworks as Highly Selective, High-Capacity Adsorbents for Olefin/Paraffin Separations.....	112
Section 4.1. Introduction	112
Section 4.2. Experimental	113
Section 4.3. Results and Discussion	116
Section 4.4. Outlook and Conclusions	123
Section 4.5. Acknowledgements	123
Section 4.6. References and Supplementary Data	124
Chapter 5: Separation of Xylene Isomers through Multiple Metal Site Interactions in Metal-Organic Frameworks	134
Section 5.1. Introduction	134
Section 5.2. Experimental	136
Section 5.3. Results and Discussion	140
Section 5.4. Outlook and Conclusions	148

Section 5.5. Acknowledgements	149
Section 5.6. References and Supplementary Data	149

Chapter 6: Acetylene/Ethylene Separation in the Metal-Organic Framework Cu[Ni(pdt)₂] via Binding in a Square Tetrapyrazine Cage	173
Section 6.1. Introduction	173
Section 6.2. Experimental	173
Section 6.3. Results and Discussion	176
Section 6.4. Outlook and Conclusions	183
Section 6.5. Acknowledgements	184
Section 6.6. References and Supplementary Data	184

Table of Figures

Chapter 1

Figure 1.1. General schematic of MOF synthesis	1
Figure 1.2. Comparison of molecular Cu paddlewheels and Cu paddlewheel MOF	2
Figure 1.3. Synthesis of $M_2(\text{dobdc})$	3
Figure 1.4. First coordination sphere of M^{2+} in $M_2(\text{dobdc})$	4
Figure 1.5. United States' energy consumption for industrial separations	7

Chapter 2

Figure 2.1. Synthesis of $H_4(m\text{-dobdc})$ and $M_2(m\text{-dobdc})$	19
Figure 2.2. Crystal structure of $\text{Co}_2(m\text{-dobdc})$	19
Figure 2.3. H_2 isosteric heat of adsorption for $M_2(m\text{-dobdc})$	21
Figure 2.4. D_2 binding sites in $\text{Co}_2(m\text{-dobdc})$ from neutron diffraction	22
Figure 2.5. Inelastic neutron scattering data for $\text{Co}_2(m\text{-dobdc})$ and $\text{Ni}_2(m\text{-dobdc})$	23
Figure 2.6. Infrared spectra of H_2 -dosed $M_2(\text{dobdc})$ and $M_2(m\text{-dobdc})$	24
Figure 2.7. Variable temperature infrared spectra of $\text{Co}_2(m\text{-dobdc})$	25
Figure 2.8. Calculated H_2 binding modes for dobdc^{4-} and $m\text{-dobdc}^{4-}$ complexes	28
Supplementary Figures for Chapter 2	33

Chapter 3

Figure 3.1. Calculation of H_2 usable capacity	87
Figure 3.2. Hydrogen adsorption isotherms for $M_2(\text{dobdc})$ and $M_2(m\text{-dobdc})$	89
Figure 3.3. $\text{Ni}_2(m\text{-dobdc})$ and pure H_2 capacities at various temperatures	91
Figure 3.4. Temperature-programmed H_2 desorption	92
Figure 3.5. D_2 binding sites in $\text{Co}_2(m\text{-dobdc})$ from neutron diffraction	93
Figure 3.6. <i>In situ</i> H_2 -dosed infrared spectra of $\text{Ni}_2(m\text{-dobdc})$	94
Figure 3.7. Comparison of infrared spectra at constant H_2 adsorption in $\text{Ni}_2(m\text{-dobdc})$	95
Supplementary Figures for Chapter 3	99

Chapter 4

Figure 4.1. Crystal structures of $\text{Co}_2(\text{dobdc})$ and $\text{Co}_2(m\text{-dobdc})$ ethylene binding	117
Figure 4.2. Isotherms and IAST selectivities for C_2 and C_3 in $M_2(m\text{-dobdc})$	118
Figure 4.3. Comparison of $M_2(m\text{-dobdc})$ and $M_2(\text{dobdc})$ IAST selectivities	120
Figure 4.4. Enthalpies of C_2 and C_3 adsorption in $M_2(m\text{-dobdc})$	121
Figure 4.5. Transient adsorption of ethylene in $\text{Fe}_2(m\text{-dobdc})$	122
Figure 4.5. Breakthrough of ethylene/ethane and propylene/propane in $\text{Co}_2(m\text{-dobdc})$	123
Supplementary Figures for Chapter 4	126

Chapter 5

Figure 5.1. Crystal structures of $\text{Co}_2(\text{dobdc})$ and $\text{Co}_2(m\text{-dobdc})$	135
Figure 5.2. Xylene isotherms and breakthrough in $\text{Co}_2(\text{dobdc})$ and $\text{Co}_2(m\text{-dobdc})$	141
Figure 5.3. Multicomponent liquid phase xylene adsorption	142

Figure 5.4. Structural distortion of $\text{Co}_2(\text{dobdc})$ with adsorbed <i>o</i> -xylene	144
Figure 5.5. $\text{Co}_2(\text{dobdc})$ <i>o</i> -xylene isotherms at different temperatures	145
Figure 5.6. Crystal structures of all four xylenes in $\text{Co}_2(\text{dobdc})$	146
Figure 5.7. Crystal structures of <i>o</i> -xylene and ethylbenzene in $\text{Co}_2(m\text{-dobdc})$	148
Supplementary Figures for Chapter 5	153

Chapter 6

Figure 6.1. Powder X-ray diffraction pattern of $\text{Cu}[\text{Ni}(\text{pdt})_2]$	177
Figure 6.2. Adsorption of N_2 at 77 K in $\text{Cu}[\text{Ni}(\text{pdt})_2]$	177
Figure 6.3. Structure of $\text{Cu}[\text{Ni}(\text{pdt})_2]$	178
Figure 6.4. Acetylene and ethylene isotherms in $\text{Cu}[\text{Ni}(\text{pdt})_2]$	178
Figure 6.5. IAST selectivities for acetylene/ethylene in $\text{Cu}[\text{Ni}(\text{pdt})_2]$	179
Figure 6.6. Crystal structures comparing activated and C_2H_2 -dosed $\text{Cu}[\text{Ni}(\text{pdt})_2]$	180
Figure 6.7. Comparison of $\text{Cu}[\text{Ni}(\text{pdt})_2]$ and $\text{M}_2(m\text{-dobdc})$ IAST selectivities	181
Figure 6.8. Infrared spectrum of evacuated and acetylene-dosed $\text{Cu}[\text{Ni}(\text{pdt})_2]$	182
Figure 6.9. Acetylene-dosed infrared spectra of $\text{Cu}[\text{Ni}(\text{pdt})_2]$ C–H stretch	182
Figure 6.10. Acetylene-dosed infrared spectra of $\text{Cu}[\text{Ni}(\text{pdt})_2]$ C–H bend	183
Supplementary Figures for Chapter 6	185

Table of Tables

Chapter 1

Table 1.1. DOE targets for hydrogen storage in light-duty vehicles	5
Table 1.2. Properties of components of the C_8 alkylaromatics mixture	8

Chapter 2

Table 2.1. Summary of $\text{M}_2(\text{dobdc})$ and $\text{M}_2(m\text{-dobdc})$ surface areas	20
Table 2.2. Zero-coverage H_2 isosteric heats of adsorption in $\text{M}_2(\text{dobdc})$ & $\text{M}_2(m\text{-dobdc})$	21
Table 2.3. Entropies and enthalpies of H_2 adsorption in $\text{M}_2(\text{dobdc})$ and $\text{M}_2(m\text{-dobdc})$	26
Table 2.4. ALMO energy decomposition analysis in dobdc^{4-} and $m\text{-dobdc}^{4-}$ complexes	27
Table 2.5. Forward and backbonding contributions to H_2 charge transfer	28

Chapter 3

Table 3.1. DOE targets for hydrogen storage in light-duty vehicles	86
Table 3.2. Comparison of volumetric usable capacities	90
Table 3.3. Selected D_2 — D_2 distances in $\text{Co}_2(m\text{-dobdc})$	93

Chapter 5

Table 5.1. Physical properties of the C_8 alkylaromatic	134
Table 5.2. C_8 isomer selectivities from liquid phase adsorption	143

Chapter 6

Table 6.1. Summary of vibrational modes in C_2H_2	183
---	-----

Acknowledgements

Graduate school presents each student with an enormous task. A challenge as great as adding to the scope of human knowledge is daunting, and having the support of my friends and family has been just about the only way I could take on such an adventure. I have had the great fortune of getting to know a number of intelligent and inspiring people over the course of my life who have helped me to get to the position I'm in today. In particular, my time at Berkeley has been a time of fruitful growth for myself both as a scientist and an individual, and the people I've encountered and become friends with throughout graduate school have been a large part of that growth. To the people listed below I am forever indebted for having some part, large or small, in that change.

The most significant decision I've made during graduate school is joining Jeff Long's group. Jeff had me come to Berkeley to do research as an undergraduate (during which I nearly did some milestone work on CO₂ capture), but what really struck me in my time there was how welcoming and fun the group was and how Jeff created an outstanding atmosphere for doing research. I liked it enough to come back for five-plus more years, and I really appreciate Jeff for letting me work on such a wide variety of projects during my Ph.D. and helping me to explore my own interests during my time here. Jeff also gave me a unique opportunity to leave for an entire summer and do an internship at ExxonMobil, which was a crucial experience for me in deciding on the research career I'm pursuing. Last but not least, thanks to Jeff for covering my bar tab many, many times and sharing many delicious beers over the years with me.

A large part of the fun, freewheeling, and somewhat boozy identity of the Long Group can be attributed to a number of the students who came before me in the lab. In particular, Eric Bloch, Tom McDonald, and Jarad Mason had a significant impact on me during my early time in the Long Group. Tom was my mentor as an undergraduate and was the first to introduce me to lab. Eric and Jarad were instrumental in helping me to get interesting projects moving when I first came as a graduate student and also were crucial in helping with the social transition into the Long Group. Thanks especially to Eric for making the group such a cohesive, tight-knit place during my initial years here. I'll always think of these guys when I hear "Country Roads."

Miguel Gonzalez, Mike Aubrey, and Dianne Xiao are the graduate students in the year preceding mine and helped to establish several interesting research projects in the group. They're each incredibly talented researchers who I look up to in terms of the quality of their work. They're also all fun people to spend time with and made the trials and tribulations of graduate school a bit more bearable. Miguel in particular has been a close collaborator of mine throughout graduate school and is without a doubt one of the most brilliant, insightful, thoughtful, and thorough scientists I've encountered. The quality of my research was elevated significantly by his efforts.

When I joined the group, I was lucky enough to be in a cohort with three other outstanding students: Phil Bunting, Doug Reed, and Lucy Darago. I've worked most directly with Doug, regularly discussing ASAP experiments and projects, but the most important thing I've developed with each of these people is a fantastic friendship. I've shared more jokes than I can count with Phil over the years, and I'll miss our time playing softball (with the Longballs [God I wish we won a championship one of those years...we were so close] and the COC Fighters), going to MOLO, and generally just being on the same wavelength in our conversations about anything and everything. Thanks also to Phil for keeping a list of "Matt Quotes" over the years; his tireless work in logging every embarrassing and outrageous thing I've ever said was

exemplary. Doug has been the person I can talk about sports with most often, which is not a given in graduate school, and is always willing to hear me talk on and on about the Pirates (I reciprocate by listening to his stuff about the NBA). Doug is one of the most reliable friends I have and I'll miss getting to come over to his desk to just shoot the breeze all the time. Phil, Doug, and I have also gone on many outings together, hiking many miles and sleeping too close to each other in small tents, including a whole week together hiking the High Sierra Trail. We've come a long way from some of those early backpacking outings and it's been great fun to get outside with them. Lucy really helps to balance out the strong personalities in our year and has become one of my most trusted friends. She's a wonderful sounding board for my thoughts about nearly everything and is always there to chat when I needed it. I'm not sure how Lucy put up with all of my shenanigans over the years (especially our time when we were pseudo-roommates while she was living with my fiancé, Rebecca), but I really appreciate how close we've become and how important of a friend she is to me.

The year after I joined the group, a new crop of graduate students came in and really laid it all on the line for science. Jon Bachman has been an incredibly close collaborator on several projects and is a very talented engineer who will have an outstanding career. Jon and I had countless conversations over the years hashing out research ideas, talking politics, and so many more things and I'll miss having him around to chat with. Rodi Torres-Gavosto was someone who I met the same summer I was at Berkeley as an undergraduate and we've been friends for a long time. Rodi and I have shared many laughs over the years and talked extensively about many (completely unimportant) things; he's also always reliable to have an interesting reddit link to check out. Mercedes Taylor and I have also worked closely together over the years (most infuriatingly on the HPVA) and she put up with me through a two week trip to a conference in Europe together. She's a good, level-headed friend who has been a great example of how to balance research and the rest of your life. Julia Oktawiec is a bright light of joy every day who I could always count on to have pictures of cute cats and dogs at random intervals. I'd also like to thank Julia for helping extensively with PXRD work for many of my samples over the years.

Rebecca Siegelman and Kristen Colwell have both continued the excellence of MOF researchers in the group. Rebecca's thoroughness in her research is motivating and her willingness to laugh at my stupid jokes over the years is appreciated. Kristen is a highly multitalented individual who started a new project in the group, which is always a challenging task, but has taken to it with aplomb and been quite successful. I've had many interesting conversations with Kristen over the years and her thoughtfulness is something I admire.

The lab ballooning in size in recent years has made it difficult to keep track of the countless younger students coming in to work on all manner of projects, but a few in particular I've enjoyed spending time with are Henry Jiang, Mike Ziebel, Colin Gould, and Naomi Biggins. I've known Henry for many years now and his commitment to research is outstanding; the fancy new IR instrument he's developed is incredibly impressive and is going to get him vast amounts of data over the coming years. Henry and I have also had adjacent desks for several years now and have shared all types of conversations about hydrogen storage, communism, labor unions, and countless other things; it's been enjoyable to be in close proximity to such an interesting person. Mike Ziebel and I have also shared many conversations over the years, starting with the time I convinced him to come to Berkeley while chatting about FBLA and work-life balance. He's always available to talk sports with and is also a very talented scientist who is going to go on to a great career. Colin Gould is another person I've known for a few years now and is someone who is a real steadying presence in the lab. His ability to remain cheerful despite mostly anything

happening is impressive and I'm going to miss talking to him regularly. Naomi Biggins is the newest member of Team Hydrogen and has been a great addition, both scientifically and for her snarky wit and fun personality. She's a strong researcher who jumped into leading a project almost immediately and I'm excited to see where she goes from here.

Numerous postdocs have helped me, both scientifically and socially, over the years and I'd like to thank a few of them in roughly chronological order. Steve Geier helped me to establish $M_2(m\text{-dobdc})$, which I've gotten amazing mileage out of in my research. Wendy Queen was a visitor in the group when I was an undergrad, but has kept in contact and been a good friend over the years as I've seen her at LBNL and various conferences. Jeff Van Humbeck sat next to me when I first joined the group and was an absolute asset when it came to troubleshooting the organic synthesis I was working on. Keith Keitz is just generally awesome and was a really fun person to hang out with. Jiwoong Lee was an outstanding addition to the Longballs softball team and was a great friend to drink with. Zach Smith is perhaps the nicest, most level-headed person I know; it was great to have a fellow Penn Stater in the group for a time and I can't wait to see what he does in his career. Tomče Runčevski has been a very close collaborator over the years and has done some really instrumental PXRD work for my research and for hydrogen storage in particular. Mike McGuirk has been a fun person to chat and drink with and talk sports with. Brandon Barnett is another great person to talk to and has been another great addition to Team Hydrogen and Hildebrand Hall.

I've also worked closely with several exceedingly talented undergraduates from whom I've likely learned more than they've learned from me. David Gygi and Raymond Yu joined around the same time I did and provided countless hours of work. David especially made a large number of ligands and MOFs during his time working on gas sorption and was always very upbeat and great to be around. Raymond is really interested in baseball and homebrewing, so we always had a lot to discuss. Jo Melville is the undergraduate who I had the honor of supervising during his time in the Long Group. Jo's enthusiasm for nearly everything he does is infectious and it was fantastic having someone so inquisitive and interesting work with me for several years. I hope Jo's enthusiasm never wavers and he continues to inspire everyone he encounters to be happy and excited like he did for me.

Working in the Long Group means having access to a wide variety of experiments and collaborators that I wouldn't have dreamed of before coming to graduate school. I've been fortunate to work with some outstanding collaborators over the years, most notably Craig Brown and Stephen FitzGerald. Craig is a real character and was always great to have a drink with at the many meetings we've attended together over the years; he's also a fantastic neutron scientist who helped me obtain many key results throughout my Ph.D. His postdocs Zeric Hulvey, Matt Hudson, and Jacob Tarver were all instrumental in helping to collect and analyze that data and were all great people to work with. Stephen FitzGerald contributed a great deal of *in situ* infrared spectroscopy work to this thesis and was a great collaborator who was always available if I needed to send him samples or gain a better understanding of the data he collected.

I've also made several great friends outside of the Long Group. Nick Settineri helped to introduce me to climbing and has been a great friend due to our close proximity to each other in Elmwood. Hopefully we'll get to go on more climbing trips in the future. Patrick Smith, Nick Lewis, and I had a lot in common and became friends during our first year here, spending too much time at Kip's and sharing many beers at Chemkeg over the years. Chemkeg likely deserves its own acknowledgement, as there was always good conversation with friends and free beer to look forward to every week. Richard Thornbury, Cindy Hong, Drew Samant, Dave Kaphan, and

Mark Levin are all great friends from my connection to the Toste Group; between Kip's trivia, Toste Group ski trips, softball, and many other things, I'm happy that I got to share a portion of my time in grad school with each of them.

Several individuals from my time prior to graduate school have helped to set me on the path to this Ph.D. Brett Criswell was my high school chemistry teacher who first inspired me to study the subject; without him I'd probably be doing something far less interesting. Mary Beth Williams was my research advisor during my undergraduate degree at Penn State. She was the first one to give me a chance to do research as a freshman undergrad, which in turn opened many doors for me that ultimately led to this thesis. Mike Russo has been a very loyal friend for all of the years we've known each other, and we've managed to stay very close despite being on opposite sides of the country.

My family has been very supportive of me throughout my time living so far away from them. My parents helped me to value my education early in my life, which is an ideal that I have carried with me throughout my Ph.D. I can also attribute a strong work ethic to the example each of them set for me, which has proven valuable countless times. They've always been there for me to talk to when I needed it and are good listeners (most of the time). Most importantly, my parents have loved me and supported me in everything that I've done, including my time in graduate school. My brother Scott has also always been supportive and, despite the distance, I feel like we've grown much closer during my time at Berkeley. Growing up with an older sibling who won't stop talking is difficult, but Scott has managed to put up with me for a commendably long time and become one of my best friends. A few other family members have been important in my journey through graduate school as well. All of my grandparents instilled in me both the importance of receiving an education (I bet they never would have guessed I'd still be in school nearly 28 years after they first met me) and how hard work can help you achieve goals. My Aunt Sharon and Uncle Don graciously housed me for over three months while I was completing my internship, which was a huge help both financially and personally. Mary and Paul Triano have also been incredibly supportive people to have in my life and I'm excited to be joining their family soon.

Despite being the last person I'm thanking, Rebecca Triano is undeniably the most important. She's been by my side for every minute of graduate school and there's not a doubt in my mind that I couldn't have made it through such a mentally and emotionally trying experience without her unwavering support. Rebecca was always there to comfort me when I felt lost, down, frustrated, or angry. It was her support that pushed me through the beginning of graduate school, the qualifying exam process, the mid-Ph.D. doldrums, a summer internship across the country that found us separated for months, my job search process, my second job search process, and finishing this Ph.D. thesis. I've also had the joy of sharing countless wonderful moments with her in our years together in Berkeley, from exploring the American West to eating homemade dinners together every night. Getting to actually live in the same place after many years apart has made me realize how lucky I am to have found such a marvelous person to spend my time with. I mentioned at the beginning of this section that I think my time in graduate school has been one of great personal change. Rebecca can be credited with having a hand in nearly every aspect of that change; she's helped me to become a more loving, caring version of myself and encouraged me to pursue goals and hobbies that have made me a more interesting, well-rounded person. I'm not sure she even knows how much I value the positive impact she's had on me as a person and how much I admire her for the way that she lives her life. Living in Berkeley together has also brought into focus so many little aspects of our relationship that I often take for granted

but are central to the love that we've built. Rebecca is perhaps the only person I know who can simultaneously be frustrated with my quirks and love me for them (for example, I've been mocked many times for my love of maps, but the ribbing is always delivered with an incredible loving warmth). She also knows me so well that she anticipates my needs and behaviors with incredible accuracy; I'm constantly impressed by how in-sync we are and how wonderful it is to have that level of understanding with another person. I'm extremely proud of Rebecca for overcoming so much during graduate school (including a broken leg!) to finish her Ph.D. as well.

There's a passage from my favorite novel, "East of Eden," in which the insightful, sagacious character Lee says "I believe a strong woman may be stronger than a man, particularly if she happens to have love in her heart. I guess a loving woman is almost indestructible." Rebecca is the strongest woman I know with the most love in her heart, and I feel so fortunate and joyous to be taking part in that love and spending my life with such an amazing person. Rebecca, thank you for everything you've given me over the past ten years and I can't wait to see where our journey takes us. I love you.

To all my friends, family, and colleagues, your support means everything. Thank you.

Chapter 1: Gas Storage and Separations in Metal-Organic Frameworks

1.1. Introduction to Metal-Organic Frameworks

In recent years, the study of a new class of inorganic materials, termed metal-organic frameworks (MOFs), has been of particular interest to researchers.¹ These materials are formed through the combination of an inorganic component, typically a metal ion or cluster of metal ions, with a multi-topic coordinating organic molecule (Figure 1.1). Under select conditions, these components can self-assemble into porous, three-dimensional materials with a wealth of structural diversity and surface areas as high as 7100 m²/g, far greater than other porous materials.² Since early seminal work in the field by Yaghi, Kitagawa, Robson, and others first drew interest to the unique properties of these materials, their study has been heavily pursued by researchers over the past three decades.^{3,4,5,6,7,8,9}

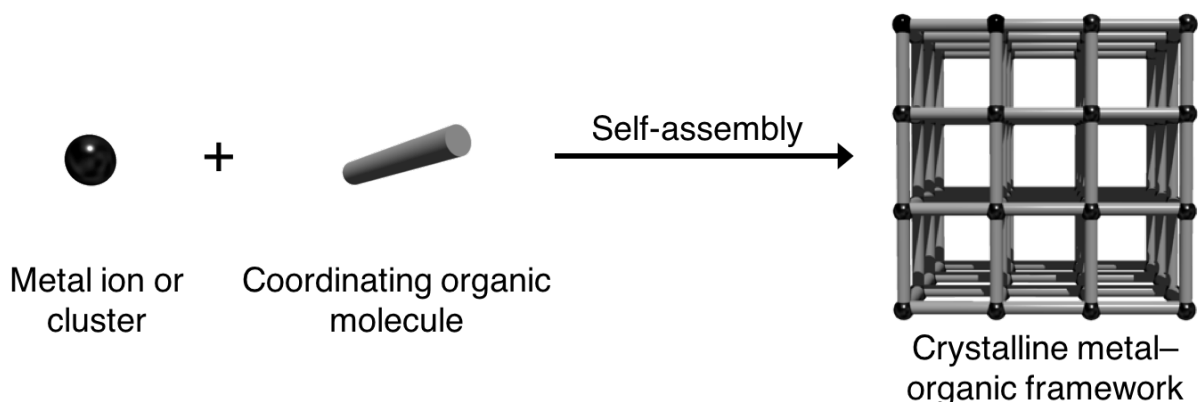


Figure 1.1. A basic schematic outlining the general synthesis of MOFs. This simple picture belies the incredible complexity that can result in this class of materials.

In the context of traditional inorganic chemistry, MOFs can be thought of as using multitopic ligands to link together discrete inorganic clusters into a three-dimensional lattice. An example of this concept is seen in Figure 1.2; by connecting classic bimetallic copper paddlewheels through the use of the tritopic benzene-1,3,5-tricarboxylic acid (btc) ligand, the acetate ligands on the paddlewheels are replaced with the carboxylate groups on btc³⁻. The paddlewheels are then linked together to form the MOF known as HKUST-1 (Cu₃btc₂).¹⁰ This general strategy of linking inorganic units into porous materials imbues the resultant material with a host of interesting properties, including high surface area, the site isolation of reactive centers, and the ability to access architectures that would not be achievable in solution-phase inorganic chemistry, such as the coordinatively unsaturated metal centers that will be discussed extensively throughout this work.

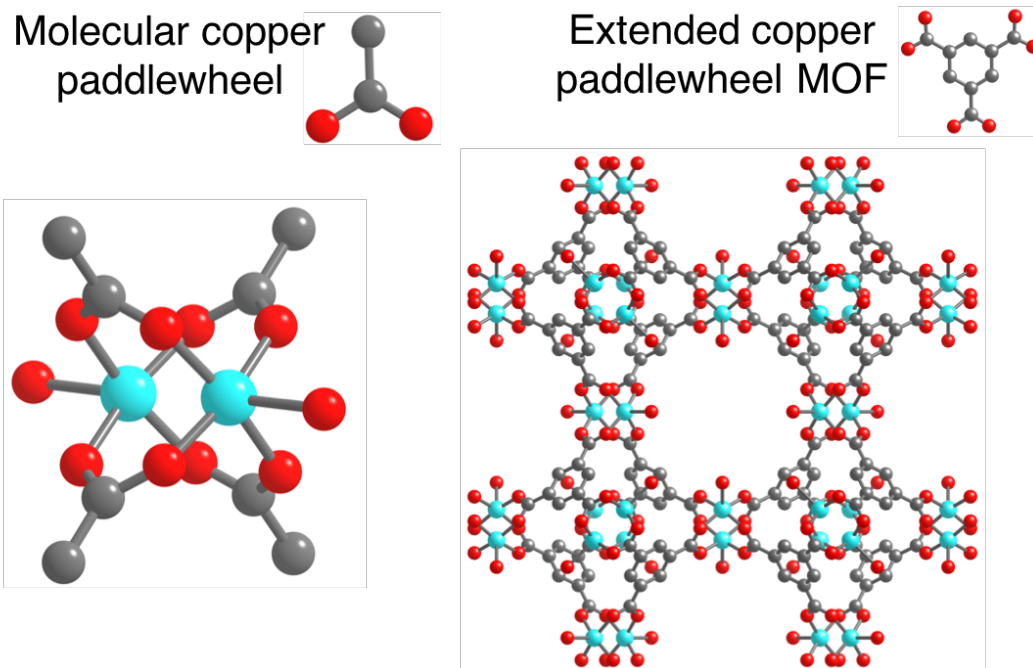


Figure 1.2. A comparison of molecular copper paddlewheels (left) formed from Cu atoms and acetate ligands and the formation of a copper paddlewheel MOF, HKUST-1 (right), by linking the acetates together in a trigonal arrangement with an aromatic ring, resulting in the linkage of the copper paddlewheels themselves into a three-dimensional porous network. Teal, red, and gray spheres represent Cu, O, and C atoms, respectively.

As such, research into porous MOF materials has exploded; approximately 70,000 MOF materials have been published in the literature (as of 2017),¹¹ which is quite remarkable given that the field has existed for less than 30 years and has only gained particular interest since the beginning of the new millennium. MOFs have been studied for a wide range of possible applications including gas storage,^{12,13,14,15} gas separations,^{16,17,18,19} solid electrolyte materials in batteries,^{20,21} catalysis,^{22,23,24} adsorptive heating and cooling,^{25,26,27} drug delivery,²⁸ photovoltaic devices,²⁹ and chemical sensing,³⁰ among others.

The primary advantage that MOFs have over other porous materials, such as zeolites and activated carbons, is their modular synthesis. MOFs have many different synthetic controls that can determine the ultimate structure that is synthesized. For example, choice of ligand and metal salt has a significant impact on the topology and connectivity of the resultant material, leading to many of the relevant properties such as thermal stability, pore size and shape, and interaction with guest species. Ligands and metal clusters can be imbued with functionalities that give the material different properties, both before and after synthesis of the parent framework. Since MOF synthesis is modular, pore size can be controlled while maintaining the same connectivity by altering the size of the ligands used, a concept known as reticular chemistry. In addition to these more conventional approaches, there are many more ways in which MOF structures can be tuned for specific applications, leading to the incredible structural variety of this class of materials.

1.2. Metal-Organic Frameworks with Open Metal Coordination Sites

It was previously mentioned that certain MOF materials contain what are known as either coordinatively unsaturated metal sites or open metal coordination sites. These are materials in which MOF formation results in at least one of the coordination sites of each metal center being occupied by a solvent molecule. Under various conditions, typically by applying vacuum and heat, these solvent molecules can be removed while retaining both the geometry around the metal center as well as the overall structure of the framework. A classic example of this is the $M_2(\text{dobdc})$ ($M^{2+} = \text{Mg, Mn, Fe, Co, Ni, Cu, Zn, Cd}$; $\text{dobdc}^{4-} = 2,5\text{-dioxido-1,4-benzenedicarboxylate}$) (variously known as M-MOF-74, CPO-27-M, and $M_2(\text{dhtp})$) series of MOFs, which are comprised of helical metal chains lining the vertices of the hexagonal pores of the MOF, linked on the sides of the hexagonal pores by the ligand (Figure 1.3).^{31,32,33,34,35,36,37,38}

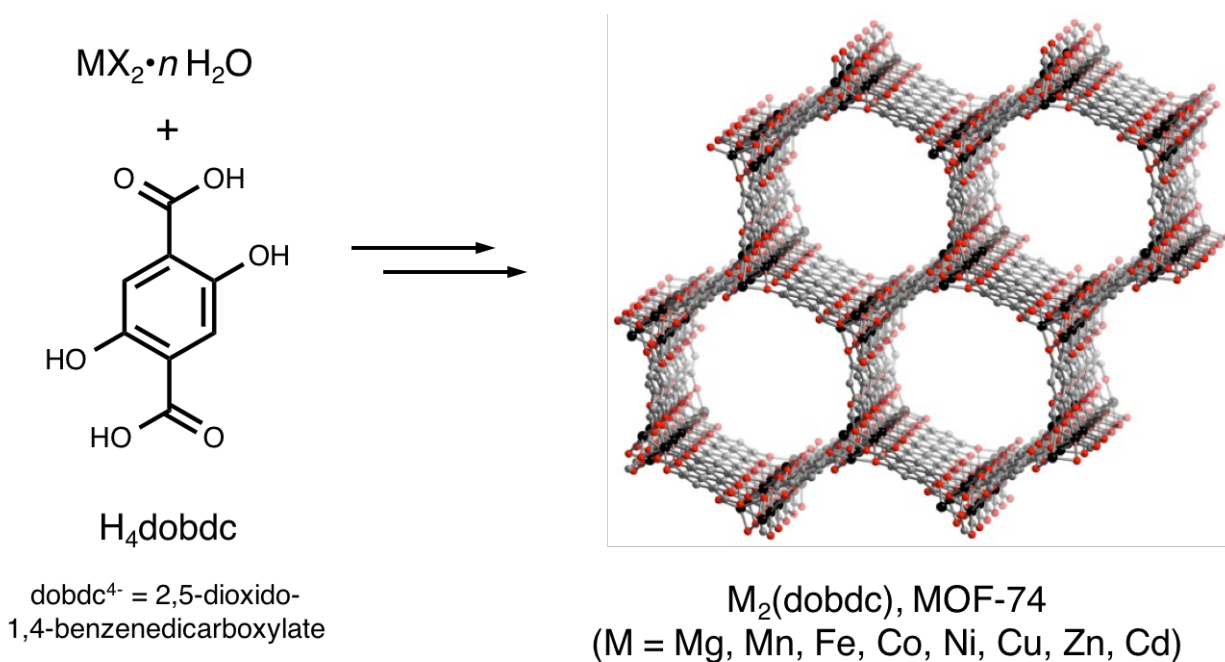


Figure 1.3. A schematic for the synthesis of the MOF $M_2(\text{dobdc})$. Black, gray, and red spheres represent M^{2+} , C, and O atoms, respectively. H atoms have been omitted.

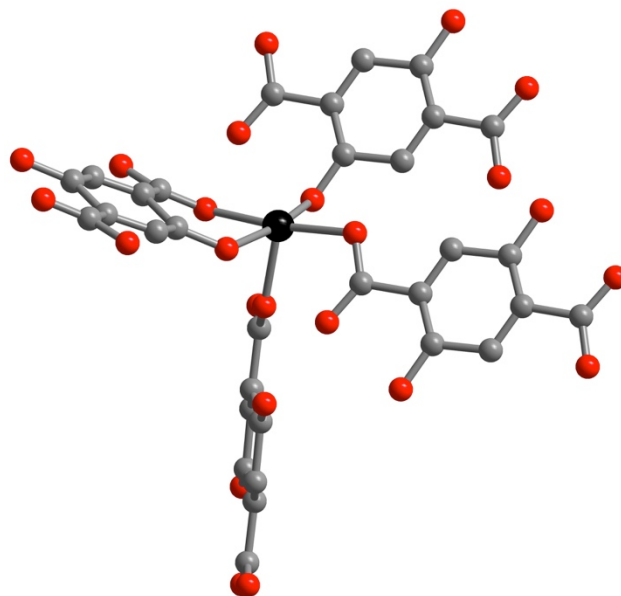


Figure 1.4. A view of the first coordination sphere of a single metal atom in the MOF $M_2(\text{dobdc})$. Note the five-coordinate, square pyramidal geometry of the metal center; the sixth coordination site points into the channel of the MOF. Black, gray, and red spheres represent M^{2+} , C, and O atoms, respectively. H atoms have been omitted.

This material is notable not only because of the open metal coordination sites that can be formed upon heating the material under vacuum, but also because of the high density of such sites, which is a result of the high charge density on the ligand. Through many studies, the open metal coordination sites have been shown to be the primary sites of interaction for nearly all guest molecules that are introduced into the pores of the framework. This interaction is typically of an electrostatic nature, with the exposed positive charge on the metal interacting strongly with the negatively charged electrons in a guest. As such, this material has been heavily studied for its use in applications including gas adsorption and gas separations, as the high density of sites able to strongly polarize guest gas molecules. Specifically, this is of potential interest in a variety of industrial applications such as hydrogen storage,^{33,35,39,40,41} natural gas storage,^{42,43} CO_2 capture,^{32,44} and hydrocarbon separations.⁴⁵

1.3. Hydrogen Storage in Metal-Organic Frameworks

Hydrogen provides promise as a clean fuel for powering small motor vehicles. In a hydrogen fuel cell, the oxidation of hydrogen produces electricity, powering a vehicle, while the concomitant reduction of protons produces only water as a byproduct. An idealized cycle could be envisioned in which hydrogen is consumed in a fuel cell to produce electricity, and subsequently regenerated from the water byproduct, completing the cycle with no waste. Given the promise of clean power from hydrogen fuel cells, there is great interest among researchers in devising ways to make systems involving hydrogen more economically viable.

In addition to the need for investment in infrastructure and clean hydrogen production, one problem with powering small vehicles using hydrogen fuel cells is the requirement for high-

pressure storage. Hydrogen is typically compressed to 350 or 700 bar for storage in current fuel cell vehicles, requiring high financial and energetic costs of compression, while simultaneously requiring heavy, bulky tanks in order to contain hydrogen at such high pressures. There is a substantial need to reduce the pressures required for storage while achieving reasonable capacities to maintain a reasonable driving range.

Metal-organic frameworks, especially those with open metal coordination sites, offer a significant opportunity to greatly reduce the pressure required for hydrogen storage by achieving high densities of stored hydrogen at lower pressures. This is accomplished through the strong interaction of hydrogen with the interior surfaces within the pores of these materials, leading to stronger interactions than those present in pure, compressed H₂. However, no material to date has met the U.S. Department of Energy 2020 H₂ storage targets (Table 1.1).⁴⁶ The need for materials that can effectively densify hydrogen to meet these targets is crucial to the widespread adoption of hydrogen fuel cell vehicles.

Table 1.1. Selected U.S. Department of Energy (DOE) targets for the onboard storage of hydrogen in light-duty vehicles.⁴⁶

Storage Parameter	Units	2020	Ultimate
System gravimetric H ₂ capacity	wt %, kg H ₂ /kg system, kWh/kg	4.5 %, 0.045, 1.5	6.5 %, 0.065, 2.2
System volumetric H ₂ capacity	g H ₂ /L system, kWh/L	30, 1.0	50, 1.7
Storage system cost	\$/kg H ₂ stored, \$/kWh net	333, 10	266, 8
Operating ambient temperature	°C	-40 to 60	-40 to 60
Min/max delivery temperature	°C	-40 to 85	-40 to 85
Operational cycle life (1/4 tank to full)	cycles	1500	1500
Min delivery pressure	bar (abs)	5	5
Max delivery pressure	bar (abs)	12	12
System fill time (5 kg)	min	3-5	3-5

Of metal-organic frameworks that have previously been studied for their hydrogen binding capabilities, there are several of note. M₂(dobdc) (M = Mg, Mn, Fe, Co, Ni, Zn) has been extensively evaluated as a hydrogen storage material, given the strong binding seen at the open metal coordination sites in this material.^{35,39,41} However, none of the M₂(dobdc) analogs meet the target H₂ binding enthalpies of -18 to -22 kJ/mol required for storage at sufficient densities.^{47,48} Another example is the MOF Cu(I)-MFU-4l, which has a very high H₂ binding enthalpy of -32 kJ/mol at the Cu(I) centers in the pores,⁴⁹ yet does not have a high capacity due to the low density of these binding sites. Research in MOFs for hydrogen storage must center around achieving a high density of strong binding sites in the pores in order to sufficiently densify hydrogen for on-board storage, in addition to studying the MOFs under relevant conditions for hydrogen storage.

1.4. Gas Separations in Metal-Organic Frameworks

The use of metal-organic frameworks as adsorbents for the separation of mixtures of gases has also been studied quite extensively.^{16,50,51} MOFs take advantage of the different strengths of interaction that two or more adsorbates in a mixture have with its interior pore surfaces and can thus separate the mixture. Notably, these adsorptive-based separations can often be accomplished at pressures relatively close to ambient, obviating the need for large energy inputs such as in the cryogenic distillation processes often used in the petroleum industry.

There are multiple mechanisms by which an adsorptive-based separation can take place. The most basic example is by leveraging the different strengths of interaction that multiple adsorbates have with the interior surfaces in order to achieve a separation. This method typically allows for fast kinetics and capacity but suffers from weak selectivity due to the difficulty in differentiating between similar molecules in a mixture. A second mechanism that can operate in porous materials is sieving, in which certain components of the mixture to be separated are excluded from the pores entirely due to their size or shape. This method leads to high (sometimes infinite) selectivities but typically suffers from low working capacities and slow diffusion of adsorbates through the pores of the adsorbent. Unique mechanisms involving phase-change materials are possible, such as previous work on amine-appended MOFs for CO₂ capture.⁵² Other mechanisms are possible, including those which rely on flexible materials to selectively open pores in response to incident gas pressure, but those are outside the scope of this work. Ideally, an adsorptive based separation would achieve some combination of high selectivity for an adsorbate mixture that is of interest while simultaneously allowing rapid diffusion of the mixture through the pores.

1.4.1. Separation of Olefin/Paraffin Mixtures. Olefins, especially the high-value chemicals ethylene and propylene, are ubiquitous in the synthesis of plastics. During production, small olefins are produced as a mixture with the corresponding paraffins. Separations of several of these mixtures are some of the most energy-intensive processes that humans conduct, requiring very large distillation columns and energy inputs. All distillation-based separations in total use nearly 8% of the United States' total energy consumption annually,⁵³ of which olefin/paraffin separations is a major component. Adsorptive-based separations of olefin/paraffin mixtures provide a much more energy-efficient alternative. For example, a previous study on olefin/paraffin separations in the open metal site-containing MOF Fe₂(dobdc) showed IAST selectivities as high as 18 for equimolar ethylene/ethane and 15 for equimolar propylene/propane at 318 K.⁴⁵ Further studies demonstrated that the Fe₂(dobdc) analog has the highest selectivity among the M₂(dobdc) series for ethylene/ethane and the second highest, to Mn₂(dobdc), for propylene/propane.⁵⁴

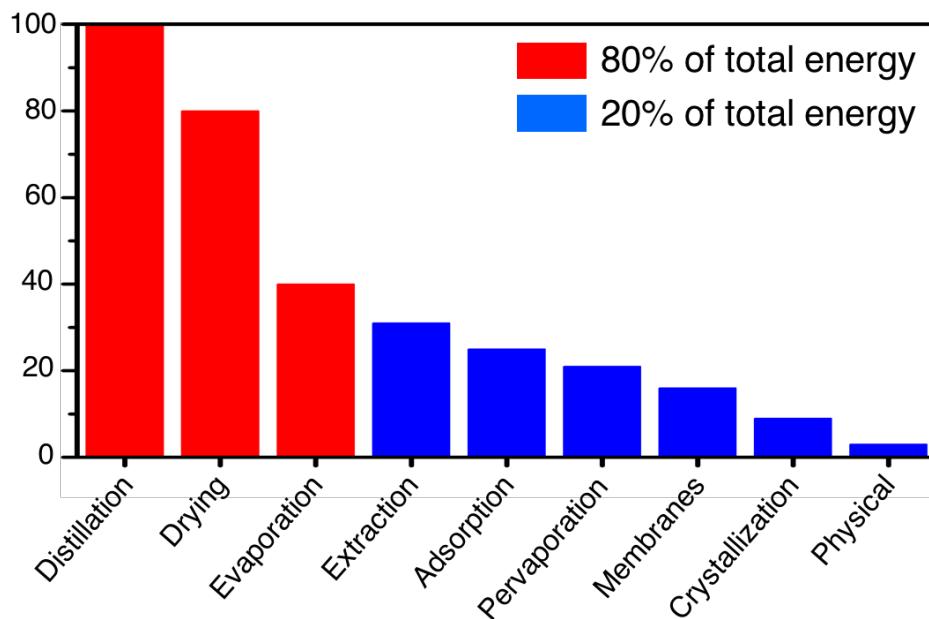
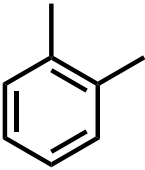
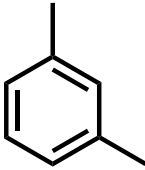

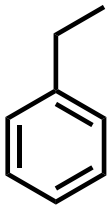


Figure 1.5. Relative energy consumption of industrial separations in the United States.⁵⁵ The three bars in red are all thermally-driven separations and account for approximately 80% of energy used on industrial separations; replacing these with physical separations, such as adsorption, would provide significant energy savings.

1.4.2. Separation of Xylene Isomers (C_8 Alkylaromatics). Another hydrocarbon separation of great importance to the chemical industry is that of xylene isomer mixtures, *o*-, *m*-, and *p*-xylene as well as ethylbenzene, in approximately a 1:2:1:1 ratio, respectively. The *p*-xylene isomer especially is in high demand; in 2008, production of this isomer was 33.0 Mt, accounting for 84% of total xylenes production. This *p*-xylene was primarily used as a precursor in the production of terephthalic acid for the synthesis of polyesters and polyamides. While ethylbenzene is also heavily produced for the production of polystyrenes, production of this isomer is almost exclusively from the reaction of ethylene and benzene and not from separation out of this mixture. Since the feed composition does not match demand, separation of this mixture must occur to primarily obtain *p*-xylene, with the majority of the remaining portion being reisolomerized to equilibrium. MOFs have been studied for this separation previously, including MIL-47 (V(O)(bdc); bdc²⁻ = 1,4-benzenedicarboxylate)^{56,57} and MIL-53-M (M(OH)(bdc); M = Al, Fe).⁵⁸ These materials completed the separation of the xylenes mixtures through the use of differences in the isomer packing and adsorbate-adsorbate interactions. Another study in Ni₂(dobdc) showed separation of binary mixtures of xylenes, but a full understanding of the mechanism behind the separation was not developed.⁵⁹ Finding other porous materials capable of the separation of these components could be advantageous to the chemical industry.

Table 1.2. A summary of the properties of the components in the C₈ alkylaromatics (xylenes plus ethylbenzene) mixture.

				
Name	<i>o</i> -xylene	<i>m</i> -xylene	<i>p</i> -xylene	ethylbenzene
Annual Production (Mt)	3.6	0.4	33	24.7
Boiling Point (°C)	144.4	139.2	138.4	136.2

1.4.3. Separation of Acetylene/Ethylene. Another hydrocarbon separation of interest is that of the separation of acetylene (C₂H₂) from ethylene (C₂H₄). Practical uses of this separation revolve around the separation of trace amounts of acetylene from ethylene prior to polymerization in order to avoid poisoning of polymerization catalysts *via* acetylene binding. Furthermore, adsorptive-based separations of this mixture are of academic interest due to the relatively similar properties of these two gases, including their electronic unsaturation and similar kinetic diameter. Several studies have explored this separation, primarily based on small-pore MOFs that complete the separation based on packing differences between the two molecules. For example, one member of the SIFSIX (SIFSIX = hexafluorosilicate, SiF₆²⁻) family of metal-organic frameworks, SIFSIX-2-Cu-i (2 = 4,4'-dipyridylacetylene; i = interpenetrated), shows selectivities for binding acetylene over ethylene exceeding 40 for various acetylene/ethylene molar ratios.⁶⁰ Metal-organic frameworks with coordinatively unsaturated metal centers, such as Fe₂(dobdc), typically perform poorly in this separation due to the similar strengths of interaction that the unsaturated acetylene and ethylene have with the open metal coordination sites.⁴⁵ The study of this particular separation in porous materials has been limited in scope, however, and further efforts are warranted to develop new strategies for completing this separation.

1.5. References

1. Zhou, H.-C.; Long, J. R.; Yaghi, O. M.; *Chem. Rev.* **2012**, *112*, 673.
2. Farha, O. K.; Eryazici, I.; Jeong, N. C.; Hauser, B. G.; Wilmer, C. E.; Sarjeant, A. A.; Snurr, R. Q.; Nguyen, S. T.; Yazaydin, A. Ö.; Hupp, J. T. *J. Am. Chem. Soc.* **2012**, *134*, 15016.
3. Hoskins, B. F.; Robson, R. *J. Am. Chem. Soc.* **1989**, *111*, 5962.
4. Hoskins, B. F.; Robson, R. *J. Am. Chem. Soc.* **1990**, *112*, 1546.
5. Yaghi, O. M.; Li, G.; Groy, T. L. *J. Solid State Chem.* **1995**, *117*, 256.
6. Yaghi, O. M.; Li, H. *J. Am. Chem. Soc.* **1995**, *117*, 10401.
7. Yaghi, O. M.; Li, G.; Li, H. *Nature* **1995**, *378*, 703.

8. Kondo, M.; Yoshitomi, T.; Seki, K.; Matsuzaka, H.; Kitagawa, S. *Angew. Chem. Int. Ed.* **1997**, *36*, 1725.
9. Li, H.; Eddaoudi, M.; O’Keeffe, M. Yaghi, O. M. *Nature* **1999**, *402*, 276.
10. Chui, S. S.-Y.; Lo, S. M.-F.; Charmant, J. P. H.; Orpen, A. G.; Williams, I. D. *Science* **1999**, *283*, 1148.
11. Moghadam, P. Z.; Li, A.; Wiggin, S. B.; Tao, A.; Maloney, A. G. P.; Wood, P. A.; Ward, S. C.; Fairen-Jimenez, D. *Chem. Mater.* **2017**, *29*, 2618.
12. Murray, L. J.; Dincă, M.; Long, J. R. *Chem. Soc. Rev.* **2009**, *38*, 1294.
13. Suh, M. P.; Park, H. J.; Prasad, T.; Lim, D.-W. *Chem. Rev.* **2012**, *112*, 782.
14. Mason, J. A.; Veenstra, M.; Long, J. R. *Chem. Sci.* **2014**, *5*, 32.
15. He, Y.; Zhou, W.; Qian, G.; Chen, B. *Chem. Soc. Rev.* **2014**, *43*, 5657.
16. Li, J.-R.; Kuppler, R. J.; Zhou, H.-C. *Chem. Soc. Rev.* **2009**, *38*, 1477.
17. Herm, Z. R.; Bloch, E. D.; Long, J. R. *Chem. Mater.* **2014**, *26*, 323.
18. McDonald, T. M.; Mason, J. A.; Kong, X.; Bloch, E. D.; Gygi, D.; Dani, A.; Crocellà, V.; Giordanino, F.; Odoh, S. O.; Drisdell, W. S.; Vlaisavljevich, B.; Dzubak, A. L.; Poloni, R.; Schnell, S. K.; Planas, N.; Lee, K.; Pascal, T.; Wan, L. F.; Prendergast, D.; Neaton, J. B.; Smit, B.; Kortright, J. B.; Gagliardi, L.; Bordgia, S.; Reimer, J. A.; Long, J. R. *Nature* **2015**, *519*, 303.
19. Adil, K.; Belmabkhout, Y.; Pillai, R. S.; Cadiau, A.; Bhatt, P. M.; Assen, A. H.; Maurin, D.; Eddaoudi, M. *Chem. Soc. Rev.* **2017**, *46*, 3402.
20. Aubrey, M. L.; Long, J. R. *J. Am. Chem. Soc.* **2015**, *137*, 13594.
21. Wang, L.; Han, Y.; Feng, X.; Zhou, J.; Qi, P.; Wang, B. *Coord. Chem. Rev.* **2016**, *307*, 361.
22. Lee, J.; Farha, O. K.; Roberts, J.; Scheidt, K. A.; Nguyen, S. T.; Hupp, J. T. *Chem. Soc. Rev.* **2009**, *38*, 1450.
23. Chughtai, A. H.; Ahmad, N.; Younus, H. A.; Laypkov, A.; Verpoort, F. *Chem. Soc. Rev.* **2015**, *44*, 6804.
24. Rogge, S. M. J.; Bavykina, B.; Hajek, J.; Garcia, H.; Olivos-Suarez, A. I.; Sepúlveda-Escribano, A.; Vimont, A.; Clet, G.; Bazin, P.; Kapteijn, F.; Daturi, M.; Ramos-Fernandez, E. V.; Llabrés I Xamena, F. X.; Van Speybroeck, V.; Gascon, J. *Chem. Soc. Rev.* **2017**, *46*, 3134.
25. Canivet, J.; Fateeva, A.; Guo, Y.; Coasne, B.; Farrusseng, D. *Chem. Soc. Rev.* **2014**, *43*, 5594.
26. de Lange, M. F.; Verouden, K. J. F. M.; Blugt, T. J. H.; Gascon, J.; Kapteijn, F. *Chem. Rev.* **2015**, *115*, 12205.
27. Nguyen, B. T.; Bguyen, H. L.; Nguyen, T. C.; Cordova, K. E.; Furukawa, H. *Chem. Mater.* **2016**, *28*, 6243.
28. Wang, L.; Zheng, M.; Xie, Z. *J. Mater. Chem B*, **2018**, Advance Article.
29. Kaur, R.; Kim, K.-H.; Paul, A. K.; Deep, A. *J. Mater. Chem. A* **2016**, *4*, 3991.
30. Lustig, W. P.; Mukherjee, S.; Rudd, N. D.; Desai, A. V.; Li, J.; Ghosh, S. K. *Chem. Soc. Rev.* **2017**, *46*, 3242.
31. Rosi, N. L.; Kim, J.; Eddaoudi, M.; Chen, B.; O’Keeffe, M.; Yaghi, O. M. *J. Am. Chem. Soc.* **2005**, *127*, 1504.
32. Dietzel, P. D. C.; Morita, Y.; Blom, R.; Fjellvåg, H. *Angew. Chem. Int. Ed.* **2005**, *44*, 6354.

33. Dietzel, P. D. C.; Panella, B.; Hirscher, M.; Blom, R.; Fjellvåg, H. *Chem. Commun.* **2006**, 959.
34. Caskey, S. R.; Wong-Foy, A. G.; Matzger, A. H. *J. Am. Chem. Soc.* **2008**, *130*, 10870.
35. Zhou, W.; Wu, H.; Yildirim, T. *J. Am. Chem. Soc.* **2008**, *130*, 15268.
36. Bloch, E. D.; Murray, L. J.; Queen, W. L.; Chavan, S.; Maximoff, S. N.; Bigi, J. P.; Krishna, R.; Peterson, V. K.; Grandjean, F.; Long, G. J.; Smit, B.; Bordiga, S.; Brown, C. M.; Long, J. R. *J. Am. Chem. Soc.* **2011**, *133*, 14814.
37. Sanz, R.; Martínez, F.; Orcaho, G.; Wojtas, L.; Briones, D. *Dalton Trans.* **2013**, *42*, 2392.
38. Díaz-García, M.; Sánchez-Sánchez, M. *Microporous Mesoporous Mater.* **2014**, *190*, 248.
39. Queen, W. L.; Bloch, E. D.; Brown, C. M.; Hudson, M. R.; Mason, J. A.; Murray, L. J.; Ramirez-Cuesta, A. J.; Peterson, V. K.; Long, J. R. *Dalton Trans.* **2012**, *41*, 4180.
40. Liu, Y.; Kabbour, H.; Brown, C. M.; Neumann, D. A.; Ahn, C. C. *Langmuir* **2008**, *24*, 4772.
41. Sumida, K.; Brown, C. M.; Herm, Z. R.; Chavan, S.; Bordiga, S.; Long, J. R. *Chem. Commun.* **2011**, *47*, 1157.
42. Wu, H.; Zhou, W.; Yildirim, T. *J. Am. Chem. Soc.* **2009**, *131*, 4995.
43. Dietzel, P. D. C.; Besikiotis, V.; Blom, R. *J. Mater. Chem.* **2009**, *19*, 7362.
44. Dietzel, P. D. C.; Johnsen, R. E.; Fjellvåg, H.; Bordiga, S.; Groppe, E.; Chavan, S.; Blom, R. *Chem. Commun.* **2008**, 5125.
45. Bloch, E. D.; Queen, W. L.; Krishna, R.; Zadrozny, J. M.; Brown, C. M.; Long, J. R. *Science* **2012**, *335*, 1606.
46. DOE Technical Targets for Onboard Hydrogen Storage for Light-Duty Vehicles, <https://energy.gov/eere/fuelcells/doe-technical-targets-onboard-hydrogen-storage-light-duty-vehicles>, (accessed Jan. 2018).
47. Bae, Y.-S.; Snurr, R. Q. *Microporous Mesoporous Mater.* **2010**, *132*, 300.
48. Areán, C. O.; Chavan, S.; Cabello, C. P.; Garrone, E.; Palomino, G. T. *Chem. Phys. Chem.* **2010**, *11*, 3237.
49. Denysenko, D.; Grzywa, M.; Jelic, J.; Reuter, K.; Volkmer, D. *Angew. Chem. Int. Ed.*, **2014**, *53*, 5832.
50. Li, J.-R.; Sculley, J.; Zhou, H.-C. *Chem Rev.* **2012**, *112*, 869.
51. Van de Voorde, B.; Bueken, B.; Denayer, J.; De Vos, D. *Chem. Soc. Rev.* **2014**, *43*, 5766.
52. McDonald, T. M.; Mason, J. A.; Kong, X.; Bloch, E. D.; Gygi, D.; Dani, A.; Crocella, V.; Giordanino, F.; Odoh, S. O.; Drisdell, W.; Vlaisavljevich, B.; Dzubak, A. L.; Poloni, R.; Schnell, S. K.; Planas, N.; Lee, K.; Pascal, T.; Wan, L. F.; Prendergast, D.; Neaton, J. B.; Smit, B.; Kortright, J. B.; Gagliardi, L.; Bordiga, S.; Reimer, J. A.; Long, J. R. *Nature* **2015**, *519*, 303-308.
53. Scholl, D. S.; Lively, R. P. *Nature* **2016**, *532*, 435.
54. Geier, S. J.; Mason, J. A.; Bloch, E. D.; Queen, W. L.; Hudson, M. R.; Brown, C. M.; Long, J. R. *Chem. Sci.* **2013**, *4*, 2054.
55. U.S. Department of Energy. Materials for Separation Technology: Energy and Emission Reduction Opportunities (2005).
56. Alaerts, L.; Kirschhock, C. E. A.; Maes, M.; van der Veen, M. A.; Finsy, V.; Depla, A.; Martens, J. A.; Baron, G. V.; Jacobs, P. A.; Denayer, J. F. M.; De Vos, D. E. *Angew. Chem. Int. Ed.* **2007**, *46*, 4293.

57. Alaerts, L.; Maes, M.; Jacobs, P. A.; Denayer, J. F. M.; De Vos, D. E. *Phys. Chem. Chem. Phys.* **2008**, *10*, 2979.
58. Alaerts, L.; Maes, M.; Giebler, L.; Jacobs, P. A.; Martens, J. A.; Denayer, J. F. M.; Kirschhock, C. E. A.; De Vos, D. E. *J. Am. Chem. Soc.* **2008**, *130*, 14170.
59. Peralta, D.; Barthelet, K.; Pérez-Pellitero, J.; Chizallet, C.; Chaplais, G.; Simon-Masseron, A.; Pirngruber, G. D. *J. Phys. Chem. C* **2012**, *116* 21844.
60. Cui, X; Chen, K.; Xing, H.; Yang, Q.; Krishna, R.; Bao, Z.; Wu, H.; Zhou, W.; Dong, X.; Han, Y.; Li, B.; Ren, Q.; Zaworotko, M. J.; Chen, B. *Science* **2016**, *353*, 141.

Chapter 2: $M_2(m\text{-dobdc})$ ($M = \text{Mg, Mn, Fe, Co, Ni}$) Metal-Organic Frameworks Exhibiting Increased Charge Density and Enhanced H_2 Binding at the Open Metal Sites

2.1. Introduction

Metal-organic frameworks are a well-known class of porous materials comprised of inorganic units bridged by coordinating organic linkers. In addition to possessing high internal surface areas, their physical and chemical properties can be tuned for specific applications by judicious choice of the metal center and organic ligand. These properties lead to applications in storing and separating gases, in which it is particularly important to have precise control over the strength and specificity of interactions between the pore surface and various potential adsorbates.¹ Indeed, strong adsorption sites are often installed on the pore surface in order to attract specific gas molecules selectively for separation applications or to increase the density of gas molecules present for storage applications.^{1h,1j,2}

Exposed metal cations represent an important example of strong adsorption sites that have been realized in many metal-organic frameworks.³ These Lewis acidic sites, which are typically formed by removing metal-coordinated solvent molecules upon heating under reduced pressure, are highly polarizing and have strong interactions with many small gas molecules.^{3a,4} For example, the well-established $M_2(\text{dobdc})$ ($M = \text{Mg, Mn, Fe, Co, Ni, Cu, Zn}$; $\text{dobdc}^{4-} = 2,5\text{-dioxido-1,4-benzenedicarboxylate}$) structure type, also known as M-MOF-74, CPO-27-M, or $M_2(\text{dhtp})$,⁵ contains a high density of exposed metal cations and is especially promising for the storage of a wide variety of gases. As a result of its compact, highly charged tetraanionic linker, this framework is endowed with an exceptionally high density of open metal coordination sites, which are the primary binding sites for small gas molecules such as H_2 , CH_4 , C_2H_4 , and CO_2 . Consequently, $M_2(\text{dobdc})$ frameworks have been investigated for numerous potential applications involving gas adsorption, including H_2 storage,^{3a,4a,4c,6} methane storage,^{4b,7} CO_2 capture,⁸ and hydrocarbon separations.^{1i,9} All of these applications take advantage of strong interactions between gas molecules and exposed metal cations.

Discovering new frameworks with a high density of open metal coordination sites is not trivial, as it is difficult to predict what topologies will form with partial solvation of the metal nodes and will then further be amenable to desolvation. Rather, selectively tuning the most promising of the numerous existing frameworks by altering the linker, the metal, or both provides a viable strategy for developing promising new adsorbents. Since the $M_2(\text{dobdc})$ series of frameworks has high chemical and thermal stability^{8b,10} and has been shown to be outstanding for binding a high capacity of small gas molecules, we hoped to modify this framework by tuning the electronics of the exposed metal cations, which should subsequently tune the affinity for different gas molecules. For example, the binding of H_2 or CH_4 might be enhanced by increasing the positive charge density at the metal cation site, thus increasing its ability to polarize and bind adsorbing gas molecules more strongly. Furthermore, $M_2(\text{dobdc})$ offers the advantage of being an isostructural series of frameworks that can be formed with a variety of metals, thereby offering an additional level of control for tuning the framework for specific interactions. Based on the high density of exposed metal cations, isostructural nature of the these frameworks, and thermal stability, a combination of properties that is not paralleled by any other structure type, $M_2(\text{dobdc})$ provides an ideal platform for exploring the tunability of metal-organic frameworks to strengthen framework–gas interactions.

This chapter outlines the synthesis of a structural isomer of the $M_2(\text{dobdc})$ framework, which will be referred to as $M_2(m\text{-dobdc})$ ($m\text{-dobdc}^{4-} = 4,6\text{-dioxido-1,3-benzenedicarboxylate}$). Rather than having *para* carboxylic acid functionalities and *para* hydroxyl substituents, as in the regular $H_4\text{dobdc}$ linker, $H_4(m\text{-dobdc})$ has *meta* carboxylic acid groups and *meta* hydroxyl substituents. The $H_4(m\text{-dobdc})$ linker was targeted due to its ease of synthesis and potentially low cost. Indeed, a solvent-free Kolbe-Schmitt reaction to produce $H_4(m\text{-dobdc})$ using only resorcinol, KHCO_3 , and CO_2 is efficient and inexpensive. In spite of this linker isomerism, it is still possible to form a framework with a similar overall structure, replete with one-dimensional hexagonal channels and a high density of open metal coordination sites. This structural isomerism takes advantage of the fact that $M_2(\text{dobdc})$ frameworks have multiple types of coordinating functional groups in the linker, which is a rarity among most well-known metal-organic frameworks.

The resulting new framework has subtle differences in the electronic structure of the ligand and overall connectivity as compared to the $M_2(\text{dobdc})$ framework, which might be expected to influence interactions with small gas molecules by changing the local environment around the open metal coordination sites. Isomers of metal-organic frameworks are known and primarily derive from what are termed “framework isomers.” The structure of $M_2(m\text{-dobdc})$, however, is an example of a ligand-originated isomer.¹¹ Relatedly, a recent $M_2(\text{dobdc})$ analogue was synthesized with thiols rather than phenols,¹² but a purely structural isomer of $M_2(\text{dobdc})$ has never before been synthesized.

Here, H_2 adsorption is used as a probe to determine whether this new framework exhibits enhanced gas adsorption properties. The choice of H_2 as a probe molecule originates from its simplicity, low polarizability, and potential use as a clean, renewable fuel.^{2a,13} Through the use of H_2 adsorption isotherms, powder neutron diffraction, inelastic neutron scattering, infrared spectroscopy, and first-principles electronic structure calculations, we provide a careful comparison of the differences between $M_2(\text{dobdc})$ and $M_2(m\text{-dobdc})$ that contribute to the differences in their H_2 adsorption properties.

2.2. Experimental

2.2.1. General Considerations. Methanol was purchased from commercial vendors, further dried over molecular sieves, and deoxygenated by purging with N_2 . All other reagents were purchased from commercial vendors and used without further purification, unless otherwise noted.

2.2.2. Synthesis of $H_4(m\text{-dobdc})$. Resorcinol (1,3-dihydroxybenzene; 37.6 g, 0.341 mol) was pulverized and dried under vacuum. KHCO_3 (100 g, 0.99 mmol) was separately pulverized and dried under reduced pressure. The two powders were mixed together thoroughly and placed in a glass jar, which was sealed in a Parr reaction bomb equipped with an internal thermocouple and a pressure gauge. The reaction bomb was evacuated under vacuum and then CO_2 was dosed to a pressure of 40 bar. The bomb was heated to 250 °C (as measured by the internal thermocouple) in a sand bath for 24 h and then slowly cooled to room temperature. The pressure was vented and 1 L of water was added to the solid, which was broken up mechanically and the mixture was sonicated. The resulting suspension was filtered, and the filtrate was acidified with 12 M HCl until a pH < 2 was achieved and a white solid had precipitated. This solid was collected by filtration and dried in air to yield 53.2 g (79 %) of product. ^1H NMR (400 MHz,

DMSO- d_6) δ 9.22 (br, 4H), 8.28 (s, 1H), 6.22 (s, 1H); ^{13}C NMR (400 MHz, DMSO- d_6) δ 172.0, 167.7, 134.3, 107.3, 103.0.

2.2.3. Synthesis of $\text{M}_2(m\text{-dobdc})$ ($\text{M} = \text{Mn, Fe, Co, Ni}$). Anhydrous MCl_2 (3.0 mmol) and $\text{H}_4(m\text{-dobdc})$ (240 mg, 1.2 mmol) were added to 80 mL of a mixed solvent ($x\%$ MeOH by volume in dimethylformamide (DMF), where for Mn, $x = 15$; Fe, $x = 15$; Co, $x = 50$; Ni, $x = 35$) in a nitrogen-filled glove box for $\text{M} = \text{Mn, Fe}$ and in air for $\text{M} = \text{Co, Ni}$. The solution was dispensed into eight 20-mL scintillation vials, which were each sealed with a PTFE-lined cap and heated at 120 °C for 18 h. The resulting solid from each vial was combined, submerged in 20 mL of DMF, and heated at 70 °C for 24 h. The DMF was decanted and replaced with 20 mL of methanol. The resulting suspension was heated at 70 °C for 4 days, during which time the methanol was replaced every 24 h. The material was activated by heating it at 150 °C under dynamic vacuum on a Schlenk line for 12 h, followed by further activation of a small amount of the sample by heating the solid under dynamic vacuum ($<10 \mu\text{bar}$) at 180 °C (160 °C for $\text{Fe}_2(m\text{-dobdc})$) for 24 h at a ramp rate of 0.5 °C/min. It should be noted that larger scale syntheses of $\text{Co}_2(m\text{-dobdc})$ and $\text{Ni}_2(m\text{-dobdc})$ were also accomplished with no loss in crystallinity or surface area by stirring at room temperature in a round-bottom flask equipped with a reflux condenser at a concentration of 20.2 mmol $\text{H}_4(m\text{-dobdc})$ and 50.5 mmol MCl_2 ($\text{M} = \text{Co, Ni}$) in 1250 mL solvent. Times and temperatures were identical to the small-scale synthesis, but 200 mL of solvent was used for each exchange.

$\text{Mn}_2(m\text{-dobdc})$: Synthesis yielded a pink solid that remained pink upon evacuation. IR (neat): 1602 (s), 1547 (s), 1486 (m), 1454 (m), 1387 (s), 1338 (m), 1284 (s), 1172 (s), 1088 (w), 884 (w), 866 (w), 729 (m), 659 (w), 626 (s); Anal. Calcd for $\text{Mn}_2\text{C}_8\text{H}_2\text{O}_6$: C, 31.61; H, 0.66. Found: C, 31.68; H, 0.74.

$\text{Fe}_2(m\text{-dobdc})$: Synthesis yielded a beige powder that turned brown upon evacuation. IR (neat): 1605 (m), 1544 (s), 1488 (m), 1453 (m), 1392 (s), 1288 (s), 1164 (s), 1090 (w), 889 (w), 868 (w), 836 (w), 813 (w), 791 (w), 775 (w), 735 (m), 699 (m), 663 (w), 629 (s); Anal. Calcd for $\text{C}_8\text{H}_2\text{Fe}_2\text{O}_6$: C, 31.42; H, 0.66. Found: C, 31.77; H, 0.98.

$\text{Co}_2(m\text{-dobdc})$: Synthesis yielded a pink solid that turned deep purple upon evacuation. IR (neat): 1600 (s), 1555 (s), 1484 (m), 1451 (m), 1390 (s), 1345 (w), 1284 (s), 1167 (s), 1088 (w), 886 (w), 869 (w), 736 (m), 629 (s); Anal. Calcd for $\text{C}_8\text{H}_2\text{Co}_2\text{O}_6$: C, 30.80; H, 0.65. Found: C, 31.60; H, 0.68.

$\text{Ni}_2(m\text{-dobdc})$: Synthesis yielded a green solid that turned a dark yellow-brown upon evacuation. IR (neat): 1600 (m), 1555 (s), 1489 (w), 1449 (m), 1381 (s), 1342 (m), 1285 (s), 1168 (s), 1088 (w), 1012 (w), 871 (w), 741 (m), 631 (m); Anal. Calcd for $\text{C}_8\text{H}_2\text{Ni}_2\text{O}_6$: C, 30.85; H, 0.65. Found: C, 31.26; H, 0.60.

2.2.4. Synthesis of $\text{Mg}_2(m\text{-dobdc})$. This compound was synthesized in air in a round-bottom flask by adding 300 mg of $\text{Mg}(\text{NO}_3)_2 \cdot 6\text{H}_2\text{O}$ and 93 mg of $\text{H}_4(m\text{-dobdc})$ to 14 mL MeOH in 31 mL DMF and stirring at 120 °C for 8 h, then filtering off the resulting solid.

2.2.5. Physical Measurements. Thermogravimetric analyses were carried out at a ramp rate of 2 °C/min under a 25 mL/min N_2 flow with a TA Instruments TGA Q5000. Infrared spectra were collected on a Perkin-Elmer Avance Spectrum 400 FTIR spectrometer equipped with a Pike attenuated total reflectance (ATR) accessory. Diffraction data were collected with 0.02° steps using a Bruker AXS D8 Advance diffractometer equipped with Cu-K α radiation ($\lambda =$

1.5418 Å), a Göbel mirror, a Lynxeye linear position-sensitive director, and mounting the following optics: fixed divergence slit (0.6 mm), receiving slit (3 mm), and secondary beam Soller slits (2.5°). The generator was set at 40 kV and 40 mA. Samples were either loaded on zero background sample holders or packed into air-free capillaries in a nitrogen-filled glove box and mounted using a capillary stage. Elemental analyses were obtained from the Microanalytical Laboratory of the University of California, Berkeley.

2.2.6. Gas Adsorption Measurements. Gas adsorption isotherms for pressures in the range 0–1.2 bar were measured using a volumetric method using either a Micromeritics ASAP2020 or ASAP2420 instrument. Samples were transferred under a dinitrogen atmosphere to preweighed analysis tubes, then capped with a Transeal. The samples were evacuated at elevated temperature until the outgas rate was less than 1 μ bar/min, at which point the tube was weighed to determine the mass of the activated sample, which was typically 50–200 mg. The tube was transferred to the analysis port of the instrument and the outgas rate was again checked to ensure that it was less than 1 μ bar/min. UHP-grade (99.999% purity) N₂, H₂, and He were used for all adsorption measurements. For all isotherms, warm and cold free spaces were measured using He; N₂ and H₂ isotherms at 77 K and 87 K were measured in liquid nitrogen and liquid argon baths, respectively. Oil-free vacuum pumps and oil-free pressure regulators were used for all measurements. Brunauer-Emmett-Teller (BET) and Langmuir surface areas were determined from N₂ adsorption data at 77 K using Micromeritics software.

The dual-site Langmuir-Freundlich expression (Equation 1) was used to independently fit the combined isotherm data at 77 K and 87 K for Mn₂(*m*-dobdc), Fe₂(*m*-dobdc), and Co₂(*m*-dobdc), where n is the amount adsorbed (mmol/g), q_{sat} is the saturation loading for site A or B (mmol/g), b is the Langmuir parameter associated with either site A or B (bar^{- ν}), p is the pressure, and ν is a constant.

$$n = \frac{q_{\text{sat},A} b_A p^{\nu_A}}{1 + b_A p^{\nu_A}} + \frac{q_{\text{sat},B} b_B p^{\nu_B}}{1 + b_B p^{\nu_B}} \quad (1)$$

This equation provides the best fit for adsorption in metal-organic frameworks with exposed metal sites and is accurate at both low- and high-pressure extremes; the fits given are generally much better than those using the virial method.¹⁸ It should be noted that the Tóth equation was also explored for fitting isotherms based on a report that it was more accurate at extreme pressures,¹⁴ but essentially equivalently accurate fits were found.

The Ni₂(*m*-dobdc) and Ni₂(dobdc) data were fit with the tri-site Langmuir expression (Equation 2). The data at 77 K and 87 K was fit simultaneously for each sample, respectively. This fitting method was necessary to find a quality fit due to the extreme steepness in the low-pressure regime of the isotherm data, which led to inadequate fits with the dual-site Langmuir-Freundlich expression being fit at each temperature independently. In the Langmuir expression, q_{sat} is the saturation loading for site A, B, or C (mmol/g), b is the Langmuir parameter associated with site A, B, or C (bar⁻¹), and p is the pressure. The value for b is calculated per equation 3.

$$n = \frac{q_{\text{sat},A} b_A p}{1 + b_A p} + \frac{q_{\text{sat},B} b_B p}{1 + b_B p} + \frac{q_{\text{sat},C} b_C p}{1 + b_C p} \quad (2)$$

$$b = b_0 e^{\frac{-E}{RT}} \quad (3)$$

The equation was fit using the statistical software package of OriginPro 8. The quality of fits was determined by comparing the adjusted R^2 and residual sum of squares values, as well as by visual inspection. Wolfram Mathematica 7 was then used to create a series of data points corresponding to points on the fit curve. The isosteric heat of adsorption Q_{st} was then calculated using the data points from Mathematica for both the 77 K and 87 K isotherms using the Clausius-Clapeyron relation (Equation 4) at equivalent loadings (n , mmol/g). Q_{st} is the isosteric heat of adsorption (kJ/mol), R is the gas constant (L*bar/[mol*K]), and P is the pressure at a given n at either T_2 (87 K) or T_1 (77 K).

$$Q_{st} = - \frac{R[\ln(P_{T_2}) - \ln(P_{T_1})]}{T_2^{-1} - T_1^{-1}} \quad (4)$$

2.2.7. Powder Neutron and X-ray Diffraction Experiments. Neutron powder diffraction (NPD) experiments were carried out on 0.8358, 0.9567, and 0.9702 g activated $\text{Co}_2(m\text{-dobdc})$, $\text{Ni}_2(m\text{-dobdc})$, and $\text{Co}_2(\text{dobdc})$ samples respectively, using the high-resolution neutron powder diffractometer, BT1, at the National Institute of Standards and Technology Center for Neutron Research (NCNR). The samples were placed in a He purged glove box and loaded into a vanadium sample can equipped with a valve for gas loading, and sealed using an indium O-ring. NPD data were collected using a Ge(311) monochromator with an in-pile 60' collimator corresponding to a wavelength of 2.078 Å. The samples were loaded onto bottom-loading closed cycle refrigerators and initial data collected on the activated $\text{Co}_2(m\text{-dobdc})$ and $\text{Ni}_2(m\text{-dobdc})$ frameworks at 10 K. As part of the initial structure solution, x-ray diffraction (XRD) measurements were carried out on 12.8 mg of $\text{Co}_2(m\text{-dobdc})$ at the Advanced Photon Source (APS) on the 17-BM materials diffractometer ($\lambda=0.7291$ Å) at 298 K. The activated $\text{Co}_2(m\text{-dobdc})$ sample was transferred into quartz capillary in a He purged glovebox and wax sealed for the X-ray measurements. For comparison of the D_2 structural dependence on ligand connectivity, $\text{Co}_2(\text{dobdc})$ and $\text{Co}_2(m\text{-dobdc})$ were each individually connected to a gas manifold of known volume and exposed to a known dose, approximately 0.75 and 2.25 D_2 per Co^{2+} , at 100 K (refined composition given in Tables 2.S12–2.S14, 2.S19). Both samples were slow cooled from 100 K to 10 K to ensure full equilibration and complete adsorption, as evidenced by a zero pressure reading on the barometer by 25 K, for data collection. Further D_2 structural data was collected on $\text{Co}_2(m\text{-dobdc})$ and $\text{Ni}_2(m\text{-dobdc})$ as a function of dose with final loadings of 0.75, 1.25, 1.5, 1.75, 2.0, 2.25, and 3.0 D_2 per Co^{2+} and 1.0, 2.0, and 3.0 D_2 per Ni^{2+} . Structural data for H_2 was measured on $\text{Co}_2(m\text{-dobdc})$ at a loading of 0.7 H_2 per Co^{2+} . Refined compositions are given in Tables 2.S12 and 2.S15–2.S20 (Co) and Tables 2.S21–2.S23 (Ni).

The structure solution for $\text{Co}_2(m\text{-dobdc})$ was completed from both neutron and X-ray diffraction data. The X-ray powder pattern for $\text{Co}_2(m\text{-dobdc})$ indexed to $R3$ with lattice parameters of approximately $a = 25.89$ Å and $c = 6.76$ Å using the GSASII software program.¹⁵ The FOX crystallographic software program was used to perform *ab initio* structure solution by simulated annealing algorithms from the powder X-ray data using the indexed lattice constants and space group and inputting stoichiometric quantities of metal ions and *m*-dobdc ligand into the unit cell.¹⁶ The *m*-dobdc ligand was fixed as a rigid body with the carboxyl group coplanar with the benzene ring. Initial attempts at solving the structure by simulated annealing confined in the $R3$ space group were unsuccessful, however, after consideration of how the dobdc ligand has a rotoinversion axis ($R\bar{3}$) versus the potential for a mirror plane in the *m*-dobdc, the space group was amended to $R3m$. Simulated annealing of the X-ray data resulted in a general connectivity

resembling hexagonal channels with cobalt ions in the vertices at slightly exaggerated distances and angles from reality. The overall connectivity and ligand orientation for $\text{Co}_2(m\text{-dobdc})$ was determined from a full Rietveld analysis of the neutron and X-ray diffraction data as implemented in EXPGUI/GSAS.¹⁷ The structure solution from $\text{Co}_2(m\text{-dobdc})$ was used as the basis for the solution of the $\text{Ni}_2(m\text{-dobdc})$ NPD data by Rietveld refinement. For the gas dosed refinements, the starting model for the activated $\text{Co}_2(\text{dobdc})$ framework was taken from our previous data on the bare material.^{18,19} Fourier difference methods were employed to locate the adsorbed D_2 molecules in both $\text{Co}_2(\text{dobdc})$ and $\text{Co}_2(m\text{-dobdc})$. A dose of 0.75 D_2 per Co^{2+} was chosen to provide clarity in the structure model for the active site in eliminating potential D_2 intermolecular interactions based on previous knowledge of adsorption in $\text{M}_2(\text{dobdc})$. A secondary dose of 2.25 D_2 per Co^{2+} was chosen for direct comparison with our previous results.^{18,19} In all instances, the atomic positions and isotropic atomic displacement parameters (ADPs) left free to refine during the analysis process after first accounting for a significant portion of the excess D_2 scattering density via Fourier methods. In the refinement of the 2.0 and 3.0 per Co^{2+} data in $\text{Co}_2(m\text{-dobdc})$, the primary deuterium site occupancy (D1) was fixed at fully occupied 1.0 D_2 per Co^{2+} to better model the data. Refined values for D_2 occupancies are presented with standard deviations for the 0.75, 1.25, 1.5, 1.75, and 2.25 D_2 per Co^{2+} results. For the 3.0 D_2 per Ni^{2+} data, the first three deuterium sites were fixed at fully occupied 1.0 D_2 at each site to better model the data.

Unit cells were determined for all $\text{M}_2(m\text{-dobdc})$ frameworks at room temperature by performing an overnight scan in the 2θ range of $4\text{-}65^\circ$ with 0.02° steps using a Bruker AXS D8 Advance diffractometer equipped with $\text{CuK}\alpha$ radiation ($\lambda = 1.5418 \text{ \AA}$), a Lynxeye linear position-sensitive detector, and mounting the following optics: Göbel mirror, fixed divergence slit (0.6 mm), receiving slit (3 mm), and secondary beam Soller slits (2.5°). The generator was set at 40 kV and 40 mA. The unit cell for $\text{Fe}_2(m\text{-dobdc})$ was determined from data collected at the Advanced Photon Source 11-BM. A standard peak search, followed by indexing via the Single Value Decomposition approach,²⁰ as implemented in TOPAS-Academic,²¹ allowed the determination of approximate unit cell dimensions. Precise unit cell dimensions were determined by performing a structureless Le Bail refinement in TOPAS-Academic. Note that while the peak positions of the $\text{Fe}_2(m\text{-dobdc})$ powder pattern match those of the other $\text{M}_2(m\text{-dobdc})$ analogues (Figure S2), the quality of the diffraction data on this air-sensitive material were not of high enough quality to determine precise unit cell dimensions.

2.2.8. Inelastic Neutron Scattering. Inelastic neutron scattering (INS) spectra were collected using the Filter Analyzer Neutron Spectrometer (FANS)²² at the NCNR on the same samples used for the NPD experiments. Spectra were obtained at 7 K using the pyrolytic graphite (002) monochromator and $20'\text{-}20'$ collimation options. Data were first collected for the bare framework, followed by data collection for the sample loaded with *normal*- H_2 ($n\text{-H}_2$), which contains a 3:1 mixture of *ortho* ($o\text{-H}_2$) to *para* ($p\text{-H}_2$), respectively. For $\text{Co}_2(m\text{-dobdc})$, data were collected at loadings of 0.33, 0.5, 1.0, 2.0, 3.0, and 4.0 $n\text{-H}_2$ molecules per Co atom, while for $\text{Ni}_2(m\text{-dobdc})$ data were collected at loadings of 0.67, 1.0, 2.0, 3.0, and 4.0 $n\text{-H}_2$ molecules per Ni atom. Gas was loaded into the materials using the same methodology as described in the NPD experiments. The spectra of the bare frameworks were subtracted from the spectra obtained from the H_2 loaded samples and Gaussian peaks were fit to the rotational transitions using the DAVE suite of programs.²³ Further measurements of the framework vibrational densities of states for the activated $\text{Co}_2(m\text{-dobdc})$ material were made to higher energies (35 meV to 160 meV) using

the Cu(220) monochromator with 20'-20' collimation.

2.2.9. Infrared Spectroscopy. Infrared spectra were acquired using a Bomem DA3 Michelson interferometer equipped with a glowbar source, CaF₂ beamsplitter and a liquid nitrogen cooled mercury-cadmium-telluride detector. A cutoff filter above 9000 cm⁻¹ was used to prevent unwanted sample heating from the IR source. A custom-built diffuse reflectance system²⁴ with a sample chamber that allows both the temperature and atmosphere of the material to be controlled was used for all experiments. Powder samples of the frameworks (~ 10 mg) were transferred under inert atmosphere to a cup affixed to a copper slab providing thermal contact to a cold-finger cryostat (Janis ST-300T). The sample temperature was monitored by a Si-diode thermometer. Known quantities of H₂ gas were dispensed from a calibrated gas manifold by monitoring the change in pressure.

2.2.10. DFT Calculations. Due to the extended nature of the M₂(dobdc) and M₂(*m*-dobdc) structures, cluster modeling was completed on the linker of interest coordinated to a pair of Co atoms bound to either end of the organic linker. To truncate the system, the ligating oxygen atoms that are not part of the included linker were added as formaldehyde molecules in order to conserve charge. The experimentally determined crystal structures were truncated as described and frozen. The geometry of a hydrogen molecule bound to the frozen system based on neutron diffraction data was then optimized. The range-separated, dispersion corrected functional ω B97X-D implemented in the electronic structure software Q-Chem²⁵ was used with an ultra fine (99, 590) grid and a triple split-valence basis set with polarization (6-311G**).²⁶ A small core Stuttgart-Born (SRSC) effective core potential is employed to model the core electrons of the Co.²⁷ Binding is further analyzed using the ALMO EDA.²⁸ Charge transfer is accounted for using the perturbative Roothaan step approach, which allows for assignment of forward and backbonding energies as well as generation of complementary occupied-virtual orbital pairs (COVPs)²⁹ to visualize charge transfer.

2.3. Results and Discussion

2.3.1. Structural Characterization of M₂(*m*-dobdc). A less expensive regioisomer of H₄dobdc was selected in order to form a framework with the same overall topology and a high density of open sites as in M₂(dobdc), but with potentially different local geometry and electronic properties. After the synthesis of H₄(*m*-dobdc) from resorcinol, it was possible to synthesize an isostructural series of M₂(*m*-dobdc) (M = Mg, Mn, Fe, Co, or Ni) frameworks (Figure 2.1) exhibiting powder x-ray diffraction patterns (Figures 2.S1-2.S5) analogous to the respective M₂(dobdc) frameworks, indicating that the two series adopt similar structures. Thermogravimetric analyses of the Co₂(*m*-dobdc) and Ni₂(*m*-dobdc) frameworks show initial mass losses of 33% and 14%, respectively, indicative of volatilization of trapped solvent molecules and thus porosity (Figure 2.S6a). After repeatedly washing each compound with methanol to replace the metal-bound DMF, the frameworks were activated by heating under dynamic vacuum at 180 °C. Thermogravimetric analysis of the activated frameworks indicated that Mn₂(*m*-dobdc) and Co₂(*m*-dobdc) are stable to 250 °C and the Ni₂(*m*-dobdc) is stable to 350 °C.

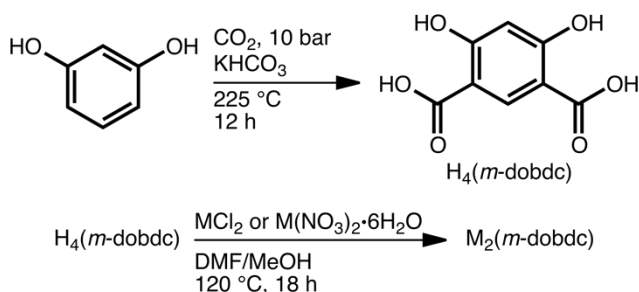


Figure 2.1. Synthesis of $H_4(m\text{-dobdc})$ and $M_2(m\text{-dobdc})$, starting from the inexpensive compound resorcinol.

To confirm that the $M_2(m\text{-dobdc})$ frameworks are indeed structurally analogous to $M_2(\text{dobdc})$, powder x-ray and neutron diffraction experiments were used to solve the crystal structure of $Co_2(m\text{-dobdc})$ (Figure 2.2). Similar to $Co_2(\text{dobdc})$, $Co_2(m\text{-dobdc})$ possesses helical chains of Co^{2+} centers running parallel to the crystallographic c axis. Upon activation and removal of a bound DMF molecule, each metal center is ligated by a combination of oxido and carboxylate donors in a square pyramidal geometry, with open coordination sites directed into the one-dimensional hexagonal channels of the framework. Based on the change in point group symmetry of the linker from C_{2h} in $H_4(\text{dobdc})$ to C_{2v} in $H_4(m\text{-dobdc})$, a change in the space group from $R\bar{3}$ in $Co_2(\text{dobdc})$ to $R3m$ in $Co_2(m\text{-dobdc})$ is observed.^{4a} Additional structural differences between the two compounds are apparent.^{9c} For instance, the orientation of the carboxylate groups of the linker is changed, with the CO_2^- unit twisting out of the plane of the aromatic ring by approximately 12.5° in $Co_2(m\text{-dobdc})$, as compared to just 3.5° in $Co_2(\text{dobdc})$. Furthermore, metal centers in $Co_2(m\text{-dobdc})$ that face into the same pore align directly along the crystallographic b axis, resulting in a $Co\cdots Co$ separation of $14.9(1)\text{ \AA}$ across the channels. In $Co_2(\text{dobdc})$, the metals are offset from each other by one third of a twist in the chain, leading to a $Co\cdots Co$ separation of $15.24(8)\text{ \AA}$ across the channels. A structureless Le Bail refinement of the other $M_2(m\text{-dobdc})$ ($M = Mg, Mn, Fe, Ni$) compounds afforded related unit cells, confirming that the entire series is isostructural.

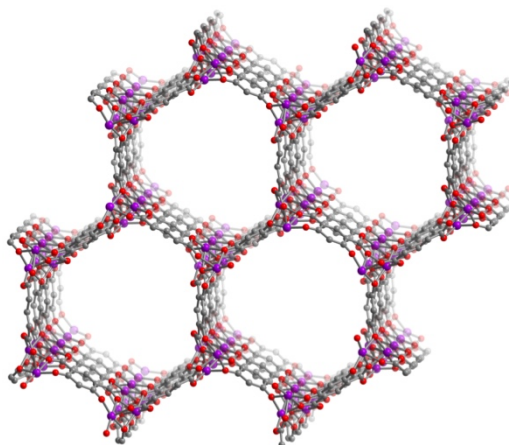


Figure 2.2. Crystal structure of $Co_2(m\text{-dobdc})$ showing one-dimensional hexagonal pores and helical metal chains.

With such similar crystal structures, the surface areas would be expected to be similar for the two types of frameworks. Indeed, a geometric approximation of the surface areas for $\text{Co}_2(m\text{-dobdc})$ and $\text{Co}_2(\text{dobdc})$ predicts them to both be $1297 \text{ m}^2/\text{g}$.³⁰ Low-pressure N_2 adsorption isotherms collected at 77 K reveal type I isotherms characteristic of microporous solids for the $\text{M}_2(m\text{-dobdc})$ ($\text{M} = \text{Mn, Fe, Co, Ni}$) compounds (Figure 2.S11). Langmuir and BET surface areas were calculated (Table 2.1) and in each case the results are comparable to those reported for $\text{M}_2(\text{dobdc})$.^{4b,4c,9e,31} Based on the similar framework structure, this indicates full evacuation of the pores and complete desolvation of the framework. Furthermore, the $\text{Co}_2(m\text{-dobdc})$ BET surface area of $1264 \text{ m}^2/\text{g}$ is very close to the predicted surface area of $1297 \text{ m}^2/\text{g}$ from the geometric calculations. Achieving complete activation of the Mg analogue has proven challenging and all efforts have thus far resulted in materials with lower than expected surface areas. As a result, the remaining data will focus only on the other four $\text{M}_2(m\text{-dobdc})$ compounds.

Table 2.1. Langmuir and BET surface areas of the $\text{M}_2(\text{dobdc})$ and $\text{M}_2(m\text{-dobdc})$ frameworks. The values for $\text{M}_2(\text{dobdc})$ are from literature sources.

		Mn ^{4b,9e}	Fe ^{4c}	Co ^{31a}	Ni ^{31b}
$\text{M}_2(\text{dobdc})$	Langmuir (m^2/g)	1797	1535	1432	1574
	BET (m^2/g)	1102	1360	1341	
$\text{M}_2(m\text{-dobdc})$	Langmuir (m^2/g)	1741	1624	1504	1592
	BET (m^2/g)	1349	1295	1264	1321

2.3.2. H_2 Adsorption Isotherms. To probe the potentially modified electronic structures at the open metal coordination sites, low-pressure H_2 adsorption isotherms were measured for the four $\text{M}_2(m\text{-dobdc})$ ($\text{M} = \text{Mn, Fe, Co, Ni}$) frameworks at 77 K and 87 K (Figures 2.S20–2.S23). As for the $\text{M}_2(\text{dobdc})$ series,^{4a} $\text{Ni}_2(m\text{-dobdc})$ has the greatest H_2 uptake at 77 K and 1 bar, followed by Fe, Mn, and Co compounds, respectively. Although the $\text{M}_2(\text{dobdc})$ frameworks have a higher H_2 uptake at 1 bar, in the very low-pressure regime, $\text{Ni}_2(m\text{-dobdc})$ has a significantly higher uptake than $\text{Ni}_2(\text{dobdc})$ at both 77 and 87 K (Figure 2.S27). This indicates that the interaction of H_2 with the exposed Ni^{2+} cations on the surface of $\text{Ni}_2(m\text{-dobdc})$ is stronger than in $\text{Ni}_2(\text{dobdc})$; since these frameworks have about the same surface area, another effect must be influencing the binding strength of H_2 .

Isosteric heats of H_2 adsorption were calculated in order to gain insight into this increased low-pressure H_2 adsorption and confirm whether there is indeed a stronger interaction between H_2 and the metal centers in the $\text{M}_2(m\text{-dobdc})$ frameworks. In order to determine the isosteric heat of adsorption (Q_{st}) using the Clausius-Clapeyron relation, H_2 isotherm data at 77 and 87 K were fit with either a dual-site Langmuir-Freundlich equation or a tri-site Langmuir equation. Similar to $\text{M}_2(\text{dobdc})$,^{4a} the isosteric heat of adsorption plots for $\text{M}_2(m\text{-dobdc})$ imply a nearly constant H_2 binding enthalpy until a loading of $0.7\text{-}0.8 \text{ H}_2/\text{M}^{2+}$, followed by a sharp decrease as all exposed metal cations become occupied and only weaker adsorption sites are available (Figure 2.3). The inflection points range from $\sim 0.75 \text{ H}_2/\text{M}$ in $\text{Co}_2(m\text{-dobdc})$ to $\sim 0.85 \text{ H}_2/\text{M}$ in $\text{Fe}_2(m\text{-dobdc})$, which corresponds with the fraction of metal sites available for H_2 binding. These values are comparable to previously observed values for the $\text{M}_2(\text{dobdc})$ series.³¹

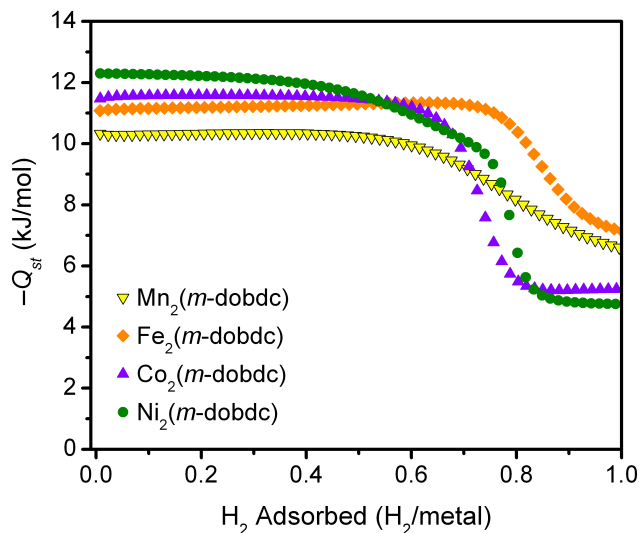


Figure 2.3. H_2 isosteric heat of adsorption curves for the $\text{M}_2(m\text{-dobdc})$ series of frameworks, as a function of the amount adsorbed.

Increasing the binding enthalpy of H_2 in metal-organic frameworks is important for practical applications, as a binding enthalpy of -15 to -20 kJ/mol is predicted to be optimal for the on-board storage of H_2 at ambient temperatures.³² The low-coverage isosteric heats of adsorption of $\text{Mn}_2(m\text{-dobdc})$, $\text{Fe}_2(m\text{-dobdc})$, $\text{Co}_2(m\text{-dobdc})$, and $\text{Ni}_2(m\text{-dobdc})$ are -10.3 , -11.1 , -11.6 , and -12.3 kJ/mol, respectively. This trend in binding enthalpies for H_2 is consistent with the Irving-Williams series, which predicts that high-spin complexes increase in stability moving from Group 7 to 10.³³ The trend further mirrors that observed for H_2 binding within $\text{M}_2(\text{dobdc})$ frameworks (Table 2.2). Calculated isosteric heat of adsorption values are highly sensitive to the fitting equation used, the temperatures at which data is collected and the quality of the fits. Given this, the values for the $\text{M}_2(\text{dobdc})$ series were calculated from isotherms collected in this work (except $\text{Fe}_2(\text{dobdc})$, which was previously reported by our group and fit using the same method^{4c}) in order to maintain consistency in the collected isotherms and the manner in which they are fit. These values all agree with the literature values for the $\text{M}_2(\text{dobdc})$ series except for $\text{Ni}_2(\text{dobdc})$, which we found to be 1 kJ/mol less than the literature value of -12.9 kJ/mol.^{4a} This discrepancy most likely arises from a difference in data collection, isotherm temperatures, and equation used to fit the data. Consequently, our data that was collected and fit in the same manner as the $\text{M}_2(m\text{-dobdc})$ data presented here is used for comparison. Importantly, the isosteric heats of adsorption for the $\text{M}_2(m\text{-dobdc})$ compounds are, on average, ~ 1.0 kJ/mol stronger than in the corresponding $\text{M}_2(\text{dobdc})$ frameworks (Table 2.2) and are as much as 1.5 kJ/mol stronger in the case of Mn, which also has the largest percent increase (17%) in binding enthalpy.

Table 2.2. Zero-coverage H_2 isosteric heat of adsorption values for each metal in the $\text{M}_2(\text{dobdc})$ and $\text{M}_2(m\text{-dobdc})$ frameworks.

	Mn	Fe	Co	Ni
$\text{M}_2(\text{dobdc})$	-8.8	-9.7	-10.8	-11.9
$\text{M}_2(m\text{-dobdc})$	-10.3	-11.1	-11.5	-12.3

2.3.3. Powder Neutron Diffraction. In an effort to understand further why the $M_2(m\text{-dobdc})$ frameworks show higher H_2 binding enthalpies than the structurally similar $M_2(\text{dobdc})$, neutron diffraction experiments were performed on microcrystalline powder samples dosed with precise quantities of D_2 . Data were collected upon successively dosing the evacuated $Co_2(m\text{-dobdc})$ and $Ni_2(m\text{-dobdc})$ samples with loadings ranging from 0.75 to 3.0 D_2 molecules per metal center and cooling to 10 K. Based on previous results for $M_2(\text{dobdc})$ frameworks,^{6c} as well as the isosteric heats of adsorption for $M_2(m\text{-dobdc})$ that begin to decrease at loadings near 1 H_2 /metal, it was anticipated that the open metal coordination site would provide the primary hydrogen binding site. Indeed, this site, designated site I, was found to be the only D_2 binding site in $Co_2(m\text{-dobdc})$ at the lowest loading of 0.75 D_2 per Co^{2+} (Figure 2.4a). The center of the D_2 electron density was observed to be at a separation of 2.23(5) Å from the metal center, closer than the 2.32(2) Å found for $Co_2(\text{dobdc})$ at the same loading (Tables 2.S12-2.S13), which is further confirmation that the hydrogen binds more strongly to the open metal sites within the *meta* framework. The same binding site is apparent in $Ni_2(m\text{-dobdc})$, with a comparable $M\cdots D_2$ distance of 2.18(4) Å at a loading of 1.0 D_2 per Ni^{2+} , which is within error of the distance of 2.201(1) Å observed for $Ni_2(\text{dobdc})$ at 4 K.³⁴

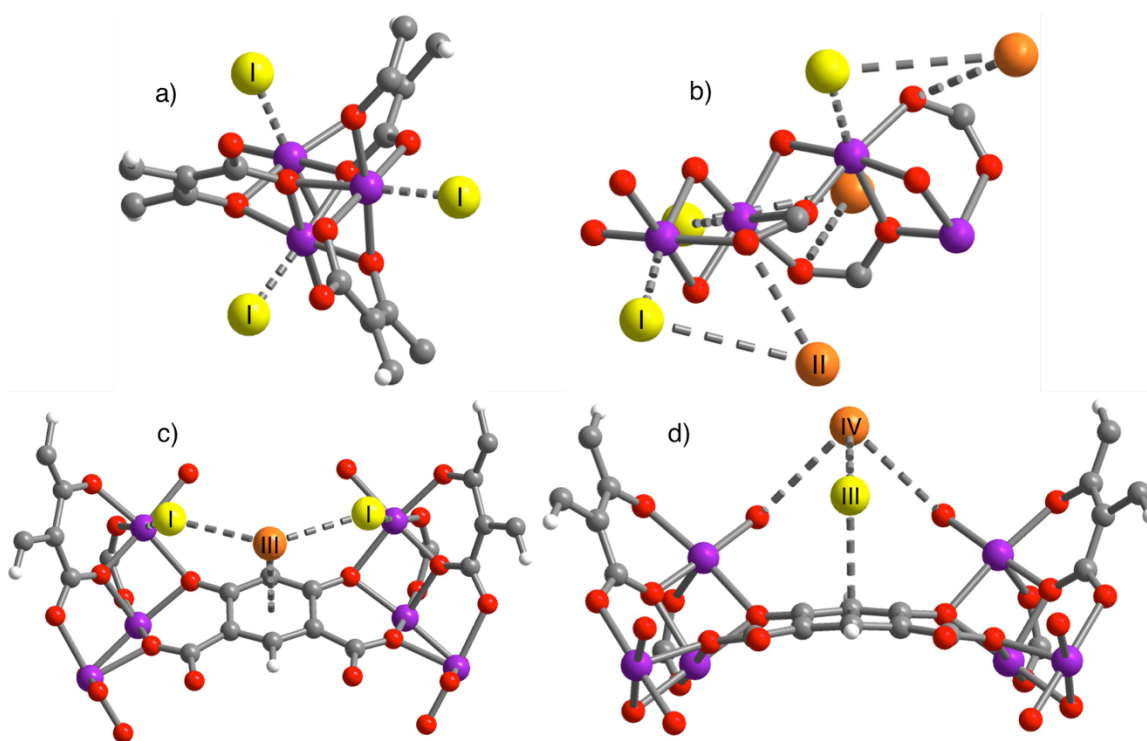


Figure 2.4. Partial crystal structures at 10 K of $Co_2(m\text{-dobdc})$ showing a) the primary binding site (site I) on the open metal site; b) binding site II interacting with the D_2 in site I; c) binding site III on the aromatic ring in the linker; and d) binding site IV, interacting with the D_2 in site III. Purple gray, red, and white spheres represent Co, C, O, and H atoms, respectively. Yellow and orange spheres represent D_2 molecules.

Increasing the D₂ loading in Co₂(*m*-dobdc) revealed several secondary binding sites. At a loading of 1.25 D₂ per metal, a second binding site (site II) adjacent to the primary site becomes populated (Figure 2.4b). This can be attributed to a D₂⋯D₂ interaction based on a short D₂⋯D₂ separation of 2.88(4) Å, combined with a D₂⋯O interaction occurring at a separation of 3.28(6) Å from the nearest framework oxygen atom. Site II is in a similar location to the secondary binding sites observed in Co₂(dobdc) and Mg₂(dobdc),^{6c} whereby the second bound D₂ appears to rely on D₂⋯D₂ interactions in all cases. The site I to site II D₂⋯D₂ separation, however, of 3.05(2) Å in Co₂(*m*-dobdc) at a loading of 2.25 D₂ per metal is significantly shorter than the 3.16(2) Å observed at the same loading in Co₂(dobdc) or the 3.16(8) Å arising for a similar loading of 1.2 D₂ per metal in Mg₂(dobdc). This closer site I to site II separation in Co₂(*m*-dobdc) is most likely a polarization effect, as the more strongly bound D₂ residing at site I has a larger induced dipole, leading to a stronger interaction with a D₂ molecule adsorbed at site II.

2.3.4. Inelastic Neutron Scattering. Inelastic neutron scattering (INS) experiments were carried out to probe the site-specific binding properties of H₂. Data for various loadings of H₂ after subtraction of the spectra for the evacuated materials are shown in Figure 2.5. At loadings up to and including 1.0 *n*-H₂ (corresponding to a 3:1 *ortho*-H₂:*para*-H₂ ratio) molecule per metal atom, two low-energy rotational lines are apparent at 7.8(1) and 9.5(1) meV for Co₂(*m*-dobdc) and 7.5(1) and 9.3(1) meV for Ni₂(*m*-dobdc). These features are similar to those observed in INS spectra for several compounds in the M₂(dobdc) series at low loadings, and have been assigned to transitions occurring from the *J* = 0 state to sublevels of the split *J* = 1 rotational state for initial H₂ molecules adsorbed at the metal centers.^{4c,6b,6c,31} This assignment has been confirmed through correlation with neutron diffraction and DFT calculations.³⁵ Presumably, there is also a higher-energy transition, not collected within this current data range, as seen in the M₂(dobdc) series. The splitting between the low energy peaks of approximately 1.6 meV for both Co₂(*m*-dobdc) and Ni₂(*m*-dobdc) is smaller than that observed for any of the M₂(dobdc) materials. The position of the first peak is at higher energies than that of the first peak of the M₂(dobdc) frameworks (except for the Zn analogue), and the position of the second peak is at lower energies than is observed for all the M₂(dobdc) compounds. The energy splitting of these peaks has been previously shown to have no correlation with the binding strength of H₂ at the open metal site.³⁶

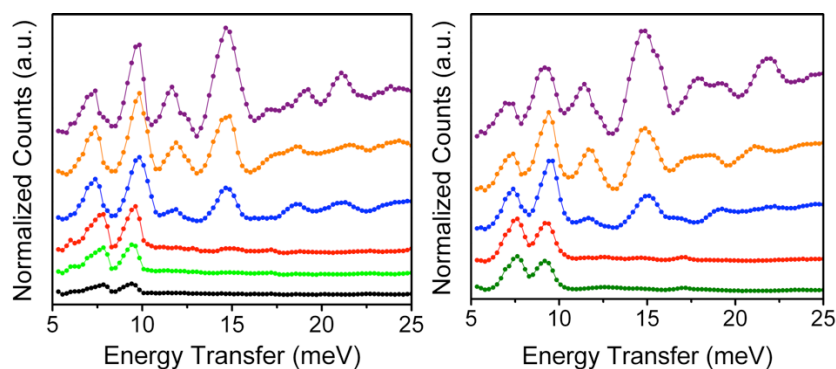


Figure 2.5. INS data for Co₂(*m*-dobdc) (left) and Ni₂(*m*-dobdc) (right) at loadings of 0.33 (black), 0.50 (dark green), 0.67 (light green), 1.0 (red), 2.0 (blue), 3.0 (yellow), and 4.0 (purple) *n*-H₂ molecules per metal atom. Data are shown after subtraction of the spectrum of the evacuated framework and offset for clarity.

At loadings above 0.75 H₂ molecules per metal, as sites II-IV begin to populate, the additional H₂ molecules affect the rotational potential for H₂ molecules at site I. This adjusts the rotational energy level, resulting in a shift of the first peak to lower energies and the second peak to higher energies. These peak shifts are similar to those observed for the M₂(dobdc) frameworks, with magnitudes of approximately 0.7 meV for Co₂(*m*-dobdc) and 0.5 meV for Ni₂(*m*-dobdc), though much less than the 1.4 meV shift observed for Fe₂(dobdc).^{4c} Adsorption of H₂ at the secondary sites also results in a significant increase in the area of the peak at 9 meV and appearance of features near 12 and 15 meV as a new subset of rotational levels associated with the rotationally hindered second adsorption site. Transitions in this energy range are also observed in spectra reported for higher loadings of the M₂(dobdc) materials, indicating the similarity in adsorption potentials at these secondary sites.^{4c,6c}

2.3.5. Infrared Spectra. Infrared Spectra. Since the higher binding enthalpies and low-coverage H₂ uptake cannot reasonably be attributed to a significant change in the macrostructure of the framework, infrared spectroscopy was used to further probe the binding of H₂ at the open metal coordination sites. The vibrational frequency of adsorbed H₂ is almost always lower than that of the molecule in the gas phase (4161 cm⁻¹), and it is now well established that for metal-organic frameworks, there is a strong correlation between the magnitude of the frequency shift and the binding energy at a particular site.³⁷ A comparison of the H₂ vibrational frequencies is shown at two different H₂ loadings for Ni₂(*m*-dobdc), Ni₂(dobdc), Co₂(*m*-dobdc), and Co₂(dobdc) (Figure 2.6) and for Mn₂(*m*-dobdc) and Mn₂(dobdc) (Figure 2.S45). At this temperature, the pure vibrational part of the spectrum consists of an *ortho-para* pair that is separated by just 6 cm⁻¹ in the gas phase. The peak near 4025 cm⁻¹ in each spectrum corresponds to the H₂ bound to the open metal site.

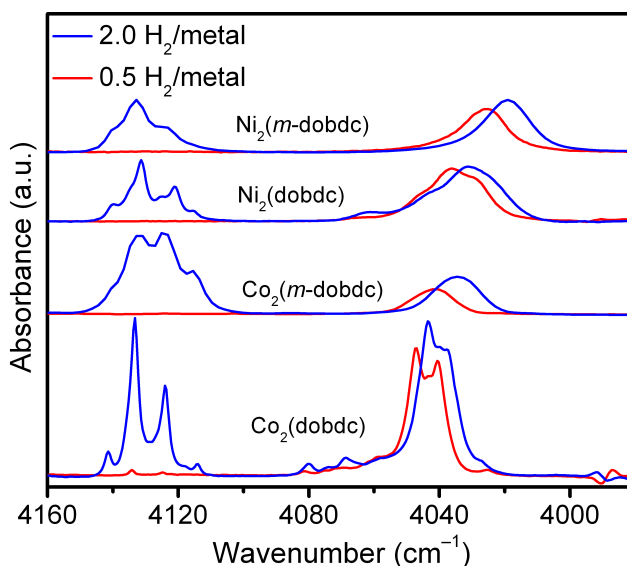


Figure 2.6. Comparison of the IR spectra of Ni₂(*m*-dobdc), Ni₂(dobdc), Co₂(*m*-dobdc), and Co₂(dobdc) at two different concentrations. The right peak shows the H₂ bound to the open metal site and the left peak shows the H₂ bound to the secondary adsorption sites. Spectra are offset for clarity.

In each case, the spectra for loadings of 0.5 H₂ molecules per metal, which are known to arise purely from H₂ bound to the open metal site, show a greater frequency shift for the Co₂(*m*-dobdc) and Ni₂(*m*-dobdc) than for Co₂(dobdc) or Ni₂(dobdc). This shift is consistent with the stronger H₂ binding observed in the M₂(*m*-dobdc) frameworks based on equilibrium adsorption isotherms and neutron diffraction studies. Upon further loading, the secondary adsorption sites begin to be populated, which is evidenced by a second peak that grows in around 4125 cm⁻¹. The energy of the peaks associated with the secondary sites is very similar to those seen for M₂(dobdc), consistent with the INS transitions for H₂ bound to the secondary sites, which were also similar between M₂(*m*-dobdc) and M₂(dobdc) compounds. This supports our hypothesis that the electronic structure at the metal center is significantly altered with the *m*-dobdc⁴⁻ linker, leading to a higher initial isosteric heat of adsorption, while the secondary sites in M₂(*m*-dobdc) and M₂(dobdc) are similar in binding potential due to structural similarities between the two frameworks. Furthermore, a consistent shift in the frequency for the metal-adsorbed H₂ molecules as a function of concentration is seen for both the Co₂(*m*-dobdc) and Ni₂(*m*-dobdc) samples, although not to the same degree in the Mn₂(*m*-dobdc) sample. These concentration shifts have previously been attributed to H₂⋯H₂ interactions, and it is interesting to note that the shifts seem largely unaffected by the change in linker. Furthermore, these shifts correlate well with the shifts seen in rotational potential as the secondary binding sites are populated in the INS data shown in Figure 2.5.

Variable-temperature infrared spectroscopy is a standard technique for establishing the enthalpy of adsorption at a particular site.³⁸ Figure 2.7 shows the spectra obtained for H₂ in Co₂(*m*-dobdc) while lowering the sample temperature from 142 to 75 K. In each case, the initial H₂ pressure for the system was set such that only the open metal site was occupied over the full temperature range. The fractional occupancy is then determined by the ratio of the area under the infrared band to that observed at complete saturation. The inset in Figure 2.7 shows the van't Hoff relationship plot used to extract both the enthalpy and entropy change upon adsorption.

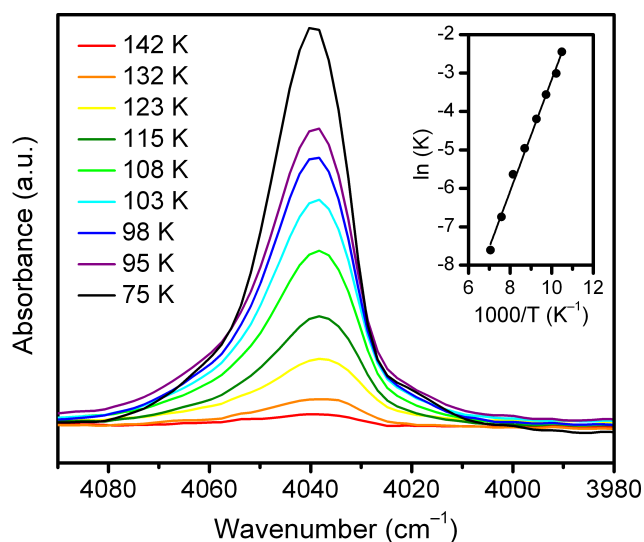


Figure 2.7. Variable temperature infrared spectra of Co₂(*m*-dobdc). The inset shows the van't Hoff plot that is used to extract the enthalpy and entropy change in H₂ upon adsorption to the open metal site.

The data obtained in this way for the different materials are summarized in Table 2.3. The slopes extracted from the van’t Hoff plots are sensitive to small variations in the maximum saturation area; as such, an error on the order of 0.5 kJ/mol is estimated. Even with these limitations, the data is consistent with the calculated isosteric heats of adsorption from the H₂ adsorption isotherms, showing an enthalpy increase from Mn to Co to Ni. More importantly, these infrared spectroscopy-based heat of adsorption values are about 1.4 kJ/mol larger than those calculated for their respective M₂(dobdc) counterparts from similar infrared experiments. The binding enthalpy of –13.7 kJ/mol in Ni₂(*m*-dobdc) is among the highest reported H₂ binding enthalpies in a metal-organic framework to date. This is consistent with the trends observed using values calculated from H₂ adsorption isotherms. We further note that the measured large entropy changes are consistent with previous studies, in which a strong correlation between the enthalpy and entropy change of the bound hydrogen in different metal-organic frameworks was observed.³⁹ Overall, the redshift seen in the infrared spectra for the adsorbed H₂ in M₂(*m*-dobdc) as compared to M₂(dobdc) indicates that the H₂ is more strongly bound and the variable-temperature data confirms the increased binding enthalpies seen from the H₂ adsorption data.

Table 2.3. Entropy and enthalpy values extracted from variable temperature infrared spectra of M₂(dobdc) and M₂(*m*-dobdc) (M²⁺ = Mn, Co, Ni).

M	M ₂ (dobdc)		M ₂ (<i>m</i> -dobdc)	
	<i>S</i> (J/mol K)	<i>H</i> (kJ/mol)	<i>S</i> (J/mol K)	<i>H</i> (kJ/mol)
Mn	—	—	–135	–10.5
Co	–136	–10.7	–147	–12.1
Ni	–148	–12.3	–147	–13.7

2.3.6. Electronic Structure Calculations. Density functional theory (DFT) was used to examine the differences in the electronic structures at the open metal sites by using representative complexes to model the M₂(dobdc) and M₂(*m*-dobdc) frameworks. DFT has shown itself to be a fairly robust method for modeling chemical systems; its major failings, self-interaction error and lack of dispersion interactions,⁴⁰ are well-known and can be corrected for by using appropriate functionals that account for these failings, namely range-separation and explicit dispersion correction.⁴¹ Previously, the ωB97X-D⁴² functional was shown to accurately model H₂ binding in metal-organic frameworks.⁴³

Modeling M₂(dobdc)-type frameworks accurately with electronic structure theory is challenging because fragmenting the structure at any point will lead to the neglect of important interactions from the chains formed by the M²⁺ ions. In an attempt to understand the nature of the differences in hydrogen binding between M₂(dobdc) and M₂(*m*-dobdc), some accuracy in the calculated energetics is sacrificed in order to learn relevant information about the differences between the two systems. In this vein, our modeling focused on the linker of interest coordinated to two Co²⁺ centers; the remaining ligands on each Co²⁺ ion were truncated as formaldehyde molecules in order to maintain charge balance. Since the key open coordination site for each Co²⁺ center in the framework is enforced by constraints on the ligands imposed by the macrostructure of the framework, which could not be explicitly included in our model, an unconstrained optimized geometry of the model would not actually reflect the structural properties of the framework in question. Thus, the geometry of the linker complex was taken from the

experimentally determined crystal structure of the framework and subsequently frozen before the interaction with H₂ was optimized. Furthermore, the Co...H₂ distance was taken from the neutron diffraction spectra and used as a constraint to ensure an accurate depiction of this interaction in the model system.

While comparing absolute energy differences gives a single number to describe H₂ binding, energy decomposition analysis (EDA) breaks down that number into physically interpretable components. An EDA based on absolutely localized molecular orbitals (ALMOs)²⁸ breaks down total binding energies into frozen energy, polarization, and charge transfer components. The frozen term is due to permanent electrostatics and Pauli repulsions, since the H₂ electron density is being brought within the van der Waals radius of the Co atom. The polarization term corresponds to the favorable interaction of electrons in the H₂ and complex fragments relaxing in the presence of the other fragment without electron transfer. Charge transfer stems from energy lowering when electrons are allowed to flow from one fragment to the other. A recent generalization of the ALMO EDA to open-shell molecules allows for the application of this method to general metal-containing systems.⁴⁴

The binding energy decomposition analysis clarifies the differences in these two species (Table 2.4). Specifically, there is more charge transfer and polarization in the *m*-dobdc⁴⁺ containing complex, which is accompanied by a partially offsetting increase in the energetically unfavorable frozen term. This larger frozen term is the result of the increased steric repulsion that stems from a shorter Co...H₂ distance in the *m*-dobdc⁴⁺ complex. The increased charge transfer energy of H₂ binding in this species is key, as that is the largest term in the total calculated binding energy.

Table 2.4. ALMO energy decomposition analysis of H₂ binding to the dobdc⁴⁺ and *m*-dobdc⁴⁺ complexes.

component	Energy (kJ/mol)	
	dobdc ⁴⁺	<i>m</i> -dobdc ⁴⁺
frozen	1.3	7.9
polarization	-4.8	-9.5
charge transfer	-12.5	-17.1
total	-16.0	-18.6

A breakdown of the charge transfer term can be seen in Table 2.5; in both cases, the largest portion of the charge transfer comes from the H₂ σ orbital to the unoccupied orbitals of the Co complex. The increased H₂ to Co forward donation is indicative of more positive charge at the metal cation in the *m*-dobdc⁴⁺ complex as compared with the dobdc⁴⁺ complex. This explains the experimentally determined increase in binding enthalpy of H₂ in the M₂(*m*-dobdc) frameworks as compared with their M₂(dobdc) analogues, as increased positive charge at the metal center leads to stronger polarization of the bound H₂. Additionally, a difference is seen in the location of the bound H₂ relative to the linker in the two complexes. In the dobdc⁴⁺ linker complex, the H₂ binds to create a nearly octahedral geometry around the Co²⁺ ion, with a distance of 3.30 Å from the H₂ to the aromatic carbon bonded to the carboxylate group (the alpha carbon). Conversely, in the *m*-dobdc⁴⁺ complex, the H₂ is reoriented toward the linker at a distance of 2.64 Å from the alpha carbon (Figure 2.8a-b). This difference suggests that a change in the charge at the alpha carbon

due to the different symmetry of the $m\text{-dobdc}^{4-}$ linker possibly facilitates a change in the binding geometry for H_2 . While this significant change may be an artifact associated with the small cluster models, it is the same trend seen experimentally for the $\text{H}_2\cdots\alpha$ carbon distance, which is 3.48(3) Å in $\text{Co}_2(m\text{-dobdc})$ and 3.59(2) Å in $\text{Co}_2(\text{dobdc})$.

Table 2.5. Forward and backbonding contributions to the charge transfer term for the dobdc^{4-} and $m\text{-dobdc}^{4-}$ complexes.

	Energy (kJ/mol)	
	dobdc^{4-}	$m\text{-dobdc}^{4-}$
$\text{H}_2 \rightarrow \text{Co}$ bonding	-9.1	-11.8
$\text{Co} \rightarrow \text{H}_2$ backbonding	-3.4	-5.3

The orbital interactions between H_2 and the Co complexes provide further insight into the stronger H_2 binding in $\text{Co}_2(m\text{-dobdc})$. While increased forward bonding is a product of increased charge density at the metal, the nature of the backbonding from the complex to H_2 is quite different. This can be seen by looking at the complementary occupied virtual orbital pairs (COVPs) that contribute most to backbonding (Figure 2.8c-d). In the dobdc^{4-} complex, the occupied orbital is primarily localized on the metal center, while in the $m\text{-dobdc}^{4-}$ species, the donating orbital includes contributions from the π system of the linker. This increased backbonding for $m\text{-dobdc}^{4-}$ agrees with the redshift seen in the H_2 infrared spectra for the $\text{M}_2(m\text{-dobdc})$ frameworks, as increased backbonding will weaken the H–H bond. This possible extra interaction with the linker in the $m\text{-dobdc}^{4-}$ complex, coupled with the larger forward donation of the H_2 to the more positively charged metal center, are the key differences between these two systems that help to explain the stronger H_2 binding seen in $\text{M}_2(m\text{-dobdc})$ versus $\text{M}_2(\text{dobdc})$.

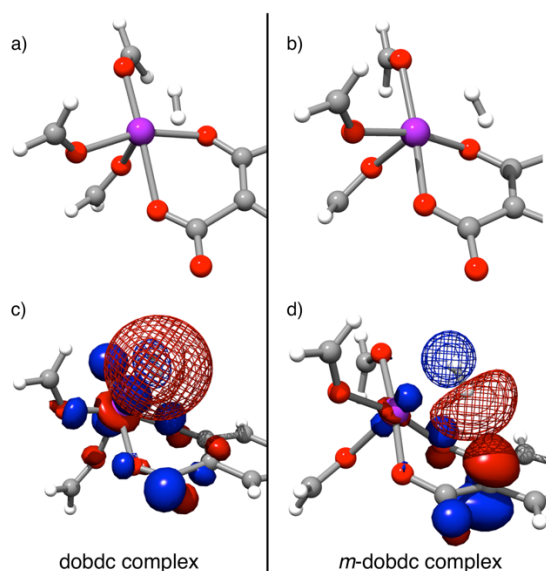


Figure 2.8. The calculated binding modes of H_2 in a) the dobdc complex and b) the $m\text{-dobdc}$ complex, in both of which the Co^{2+} is purple and the H_2 is above the Co^{2+} . The corresponding COVPs are shown for c) the dobdc complex and d) the $m\text{-dobdc}$ complex, with occupied and virtual orbitals shown as solid and mesh, respectively, at a $0.05 \text{ \AA}^{-3/2}$ isodensity.

2.4. Outlook and Conclusions

The foregoing results demonstrate the synthesis of a new family of metal-organic frameworks, $M_2(m\text{-dobdc})$ ($M = \text{Mg, Mn, Fe, Co, Ni}$), representing a potentially less expensive version of their well-known structural isomers $M_2(\text{dobdc})$. Hydrogen was used as an initial probe to determine how electronic and structural differences in the new frameworks modified the interactions of the open metal coordination sites with adsorbates. The Mn, Fe, Co, and Ni variants exhibited greater isosteric heats of H_2 adsorption by approximately 1 kJ/mol compared to the $M_2(\text{dobdc})$ compounds. The results from powder neutron diffraction, inelastic neutron scattering, and infrared spectroscopy experiments performed on hydrogen-loaded samples of $\text{Co}_2(m\text{-dobdc})$ all support this as arising from stronger interactions between the metal centers and the H_2 molecules. Future efforts will focus on the larger-scale production of $M_2(m\text{-dobdc})$ compounds, and determining whether the enhanced charge density at the metal sites leads to improvements compared to their $M_2(\text{dobdc})$ analogues in the efficacy of key gas separations, including O_2 from air,^{1j, 45} CO_2/N_2 ,^{1h, 1j, 7a, 46} CO_2/H_2 ,^{1j, 47} CO/H_2 ,^{1e, 45a, 48} ethylene/ethane,^{1i, 9} propylene/propane,^{1i, 3d, 9} and methane purification.⁴⁹

2.5. Acknowledgements

Thanks to Stephen J. Geier, Jarad A. Mason, and Dianne J. Xiao for help with sample preparation and assistance with gas adsorption experiments, Matthew R. Hudson, Zeric Hulvey, and Craig M. Brown for collection and analysis of powder neutron diffraction and inelastic neutron scattering data, David Stück and Martin Head-Gordon for work with the electronic structure calculations, and Jocienne N. Nelson, Elizabeth Gilmour, and Stephen A. FitzGerald for collection and analysis of infrared spectra. Research at Berkeley and NIST was supported through the Department of Energy, Office of Energy Efficiency and Renewable Energy (DOE-EERE), Fuel Cell Technologies Office and through the Department of Energy, Office of Science Graduate Fellowship Program (DOE SCGF), made possible in part by the American Recovery and Reinvestment Act of 2009, administered by ORISE-ORAU under contract no. DE-AC05-06OR23100. Efforts at Oberlin College were funded through NSF Grant CHE-1111896. Thanks to the 11-BM staff at the Advanced Photon Source at Argonne National Laboratory for assisting with powder x-ray diffraction experiments. Use of the Advanced Photon Source at Argonne National Laboratory was supported by the U.S. Department of Energy, Office of Science, Office of Basic Energy Sciences, under Contract No. DE-AC02-06CH11357. Thanks to the NSF for providing graduate fellowship support for M.T.K. Thanks to Dr. Greg Halder for help with the diffraction data collection on 17-BM-B at the APS, Dr. Trudy Bolin for the use of the helium glovebox in APS Sector 9, Paul Horn for assistance with the energy decomposition analysis, and Eric Bloch and Rebecca Triano for helpful discussions.

2.6. References and Supplementary Data

1. a) Eddaoudi, M.; Kim, J.; Rosi, N.; Vodak, D.; Wachter, J.; O’Keeffe, M.; Yaghi, O. M. *Science* **2002**, *295*, 469. b) Kitagawa, S.; Kitaura, R.; Noro, S.-I. *Angew. Chem., Int. Ed.* **2004**, *43*, 2334. c) Millward, A. R.; Yaghi, O. M. *J. Am. Chem. Soc.* **2005**, *127*, 17998. d) Ma, S.; Sun, D.; Simmons, J. M.; Collier, C. D.; Yuan, D.; Zhou, H.-C. *J. Am. Chem. Soc.*

- 2008, 130, 1012. e) Britt, D.; Tranchemontagne, D.; Yaghi, O. M. *Proc. Natl. Acad. Sci. U.S.A.* **2008**, 105, 11623. f) Li, J.-R.; Kuppler, R. J.; Zhou, H.-C. *Chem. Soc. Rev.* **2009**, 38, 1477. g) Britt, D.; Furukawa, H.; Wang, B.; Glover, T. G.; Yaghi, O. M. *Proc. Natl. Acad. Sci. U.S.A.* **2009**, 106, 20637. h) Sumida, K.; Rogow, D. L.; Mason, J. M.; McDonald, T. M.; Bloch, E. D.; Herm, Z. R.; Bae, T.-H.; Long, J. R. *Chem. Rev.* **2012**, 112, 724. i) Bloch, E. D.; Queen, W. L.; Krishna, K.; Zadrozny, J. M.; Brown, C. M.; Long, J. R. *Science* **2012**, 335, 1606. j) Li, J.-R.; Sculley, J.; Zhou, H.-C. *Chem. Rev.* **2012**, 112, 869.
2. a) Suh, M. P.; Park, H. J.; Prasad, T. K.; Lim, D.-W. *Chem. Rev.* **2012**, 112, 782. b) Konstas, K.; Osl, T.; Yang, Y.; Batten, M.; Burke, N.; Hill, A. J.; Hill, M. R. *J. Mater. Chem.* **2012**, 22, 16698.
 3. a) Dincă, M.; Dailly, A.; Liu, Y.; Brown, C. M.; Neumann, D. A.; Long, J. R. *J. Am. Chem. Soc.* **2006**, 128, 16876. b) Dietzel, P. D. C.; Johnsen, R. E.; Blom, R.; Fjellvåg, H. *Chem. Eur. J.* **2008**, 14, 2389. c) Vitillo, J. G.; Regli, L.; Chavan, S.; Ricchiardi, G.; Spoto, G.; Dietzel, P. D. C.; Bordiga, S.; Zecchina, A. *J. Am. Chem. Soc.* **2008**, 130, 8386. d) Bae, Y.-S.; Lee, C. Y.; Kim, K. C.; Farha, O. K.; Nicklas, P.; Hupp, J. T.; Nguyen, S.; Snurr, R. Q. *Angew. Chem. Int. Ed.* **2012**, 51, 1857. e) Li, Y.-W.; Li, J.-R.; Wang, L.-F.; Zhou, B.-Y.; Chen, Q.; Bu, Z.-H. *J. Mater. Chem. A* **2013**, 1, 495. f) Duan, X.; Cai, J.; Yu, J.; Wu, C.; Cui, Y.; Yang, Y.; Qian, G. *Microporous Mesoporous Mater.* **2013**, 181, 99. g) Cai, J.; Yu, J.; Xu, H.; He, Y.; Duan, X.; Cui, Y.; Wu, C.; Chen, B.; Qian, G. *Cryst. Growth Des.* **2013**, 13, 2094.
 4. a) Zhou, W.; Wu, H.; Yildirim, T. *J. Am. Chem. Soc.* **2008**, 130, 15268. b) Wu, H.; Zhou, W.; Yildirim, R. *J. Am. Chem. Soc.* **2009**, 131, 4995. c) Queen, W. L.; Bloch, E. D.; Brown, C. M.; Hudson, M. R.; Mason, J. A.; Murray, L. J.; Ramirez-Cuesta, A. J.; Peterson, V. K.; Long, J. R. *Dalton Trans.* **2012**, 41, 4180.
 5. Rosi, N. L.; Kim, J.; Eddaoudi, M.; Chen, B.; O’Keeffe, M.; Yaghi, O. M. *J. Am. Chem. Soc.* **2005**, 127, 1504.
 6. a) Dietzel, P. D. C.; Panella, B.; Hirscher, M.; Blom, R.; Fjellvåg, H. *Chem. Commun.* **2006**, 959. b) Liu, Y.; Kabbour, H.; Brown, C. M.; Neumann, D. A.; Ahn, C. C. *Langmuir* **2008**, 24, 4772. c) Sumida, K.; Brown, C. M.; Herm, Z. R.; Chavan, S.; Bordiga, S.; Long, J. R. *Chem. Commun.* **2011**, 47, 1157.
 7. a) Dietzel, P. D. C.; Besikiotis, V.; Blom, R. *J. Mater. Chem.* **2009**, 19, 7362. b) Makal, T. A.; Li, J.-R.; Lu, W.; Zhou, H.-C. *Chem. Soc. Rev.* **2012**, 41, 7761. c) Peng, Y.; Krungleviciute, V.; Eryazici, I.; Hupp, J. T.; Farha, O. K.; Yildirim, T. *J. Am. Chem. Soc.* **2013**, 135, 11887.
 8. a) Dietzel, P. D. C.; Johnsen, R. E.; Fjellvåg, H.; Bordiga, S.; Groppo, E.; Chavan, S.; Blom, R. *Chem. Commun.* **2008**, 5125. b) Caskey, S. R.; Wong-Foy, A. G.; Matzger, A. J. *J. Am. Chem. Soc.* **2008**, 130, 10870. c) McDonald, T. M.; Lee, W. R.; Mason, J. A.; Wiers, B. M.; Hong, C. S.; Long, J. R. *J. Am. Chem. Soc.* **2012**, 134, 7056. d) Yu, D.; Yazaydin, A. O.; Lane, J. R.; Dietzel, P. D. C.; Snurr, R. Q. *Chem. Sci.* **2013**, , 3544.
 9. a) Bao, Z.; Alnemrat, S.; Yu, L.; Vasiliev, I.; Ren, Q.; Lu, X.; Deng, S. *Langmuir* **2011**, 27, 13554. b) He, Y.; Krishna, R.; Chen, B. *Energy Environ. Sci.* **2012**, 5, 9107. c) He, Y.; Zhou, W.; Krishna, R.; Chen, B. *Chem. Commun.* **2012**, 48, 11813. d) Wu, H.; Gong, Q.; Olson, D. H.; Li, J. *Chem. Rev.* **2012**, 112, 836. e) Geier, S. J.; Mason, J. A.; Bloch, E. D.;

- Queen, W. L.; Hudson, M. R.; Brown, C. M.; Long, J. R. *Chem. Sci.* **2013**, *4*, 2054. f) Herm, Z. R.; Bloch, E. D.; Long, J. R. *Chem. Mater.* **2014**, *26*, 323.
10. a) Liu, J.; Wang, Y.; Benin, A. I.; Jakubczak, P.; Willis, R. R.; LeVan, M. D. *Langmuir* **2010**, *26*, 14301. b) Liu, J.; Benin, A. I.; Furtado, A. M. B.; Jakubczak, P.; Willis, R. R.; LeVan, M. D. *Langmuir* **2011**, *27*, 11451.
 11. Makal, T. A.; Yakovenko, A. A.; Zhou, H.-C. *J. Phys. Chem. Lett.* **2011**, *2*, 1682.
 12. Sun, L.; Miyaki, T.; Seki, S.; Dincă, M. *J. Am. Chem. Soc.* **2013**, *135*, 8185.
 13. a) Schlapbach, L.; Züetli, A. *Nature* **2001**, *414*, 353. b) Collins, D. J.; Zhou, H.-C. *J. Mater. Chem.* **2007**, *17*, 3154. c) van den Berg, A. W. C.; Areán, C. O. *Chem. Commun.* **2008**, 668. d) Murray, L. J.; Dincă, M.; Long, J. R. *Chem. Soc. Rev.* **2009**, *38*, 1294.
 14. Tedds, S.; Walton, A.; Broom, D. P.; Book, D. *Faraday Discuss.* **2011**, *151*, 75-94.
 15. Toby, B. H.; Von Dreele, R. B. *J. Appl. Cryst.* **2013**, *46*, 544-549.
 16. Favre-Nicolin, V.; Černý, R. *J. Appl. Cryst.* **2002**, *35*, 734-743.
 17. a) Toby, B. H. *J. Appl. Cryst.* **2001**, *34*, 210. b) Larson, A. C.; Von Dreele, R. B. "General Structure Analysis System (GSAS)", Los Alamos National Laboratory Report LAUR, 86-748, **1994**.
 18. Queen, W. L.; Bloch, E. D.; Brown, C. M.; Hudson, M. R.; Mason, J. A.; Murray, L. J.; Ramirez-Cuesta, A. J.; Peterson, V. K.; Long, J. R. *Dalton Trans.* **2012**, *41*, 4180-4187.
 19. Sumida, K.; Brown, C. M.; Herm, Z. R.; Chavan, S.; Bordiga, S.; Long, J. R. *Chem. Commun.* **2011**, *47*, 1157-1159.
 20. Coelho, A. *Appl. Cryst.* **36**, 86 (2003).
 21. Coelho, A. *TOPAS-Academic*, Version 4.1, Coelho Software, Brisbane, **2007**.
 22. Udovic, T. J.; Brown, C. M.; Leao, J. B.; Brand, P. C.; Jiggets, R. D.; Zeitoun, R.; Pierce, T. A.; Peral, I.; Copley, J. R. D.; Huang, Q.; Neumann, D. A.; Fields, R. J. *Nucl. Inst. and Meth. Phys. Res. A* **2008**, *588*, 406.
 23. Azuah, R. T.; Kneller, L. R.; Qiu, Y.; Tregenna-Piggott, P. L. W.; Brown, C. M.; Copley, J. R. D.; Dimeo, R. M. *J. Res. Natl. Inst. Stan. Technol.* **2009**, *114*, 241.
 24. FitzGerald, S. A.; Churchill, H. O. H.; Korngut, P. M.; Simmons, C. B.; Strangas, Y. E. *Rev. Sci. Instrum.* **2006**, *77*, 093110.
 25. Shao, Y.; Fusti Molnar, L.; Jung, Y.; Kussmann, J.; Ochsenfeld, C.; Brown, S. T.; Gilbert, A. T. B.; Slipchenko, L. V.; Levchenko, S. V.; O'Neill, D. P.; DiStasio Jr, R. A.; Lochan, R. C.; Wang, T.; Beran, G. J. O.; Besley, N. A.; Herbert, J. M.; Lin, C. Y.; Van Voorhis, T.; Chien, S. H.; Sodt, A.; Steele, R. P.; Rassolov, V. A.; Maslen, P. E.; Korambath, P. P.; Adamson, R. D.; Austin, B.; Baker, J.; Byrd, E. F. C.; Dachsel, H.; Doerksen, R. J.; Dreuw, A.; Dunietz, B. D.; Dutoi, A. D.; Furlani, T. R.; Gwaltney, S. R.; Heyden, A.; Hirata, S.; Hsu, C.-P.; Kedziora, G.; Khalliulin, R. Z.; Klunzinger, P.; Lee, A. M.; Lee, M. S.; Liang, W. Z.; Lotan, I.; Nair, N.; Peters, B.; Proynov, E. I.; Pieniazek, P. A.; Rhee, Y. M.; Ritchie, J.; Rosta, E.; Sherrill, C. D.; Simmonett, A. C.; Subotnik, J. E.; Woodcock III, H. L.; Zhang, W.; Bell, A. T.; Chakraborty, A. K.; Chipman, D. M.; Keil, F. J.; Warshel, A.; Hehre, W. J.; Schaefer III, H. F.; Kong, J.; Krylov, A. I.; Gill, P. M. W.; Head-Gordon, M. *Phys. Chem. Chem. Phys.* **2006**, *8*, 3172.
 26. a) Krishnan, R.; Binkley, J. S.; Seeger, R.; Pople, J. A. *J. Chem. Phys.* **1980**, *72*, 650. b) McLean, A. D.; Chandler, G. S. *J. Chem. Phys.* **1980**, *72*, 5639.
 27. Dolg, M.; Wedig, U.; Stoll, H.; Preuss, H. *J. Chem. Phys.* **1987**, *86*, 2123.

28. Khaliullin, R. Z.; Cobar, E. A.; Lochan, R. C.; Bell, A. T.; Head-Gordon, M. *J. Phys. Chem. A* **2007**, *111*, 8753.
29. Khaliullin, R. Z.; Bell, A. T.; Head-Gordon, M. *J. Chem. Phys.* **2008**, *128*, 184112
30. Düren, T.; Millange, F.; Férey, G.; Walton, K. S.; Snurr, R. Q. *J. Phys. Chem. C* **2007**, *111*, 15350.
31. a) Dietzel, P. D. C.; Georgiev, P. A.; Eckert, J.; Blom, R.; Strässle, T.; Unruh, T. *Chem. Commun.* **2010**, *46*, 4962. b) Mason, J.A.; Veenstra, M.; Long, J. R. *Chem. Sci.* **2014**, *5*, 32.
32. a) Bhatia, S. K.; Myers, A. L. *Langmuir* **2006**, *22*, 1688. b) Garrone, E.; Bonelli, B.; Otero Areán, C. *Chem. Phys. Lett.* **2008**, *456*, 68. c) Bae, Y.-S.; Snurr, R. Q. *Microporous Mesoporous Mater.* **2010**, *132*, 300.
33. Irving, H.; Williams, J. P. *Nature* **1948**, *162*, 746.
34. Brown, C. M.; Ramirez-Cuesta, A. J.; Her, J.-H.; Wheatley, P. S.; Morris, R. E. *Chem. Phys.* **2013**, *427*, 3.
35. Kong, L.; Román-Pérez, G.; Soler, J. M.; Langreth, D. C. *Phys. Rev. Lett.* **2009**, *103*, 096103.
36. Forster, P. M.; Eckert, J.; Heiken, B. D.; Parise, J. B.; Yoon, J. W.; Jung, S. H.; Chang, J.-S.; Cheetham, A. K. *J. Am. Chem. Soc.* **2006**, *128*, 16846.
37. FitzGerald, S. A.; Burkholder, B.; Friedman, M.; Hopkins, J. B.; Pierce, C. J.; Schloss, J. M.; Thompson, B.; Rowsell, J. L. C. *J. Am. Chem. Soc.* **2011**, *133*, 20310.
38. a) Garrone, E.; Bonelli, B.; Otero Areán, C. *Chem. Phys. Lett.* **2008**, *456*, 68. b) Otero Areán, C.; Chavan, S.; Cabello, C. P.; Garrone, E.; Palomino, G. T. *ChemPhysChem* **2010**, *11*, 3237.
39. Areán, C. O.; Chavan, S.; Cabello, C. P.; Garrone, E.; Palomino, G. T. *ChemPhysChem*, **2010**, *11*, 3237.
40. a) Perdew, J. P.; Zunger, A. *Phys. Rev. B* **1981**, *23*, 5048. b) Kristyán, S.; Pulay, P. *Chem. Phys. Lett.* **1994**, *229*, 175. c) Dutoi, A. D.; Head-Gordon, M. *Chem. Phys. Lett.* **2006**, *422*, 230.
41. a) Wu, X.; Vargas, M. C.; Nayak, S.; Lotrich, V.; Scoles, G. *J. Chem. Phys.* **2001**, *115*, 8748. b) Wu, Q.; Yang, W. *J. Chem. Phys.* **2002**, *116*, 515. c) Chai, J.-D.; Head-Gordon, M. *J. Chem. Phys.* **2008**, *128*, 084106.
42. Chai, J.-D.; Head-Gordon, M. *Phys. Chem. Chem. Phys.* **2008**, *10*, 6615.
43. Sumida, K.; Stück, D.; Mino, L.; Chai, J.-D.; Bloch, E.; Zavorotynska, O.; Murray, L.; Dincă, M.; Chavan, S.; Bordiga, S.; Head-Gordon, M.; Long, J. R. *J. Am. Chem. Soc.* **2013**, *135*, 1083.
44. Horn, P. R.; Sundstrom, E. J.; Baker, T. A.; Head-Gordon, M. *J. Chem. Phys.* **2013**, *138*, 134119.
45. a) Kerry, F. G. *Industrial Gas Handbook: Gas Separation and Purification*; CRC Press: Boca Raton, FL, 2007. b) Bloch, E. D.; Murray, L. J.; Queen, W. L.; Chavan, S.; Maximoff, S. N.; Bigi, J. P.; Krishna, R.; Peterson, V. K.; Grandjean, F.; Long, G. J.; Smit, B.; Bordiga, S.; Brown, C. M.; Long, J. R. *J. Am. Chem. Soc.* **2011**, *133*, 14814.
46. a) Yazaydin, A. O.; Benin, A. I.; Faheem, S. A.; Jakubczak, P.; Low, J. J.; Willis, R. R.; Snurr, R. Q. *Chem. Mater.* **2009**, *21*, 1425. b) Férey, G.; Serre, C.; Devic, T.; Maurin, G.; Jobic, H.; Llewellyn, P. L.; De Weireld, G.; Vimont, A.; Daturi, M.; Chang, J.-S. *Chem.*

- Soc. Rev.* **2011**, *40*, 550. c) Li, J.-R.; Ma, Y.; McCarthy, M. C.; Sculley, J.; Yu, J.; Jeong, H.-K.; Balbuena, P. B.; Zhou, H.-C. *Coord. Chem. Rev.* **2011**, *255*, 1791.
47. Herm, Z. R.; Swisher, J. A.; Smit, B.; Krishna, R.; Long, J. R. *J. Am. Chem. Soc.* **2011**, *133*, 5664.
48. a) McCandless, F. P. *Ind. Eng. Chem. Process Des. Dev.* **1972**, *11*, 470. b) Miyajima, H.; Kodama, A.; Goto, M.; Hirose, T. *Adsorption* **2005**, *11*, 625. c) Karra, J. S.; Walton, K. S. *Langmuir* **2008**, *24*, 8620.
49. a) Zhang, Y. F.; Musseman, I. H.; Ferraris, J. P.; Balkus, K. J.; *J. Membr. Sci.* **2008**, *313*, 170. b) Bastin, L.; Barcia, P. S.; Hurtado, E. J.; Silva, J. A. C.; Rodrigues, A. E.; Chen, B. *J. Phys. Chem. C* **2008**, *112*, 1575. c) Bae, Y. S.; Farha, O. K.; Spokoyny, A. M.; Mirkin, C. A.; Hupp, J. T.; Snurr, R. Q. *Chem. Commun.* **2008**, 4135. d) Mu, B.; Li, F.; Walton, K. S. *Chem. Commun.* **2009**, 2493. e) Lee, J. Y.; Roberts, J. M.; Farha, O. K.; Sarjeant, A. A.; Scheidt, K. A.; Hupp, J. T. *Inorg. Chem.* **2009**, *48*, 9971. f) Couck, S.; Denayer, J. F. M.; Baron, G. V.; Remy, T.; Gascon, J.; Kaptejin, F. *J. Am. Chem. Soc.* **2009**, *131*, 6326. g) Lee, K.; Isley III, W. C.; Dzubak, A. L.; Verma, P.; Stoneburner, S. J.; Lin, L.-C.; Howe, J. D.; Bloch, E. D.; Reed, D. A.; Hudson, M. R.; Brown, C. M.; Long, J. R.; Neaton, J. B.; Smit, B.; Cramer, C. J.; Truhlar, D. G.; Gagliardi, L. *J. Am. Chem. Soc.* **2014**, *136*, 698.

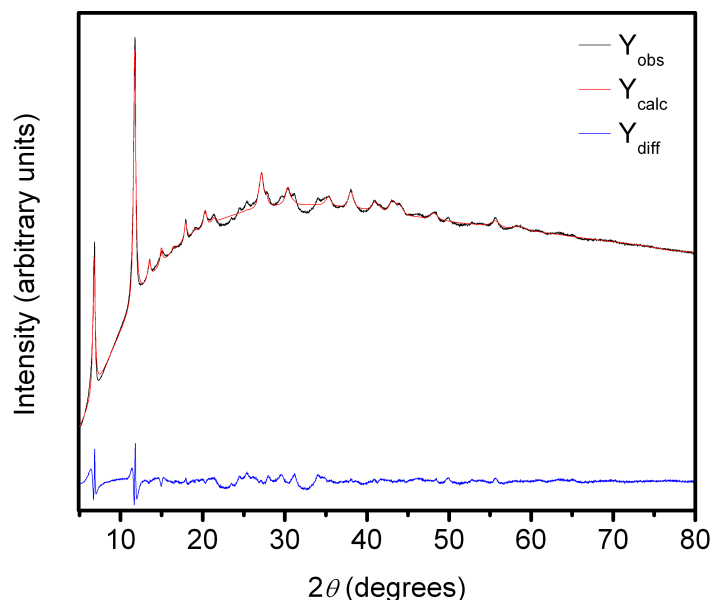


Figure 2.S1. Experimental X-ray powder diffraction pattern (wavelength = 1.5406 Å) of $\text{Mn}_2(m\text{-dobdc})$ (black) with calculated diffraction pattern (red) from Le Bail refinement and difference (blue). Unit cell parameters: a axis, 25.8225(6) Å; c axis, 6.71(1) Å.

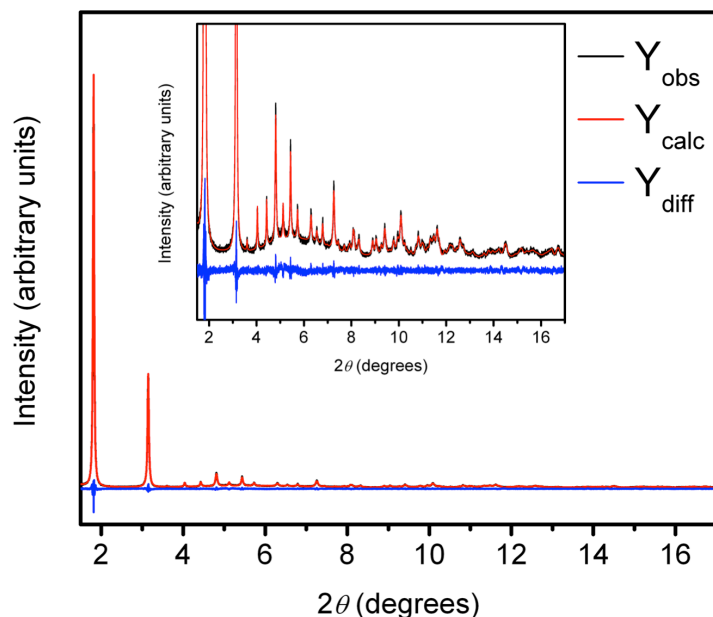


Figure 2.S2. Experimental X-ray powder diffraction pattern (wavelength = 0.413713 Å) of Fe₂(*m*-dobdc) (black) with calculated diffraction pattern (red) from Le Bail refinement and difference (blue). Unit cell parameters: *a* axis, 26.0893(6) Å; *c* axis, 6.8740(2) Å.

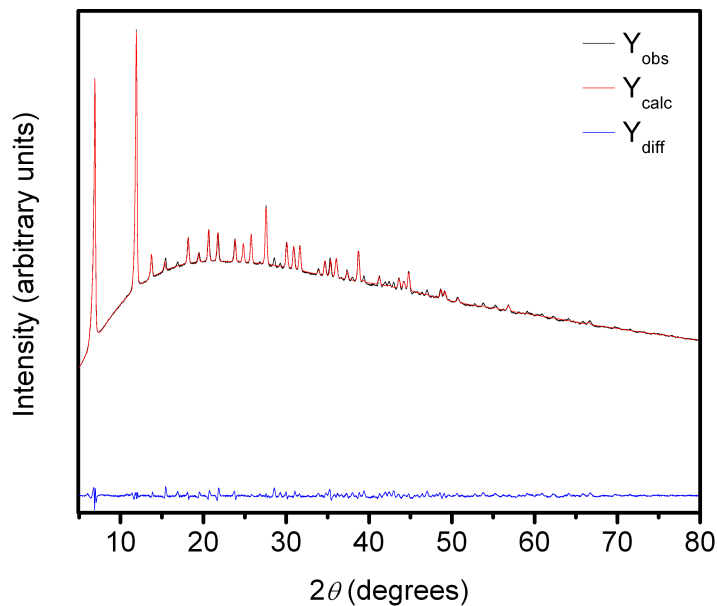


Figure 2.S3. Experimental X-ray powder diffraction pattern (wavelength = 1.5406 Å) of Co₂(*m*-dobdc) (black) with calculated diffraction pattern (red) from Le Bail refinement and difference (blue). Unit cell parameters: *a* axis, 26.21(2) Å; *c* axis, 6.95(1) Å.

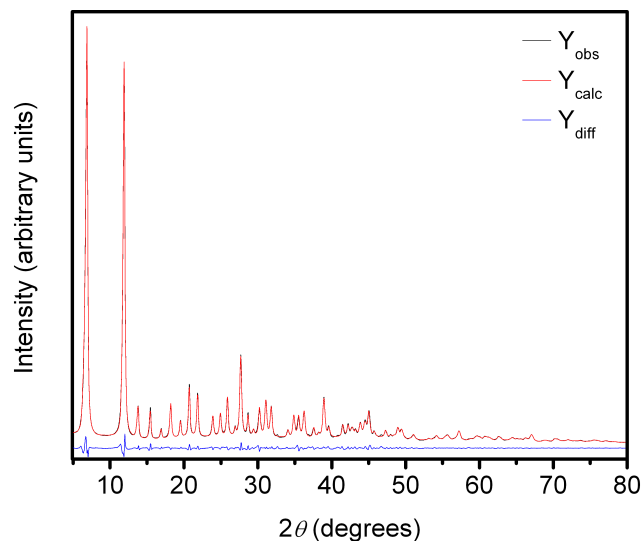


Figure 2.S4. Experimental X-ray powder diffraction pattern (wavelength = 1.5406 Å) of $\text{Ni}_2(m\text{-dobdc})$ (black) with calculated diffraction pattern (red) from Le Bail refinement and difference (blue). Unit cell parameters: a axis, 25.936(2) Å; c axis, 6.79(1) Å.

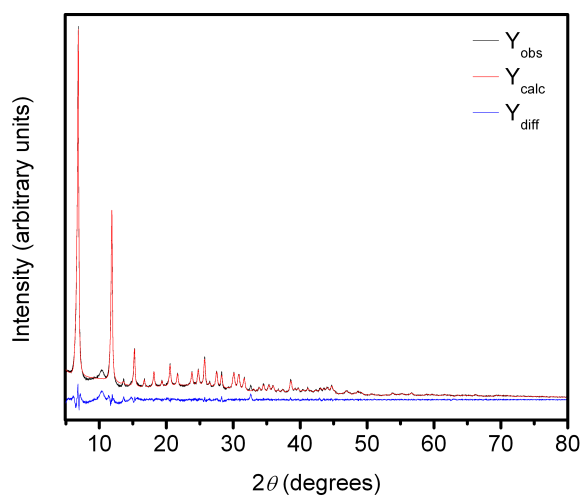


Figure 2.S5. Experimental X-ray powder diffraction pattern of $\text{Mg}_2(m\text{-dobdc})$ (black) with calculated diffraction pattern (red) from Le Bail refinement and difference (blue). Unit cell parameters: a axis, 25.893(2) Å; c axis, 6.81(1) Å.

Table 2.S1. Unit cell parameters for $\text{Mn}_2(m\text{-dobdc})$, $\text{Co}_2(m\text{-dobdc})$, $\text{Ni}_2(m\text{-dobdc})$, and $\text{Mg}_2(m\text{-dobdc})$ along with literature $\text{Mg}_2(\text{dobdc})$ and $\text{Ni}_2(\text{dobdc})$ unit cell parameters found from powder X-ray diffraction. $\text{Mg}_2(\text{dobdc})$ data is loaded with 0.5 CO_2/metal , but this was shown to have little effect on the unit cell.

	a axis (Å)	c axis (Å)	Volume (Å ³)	Temp. (K)
$\text{Mn}_2(m\text{-dobdc})$	25.8225(6)	6.71(1)	3874(1)	298
$\text{Fe}_2(m\text{-dobdc})$	26.0893(6)	6.8740(2)	4051.9(2)	295
$\text{Co}_2(m\text{-dobdc})$	26.21(2)	6.95(1)	4132(6)	298
$\text{Ni}_2(m\text{-dobdc})$	25.936(2)	6.79(1)	3957(1)	298
$\text{Mg}_2(m\text{-dobdc})$	25.893(2)	6.81(1)	3955(1)	298
$\text{Mg}_2(\text{dobdc})$	25.863(2)	6.8919(9)	3992.3(5)	300
$\text{Ni}_2(\text{dobdc})$	25.7856(12)	6.7701(10)	3898.34	295

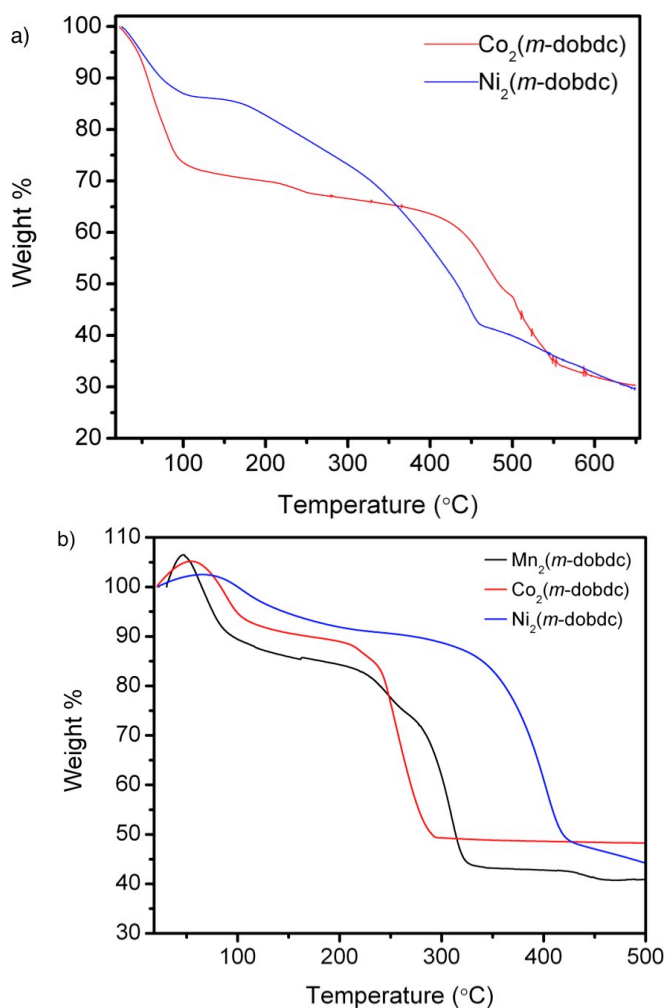


Figure 2.S6. Thermogravimetric analysis of a) unactivated $\text{Co}_2(m\text{-dobdc})$ (red) and $\text{Ni}_2(m\text{-dobdc})$ (blue) demonstrating solvent loss and b) activated $\text{Mn}_2(m\text{-dobdc})$, $\text{Co}_2(m\text{-dobdc})$, and $\text{Ni}_2(m\text{-dobdc})$ showing thermal stability. All samples were run at a ramp rate of 2 °C per min.

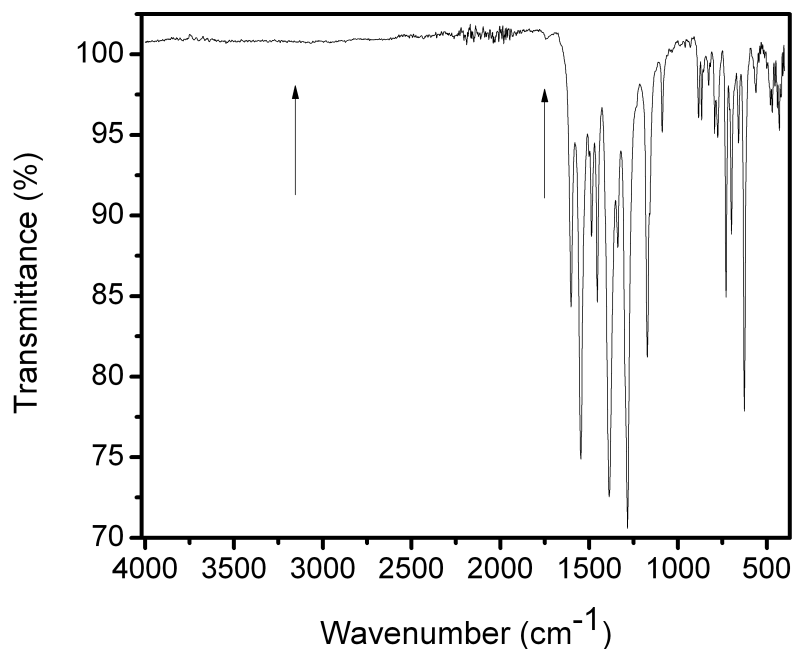


Figure 2.S7. Infrared spectrum of the fully evacuated sample of $\text{Mn}_2(m\text{-dobdc})$. Note the loss of the DMF and MeOH peaks indicated by arrows.

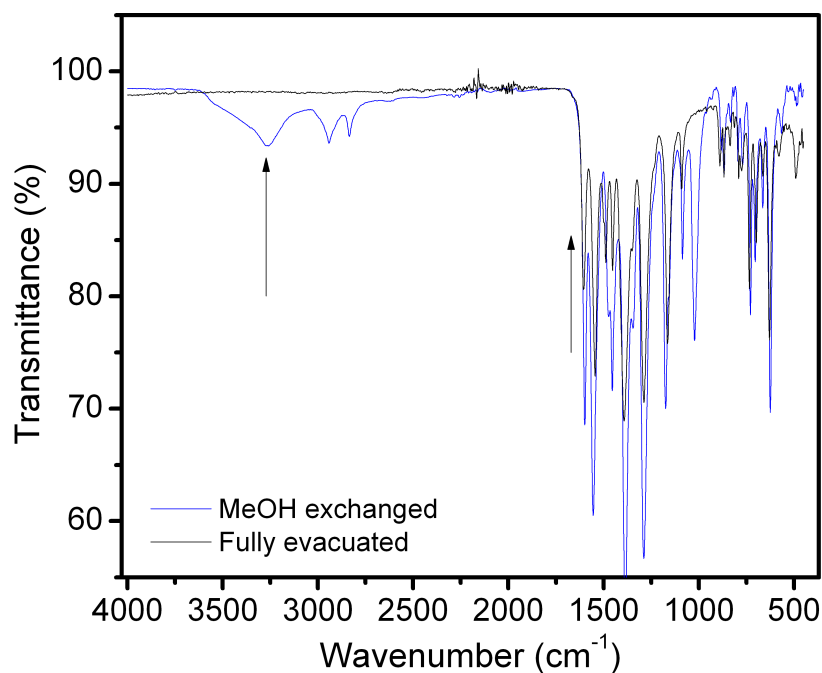


Figure 2.S8. Infrared spectrum of the MeOH exchanged and fully evacuated samples of $\text{Fe}_2(m\text{-dobdc})$. Note the loss of the DMF and MeOH peaks indicated by arrows.

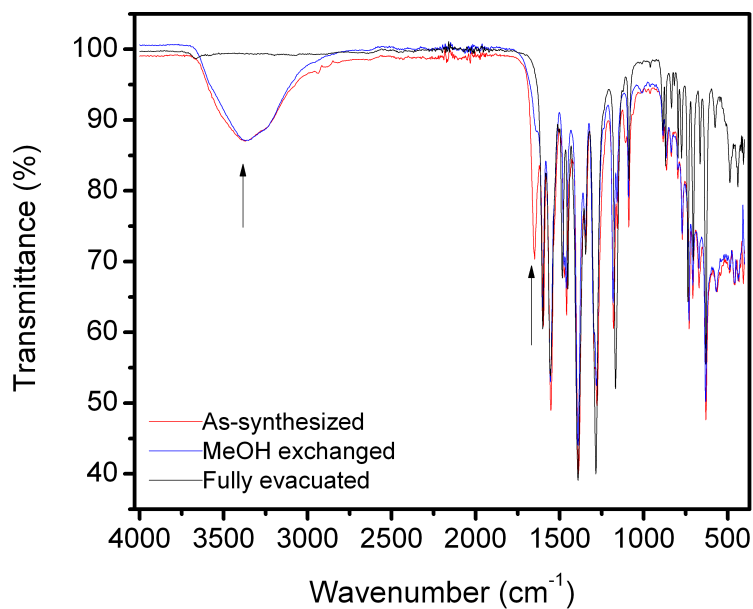


Figure 2.S9. Infrared spectra of $\text{Co}_2(m\text{-dobdc})$ showing the loss of MeOH and DMF upon evacuation, with arrows noting the MeOH and DMF peaks.

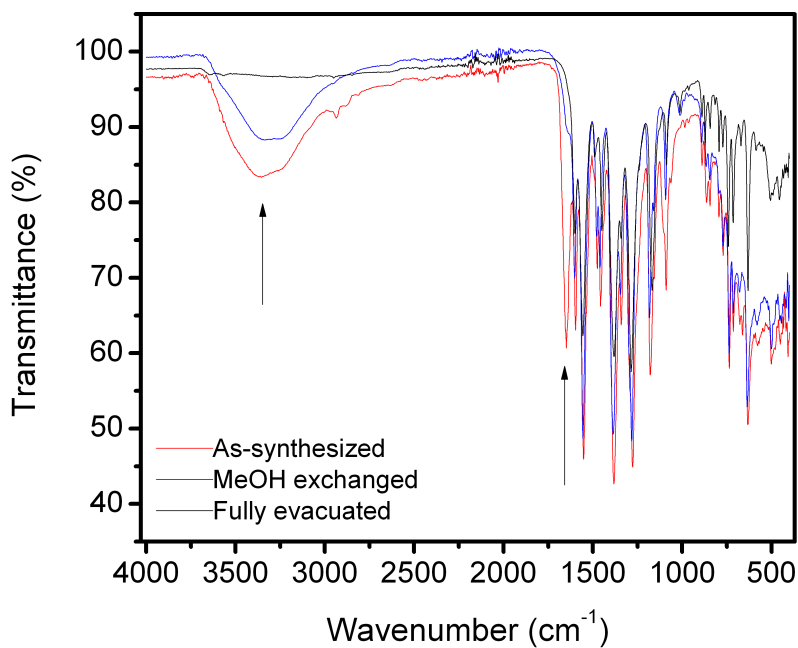


Figure 2.S10. Infrared spectra of $\text{Ni}_2(m\text{-dobdc})$ showing the loss of MeOH and DMF upon evacuation, with arrows noting the MeOH and DMF peaks.

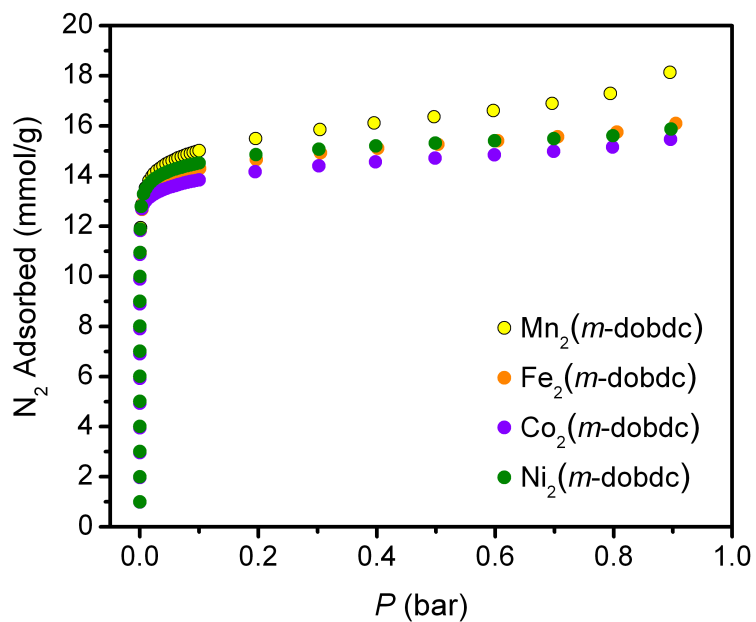


Figure 2.S11. N₂ adsorption isotherms at 77 K used to calculate the Langmuir and BET surface areas of Mn₂(m-dobdc), Fe₂(m-dobdc), Co₂(m-dobdc), and Ni₂(m-dobdc).

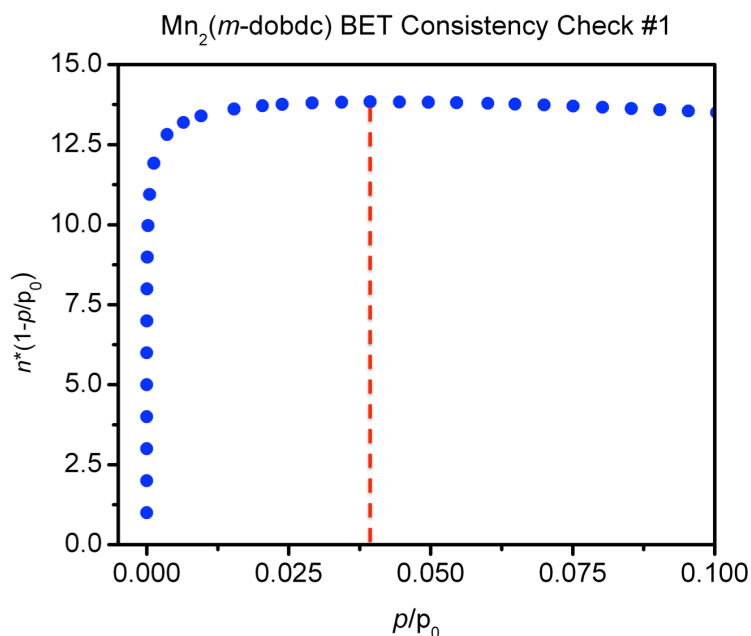


Figure 2.S12. A plot of $n^*(1-p/p_0)$ vs. p/p_0 to determine the maximum value of p/p_0 that is used for fitting the BET isotherm of Mn₂(m-dobdc), according to the first BET consistency criterion.

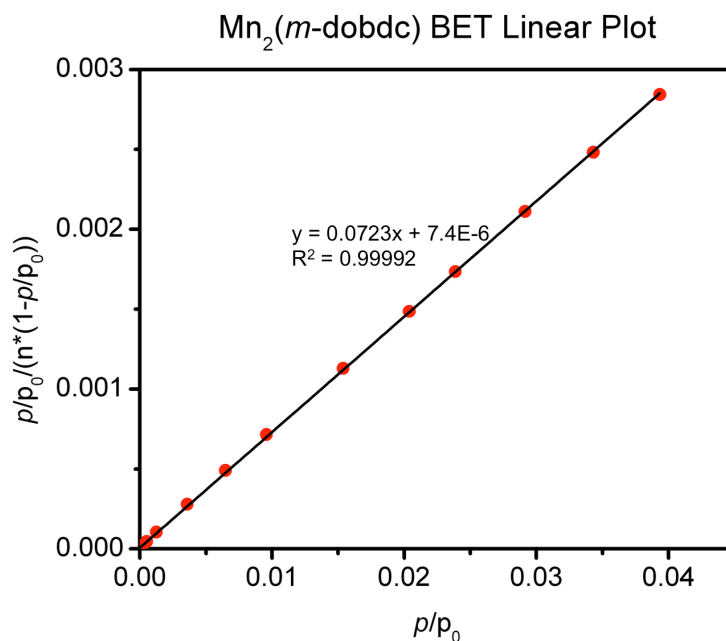


Figure 2.S13. Plot of $p/p_0/(n^*(1-p/p_0))$ vs. p/p_0 to determine the BET surface area of Mn₂(m-dobdc). The y-intercept calculated from the best fit line fulfill the second BET consistency criterion since the y-intercept is a positive value, giving a BET surface area of 1349 m²/g.

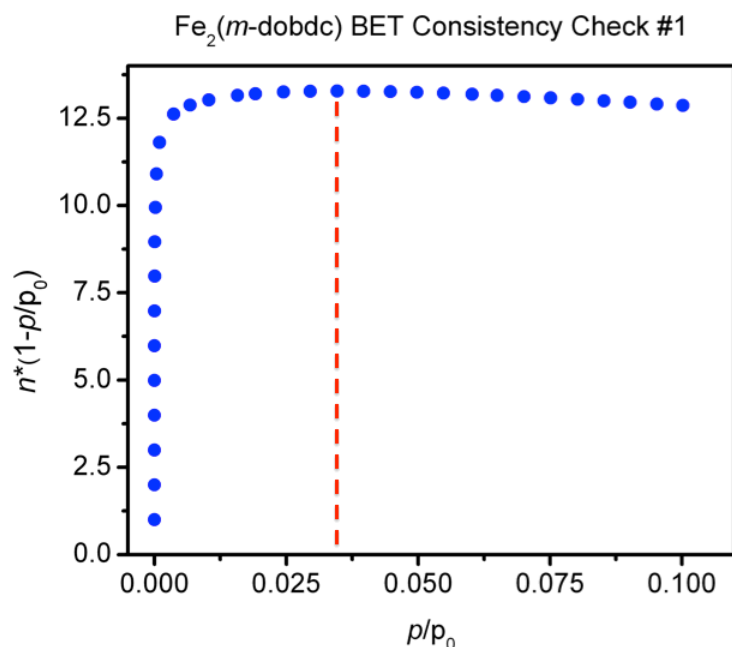


Figure 2.S14. A plot of $n^*(1-p/p_0)$ vs. p/p_0 to determine the maximum value of p/p_0 that is used for fitting the BET isotherm of $\text{Fe}_2(m\text{-dobdc})$, according to the first BET consistency criterion.

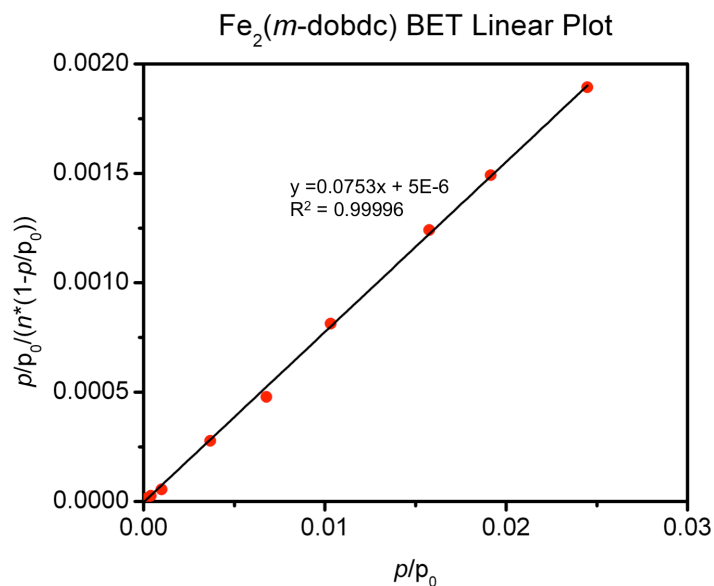


Figure 2.S15. Plot of $p/p_0/(n^*(1-p/p_0))$ vs. p/p_0 to determine the BET surface area of $\text{Fe}_2(m\text{-dobdc})$. The y-intercept calculated from the best fit line fulfill the second BET consistency criterion since the y-intercept is a positive value, giving a BET surface area of $1295 \text{ m}^2/\text{g}$.

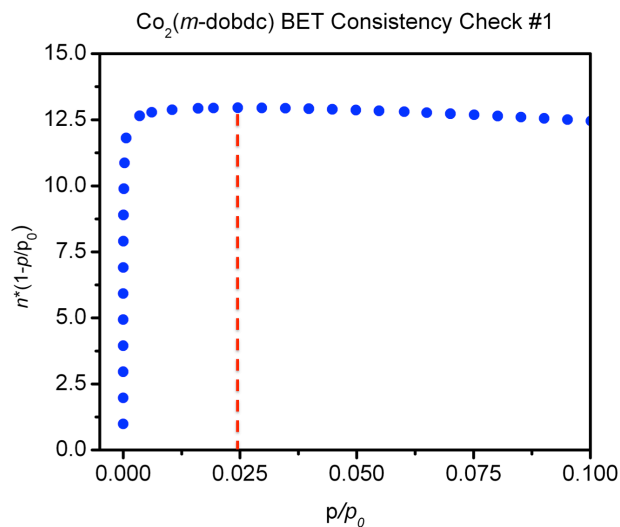


Figure 2.S16. A plot of $n^*(1-p/p_0)$ vs. p/p_0 to determine the maximum value of p/p_0 that is used for fitting the BET isotherm of $\text{Co}_2(m\text{-dobdc})$, according to the first BET consistency criterion.

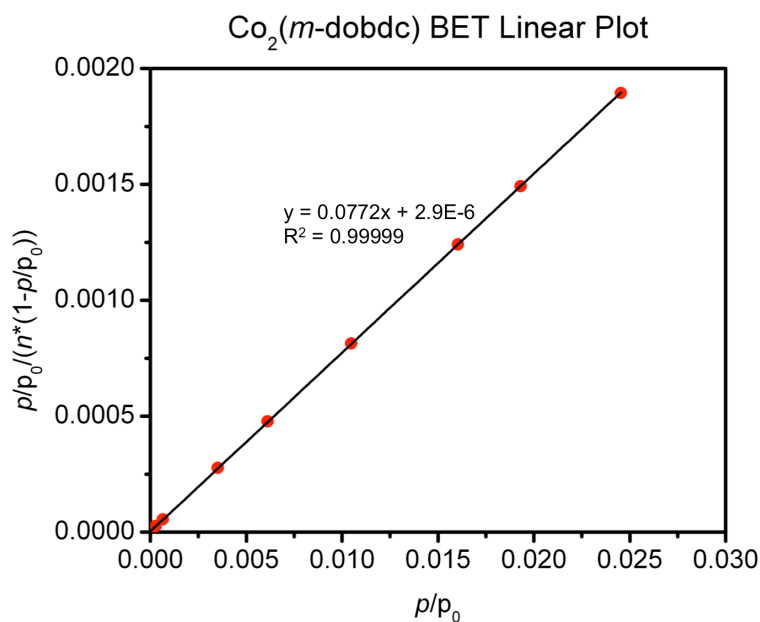


Figure 2.S17. Plot of $p/p_0/(n^*(1-p/p_0))$ vs. p/p_0 to determine the BET surface area of $\text{Co}_2(m\text{-dobdc})$. The y-intercept calculated from the best fit line fulfill the second BET consistency criterion since the y-intercept is a positive value, giving a BET surface area of $1264 \text{ m}^2/\text{g}$.

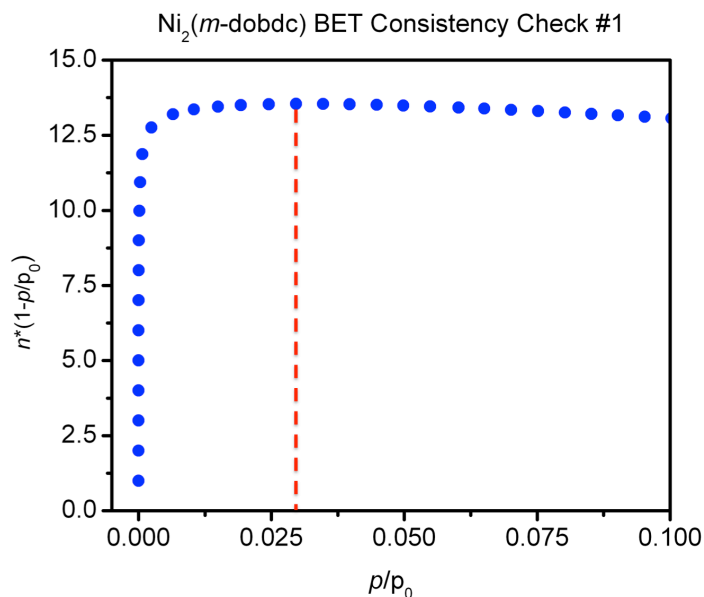


Figure 2.S18. A plot of $n^*(1-p/p_0)$ vs. p/p_0 to determine the maximum value of p/p_0 that is used for fitting the BET isotherm of $\text{Ni}_2(m\text{-dobdc})$, according to the first BET consistency criterion.

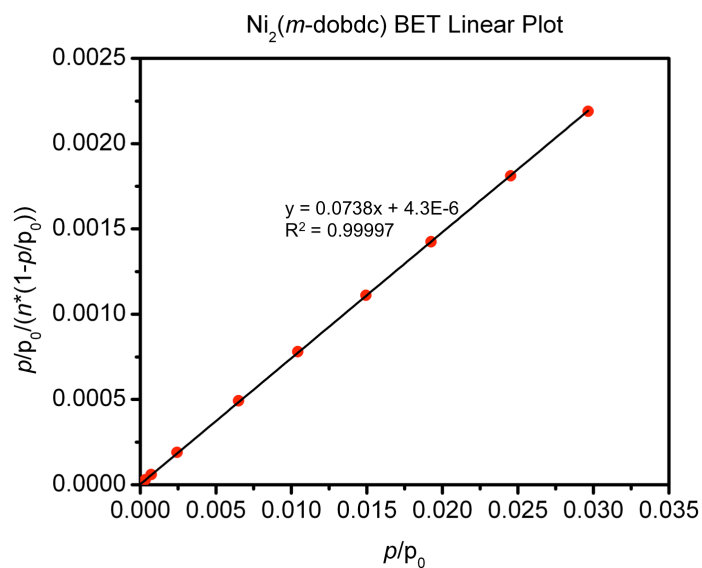


Figure 2.S19. Plot of $p/p_0/(n^*(1-p/p_0))$ vs. p/p_0 to determine the BET surface area of $\text{Ni}_2(m\text{-dobdc})$. The y-intercept calculated from the best fit line fulfill the second BET consistency criterion since the y-intercept is a positive value, giving a BET surface area of $1321 \text{ m}^2/\text{g}$.

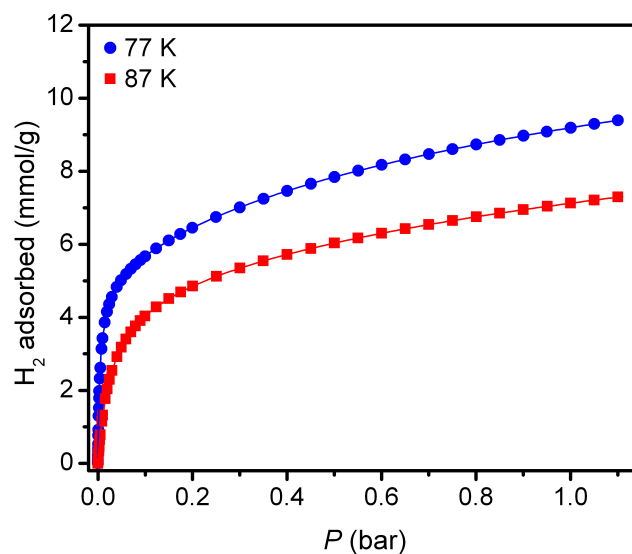


Figure 2.S20. H₂ adsorption isotherms at 77 K and 87 K for Mn₂(*m*-dobdc). The solid lines represent the dual-site Langmuir fit to the data, using the parameters tabulated in Table 2.S2.

Table 2.S2. Dual-site Langmuir fit parameters for the H₂ isotherms for Mn₂(*m*-dobdc) in Figure 2.S20.

	77 K	87 K
$q_{sat,A}$	4.56	4.34
b_A	212.50	34.65
v_A	0.98	0.98
$q_{sat,B}$	13.19	9.27
b_B	0.54	0.46
v_B	0.69	0.80

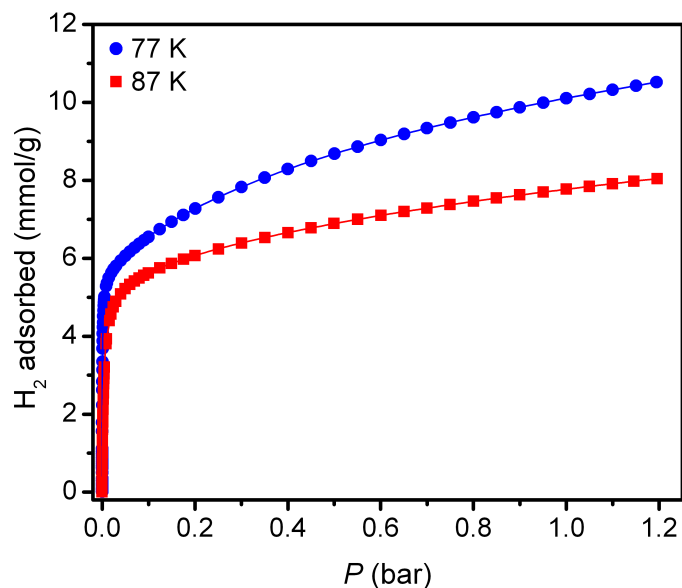


Figure 2.S21. H₂ adsorption isotherms at 77 K and 87 K for Fe₂(*m*-dobdc). The solid lines represent the dual-site Langmuir fit to the data, using the parameters tabulated in Table 2.S3.

Table 2.S3. Dual-site Langmuir fit parameters for the H₂ isotherms for Fe₂(*m*-dobdc) in Figure 2.S21.

	77 K	87 K
$q_{sat,A}$	5.40	5.21
b_A	1135.56	189.00
ν_A	0.91	0.91
$q_{sat,B}$	12.91	13.15
b_B	0.58	0.25
ν_B	0.75	0.69

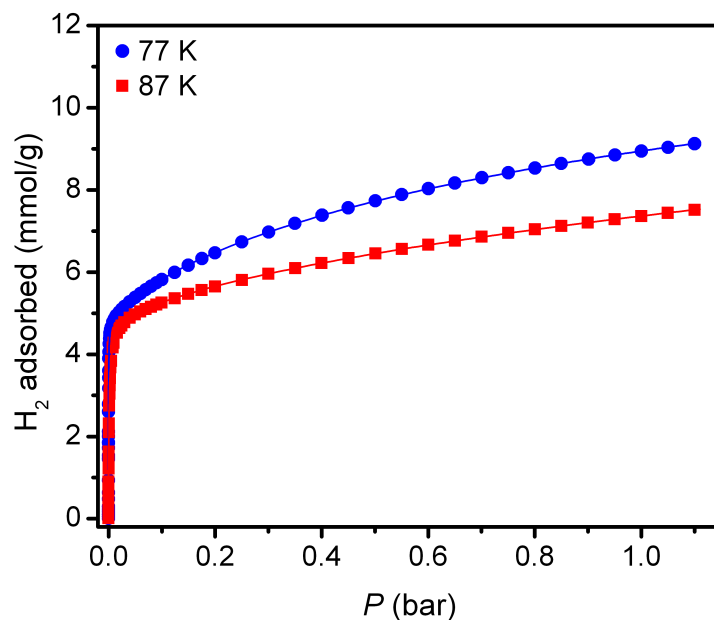


Figure 2.S22. H₂ adsorption isotherms at 77 K and 87 K for Co₂(*m*-dobdc). The solid lines represent the dual-site Langmuir fit to the data, using the parameters tabulated in Table 2.S4.

Table 2.S4. Dual-site Langmuir fit parameters for the H₂ isotherms for Co₂(*m*-dobdc) in Figure 2.S22.

	77 K	87 K
$q_{sat,A}$	4.67	4.66
b_A	3380.04	501.49
v_A	0.90	0.90
$q_{sat,B}$	10.89	24.81
b_B	0.65	0.12
v_B	0.73	0.65

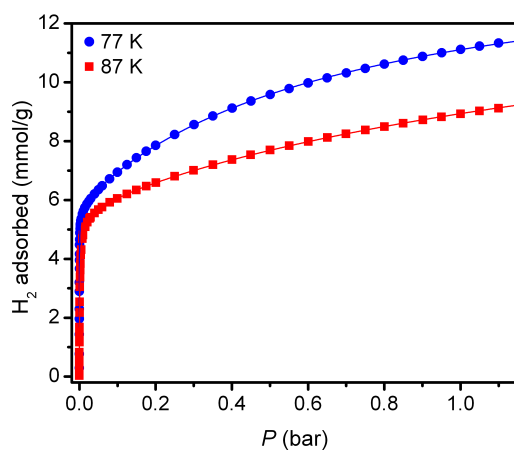


Figure 2.S23. H₂ adsorption isotherms at 77 K and 87 K for Ni₂(*m*-dobdc). The solid lines represent the tri-site Langmuir fit to the data, using the parameters tabulated in Table 2.S5.

Table 2.S5. Tri-site Langmuir fit parameters for the H₂ isotherms for Ni₂(*m*-dobdc) in Figure 2.S23.

77 and 87 K	
$q_{sat,A}$	3.78
b_A	1.59E-4
E_A	12.56
$q_{sat,B}$	6.89
b_B	9.97E-4
E_B	4.79
$q_{sat,C}$	1.30
b_C	1.25E-3
E_C	9.40

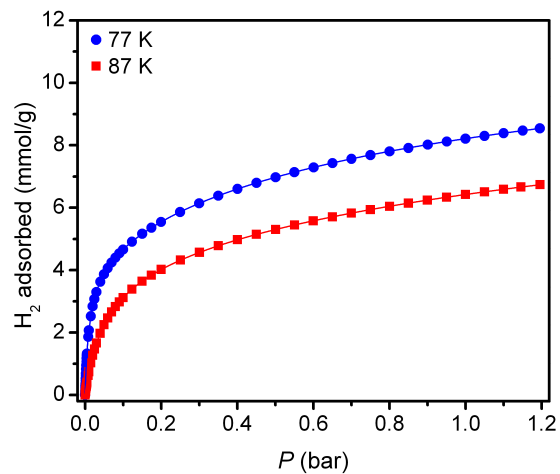


Figure 2.S24. H₂ adsorption isotherms at 77 K and 87 K for Mn₂(dobdc). The solid lines represent the dual-site Langmuir fit to the data, using the parameters tabulated in Table 2.S6.

Table 2.S6. Dual-site Langmuir fit parameters for the H₂ isotherms for Mn₂(dobdc) in Figure 2.S24.

	77 K	87 K
$q_{sat,A}$	9.65	8.29
b_A	0.91	0.50
v_A	0.74	0.84
$q_{sat,B}$	3.64	3.84
b_B	92.32	19.34
v_B	0.99	0.99

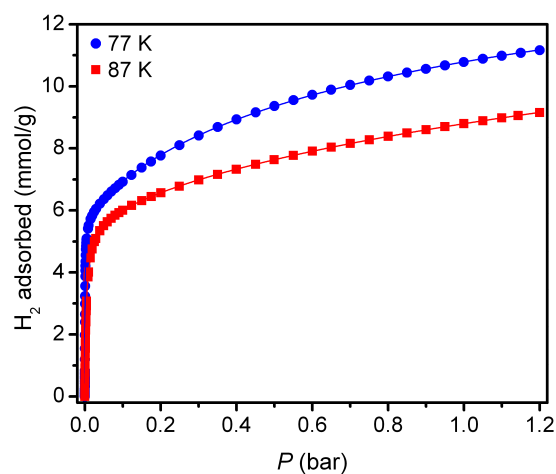


Figure 2.S25. H₂ adsorption isotherms at 77 K and 87 K for Co₂(dobdc). The solid lines represent the dual-site Langmuir fit to the data, using the parameters tabulated in Table 2.S7.

Table 2.S7. Dual-site Langmuir fit parameters for the H₂ isotherms for Co₂(dobdc) in Figure 2.S25.

	77 K	87 K
$q_{sat,A}$	10.78	15.58
b_A	0.96	0.28
v_A	0.79	0.72
$q_{sat,B}$	5.52	5.41
b_B	1782.70	244.57
v_B	0.99	0.99

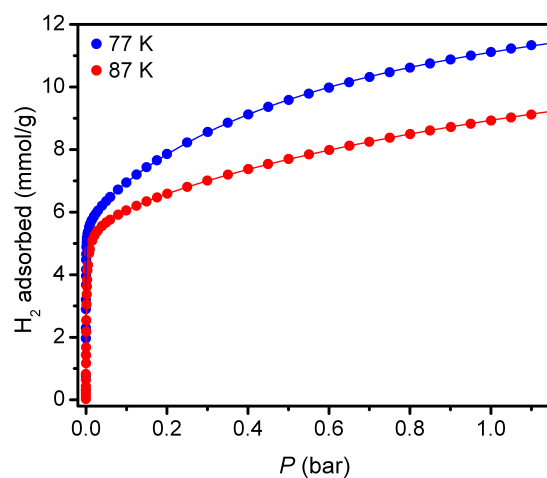


Figure 2.S26. H₂ adsorption isotherms at 77 K and 87 K for Ni₂(dobdc). The solid lines represent the tri-site Langmuir fit to the data, using the parameters tabulated in Table 2.S8.

Table 2.S8. Tri-site Langmuir fit parameters for the H₂ isotherms for Ni₂(dobdc) in Figure 2.S26.

	77 and 87 K
$q_{sat,A}$	5.17
b_A	4.55E-5
E_A	12.23
$q_{sat,B}$	8.81
b_B	2.30E-4
E_B	5.63
$q_{sat,C}$	0.73
b_C	7.58E-5
E_C	9.10

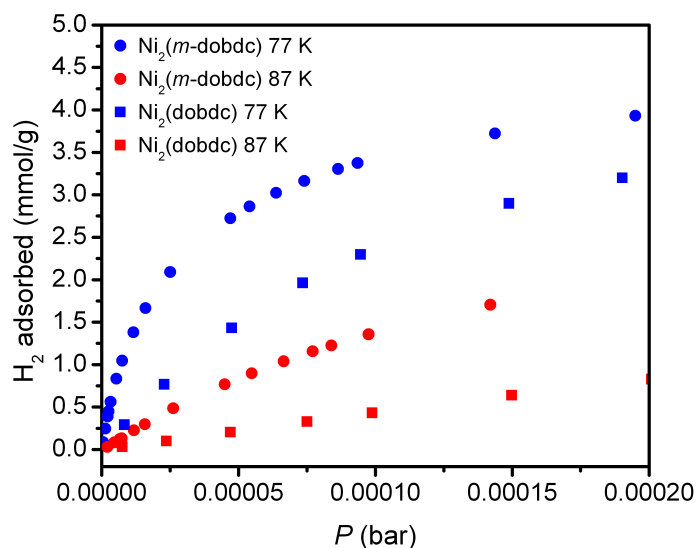


Figure 2.S27. A low-pressure comparison of $\text{Ni}_2(m\text{-dobdc})$ (circles) and $\text{Ni}_2(\text{dobdc})$ (squares) at 77 K (blue) and 87 K (red). Note the steepness of the $\text{Ni}_2(m\text{-dobdc})$ isotherms as compared to the $\text{Ni}_2(\text{dobdc})$ isotherms.

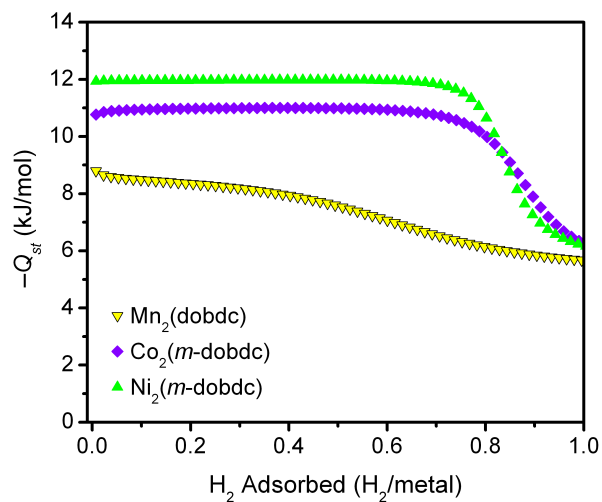


Figure 2.S28. Isosteric heat of adsorption curve for $\text{M}_2(\text{dobdc})$ ($\text{M} = \text{Mn}, \text{Co}, \text{Ni}$) as a function of the amount adsorbed.

Table 2.S9. Atomic parameters from Rietveld refinement of desolvated Co₂(*m*-dobdc) at 10 K [NCNR, BT1], *R3m*, *a* = 25.873(2) Å, *c* = 6.7677(9) Å, *V* = 3923.6(6) Å³. Values in parentheses indicate one standard deviation in the refined value. Goodness-of-fit parameters: $\chi^2 = 0.87$; wRp = 5.42 %; Rp = 4.32 %. Refined composition: Co₁₈H₁₈C₇₂O₅₄.

Atom	X	Y	Z	Occupancy	U _(ISO) (Å ²)	Multiplicity
C1	0.658(1)	0.878(1)	0.837(4)	1	0.044(9)	18
C2	0.665(1)	0.8327(7)	0.744(5)	1	0.02(1)	9
C6	0.639(1)	0.8661(8)	0.040(4)	1	0.015(6)	18
C11	0.6322(8)	0.9088(8)	0.163(3)	1	0.013(5)	18
Co1	0.328(3)	0.376(2)	0.556(8)	1	0.02(2)	18
H7	0.680(3)	0.840(1)	0.59(1)	1	0.04(2)	9
O9	0.670(1)	0.926(1)	0.748(4)	1	0.031(9)	18
O12	0.652(1)	0.962(1)	0.096(3)	1	0.019(7)	18
O15	0.610(1)	0.891(1)	0.334(4)	1	0.034(7)	18
C2m	0.628(1)	0.8141(6)	0.125(4)	1	0.026(9)	9
H7m	0.617(2)	0.809(1)	0.282(8)	1	0.03(1)	9

Table 2.S10. Atomic parameters from Rietveld refinement of desolvated Co₂(*m*-dobdc) at 298 K [APS, 17-BM-B], *R3m*, *a* = 25.8902(7) Å, *c* = 6.7905(3) Å, *V* = 3941.9(2) Å³. Values in parentheses indicate one standard deviation in the refined value. Goodness-of-fit parameters: $\chi^2 = 4.505$; wRp = 3.71 %; Rp = 2.94 %. Refined composition: Co₁₈H₁₈C₇₂O₅₄.

Atom	X	Y	Z	Occupancy	U _(ISO) (Å ²)	Multiplicity
C1	0.658(2)	0.877(2)	0.837(9)	1	0.17(2)	18
C2	0.669(3)	0.835(2)	0.74(1)	1	0.11(2)	9
C6	0.639(1)	0.866(1)	0.036(7)	1	0.026(8)	18
C11	0.632(1)	0.908(1)	0.163(8)	1	0.022(9)	18
Co1	0.3276(3)	0.3751(2)	0.557(6)	1	0.0213(6)	18
H7	0.69(1)	0.845(6)	0.58(4)	1	0.2(1)	9
O9	0.6704(9)	0.9263(6)	0.747(8)	1	0.022(5)	18
O12	0.6516(7)	0.9614(8)	0.098(7)	1	0.067(8)	18
O15	0.6103(6)	0.8919(7)	0.339(6)	1	0.052(7)	18
C2m	0.627(2)	0.813(1)	0.127(7)	1	0.09(2)	9
H7m	0.63(1)	0.813(5)	0.29(4)	1	0.06(9)	9

Table 2.S11. Atomic parameters from Rietveld refinement of desolvated Ni₂(*m*-dobdc) at 10 K [NCNR, BT1], *R3m*, *a* = 25.797(5) Å, *c* = 6.729(2) Å, *V* = 3878.(1) Å³. Values in parentheses indicate one standard deviation in the refined value. Goodness-of-fit parameters: $\chi^2 = 1.10$; wRp = 4.27 %; Rp = 3.48 %. Refined composition: Ni₁₈H₁₈C₇₂O₅₄.

Atom	X	Y	Z	Occupancy	U _(iso) (Å ²)	Multiplicity
C1	0.658(2)	0.878(1)	0.837(6)	1	0.03(1)	18
C2	0.666(3)	0.833(1)	0.75(1)	1	0.03(2)	9
C6	0.639(2)	0.866(1)	0.043(6)	1	0.01(1)	18
C11	0.632(1)	0.909(1)	0.166(5)	1	0.011(9)	18
Ni1	0.326(1)	0.376(1)	0.555(3)	1	0.020(6)	18
H7	0.679(4)	0.839(2)	0.58(1)	1	0.05(4)	9
O9	0.669(2)	0.925(2)	0.749(7)	1	0.02(1)	18
O12	0.652(1)	0.962(2)	0.096(5)	1	0.02(2)	18
O15	0.610(2)	0.891(2)	0.338(7)	1	0.04(1)	18
C2m	0.628(2)	0.814(1)	0.128(7)	1	0.01(1)	9
H7m	0.619(3)	0.809(2)	0.28(1)	1	0.01(2)	18

Table 2.S12. Atomic parameters from Rietveld refinement of Co₂(*m*-dobdc) dosed with 0.75 D₂ per Co²⁺ at 10 K [NCNR, BT1], *R3m*, *a* = 25.842(2) Å, *c* = 6.7810(7) Å, *V* = 3921.7(5) Å³. Values in parentheses indicate one standard deviation in the refined value. Goodness-of-fit parameters: $\chi^2 = 0.83$; wRp = 4.98 %; Rp = 3.91 %. Refined composition: Co₁₈H₁₈C₇₂O₅₄D_{30.466}.

Atom	X	Y	Z	Occupancy	U _(iso) (Å ²)	Multiplicity
C1	0.6573(8)	0.8763(8)	0.838(3)	1	0.018(5)	18
C2	0.665(1)	0.8323(5)	0.747(4)	1	0.013(8)	9
C6	0.6399(7)	0.8669(7)	0.045(3)	1	0.015(5)	18
C11	0.6321(6)	0.9089(6)	0.164(2)	1	0.004(3)	18
Ni1	0.330(2)	0.376(2)	0.559(6)	1	0.001(9)	18
H7	0.678(3)	0.839(1)	0.59(1)	1	0.06(2)	9
O9	0.6700(8)	0.9255(7)	0.748(3)	1	0.010(5)	18
O12	0.6497(9)	0.9617(9)	0.090(3)	1	0.021(7)	18
O15	0.6084(8)	0.8903(7)	0.330(3)	1	0.011(4)	18
C2m	0.629(1)	0.8142(6)	0.125(4)	1	0.026(8)	9
H7m	0.616(2)	0.808(1)	0.285(8)	1	0.04(1)	9
D1	0.2042(6)	0.2155(6)	0.018(2)	1.69(5)	0.090(6)	18

Table 2.S13. Atomic parameters from Rietveld refinement of Co₂(dobdc) dosed with 0.75 D₂ per Co²⁺ at 10 K [NCNR, BT1], $R-3$, $a = 25.871(1)$ Å, $c = 6.8687(4)$ Å, $V = 3981.3(3)$ Å³. Values in parentheses indicate one standard deviation in the refined value. Goodness-of-fit parameters: $\chi^2 = 1.356$; wRp = 2.79 %; Rp = 2.29 %. Refined composition: Co₁₈H₁₈C₇₂O₅₄D_{28.61}.

Atom	X	Y	Z	Occupancy	U _(iso) (Å ²)	Multiplicity
Co	0.386(1)	0.355(1)	0.134(3)	1	0.004(6)	18
O1	0.3229(5)	0.2946(5)	0.372(2)	1	0.017(3)	18
O2	0.3040(5)	0.2292(5)	0.601(1)	1	0.005(3)	18
O3	0.3577(5)	0.2742(5)	0.002(2)	1	0.005(3)	18
C1	0.3147(5)	0.2463(5)	0.428(1)	1	0.030(3)	18
C2	0.3300(4)	0.2086(4)	0.281(1)	1	0.018(3)	18
C3	0.3491(4)	0.2278(4)	0.090(1)	1	0.010(3)	18
C4	0.3525(4)	0.1839(5)	-0.035(1)	1	0.004(3)	18
H	0.3601(7)	0.1925(6)	-0.159(3)	1	0.001(4)	18
D1	0.4659(4)	0.3498(4)	0.265(1)	1.59(3)	0.089(5)	18

Table 2.S14. Atomic parameters from Rietveld refinement of Co₂(dobdc) dosed with 2.25 D₂ per Co²⁺ at 10 K [NCNR, BT1], $R-3$, $a = 25.878(1)$ Å, $c = 6.8820(3)$ Å, $V = 3991.3(3)$ Å³. Values in parentheses indicate one standard deviation in the refined value. Goodness-of-fit parameters: $\chi^2 = 1.459$; wRp = 2.81 %; Rp = 2.34 %. Refined composition: Co₁₈H₁₈C₇₂O₅₄D_{88.56}.

Atom	X	Y	Z	Occupancy	U _(iso) (Å ²)	Multiplicity
Co	0.381(1)	0.351(1)	0.132(4)	1	0.004(7)	18
O1	0.3246(6)	0.2940(6)	0.365(2)	1	0.009(4)	18
O2	0.3006(6)	0.2281(6)	0.599(2)	1	0.009(3)	18
O3	0.3570(6)	0.2745(7)	-0.003(2)	1	0.012(4)	18
C1	0.3143(6)	0.2450(6)	0.426(1)	1	0.013(3)	18
C2	0.3296(5)	0.2087(5)	0.287(2)	1	0.010(3)	18
C3	0.3463(5)	0.2251(6)	0.088(2)	1	0.018(4)	18
C4	0.3501(5)	0.1811(6)	-0.029(2)	1	0.008(4)	18
H	0.3633(8)	0.1945(7)	-0.166(4)	1	0.010(6)	18
D1	0.4642(5)	0.3493(4)	0.250(2)	1.60(3)	0.065(4)	18
D2	0.4587(5)	0.2999(4)	0.673(2)	1.92(5)	0.130(7)	18
D3	0.2400(8)	0.4877(7)	0.852(3)	1.40(3)	0.15(1)	18

Table 2.S15. Atomic parameters from Rietveld refinement of Co₂(*m*-dobdc) dosed with 1.25 D₂ per Co²⁺ at 10 K [NCNR, BT1], *R*3m, *a* = 25.872(1) Å, *c* = 6.7881(5) Å, *V* = 3928.8(5) Å³. Values in parentheses indicate one standard deviation in the refined value. Goodness-of-fit parameters: $\chi^2 = 1.123$; wRp = 3.45 %; Rp = 2.80 %. Refined composition: Co₁₈H₁₈C₇₂O₅₄D_{42.66}.

Atom	X	Y	Z	Occupancy	U _(iso) (Å ²)	Multiplicity
C1	0.6567(6)	0.8752(6)	0.837(2)	1	0.010(4)	18
C2	0.6664(9)	0.8332(4)	0.753(4)	1	0.010(6)	9
C6	0.6414(6)	0.8682(6)	0.040(2)	1	0.014(4)	18
C11	0.6337(5)	0.9093(5)	0.160(2)	1	0.008(3)	18
Co2	0.328(2)	0.373(1)	0.570(4)	1	0.002(8)	18
H7	0.674(2)	0.837(1)	0.608(7)	1	0.05(2)	9
O9	0.6723(6)	0.9273(6)	0.743(2)	1	0.005(4)	18
O12	0.6511(7)	0.9636(7)	0.086(2)	1	0.018(5)	18
O15	0.6103(7)	0.8947(6)	0.338(2)	1	0.010(4)	18
C2m	0.6275(8)	0.8137(4)	0.136(3)	1	0.012(6)	9
H7m	0.618(2)	0.8091(9)	0.275(7)	1	0.04(1)	9
D1	0.2044(4)	0.2145(5)	0.019(1)	1.87(4)	0.071(5)	18
D2	0.791(2)	0.952(2)	0.414(6)	0.50(4)	0.15(3)	18

Table 2.S16. Atomic parameters from Rietveld refinement of Co₂(*m*-dobdc) dosed with 1.50 D₂ per Co²⁺ at 10 K [NCNR, BT1], *R*3m, *a* = 25.852(2) Å, *c* = 6.7898(7) Å, *V* = 3929.9(6) Å³. Values in parentheses indicate one standard deviation in the refined value. Goodness-of-fit parameters: $\chi^2 = 0.889$; wRp = 5.11 %; Rp = 4.06 %. Refined composition: Co₁₈H₁₈C₇₂O₅₄D_{48.78}.

Atom	X	Y	Z	Occupancy	U _(iso) (Å ²)	Multiplicity
C1	0.6571(9)	0.8745(9)	0.838(3)	1	0.014(6)	18
C2	0.664(1)	0.8322(6)	0.754(5)	1	0.012(9)	9
C6	0.6413(9)	0.8676(8)	0.044(3)	1	0.018(6)	18
C11	0.6324(7)	0.9091(8)	0.165(3)	1	0.011(5)	18
Co2	0.327(2)	0.372(2)	0.555(7)	1	0.004(13)	18
H7	0.677(3)	0.839(1)	0.59(1)	1	0.06(2)	9
O9	0.6706(8)	0.9261(8)	0.750(4)	1	0.008(6)	18
O12	0.652(1)	0.964(1)	0.091(3)	1	0.022(8)	18
O15	0.609(1)	0.8924(9)	0.336(3)	1	0.013(5)	18
C2m	0.628(1)	0.8138(6)	0.133(4)	1	0.018(9)	9
H7m	0.615(3)	0.808(1)	0.273(9)	1	0.03(2)	9
D1	0.2062(6)	0.2169(7)	0.018(2)	2.00(7)	0.096(8)	18
D2	0.778(2)	0.946(2)	0.440(7)	0.71(5)	0.12(2)	18

Table 2.S17. Atomic parameters from Rietveld refinement of Co₂(*m*-dobdc) dosed with 1.75 D₂ per Co²⁺ at 10 K [NCNR, BT1], *R*3m, *a* = 25.883(1) Å, *c* = 6.8030(4) Å, *V* = 3946.8(3) Å³. Values in parentheses indicate one standard deviation in the refined value. Goodness-of-fit parameters: $\chi^2 = 1.351$; wRp = 3.01 %; Rp = 2.47 %. Refined composition: Co₁₈H₁₈C₇₂O₅₄D_{62.46}.

Atom	X	Y	Z	Occupancy	U _(iso) (Å ²)	Multiplicity
C1	0.6567(6)	0.8755(5)	0.836(2)	1	0.012(4)	18
C2	0.6672(8)	0.8336(4)	0.746(3)	1	0.010(5)	9
C6	0.6414(6)	0.8680(5)	0.045(2)	1	0.015(4)	18
C11	0.6341(4)	0.9101(5)	0.163(2)	1	0.007(3)	18
Co2	0.328(1)	0.373(1)	0.571(4)	1	0.001(7)	18
H7	0.678(2)	0.8387(9)	0.599(8)	1	0.07(2)	9
O9	0.6732(5)	0.9279(5)	0.747(2)	1	0.008(4)	18
O12	0.6520(6)	0.9635(6)	0.092(2)	1	0.015(4)	18
O15	0.6119(6)	0.8957(6)	0.336(2)	1	0.014(4)	18
C2m	0.6287(7)	0.8143(4)	0.143(3)	1	0.009(5)	9
H7m	0.621(2)	0.8105(8)	0.272(6)	1	0.03(1)	9
D1	0.2065(4)	0.2157(4)	0.006(2)	1.76(4)	0.082(5)	18
D2	0.7777(8)	0.9466(6)	0.426(3)	1.27(3)	0.104(7)	18
D3	0.575(2)	0.149(4)	0.47(1)	0.9(1)	0.8(2)	9

Table 2.S18. Atomic parameters from Rietveld refinement of Co₂(*m*-dobdc) dosed with 2.0 D₂ per Co²⁺ at 10 K [NCNR, BT1], *R*3m, *a* = 25.881(2) Å, *c* = 6.8038(6) Å, *V* = 3946.7(6) Å³. Values in parentheses indicate one standard deviation in the refined value. Goodness-of-fit parameters: $\chi^2 = 0.84$; wRp = 5.19 %; Rp = 4.13 %. Refined composition: Co₁₈H₁₈C₇₂O₅₄D_{67.14}.

Atom	X	Y	Z	Occupancy	U _(iso) (Å ²)	Multiplicity
C1	0.6572(9)	0.8750(9)	0.835(4)	1	0.016(6)	18
C2	0.666(1)	0.8328(6)	0.749(5)	1	0.015(8)	9
C6	0.6414(9)	0.8681(8)	0.044(4)	1	0.017(6)	18
C11	0.6338(7)	0.9098(7)	0.162(3)	1	0.012(5)	18
Co2	0.325(2)	0.372(2)	0.558(7)	1	0.002(14)	18
H7	0.678(3)	0.839(1)	0.60(1)	1	0.07(2)	9
O9	0.6718(9)	0.9267(9)	0.751(4)	1	0.014(7)	18
O12	0.6523(9)	0.964(1)	0.093(3)	1	0.017(7)	18
O15	0.6107(9)	0.8939(9)	0.331(3)	1	0.018(5)	18
C2m	0.628(1)	0.8141(6)	0.131(5)	1	0.014(8)	9
H7m	0.616(2)	0.808(1)	0.280(9)	1	0.03(2)	9
D1	0.2076(7)	0.2162(7)	0.008(3)	2.0	0.110(7)	18
D2	0.775(1)	0.9469(9)	0.426(4)	1.51(6)	0.12(1)	18
D3	0.581(3)	0.163(5)	0.49(2)	0.43(8)	0.19(8)	9

Table 2.S19. Atomic parameters from Rietveld refinement of $\text{Co}_2(m\text{-dobdc})$ dosed with 2.25 D_2 per Co^{2+} at 10 K [NCNR, BT1], $R3m$, $a = 25.901(1)$ Å, $c = 6.810(4)$ Å, $V = 3956.7(4)$ Å³. Values in parentheses indicate one standard deviation in the refined value. Goodness-of-fit parameters: $\chi^2 = 1.149$; $wRp = 3.32$ %; $Rp = 2.73$ %.
Refined composition: $\text{Co}_{18}\text{H}_{18}\text{C}_{72}\text{O}_{54}\text{D}_{80.82}$.

Atom	X	Y	Z	Occupancy	$U_{(iso)}$ (Å ²)	Multiplicity
C1	0.6578(6)	0.8758(6)	0.832(3)	1	0.013(4)	18
C2	0.6676(8)	0.8338(4)	0.739(4)	1	0.009(5)	9
C6	0.6425(6)	0.8683(6)	0.041(3)	1	0.019(4)	18
C11	0.6357(5)	0.9108(6)	0.161(2)	1	0.015(4)	18
Co2	0.328(2)	0.373(1)	0.565(5)	1	0.003(8)	18
H7	0.676(1)	0.8380(7)	0.594(7)	1	0.04(1)	9
O9	0.6747(5)	0.9287(5)	0.747(2)	1	0.000(4)	18
O12	0.6538(6)	0.9638(7)	0.090(2)	1	0.011(5)	18
O15	0.6130(6)	0.8968(7)	0.332(2)	1	0.019(4)	18
C2m	0.6295(8)	0.8147(4)	0.137(3)	1	0.008(6)	9
H7m	0.620(2)	0.8102(7)	0.267(7)	1	0.018(9)	9
D1	0.2059(5)	0.2157(5)	0.001(2)	1.82(4)	0.089(6)	18
D2	0.7756(7)	0.9478(6)	0.423(3)	1.64(3)	0.104(5)	18
D3	0.576(1)	0.152(2)	0.526(6)	1.05(9)	0.23(4)	9
D4	0.587(2)	0.174(5)	0.16(2)	1.0(2)	0.8(2)	9

Table 2.S20. Atomic parameters from Rietveld refinement of Co₂(*m*-dobdc) dosed with 3.0 D₂ per Co²⁺ at 10 K [NCNR, BT1], *R*3*m*, *a* = 25.892(2) Å, *c* = 6.8115(6) Å, *V* = 3954.7(6) Å³. Values in parentheses indicate one standard deviation in the refined value. Goodness-of-fit parameters: $\chi^2 = 0.873$; wRp = 5.01 %; Rp = 4.00 %. Refined composition: Co₁₈H₁₈C₇₂O₅₄D_{101.34}.

Atom	X	Y	Z	Occupancy	U _(ISO) (Å ²)	Multiplicity
C1	0.659(1)	0.877(1)	0.837(3)	1	0.018(6)	18
C2	0.667(1)	0.8335(6)	0.752(5)	1	0.012(8)	9
C6	0.644(1)	0.8692(9)	0.047(3)	1	0.023(6)	18
C11	0.6365(8)	0.9117(9)	0.163(3)	1	0.024(6)	18
Co2	0.327(2)	0.371(2)	0.564(7)	1	0.001(13)	18
H7	0.678(2)	0.839(1)	0.583(9)	1	0.03(2)	9
O9	0.6745(9)	0.9275(9)	0.751(3)	1	0.009(6)	18
O12	0.6533(9)	0.964(1)	0.092(3)	1	0.015(7)	18
O15	0.614(1)	0.897(1)	0.333(3)	1	0.025(6)	18
C2m	0.629(1)	0.8145(6)	0.131(4)	1	0.011(8)	9
H7m	0.615(2)	0.808(1)	0.271(8)	1	0.02(2)	9
D1	0.2088(7)	0.2169(7)	0.004(2)	2.0	0.093(6)	18
D2	0.7752(8)	0.9466(9)	0.429(3)	1.91(5)	0.120(8)	18
D3	0.5789(7)	0.158(1)	0.525(4)	2.00(9)	0.19(2)	9
D4	0.5855(6)	0.171(1)	0.045(4)	1.43(6)	0.11(2)	9

Table 2.S21. Atomic parameters from Rietveld refinement of Ni₂(*m*-dobdc) dosed with 1.0 D₂ per Ni²⁺ at 10 K [NCNR, BT1], *R*3*m*, *a* = 25.749(4) Å, *c* = 6.739(1) Å, *V* = 3870.(1) Å³. Values in parentheses indicate one standard deviation in the refined value. Goodness-of-fit parameters: $\chi^2 = 0.988$; wRp = 3.77 %; Rp = 3.08 %. Refined composition: Ni₁₈H₁₈C₇₂O₅₄D_{35.46}.

Atom	X	Y	Z	Occupancy	U _(ISO) (Å ²)	Multiplicity
C1	0.658(1)	0.875(1)	0.836(5)	1	0.02(1)	18
C2	0.668(2)	0.8339(8)	0.748(7)	1	0.003(11)	9
C6	0.647(1)	0.869(1)	0.054(5)	1	0.022(9)	18
C11	0.635(1)	0.912(1)	0.172(4)	1	0.020(9)	18
Ni2	0.3262(8)	0.3720(8)	0.563(2)	1	0.006(4)	18
H7	0.671(3)	0.836(2)	0.613(9)	1	0.02(2)	9
O9	0.673(1)	0.929(1)	0.759(4)	1	0.000(7)	18
O12	0.654(1)	0.965(1)	0.100(5)	1	0.01(1)	18
O15	0.610(2)	0.893(2)	0.357(5)	1	0.04(1)	18
C2m	0.630(2)	0.8148(8)	0.135(5)	1	0.003(10)	9
H7m	0.624(2)	0.812(1)	0.27(1)	1	0.003(17)	9
D1	0.2095(9)	0.219(1)	0.018(4)	1.97(7)	0.15(2)	18

Table 2.S22. Atomic parameters from Rietveld refinement of Ni₂(*m*-dobdc) dosed with 2.0 D₂ per Ni²⁺ at 10 K [NCNR, BT1], *R*3*m*, *a* = 25.776(5) Å, *c* = 6.754(2) Å, *V* = 3887.(1) Å³. Values in parentheses indicate one standard deviation in the refined value. Goodness-of-fit parameters: $\chi^2 = 1.676$; wRp = 4.69 %; Rp = 3.70 %. Refined composition: Ni₁₈H₁₈C₇₂O₅₄D_{69.30}.

Atom	X	Y	Z	Occupancy	U _(iso) (Å ²)	Multiplicity
C1	0.660(2)	0.877(2)	0.832(7)	1	0.02(1)	18
C2	0.672(3)	0.836(1)	0.74(1)	1	0.01(2)	9
C6	0.648(2)	0.869(2)	0.051(6)	1	0.02(1)	18
C11	0.632(2)	0.909(1)	0.162(5)	1	0.01(1)	18
Ni2	0.325(1)	0.3697(9)	0.557(3)	1	0.002(6)	18
H7	0.673(4)	0.836(2)	0.59(2)	1	0.02(3)	9
O9	0.674(2)	0.928(2)	0.764(6)	1	0.01(1)	18
O12	0.656(2)	0.964(2)	0.097(7)	1	0.02(2)	18
O15	0.615(2)	0.894(2)	0.351(8)	1	0.05(2)	18
C2m	0.627(2)	0.813(1)	0.138(8)	1	0.01(2)	9
H7m	0.623(4)	0.812(2)	0.26(2)	1	0.00(3)	9
D1	0.211(1)	0.218(1)	0.009(4)	2.0(1)	0.09(2)	18
D2	0.782(2)	0.955(2)	0.434(7)	1.6(1)	0.16(3)	18
D3	0.569(3)	0.138(5)	0.48(1)	0.4(1)	0.01(5)	9

Table 2.S23. Atomic parameters from Rietveld refinement of Ni₂(*m*-dobdc) dosed with 3.0 D₂ per Ni²⁺ at 10 K [NCNR, BT1], *R*3m, *a* = 25.802(5) Å, *c* = 6.761(2) Å, *V* = 3898.(1) Å³. Values in parentheses indicate one standard deviation in the refined value. Goodness-of-fit parameters: $\chi^2 = 1.545$; wRp = 4.64 %; Rp = 3.84 %. Refined composition: Ni₁₈H₁₈C₇₂O₅₄D_{103.86}.

Atom	X	Y	Z	Occupancy	U _(iso) (Å ²)	Multiplicity
C1	0.662(2)	0.878(2)	0.827(7)	1	0.01(1)	18
C2	0.672(3)	0.836(1)	0.75(1)	1	0.00(2)	9
C6	0.647(2)	0.869(2)	0.057(6)	1	0.02(1)	18
C11	0.634(2)	0.911(2)	0.171(6)	1	0.03(1)	18
Ni2	0.327(1)	0.373(1)	0.557(4)	1	0.008(7)	18
H7	0.670(6)	0.835(3)	0.61(2)	1	0.07(5)	9
O9	0.671(2)	0.923(2)	0.763(7)	1	0.01(1)	18
O12	0.655(2)	0.963(2)	0.083(8)	1	0.02(2)	18
O15	0.612(3)	0.892(3)	0.35(1)	1	0.07(2)	18
C2m	0.631(2)	0.816(1)	0.129(7)	1	0.01(2)	9
H7m	0.620(4)	0.810(2)	0.28(2)	1	0.02(3)	9
D1	0.210(1)	0.217(1)	0.013(4)	2.0	0.08(1)	18
D2	0.778(2)	0.953(2)	0.419(6)	2.0	0.17(2)	18
D3	0.5778(9)	0.156(2)	0.530(6)	2.0	0.10(1)	9
D4	0.587(2)	0.173(4)	-0.02(1)	1.5(1)	0.26(7)	9

Table 2.S24. Atomic parameters from Rietveld refinement of Co₂(*m*-dobdc) dosed with 0.7 H₂ per Co²⁺ at 10 K [NCNR, BT1], *R*3m, *a* = 25.860(1) Å, *c* = 6.7766(4) Å, *V* = 3924.5(3) Å³. Values in parentheses indicate one standard deviation in the refined value. Goodness-of-fit parameters: $\chi^2 = 0.973$; wRp = 2.53 %; Rp = 2.12 %. Refined composition: Co₁₈H_{54.9}C₇₂O₅₄.

Atom	X	Y	Z	Occupancy	U _(iso) (Å ²)	Multiplicity
C1	0.6571(4)	0.8756(4)	0.841(2)	1	0.011(4)	18
C2	0.6687(8)	0.8344(4)	0.752(3)	1	0.018(5)	9
C6	0.6388(5)	0.8658(4)	0.045(2)	1	0.010(3)	18
C11	0.6325(4)	0.9102(4)	0.171(1)	1	0.012(3)	18
Co2	0.327(1)	0.375(1)	0.560(4)	1	0.02	18
H7	0.680(1)	0.8399(6)	0.597(4)	1	0.029(9)	9
O9	0.6715(4)	0.9268(5)	0.748(2)	1	0.010(4)	18
O12	0.6529(4)	0.9633(5)	0.095(2)	1	0.014(4)	18
O15	0.6076(4)	0.8932(5)	0.345(2)	1	0.015(3)	18
C2m	0.6288(6)	0.8145(3)	0.139(2)	1	0.002(4)	9
H7m	0.619(1)	0.8094(6)	0.273(4)	1	0.021(7)	9
H1	0.207(1)	0.214(1)	0.035(3)	1.05(3)	0.09(1)	18

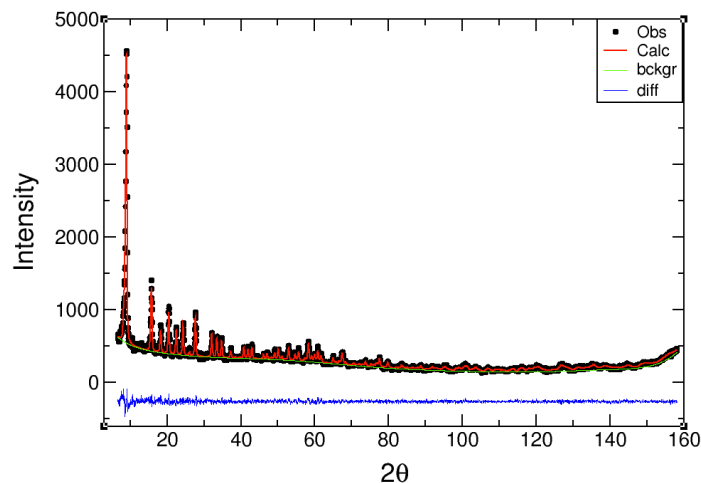


Figure 2.S29. Rietveld refinement of the experimental neutron diffraction pattern (10 K) of $\text{Co}_2(m\text{-dobdc})$. The calculated pattern (red trace) is in good agreement with the experimental data (circles) as evidenced by the difference pattern (blue trace) between calculated and experimental data. Final Rietveld fit parameter was $\chi^2 = 0.87$.

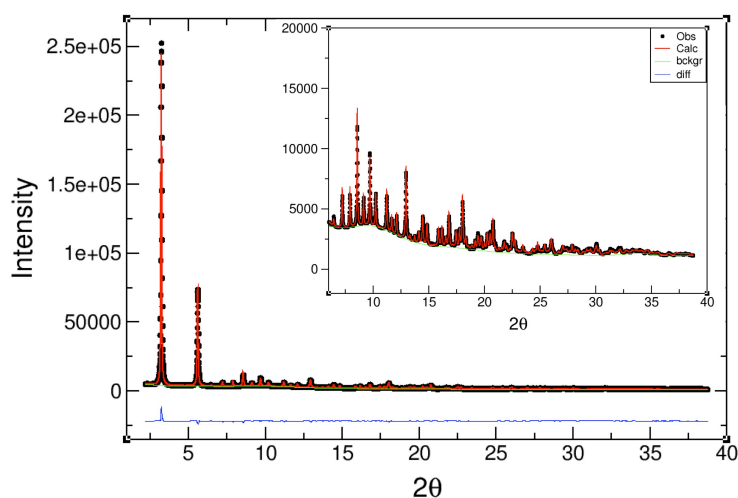


Figure 2.S30. Rietveld refinement of the experimental synchrotron X-ray diffraction pattern (298 K) of $\text{Co}_2(m\text{-dobdc})$. The calculated pattern (red trace) is in good agreement with the experimental data (circles) as evidenced by the difference pattern (blue trace) between calculated and experimental data. Final Rietveld fit parameter was $\chi^2 = 4.505$.

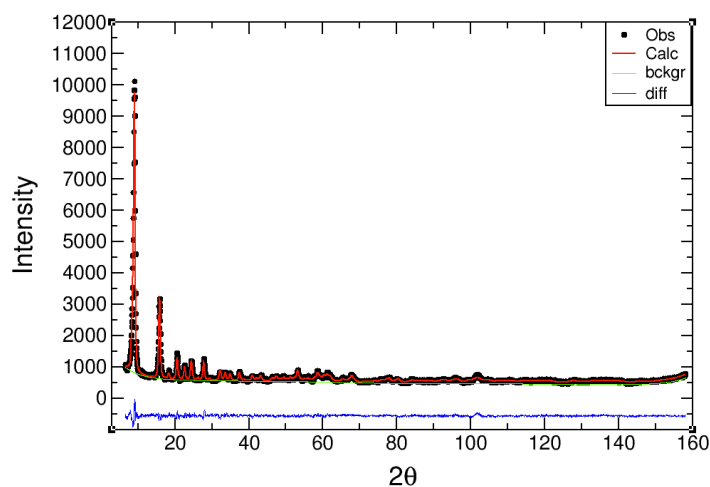


Figure 2.S31. Rietveld refinement of the experimental neutron diffraction pattern (10 K) of $\text{Ni}_2(m\text{-dobdc})$. The calculated pattern (red trace) is in good agreement with the experimental data (circles) as evidenced by the difference pattern (blue trace) between calculated and experimental data. Final Rietveld fit parameter was $\chi^2 = 1.10$.

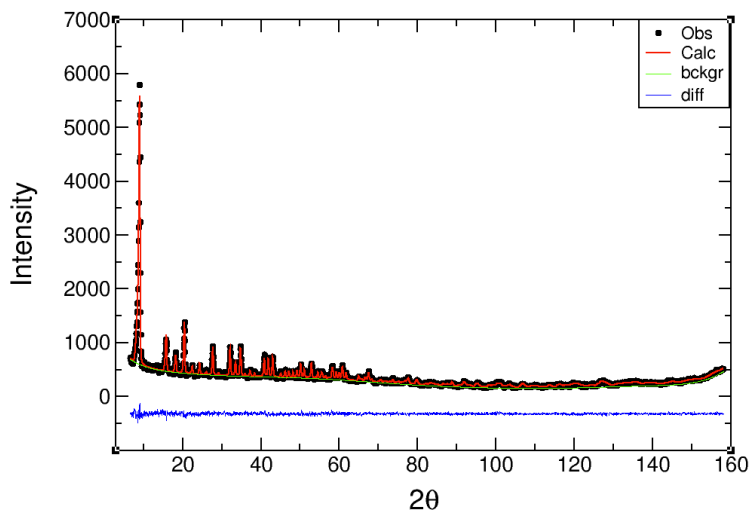


Figure 2.S32. Rietveld refinement of the experimental neutron diffraction pattern (10 K) of $\text{Co}_2(m\text{-dobdc})$ dosed with 0.75 D_2 per Co^{2+} as described in the text. The calculated pattern (red trace) is in good agreement with the experimental data (circles) as evidenced by the difference pattern (blue trace) between calculated and experimental data. Final Rietveld fit parameter was $\chi^2 = 0.83$.

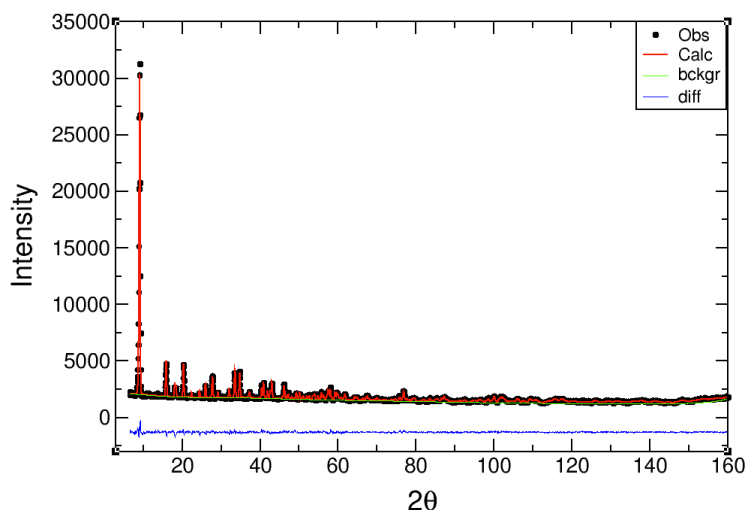


Figure 2.S33. Rietveld refinement of the experimental neutron diffraction pattern (10 K) of $\text{Co}^2(\text{dobdc})$ dosed with 0.75 D_2 per Co^{2+} as described in the text. The calculated pattern (red trace) is in good agreement with the experimental data (circles) as evidenced by the difference pattern (blue trace) between calculated and experimental data. Final Rietveld fit parameter was $\chi^2 = 1.356$.

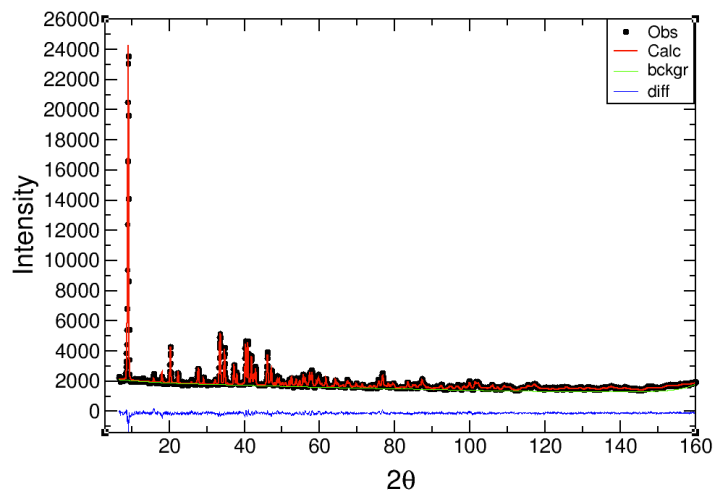


Figure 2.S34. Rietveld refinement of the experimental neutron diffraction pattern (10 K) of $\text{Co}_2(\text{dobdc})$ dosed with 2.25 D_2 per Co^{2+} as described in the text. The calculated pattern (red trace) is in good agreement with the experimental data (circles) as evidenced by the difference pattern (blue trace) between calculated and experimental data. Final Rietveld fit parameter was $\chi^2 = 1.459$.

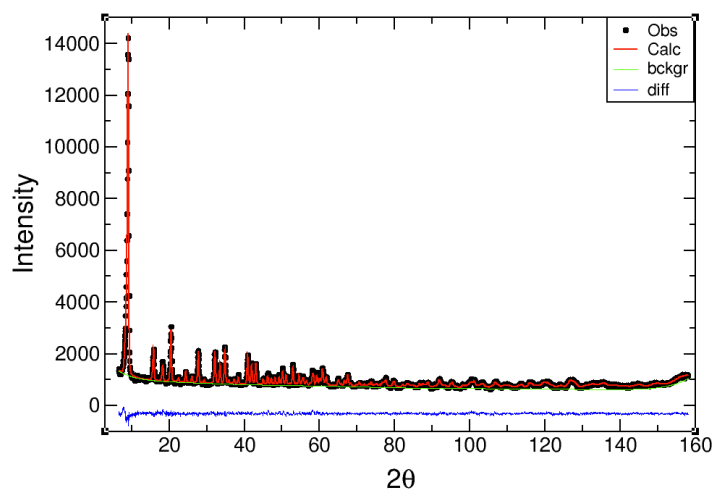


Figure 2.S35. Rietveld refinement of the experimental neutron diffraction pattern (10 K) of $\text{Co}_2(m\text{-dobdc})$ dosed with 1.25 D_2 per Co^{2+} as described in the text. The calculated pattern (red trace) is in good agreement with the experimental data (circles) as evidenced by the difference pattern (blue trace) between calculated and experimental data. Final Rietveld fit parameter was $\chi^2 = 1.123$.

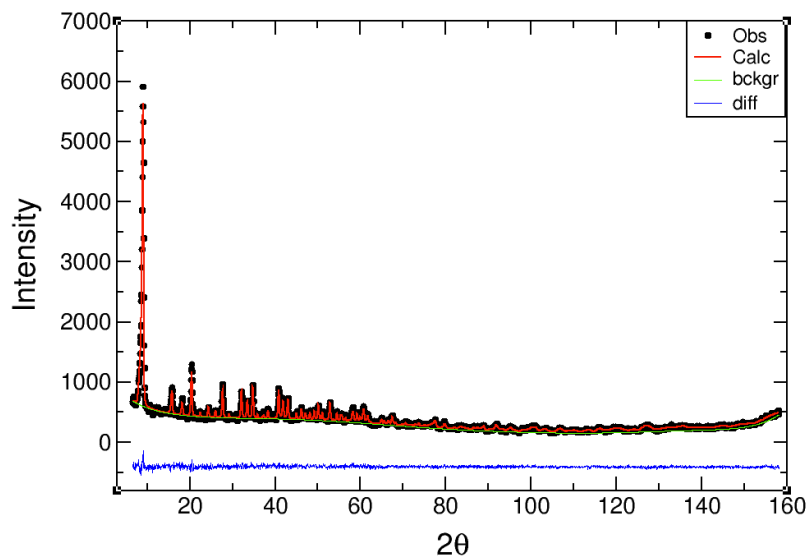


Figure 2.S36. Rietveld refinement of the experimental neutron diffraction pattern (10 K) of $\text{Co}_2(m\text{-dobdc})$ dosed with 1.5 D_2 per Co^{2+} as described in the text. The calculated pattern (red trace) is in good agreement with the experimental data (circles) as evidenced by the difference pattern (blue trace) between calculated and experimental data. Final Rietveld fit parameter was $\chi^2 = 0.889$.

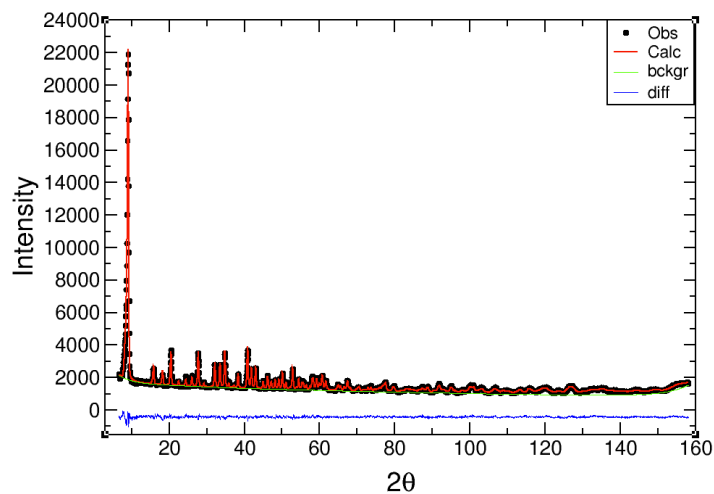


Figure 2.S37. Rietveld refinement of the experimental neutron diffraction pattern (10 K) of $\text{Co}_2(m\text{-dobdc})$ dosed with 1.75 D_2 per Co^{2+} as described in the text. The calculated pattern (red trace) is in good agreement with the experimental data (circles) as evidenced by the difference pattern (blue trace) between calculated and experimental data. Final Rietveld fit parameter was $\chi^2 = 1.351$.

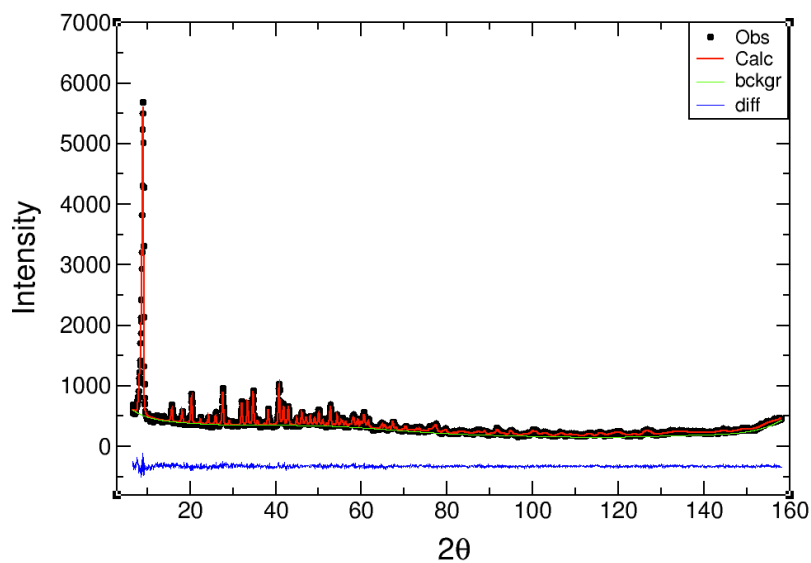


Figure 2.S38. Rietveld refinement of the experimental neutron diffraction pattern (10 K) of $\text{Co}_2(m\text{-dobdc})$ dosed with 2.0 D_2 per Co^{2+} as described in the text. The calculated pattern (red trace) is in good agreement with the experimental data (circles) as evidenced by the difference pattern (blue trace) between calculated and experimental data. Final Rietveld fit parameter was $\chi^2 = 0.84$.

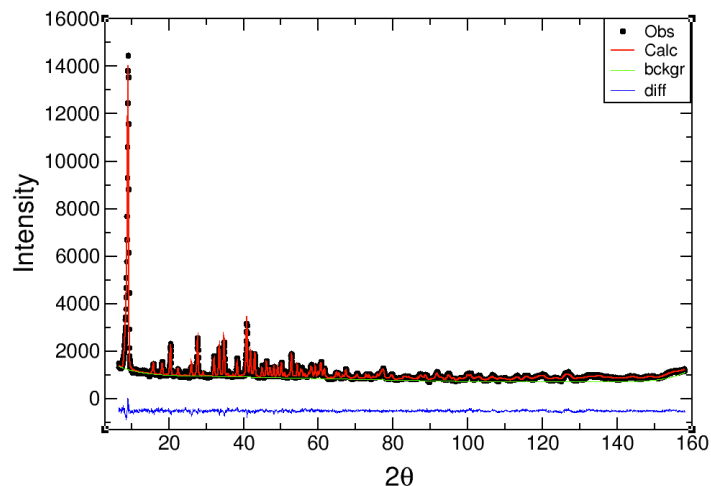


Figure 2.S39. Rietveld refinement of the experimental neutron diffraction pattern (10 K) of $\text{Co}_2(m\text{-dobdc})$ dosed with 2.25 D_2 per Co^{2+} as described in the text. The calculated pattern (red trace) is in good agreement with the experimental data (circles) as evidenced by the difference pattern (blue trace) between calculated and experimental data. Final Rietveld fit parameter was $\chi^2 = 1.149$.

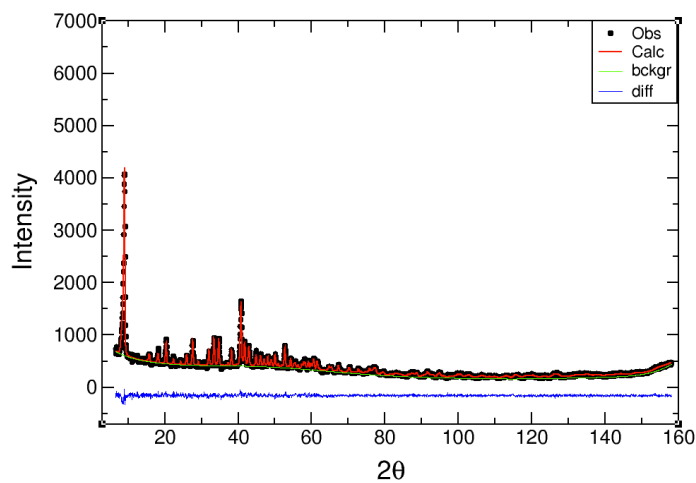


Figure 2.S40. Rietveld refinement of the experimental neutron diffraction pattern (10 K) of $\text{Co}_2(m\text{-dobdc})$ dosed with 3.0 D_2 per Co^{2+} as described in the text. The calculated pattern (red trace) is in good agreement with the experimental data (circles) as evidenced by the difference pattern (blue trace) between calculated and experimental data. Final Rietveld fit parameter was $\chi^2 = 0.873$.

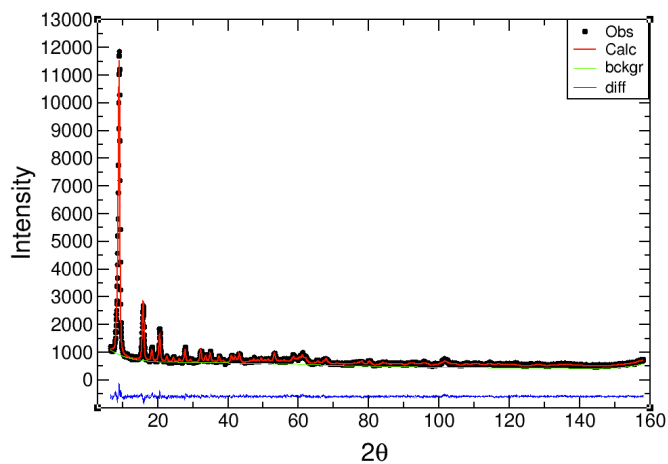


Figure 2.S41. Rietveld refinement of the experimental neutron diffraction pattern (10 K) of $\text{Ni}_2(m\text{-dobdc})$ dosed with 1.0 D_2 per Ni^{2+} as described in the text. The calculated pattern (red trace) is in good agreement with the experimental data (circles) as evidenced by the difference pattern (blue trace) between calculated and experimental data. Final Rietveld fit parameter was $\chi^2 = 0.998$.

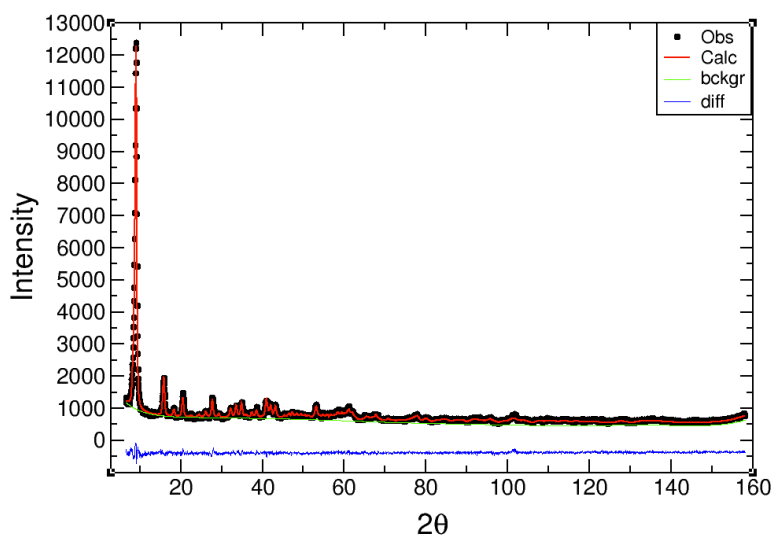


Figure 2.S42. Rietveld refinement of the experimental neutron diffraction pattern (10 K) of $\text{Ni}_2(m\text{-dobdc})$ dosed with 2.0 D_2 per Ni^{2+} as described in the text. The calculated pattern (red trace) is in good agreement with the experimental data (circles) as evidenced by the difference pattern (blue trace) between calculated and experimental data. Final Rietveld fit parameter was $\chi^2 = 1.676$.

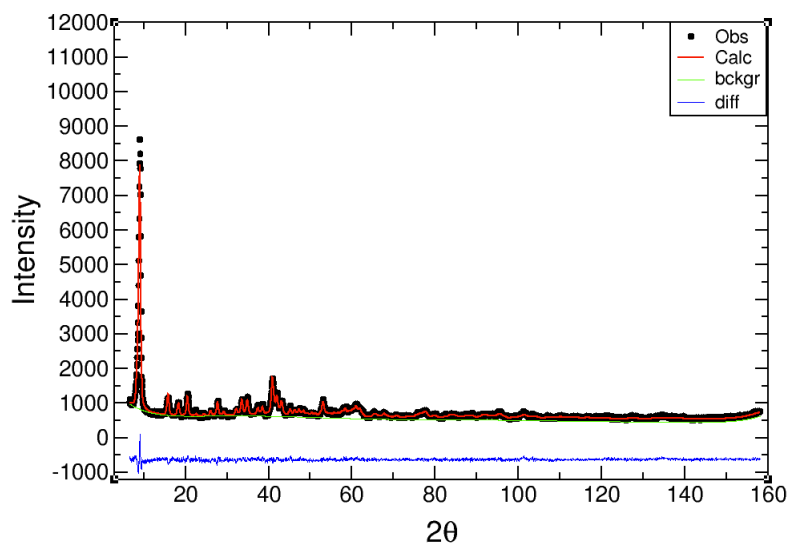


Figure 2.S43. Rietveld refinement of the experimental neutron diffraction pattern (10 K) of $\text{Ni}_2(m\text{-dobdc})$ dosed with 3.0 D_2 per Ni^{2+} as described in the text. The calculated pattern (red trace) is in good agreement with the experimental data (circles) as evidenced by the difference pattern (blue trace) between calculated and experimental data. Final Rietveld fit parameter was $\chi^2 = 1.545$.

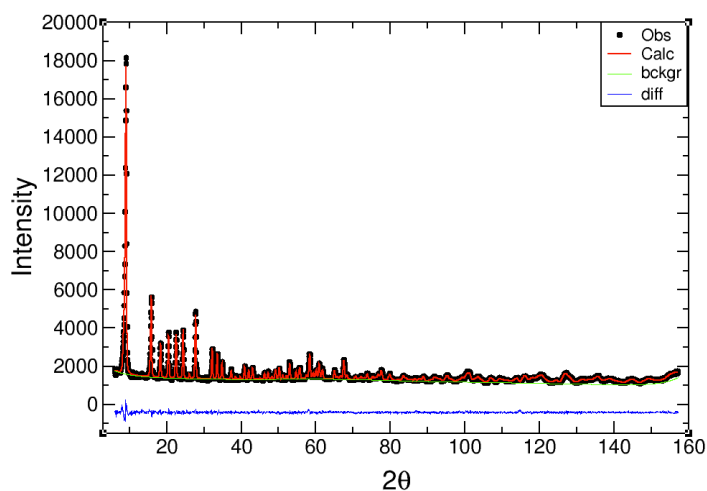


Figure 2.S44. Rietveld refinement of the experimental neutron diffraction pattern (10 K) of $\text{Co}_2(m\text{-dobdc})$ dosed with 0.7 H_2 per Co^{2+} as described in the text. The calculated pattern (red trace) is in good agreement with the experimental data (circles) as evidenced by the difference pattern (blue trace) between calculated and experimental data. Final Rietveld fit parameter was $\chi^2 = 0.973$.

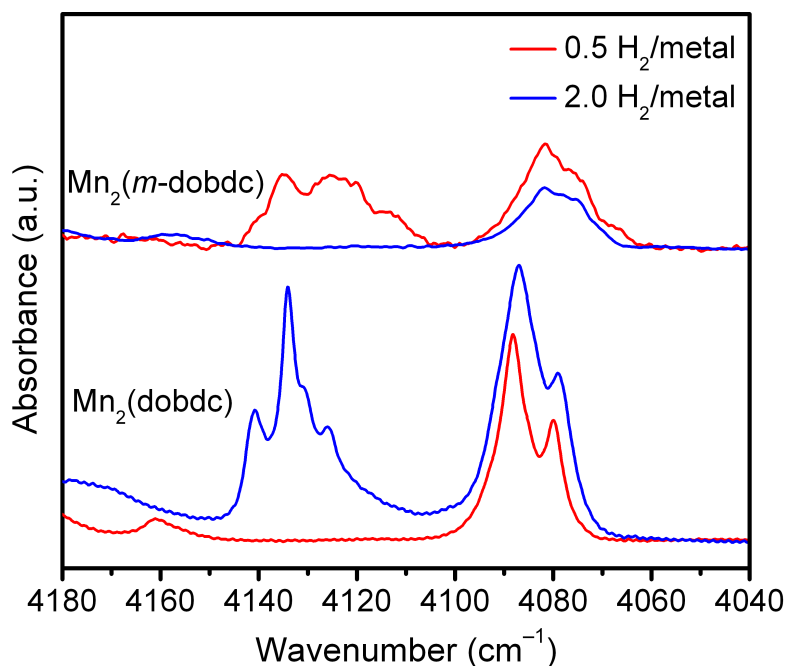


Figure 2.S45. Comparison of the IR spectra of $\text{Mn}_2(m\text{-dobdc})$ and $\text{Mn}_2(\text{dobdc})$ at different concentrations. The slight shift in the peak around 4080 cm^{-1} to lower frequency in $\text{Mn}_2(m\text{-dobdc})$ is indicative of a more strongly bound H_2 to the open metal center. Spectra are offset for clarity.

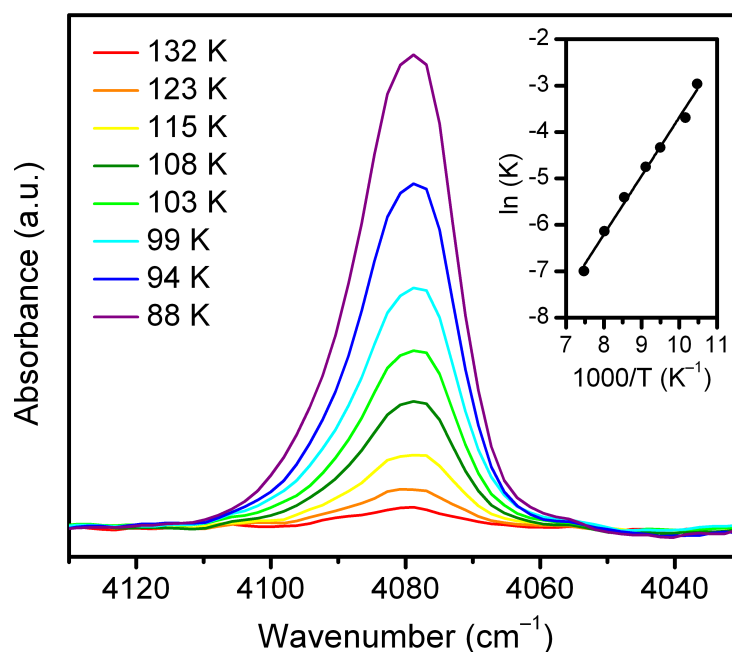


Figure 2.S46. The variable temperature infrared spectra of $\text{Mn}_2(m\text{-dobdc})$. The inset shows the van't Hoff relationship plot that is used to extract the enthalpy and entropy change in H_2 upon adsorption.

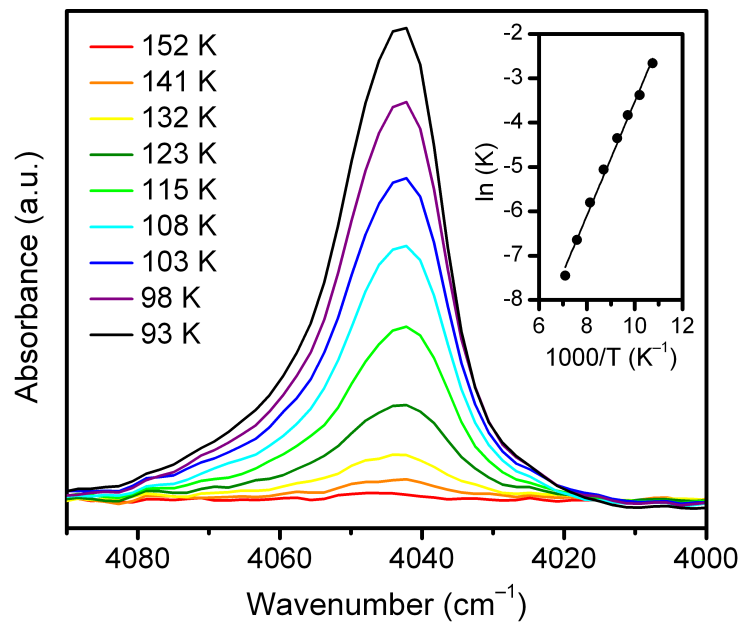


Figure 2.S47. The variable temperature infrared spectra of $\text{Co}_2(\text{dobdc})$. The inset shows the van't Hoff relationship plot that is used to extract the enthalpy and entropy change in H_2 upon adsorption.

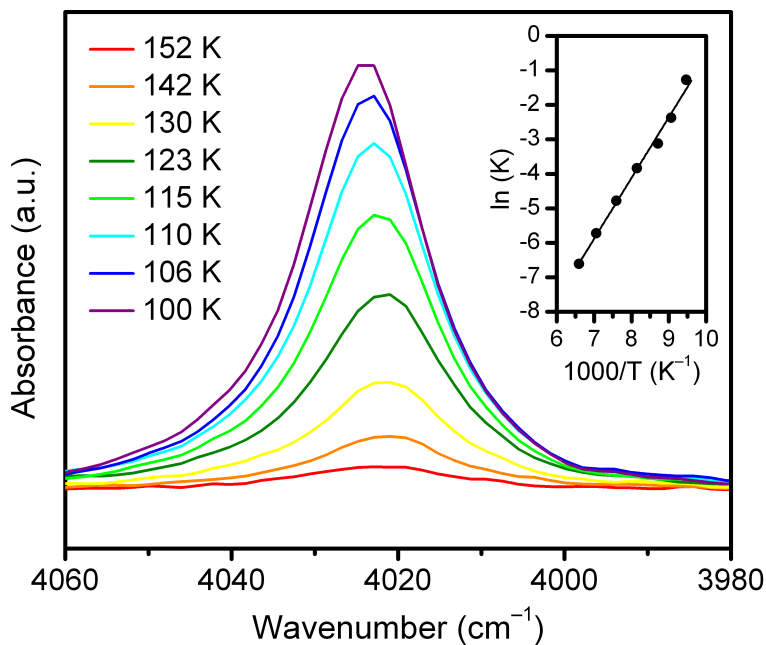


Figure 2.S48. The variable temperature infrared spectra of $\text{Ni}_2(m\text{-dobdc})$. The inset shows the van't Hoff relationship plot that is used to extract the enthalpy and entropy change in H_2 upon adsorption.

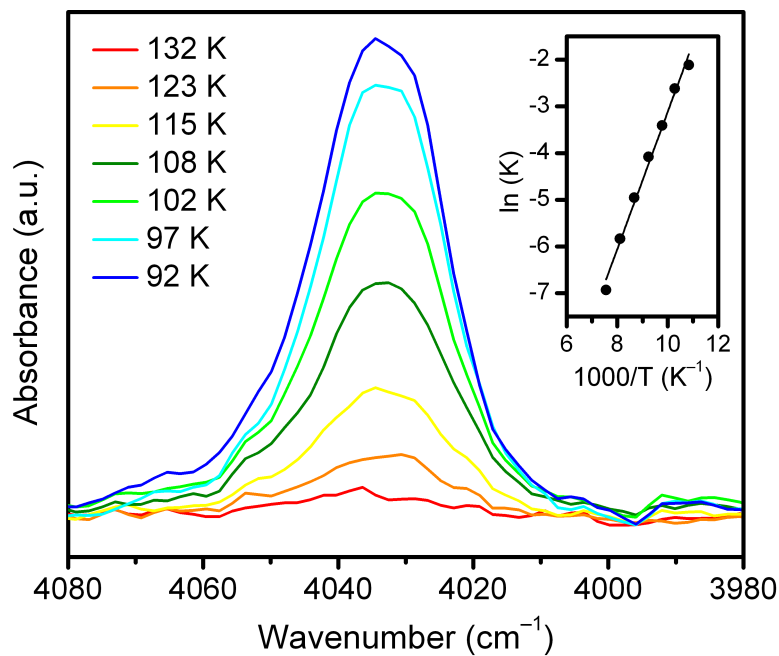


Figure 2.S49. The variable temperature infrared spectra of $\text{Ni}_2(\text{dobdc})$. The inset shows the van't Hoff relationship plot that is used to extract the enthalpy and entropy change in H_2 upon adsorption.

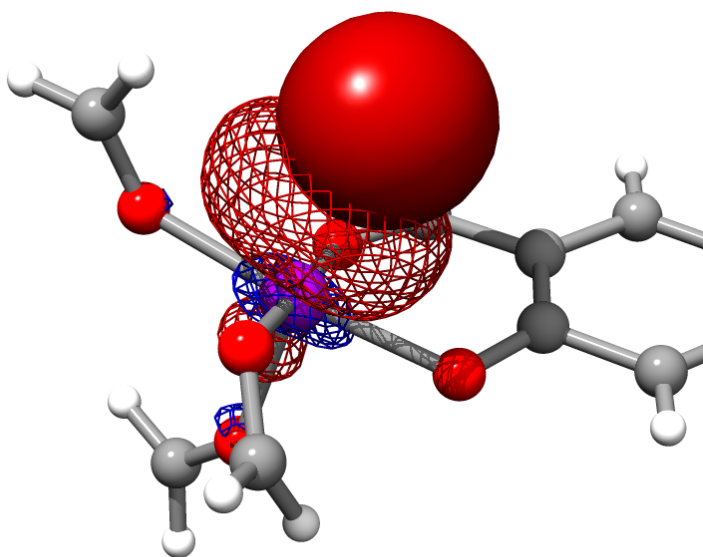


Figure 2.S50. The occupied and virtual orbitals, shown as solid and mesh, respectively, for the forward bonding pair COVP 1 (Table 2.S24) for the dobdc complex.

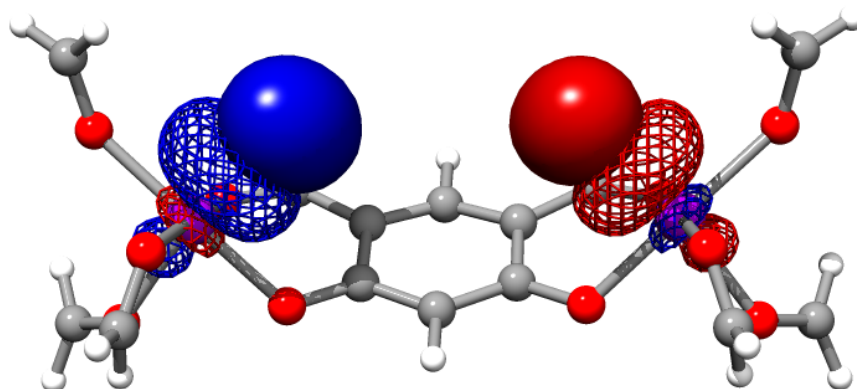


Figure 2.S51. The occupied and virtual orbitals, shown as solid and mesh, respectively, for the forward bonding pair COVP 1 (Table 2.S24) for the *m*-dobdc complex.

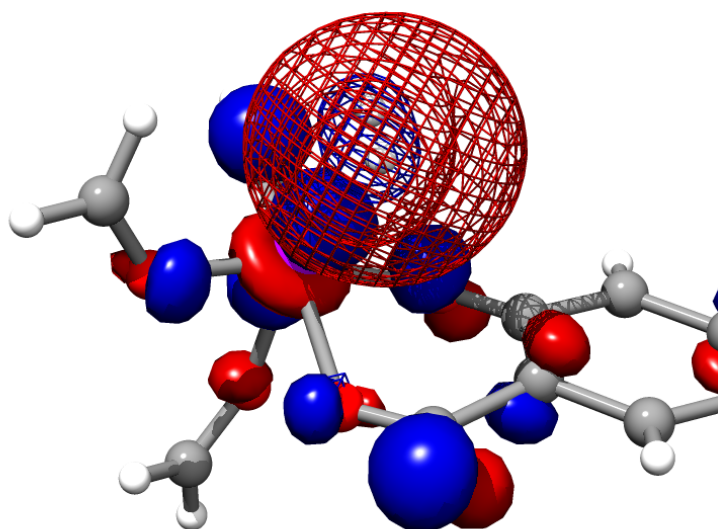


Figure 2.S52. The occupied and virtual orbitals, shown as solid and mesh, respectively, for the backbonding pair COVP 1 (Table 2.S24) for the dobdc complex.

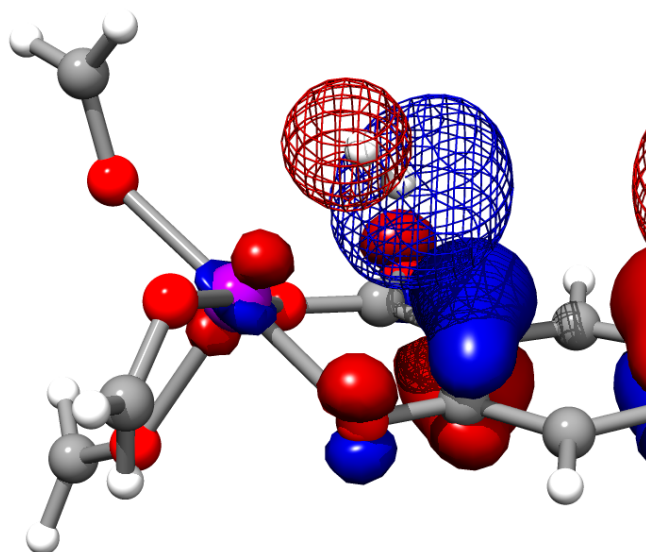


Figure 2.S53. The occupied and virtual orbitals, shown as solid and mesh, respectively, for the backbonding pair COVP 1 (Table 2.S24) for the *m*-dobdc complex.

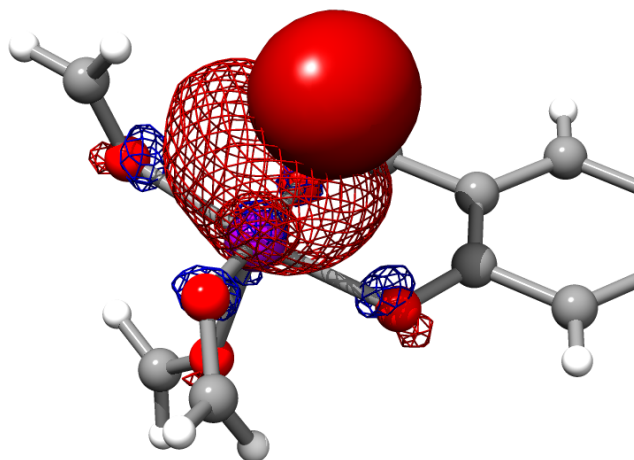


Figure 2.S54. The occupied and virtual orbitals, shown as solid and mesh, respectively, for the forward bonding pair COVP 2 (Table 2.S24) for the dobdc complex.

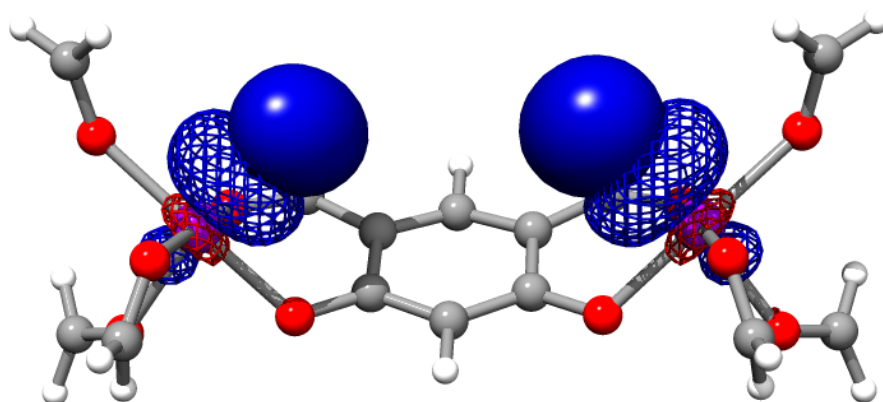


Figure 2.S55. The occupied and virtual orbitals, shown as solid and mesh, respectively, for the forward bonding pair COVP 2 (Table 2.S24) for the *m*-dobdc complex.

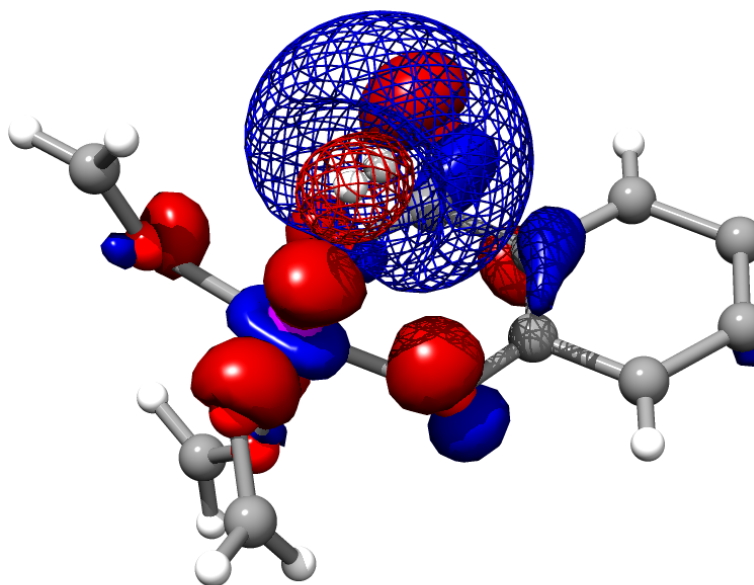


Figure 2.S56. The occupied and virtual orbitals, shown as solid and mesh, respectively, for the backbonding pair COVP 2 (Table 2.S24) for the dobdc complex.

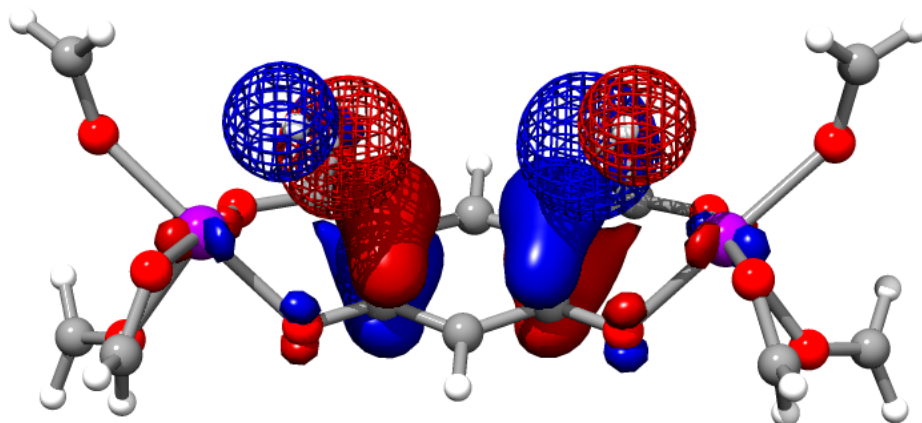


Figure 2.S57. The occupied and virtual orbitals, shown as solid and mesh, respectively, for the backbonding pair COVP 2 (Table 2.S24) for the *m*-dobdc complex.

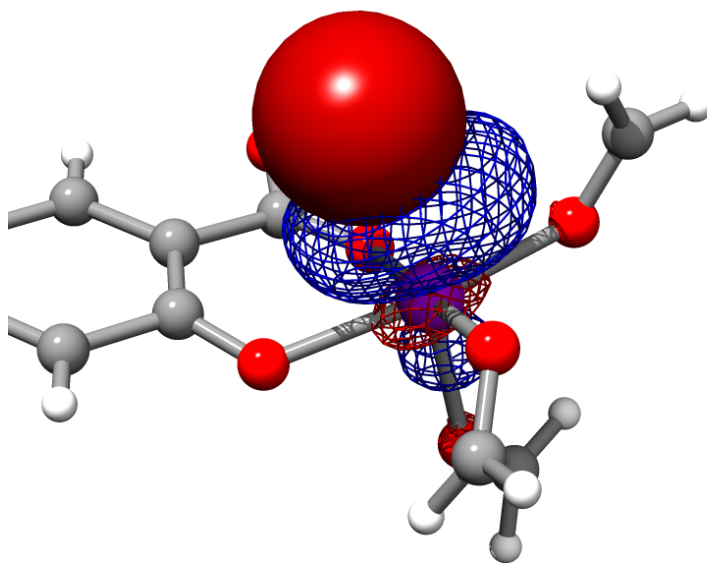


Figure 2.S58. The occupied and virtual orbitals, shown as solid and mesh, respectively, for the forward bonding pair COVP 3 (Table 2.S24) for the dobdc complex.

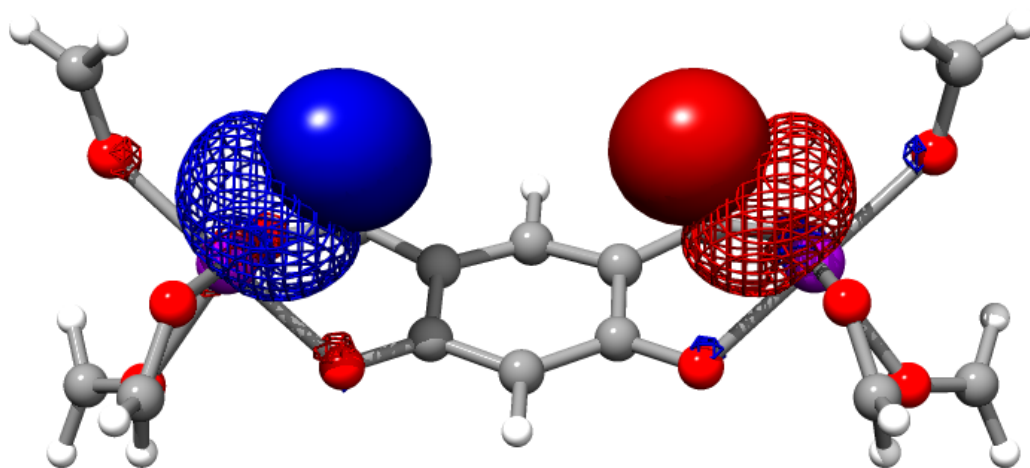


Figure 2.S59. The occupied and virtual orbitals, shown as solid and mesh, respectively, for the forward bonding pair COVP 3 (Table 2.S24) for the *m*-dobdc complex.

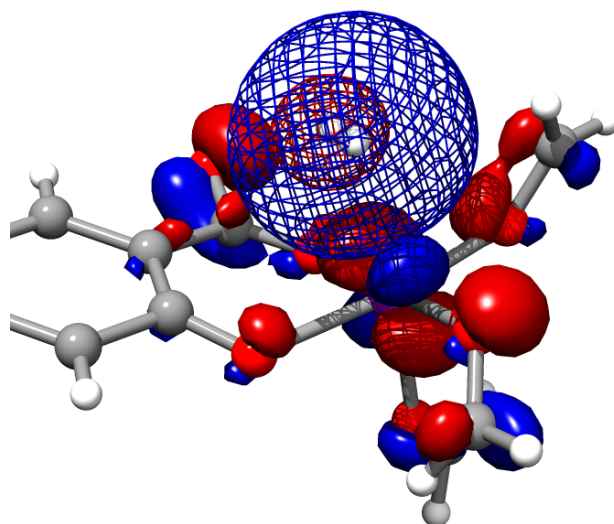


Figure 2.S60. The occupied and virtual orbitals, shown as solid and mesh, respectively, for the backbonding pair COVP 3 (Table 2.S24) for the dobdc complex.

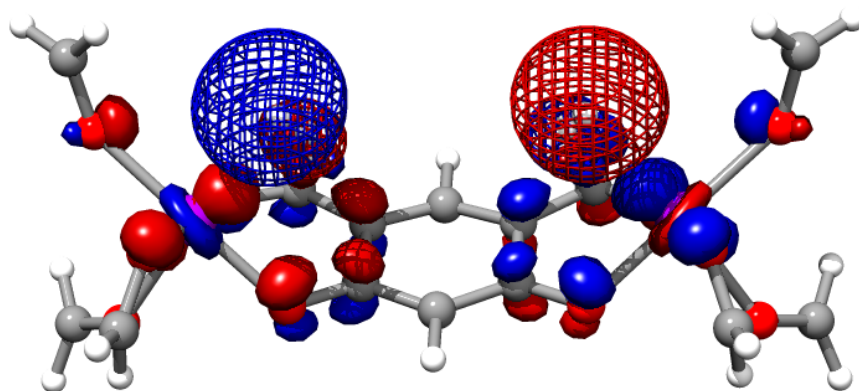


Figure 2.S61. The occupied and virtual orbitals, shown as solid and mesh, respectively, for the backbonding pair COVP 3 (Table 2.S24) for the *m*-dobdc complex.

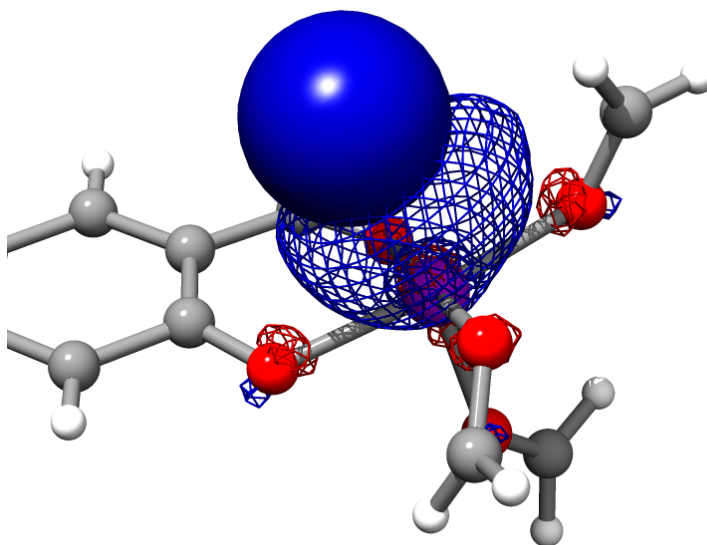


Figure 2.S62. The occupied and virtual orbitals, shown as solid and mesh, respectively, for the forward bonding pair COVP 4 (Table 2.S24) for the dobdc complex.

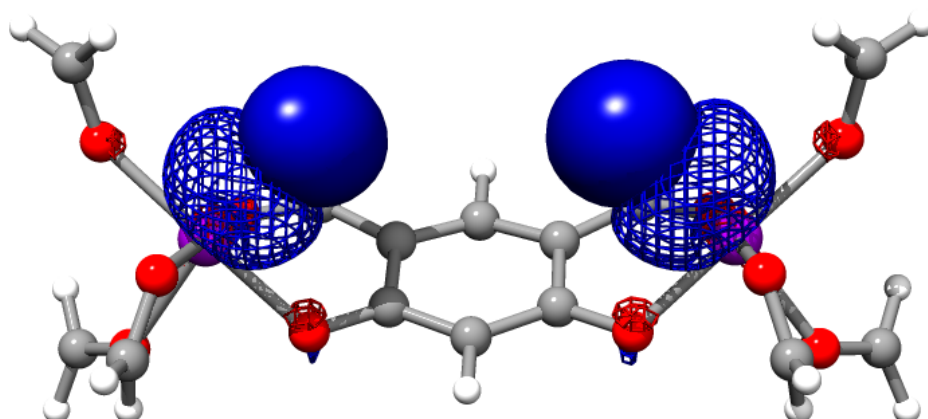


Figure 2.S63. The occupied and virtual orbitals, shown as solid and mesh, respectively, for the forward bonding pair COVP 4 (Table 2.S24) for the *m*-dobdc complex.

Table 2.S25. Breakdown of the energies of the most important forward bonding and backbonding charge transfer COVPs for the dobdc and *m*-dobdc complexes.

		Energy (kJ/mol/H ₂)	
	COVP	dobdc complex	<i>m</i> -dobdc complex
Backbonding	1	-0.43	-0.84
	2	-0.33	-0.84
	3	-0.32	-0.51
Forward bonding	1	-3.29	-3.62
	2	-2.25	-3.58
	3	-2.17	-2.30
	4	-1.36	-2.25

Chapter 3: Record High Hydrogen Storage Capacity in the Metal-Organic Framework $\text{Ni}_2(m\text{-dobdc})$ at Near-Ambient Temperatures

3.1. Introduction

While hydrogen has exceptional potential to serve as an environmentally benign fuel in motor vehicles, current hydrogen storage technologies require energy-intensive compression and/or cooling in order to achieve an acceptable driving range. Filling the fuel tank with an adsorbent capable of lowering the loading pressure to 100 bar at near-ambient temperatures could result in significant energetic and economic savings by obviating the need for more costly storage conditions. However, materials that can successfully store hydrogen at lower pressures must maintain or improve upon the density of pure, compressed H_2 , typically loaded at a pressure of 700 bar, while simultaneously providing access to H_2 on demand. A possible route to achieving practical storage capacities at reduced pressures without the need for cryogenics is to target porous materials containing coordinatively-unsaturated metal cations capable of polarizing H_2 . In this work, we evaluate metal-organic frameworks featuring a high density of such sites for their H_2 adsorption properties under conditions relevant to fuel cell vehicles, showing that $\text{Ni}_2(m\text{-dobdc})$ is the best current adsorbent for high-density hydrogen storage at near-ambient temperatures.

Molecular hydrogen (H_2) holds significant promise as a transportation fuel and is already used in some motor vehicles and for certain specialty applications, such as forklifts. Because water is the only byproduct of the fuel cell cycle, hydrogen fuel cell vehicles could, in principle, provide zero-emission transportation.¹ An economy can be envisioned in which solar energy is used to inexpensively produce hydrogen and oxygen from water; these products are then consumed in fuel cells to produce water and electricity that power the vehicle and close the cycle. Achieving such an economy, however, requires the successful development of each aspect of this process to both efficiently produce H_2 for use in fuel cells and consume H_2 in the production of electricity.

Significant investment in infrastructure supporting hydrogen fuel cell vehicles is underway around the world. As of 2017, the United States has 34 publicly accessible hydrogen fueling stations, with 31 of these in California.² The “California Hydrogen Highway” is a planned expansion of the current distribution network to 100 hydrogen fueling stations in California, primarily linking San Diego, Los Angeles, and the San Francisco Bay Area.³ Other countries including Japan, France, Germany, and the United Kingdom have made significant investments in hydrogen infrastructure both in anticipation of and to help bring about the wider use of hydrogen fuel cell vehicles.⁴ Public-private partnerships further these efforts and provide a basis for the future of hydrogen fuel cell vehicles to provide a clean alternative to traditional fossil-fuel based transportation.⁵

In addition to infrastructure developments, further scientific advances are imperative in order to realize the widespread adoption of hydrogen as a commercial fuel. Notable among such desired advances is the development of efficient hydrogen storage systems.⁶ While containing 2.6 to 3 times more energy per unit mass than gasoline,^{7,8} hydrogen poses challenges in the pursuit of storage at high volumetric densities. Hydrogen is a weakly interacting gas at ambient temperature and pressure and thus requires cooling and/or compression for storage at densities

sufficient for acceptable driving ranges in automobiles. However, cryogenic storage requires the use of large, expensive, and well-insulated systems in order to maintain a low temperature.^{6,9} Similarly, compression of H₂ at high pressures, typically up to 700 bar, is costly and requires heavy, expensive, and bulky storage tanks.^{10,11} Both of these solutions therefore add to the price of the vehicle in addition to providing significant engineering challenges given the wide operating temperature range for passenger vehicles (−40 to 60 °C). Furthermore, compression to 700 bar only results in a hydrogen volumetric energy density of 5.6 MJ/L at 298 K, significantly lower than the 32.4 MJ/L for gasoline.⁸ While the use of a metal or chemical hydride as a storage medium could mitigate the need for low temperature or high pressure storage vessels, these materials tend to suffer from either capacity limitations or problems arising from large activation energies and reversibility issues.^{12,13,14,15}

An alternative to either cryogenic or compressive storage involves the use of an adsorbent material, such as a zeolite¹⁶ or activated carbon,¹⁷ to boost the hydrogen density in a tank under more ambient conditions. With just two electrons and a low polarizability, H₂ is capable of engaging in only weak van der Waals interactions, leading to an adsorption enthalpy that is typically on the order of −5 kJ/mol. Accordingly, adsorption sites capable of strongly polarizing H₂ must be introduced to achieve sufficient densification and a reasonable driving range. Cryo-adsorption, which entails a combination of adsorption and cryogenic storage, is one possible strategy to yield high capacities.^{18,19} However, the ideal situation would involve adsorption under ambient temperature conditions, with a relatively low fill pressure of 100 bar or lower. Such a system would be expected to lower costs significantly because a conformable, lightweight storage vessel could potentially be used and no on-board cooling system would be required.

Metal-organic frameworks (MOFs) are a class of materials with great potential for hydrogen storage, among other applications related to gas storage and separations.²⁰ The inherent synthetic tunability of these structures has led to a wide range of interesting properties such as high surface areas,²¹ negative gas adsorption,²² and precisely engineered pore environments.²³ Such tunability can be used to improve their properties for a desired application, including hydrogen storage,^{24,25,26,27} and has made MOFs one of the most intensely-studied fields in modern inorganic chemistry. For example, it is possible to create MOFs featuring pore surfaces with a high concentration of strong H₂ adsorption sites, a feature less readily achieved in zeolites and activated carbon adsorbents. Computationally predicted hydrogen adsorption isotherms in MOFs have shown high hydrogen capacities at near-ambient temperatures, but these materials have yet to be evaluated experimentally.^{28,29,30,31} MOFs can thus, in principle, be designed to exhibit H₂ binding enthalpies in the optimal range of −15 to −20 kJ/mol,³² leading to a high storage capacity under conditions relevant to light-duty fuel cell vehicles.³³ The appeal of this approach is apparent in the many studies of MOFs for H₂ storage that have often focused on materials containing coordinatively-unsaturated (open) metal sites.³⁴ These exposed positive charges are able to polarize H₂ more strongly than the typical surfaces available for physisorption in most storage materials.^{35,36,37,38} Thus far, however, no MOFs have been shown to achieve the necessary binding enthalpies or the capacity metrics set forth by the U.S. Department of Energy.³³

The most promising metal-organic framework identified to date for H₂ storage is Ni₂(*m*-dobdc) (*m*-dobdc^{4−} = 4,6-dioxido-1,3-benzenedicarboxylate), which was shown previously to display an H₂ binding enthalpy of −13.7 kJ/mol, as measured by variable-temperature infrared spectroscopy and representing the largest value yet observed in a MOF by this method.³⁹ Ni₂(*m*-dobdc) is a structural isomer of Ni₂(dobdc) (dobdc^{4−} = 2,5-dioxido-1,4-benzenedicarboxylate; Ni-MOF-74), and its record binding enthalpy is largely a result of a higher charge density at its

coordinatively-unsaturated Ni²⁺ centers. These sites strongly polarize H₂, providing the primary binding sites for H₂ within the pores of the material and leading to a high volumetric storage capacity of greater than 11 mmol/g (2.2 wt %) at 77 K and 1 bar. Recent reports have shown that the material Cu(I)-MFU-4l exhibits an H₂ isosteric heat of adsorption of -32 kJ/mol;⁴⁰ however, the volumetric density of these open metal coordination sites in this material is about 10% of that in Ni₂(*m*-dobdc), rendering it perhaps more suitable for H₂/D₂ separations than H₂ storage.⁴¹

In this work, the hydrogen storage properties of Ni₂(*m*-dobdc) and other related top-performing MOFs, specifically Co₂(*m*-dobdc), Co₂(dobdc), and Ni₂(dobdc), are investigated under more practical conditions. Adsorption isotherms at multiple temperatures in the range of 198 to 373 K were measured to determine capacities at pressure up to 100 bar, while *in situ* powder neutron diffraction and infrared spectroscopy experiments were employed to probe the nature of the interactions of hydrogen within the pores of the materials.

3.2. Experimental

3.2.1. Synthesis of H₄(*m*-dobdc). See Section 2.2.2.

3.2.2. Synthesis of Co₂(*m*-dobdc). Aliquots of 310 mL of methanol and 310 mL of *N,N*-dimethylformamide (DMF) were added to a 1-L three-neck round-bottom flask equipped with a reflux condenser and sparged with N₂ with stirring for 1 h. The solids H₄(*m*-dobdc) (2.00 g, 10.1 mmol) and CoCl₂ (3.27 g, 25.2 mmol) were added under N₂ pressure, and the reaction mixture was vigorously stirred and heated at 120 °C for 18 h. The mixture was then cooled to ambient temperature and filtered, affording a pink microcrystalline powder. The powder was soaked in 500 mL of DMF for 24 h, then soaked in three successive aliquots of 500 mL of methanol for 24 h each. The resulting pink powder was collected by filtration and heated at 180 °C under dynamic vacuum until the outgas rate was <1 μbar/min, yielding 1.71 g (54.3 %) of activated product.

3.2.3. Synthesis of Ni₂(*m*-dobdc). An identical procedure was used as for Co₂(*m*-dobdc) above, except that the solvent consisted of 220 mL of methanol and 405 mL DMF, and NiCl₂ (3.27 g, 25.2 mmol) was used in place of CoCl₂. The reaction yielded 1.69 g (54.4 %) of activated product.

3.2.4. Synthesis of M₂(dobdc) (M = Co, Ni). These materials were synthesized using identical procedures to their M₂(*m*-dobdc) congeners above, with the substitution of like amounts of the isomeric H₄(dobdc) ligand for the H₄(*m*-dobdc) ligand. These reactions yielded 2.06 g (65.4%) of activated Co₂(dobdc) and 2.25 g (80.1%) of activated Ni₂(dobdc).

3.2.5. Synthesis of MOF-5. The synthesis of MOF-5 was carried out according to a previously published procedure.^{42,43}

3.2.6. Measurement of Gas Adsorption Isotherms. All gas adsorption isotherms in the range 198 to 373 K were measured on a Particulate Systems HPVA II instrument. The sample holder was custom-built using a Swagelok valve connected to a sample holder. Typically, 1.0-2.0 g of sample was used for each measurement to ensure that measurement and mass errors were minimized. These samples were activated in standard glass sample tubes as loose powders on a

Micromeritics ASAP 2420 instrument and transferred to the custom HPVA sample holder in a dry box. Once the sample holder was connected to the HPVA instrument, the sample was immersed in a recirculating fluid bath connected to a Julabo FP89-HL/TK filled with Dow Syltherm fluid.[‡] During the data collection, a portion of the sample holder was exposed above the fluid in the temperature bath but below the temperature-controlled dosing manifold of the HPVA-II instrument. The resulting existence of three temperature zones leads to challenges in performing the required volume calibrations, which are essential to properly determining the gas uptake of a sample. The volume of each temperature zone was therefore experimentally determined based on He measurements at multiple temperatures, and the results were applied in obtaining corrected adsorption data. A more complete discussion of this calibration method can be found in a similar paper discussing the measurement of methane adsorption in MOFs.⁴²

Importantly, the background adsorption of H₂ within the sample in an empty sample holder should be close to zero at all pressures, assuming the proper calibrations are in place. While this is true for isotherms being measured at close to ambient temperature (at which the temperatures of the two parts of the sample holder are very similar, resulting in a minimal temperature gradient), isotherms measured at temperatures further from ambient will see a larger temperature gradient and a commensurate deviation from null adsorption. To account for this deviation, background adsorption measurements for H₂ were repeated three times at each temperature and fit using a third-order polynomial, which was then used to perform a background correction on all subsequently collected data at each temperature. The uptake in these background adsorption isotherms was typically on the order of 10 v/v (volume of H₂ per volume of MOF) and the measured values were subtracted from the total adsorption isotherms of the metal-organic frameworks. Such error primarily stems from minor temperature fluctuations in the three-zone experimental setup, as well as small valve volumes. Pore volumes were determined experimentally using N₂ adsorption isotherm data. Crystallographic densities were used in all calculations to obtain volumetric capacities.

Adsorption isotherms at 77 K and 100 K (Figures 3.S2-3.S3) were collected on a custom-built volumetric adsorption apparatus at the National Renewable Energy Laboratory (NREL). The H₂ gas adsorption measurement at -197 °C at higher pressures (~5 to 105 bar Figure S2) was collected on a volumetric adsorption apparatus at the National Renewable Energy Laboratory (NREL). (The temperature of liquid N₂ at the elevation in Golden, CO is 75.6 K). The sample was packed in the custom-made sample holder in a dry box and transported to NREL in argon atmosphere. The sample holder includes a VCR diaphragm isolation valve, 1/8" tubing, and a 1/4" Swagelok VCR union and cap where the sample is located. There is a 2 micron filter gasket to ensure the sample remains in the sample holder. The sample was degassed to 180 °C at a heating rate of 2 °C/min, held at 180 °C for 12 hours, and cooled to ambient temperature at 2 °C/min. The H₂ adsorption isotherm was measured on a custom modified PCTPro 2000. The mass of the sample after measuring the isotherm was 256 mg. This system has been previously described in detail.⁵ Modifications to the system include water-cooled copper jacket fittings to maintain extended temperature control of the gas dosing arm and the sample holder. For measurements at -197 °C, the bottom portion of the sample holder containing the sample is placed in a liquid nitrogen bath. It is essential that the level of the liquid nitrogen bath remain constant throughout the measurement, as to not change the temperature profile of the sample holder as this would change the headspace calibration for the instrument. All calculations are performed using custom software, where the calibrated volumes are calculated directly from the empty cell measurements, and the number of hydrogen moles adsorbed is directly calculated

based on these volumes. A detailed description of the calculations for determining capacities is provided elsewhere.⁶

The same experimental setup was used to measure the isotherm at 100 K (1 to 154 bar, Figure S3) with the exception that a cryostat was used to control the temperature of the sample and the sample mass was 1.0117 g.

High pressure hydrogen capacity measurements were performed on a modified commercial Sieverts system (PCTPro 2000) that was integrated with an Advanced Research System's cryo-cooler (DE-110 with ARS-10HW). This allows PCT measurements at arbitrary temperatures from 40 K to 350 K. A custom designed and built copper assembly interfaces the cryo-cooler with the stainless-steel sample holder to ensure a highly isothermal sample volume. Special care was taken to control heat flow and maintain a static and reproducible temperature profile for the instrument, which is critical to accurately calibrate the headspace. This hardware modification included supplementing the as-received temperature-control system so that the temperature-controlled region was expanded to include the sample support arm and the sample chamber assembly (sample chamber, manual isolation valve, and 0.125 inch OD connection tubing) using temperature-controlled water circulating through copper components physically connected to the sample chamber assembly. The temperatures of the internal cabinet and the external circulator were equal and this modification greatly improved the overall temperature stability of the apparatus. Another hardware modification consisted of adding a manifold to the high-pressure gas inlet that allows either hydrogen or helium to be introduced. In this way, the exact same protocol for the hydrogen measurement could also occur for the helium calibration procedure (vide infra). All these measures allow the temperature profile of the sample volume to be stable and reproducible and yield accurate headspace calibrations. For the 100K measurement, the temperature was allowed to equilibrate overnight and multiple temperature sensors showed that the temperature uniformity at the low-temperature portion of the sample volume (where the sample was entirely contained) was within ± 0.1 K.

The samples were degassed on a custom-built degassing station with two turbo pumps yielding a base pressure of 10^{-7} torr and the effluents from the sample can be monitored by a mass spectrometer. Typically, samples are evacuated at room temperature for 1 hour, then the temperature is increased to 110 °C over two hours, and then held at 110 °C for ~ 14 hours, all under evacuation. Since the sample chamber assembly has a manual isolation valve, the sample chamber can be transferred between the degassing station and the Sieverts apparatus without exposure to air.

The Sieverts protocol consists of the following sequence after the degassing was accomplished:

- 1) Measure hydrogen capacity of sample at 100K.
- 2) Warm to 303 K and pump off hydrogen (base pressure 10^{-5} torr) for 1 hour.
- 3) Perform helium calibration at 303 K with sample present.
- 4) Remove sample material and reassemble empty sample chamber assembly.
- 5) Perform helium calibration at 100K on empty sample chamber.
- 6) Perform helium calibration at 303 K on empty sample chamber.

For each hydrogen measurement step, the pressure was held for 15 minutes to allow the sample to come to equilibrium, which is consistent with the physisorption mechanism expected in these materials. For the helium calibration steps, the pressure was held for 6 minutes as little

adsorption occurs and equilibrium occurs more quickly. These steps allow calculation of the sample skeletal volume (steps 3 and 6) and the calculation of the warm and cold empty volumes (steps 5 and 6). The sample skeletal volume can then be subtracted from the empty volumes to yield the cold volume with the sample present. The volume and gas density for the temperature gradient region is calculated directly assuming a linear temperature gradient and the geometrical dimension of the tubing. The critical requirements needed for the above protocol are that the sample chamber volume be repeatable to a high degree upon disassembly and re-assembly as well as the repeatability of the temperature profile both at 303 K, any temperature gradients, and the volume at non-ambient temperatures. These requirements have been thoroughly verified through control experiments on empty sample chambers.

The above protocol avoids helium adsorption effects on the sample at low temperatures for the calibration steps when it is expected to be the most significant. Instead, the sample is only exposed to helium at 303 K when the effects are much reduced. The helium adsorption that occurs at 303 K is assumed to be negligible from necessity as it is very difficult to accurately determine this adsorption and compensate for its effects on the hydrogen adsorption determination. This is especially true for samples that cannot be heated to high temperatures such as MOFs. Not compensating for helium adsorption effects will yield capacity measurements that *underestimate the hydrogen adsorption*. As mentioned above, because of the modification that allows helium to be introduced into the high-pressure port of the instrument, the exact same measurement protocol used for hydrogen can also be done with helium. This provides a higher degree of confidence for the helium calibration and can also investigate any calibration effects dependent on pressure.

Data analysis to determine hydrogen capacities was performed using custom analysis procedures to ensure the highest accuracy and proper handling for the temperature profile of the sample chamber. The analysis is based on a mass-balance model of the gas phase where missing gas is assumed to be adsorbed onto the sample and surplus gas is assumed to have desorbed from the sample. A real equation of state was used for the gases and the compressibility factor was based on calculations using GASPAC for helium and hydrogen.

3.2.7. Temperature-Programmed Desorption. The temperature-programmed desorption (TPD) data were collected on a custom-built NREL TPD apparatus that allows for identification and quantification of effluent gases, as described elsewhere.⁴⁴ In summary, calibrated adsorption capacities and desorption activation energies and kinetics can be investigated using the system, in which it is possible to heat or cool samples in vacuum to temperatures between 77 K and 1200 K. Samples may be exposed to hydrogen (99.9999%) at pressures up to ~1000 Torr, and the system can achieve pressures as low as 10^{-9} Torr. The TPD system is equipped with a mass spectrometer with detection range of 0–100 atomic mass units to detect impurities present in materials both during degas and after hydrogen exposures.

3.2.8. Powder Neutron Diffraction Measurements. Powder neutron diffraction data were collected on the high resolution neutron powder diffractometer, BT-1, at the National Institutes of Standards and Technology (NIST) Center for Neutron Research (NCNR), with a Ge-(311) monochromator using an in-pile 60' collimator corresponding to a wavelength of 2.077 Å. Measurements were performed on 1.11 g of activated $\text{Co}_2(m\text{-dobdc})$. The activated sample was transferred into a He-purged glove box equipped with oxygen and water monitors. The sample was loaded into an aluminum can equipped with a valve for gas loading up to pressures of 100

bar and loaded into a top-loading closed-cycle refrigerator. Data collection was performed at 77 and 198 K for the activated sample. At 77 K, one loading of 78 bar of D₂ was measured. At 198 K, the sample was initially exposed to 79 bar of D₂ and allowed to reach equilibrium. Additional measurements were performed at reduced pressures of 54 and 36 bar of D₂. Aluminum Bragg peaks were removed from the data during analysis.

Diffraction patterns were analyzed using the Rietveld refinement method as implemented within GSAS¹ and EXPGUI² was used to perform all refinements. A previously determined starting model for the bare material³ was refined against the bare sample data first, with soft restraints placed on the internal bond distances and bond angles of the M₂(*m*-dobdc); this refined model was then used as the starting point for refinements of the sample dosed at 78 bar or 79 bar D₂. Fourier difference maps were used to approximate the position of D₂ adsorption sites with values for the D₂ fractional coordinates, occupancies, and thermal parameters then obtained by Rietveld refinement. Deuterium molecules were treated as D-atoms with double occupancy and a large thermal factor as determined previously.⁴ Subsequent refinements of the measurements performed at 54 and 36 bar D₂ were made by holding all variables constant except occupancy.

3.2.9. *In situ* Infrared Spectroscopy. Infrared spectra were acquired using a Bomem DA3 Michelson interferometer equipped with a quartz-halogen source, a CaF₂ beamsplitter, and a liquid nitrogen-cooled mercury-cadmium-telluride detector. A cutoff filter above 9000 cm⁻¹ was used to prevent unwanted sample heating from the IR source. A custom-built diffuse reflectance system with a sample chamber that allows both the temperature and atmosphere of the material to be controlled was utilized for all experiments.⁴⁵ Activated powder samples (~10 mg) were transferred to a Cu sample holder within an Ar-purged glove box. The samples were sealed within a dome containing sapphire windows and a valve for gas loading. Seals were achieved using either indium or Teflon gaskets depending on the pressure and temperature of the specific experiment. The dome was bolted to a copper slab providing thermal contact to a cold-finger cryostat (Janis ST-300T). The sample temperature was monitored by a Si-diode thermometer bolted directly to the copper slab. A reference infrared spectrum was obtained at each temperature. Hydrogen gas was introduced from a dosing manifold to a desired pressure while maintaining the sample at constant temperature. Multiple infrared spectra were obtained at each pressure step up to a maximum pressure of 100 bar. These spectra were then referenced to the initial spectrum without H₂.

Infrared spectra measured at LBNL were collected on a Bruker Vertex 70 spectrometer equipped with a custom DRIFTS apparatus and an external mercury-cadmium-telluride detector. Powdered samples of activated framework (~20 mg) were transferred under an inert atmosphere to a homebuilt IR cell in which the atmosphere could be controlled. H₂ gas was dispensed to the sample to target pressures from a UHP (99.999%) hydrogen cylinder. A forthcoming publication will provide the full instrument setup and capabilities.

3.3. Results and Discussion

3.3.1. General Considerations for H₂ Storage in Adsorbents. As introduced earlier, adsorbent materials have the potential to store H₂ at reduced pressures and temperatures relative to cryogenic or high-pressure technologies and therefore offer a more energetically and financially promising solution. The United States Department of Energy (DOE) has released

guidelines for hydrogen storage in light-duty and specialty vehicles (e.g. passenger vehicles, forklifts, golf carts, and specialized airport vehicles, among others). A subset of the system-based targets associated with these guidelines and relevant to adsorbent-based storage is reproduced in Table 3.1.

Table 3.1. Selected U.S. Department of Energy (DOE) targets for the onboard storage of hydrogen in light-duty vehicles.

Storage Parameter	Units	2020	Ultimate
System gravimetric H₂ capacity	wt %, kg H ₂ /kg system, kWh/kg	4.5 %, 0.045, 1.5	6.5 %, 0.065, 2.2
System volumetric H₂ capacity	g H ₂ /L system, kWh/L	30, 1.0	50, 1.7
Storage system cost	\$/kg H ₂ stored, \$/kWh net	333, 10	266, 8
Operating ambient temperature	°C	-40 to 60	-40 to 60
Min/max delivery temperature	°C	-40 to 85	-40 to 85
Operational cycle life (1/4 tank to full)	cycles	1500	1500
Min delivery pressure from storage system	bar (abs)	5	3
Max delivery pressure from storage system	bar (abs)	12	12
System fill time (5 kg)	min	3-5	3-5

To date, no adsorbents have been produced that satisfy the 2020 target capacity requirements of 4.5 wt % and 30 g/L H₂. The trade-off between volumetric and gravimetric H₂ density in MOFs has been previously studied, however, showing maximization of both to be difficult.^{46,47} While pressure ranges are not explicitly given, operating pressures below 100 bar have the potential to reduce storage vessel and compression costs while maintaining reasonable capacities. Importantly, these target capacity requirements are full system capacities. Therefore, potential adsorbent materials must actually exceed target capacities, as the full system will involve more mass and volume than that of the adsorbent alone.

The volumetric capacity is the primary consideration when evaluating MOF materials for H₂ storage, because in light-duty vehicles, the available volume for a tank for adsorbent-based storage of H₂ is the limiting factor in determining the driving range of a vehicle. This concept has been discussed in detail elsewhere for natural gas storage,⁴² and the same principles will apply to H₂ storage. For example, a given percent increase in volumetric storage capacity will yield a commensurate percent increase in driving range assuming a fixed-volume tank. In contrast, the same percent increase in gravimetric capacity will only yield a small percent increase in driving range due to the savings in weight of the adsorbent in the fuel tank; therefore, targeting materials based on their total volumetric capacity is a more useful means of identifying candidate materials for H₂ storage. Crystallographic densities are used herein to calculate volumetric capacities as an upper bound of storage capacity, as these represent an intrinsic property of each material and allow for the comparative evaluation of materials across multiple studies without needing to account for sample preparation or measurement of other densities. The actual storage capacity in

a system, however, will depend on the bulk density, shaping, and packing of the storage material, which is outside the scope of this report.⁴⁸

Furthermore, the volumetric usable capacity is the most important consideration when evaluating adsorbents for hydrogen storage. For the purposes of this work, usable capacity is defined as the total amount of H₂ adsorbed between 5 and 100 bar in the total adsorption isotherm (Figure 3.1). The total adsorption isotherm is calculated by accounting for the excess capacity plus the amount of bulk H₂ present under the conditions at which the isotherm was measured. The total adsorption thus gives the total amount of gas contained within the volume of a crystal of the adsorbent. A minimum pressure of 5 bar is assumed to be necessary for the fuel injector in the vehicle, such that any H₂ stored below 5 bar is inaccessible as fuel. Thus, all H₂ uptake would ideally occur after 5 bar and the total capacity would be equal to the usable capacity.⁴⁹ In practice, however, materials that strongly bind H₂ typically adsorb large quantities of H₂ at lower pressures, which are then inaccessible to use in the fuel cell.

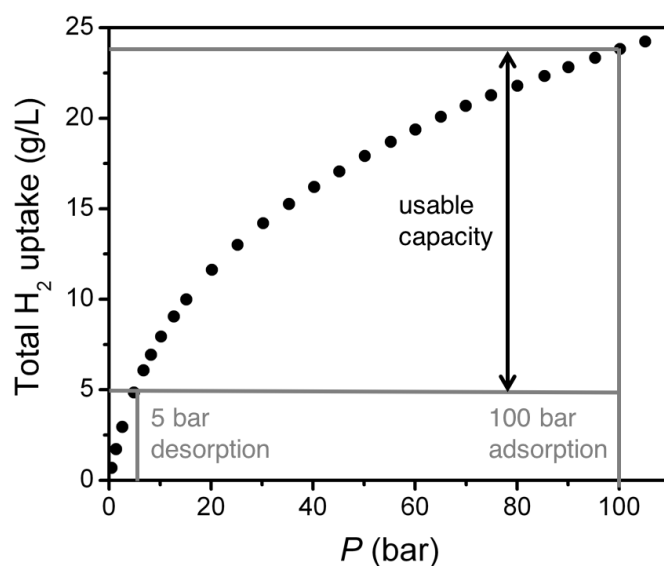


Figure 3.1. An illustration of how usable capacity is calculated, considering adsorption at 100 bar and desorption at 5 bar. For MOFs, usable volumetric capacity is determined from the total uptake and crystallographic density of the material for easy comparison across multiple studies.

There are many considerations when measuring adsorption isotherms at high pressures that are crucial for properly evaluating materials for their H₂ adsorption properties. For example, it is important to use a large mass of material to minimize mass errors that may significantly affect the gas uptake. Furthermore, all volumes must be carefully calibrated in order to ensure reproducibility and accuracy of measurements. Maintaining isothermal control is also essential; regardless of the number of temperature zones in the measurement, consistent volumes at consistent temperatures must be maintained to ensure accuracy across multiple isotherm collections.

The adsorbent cost, which impacts the entire system cost, is another important metric, as the H₂ storage system must be economically competitive with gasoline storage tanks. This necessity is quite challenging, owing to the relative difficulty of containing a compressed gas versus a liquid fuel. Further, the complexity of synthesis and high precursor expenses for many metal-

organic frameworks can render them costly to prepare, limiting their industrial application in gas storage, gas separations, and catalysis. Zeolites currently used in such applications are generally less expensive based on their aluminosilicate composition, although a recent report shows that alternative synthetic routes for MOFs can significantly reduce their cost, making some competitive with zeolites.⁵⁰ Furthermore, among MOFs, the $M_2(m\text{-dobdc})$ series of materials is particularly poised as a low-cost adsorbent with useful gas adsorption properties. The cost of the $H_4(m\text{-dobdc})$ linker is low, as it can be formed in a one-step reaction from cheaply available resorcinol, potassium bicarbonate, and CO_2 , with no solvent needed other than water during isolation of the product. The overall cost of $M_2(m\text{-dobdc})$ itself is thus largely dependent on the metal salt, but can be as low as $\sim \$3/\text{kg}$ for raw materials for the $Mg_2(m\text{-dobdc})$ analog. Such economic considerations are paramount to the successful deployment of MOFs in gas storage applications.

3.3.2. High-Pressure H_2 Adsorption Isotherms. Structural characterization and low-pressure H_2 adsorption isotherms of $Co_2(m\text{-dobdc})$, $Ni_2(m\text{-dobdc})$, $Co_2(\text{dobdc})$, $Ni_2(\text{dobdc})$, and MOF-5 have been reported previously.^{20,37,39,43} In this study, the high-pressure H_2 adsorption isotherms of these five materials were measured between 0 and 100 bar at temperatures of -75 , -50 , -40 , -25 , 0 , 25 , 50 , 75 , and 100 °C. Increments of 25 °C were chosen to provide a wide range of conditions for considering temperature swings when determining the volumetric usable capacity of these materials; -40 °C was also measured because it is the temperature at which hydrogen is stored at and dispensed from fueling stations.⁵¹ These isotherms for $Co_2(m\text{-dobdc})$, $Ni_2(m\text{-dobdc})$, $Co_2(\text{dobdc})$, and $Ni_2(\text{dobdc})$ materials are shown in Figure 3.2 and for MOF-5 in Figure 3.S1.

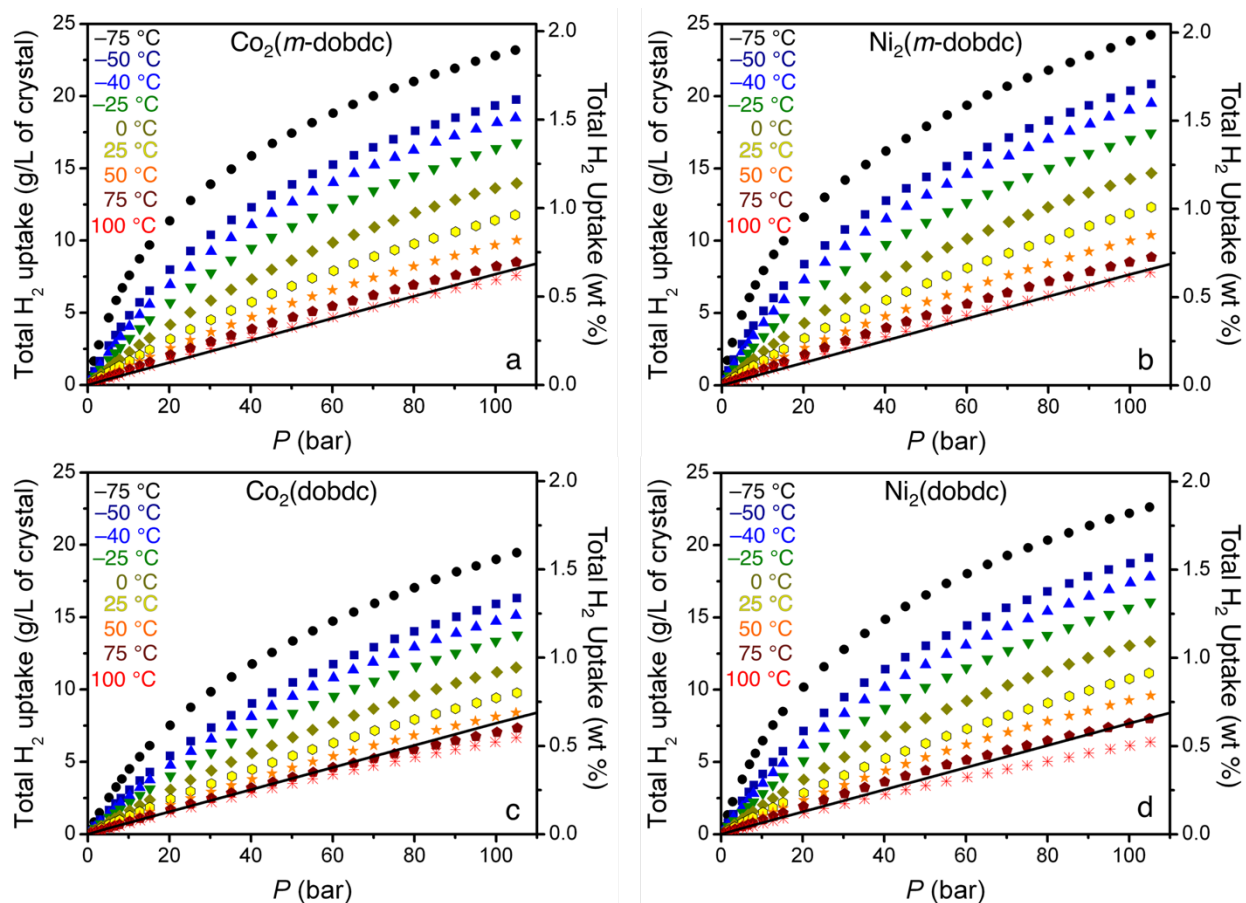


Figure 3.2. Hydrogen adsorption isotherms for a) $\text{Co}_2(m\text{-dobdc})$, b) $\text{Ni}_2(m\text{-dobdc})$, c) $\text{Co}_2(\text{dobdc})$, and d) $\text{Ni}_2(\text{dobdc})$ at -75 (black circles), -50 (navy squares), -40 (blue triangles), -25 (green upside-down triangles), 0 (gold diamonds), 25 (yellow hexagons), 50 (orange stars), 75 (dark red pentagons), and 100 °C (bright red crosses) measured between 0 and 100 bar and plotted in terms of total volumetric and gravimetric capacity. The black line in each plot represents the volumetric density of pure compressed H_2 at 25 °C.

Among the five measured materials, $\text{Ni}_2(m\text{-dobdc})$ exhibits the highest adsorption capacities at all temperatures and pressures, and all isotherms in this material at 75 °C and below exhibit a higher H_2 capacity than pure compressed H_2 at 25 °C. At 25 °C and 100 bar, $\text{Ni}_2(m\text{-dobdc})$ takes up 11.9 g of H_2 per L of crystal, which is the highest among the MOFs measured in this study and, to our knowledge, the highest for any known adsorbent. The usable capacity under these conditions is slightly reduced to 11.0 g/L, however, due to the uptake of 0.9 g/L at 5 bar. This still outperforms compressed hydrogen, which would require compression to over 150 bar to obtain the same total volumetric usable capacity at 25 °C. At 100 bar and the lowest measured temperature of -75 °C, $\text{Ni}_2(m\text{-dobdc})$ takes up a total of 23.8 g/L H_2 , corresponding to a total usable capacity of 19.0 g/L. Notably, H_2 adsorption data collected at 75.6 K exhibit a total capacity of 57.3 g/L at 105 bar (Figure 3.S2), a value that exceeds the DOE system capacity target, albeit at cryogenic temperatures. Furthermore, data collected at 100 K show capacities

approaching the DOE system capacity targets, which is notable given that measured sample densities were used in calculating the capacity (Figure 3.S3).

If the possibility of using a temperature swing in a storage system through application of active cooling at high filling levels, the usable capacities attained with Ni₂(*m*-dobdc) are even higher. For example, adsorption at –40 °C with desorption at 25 °C affords a usable capacity of 18.2 g/L. An even more extreme temperature swing from adsorption at –75 °C to desorption at 25 °C gives a usable capacity of 23.0 g/L. This enhanced usable capacity represents 77% of the DOE system target of 30 g/L, which is the highest H₂ volumetric usable capacity achieved to date for an adsorbent operating in this temperature range. It is relevant to note that increasing the desorption temperature to 100 °C only offers only an additional 0.4 g/L of usable capacity over desorption at 25 °C, which is not likely to be worthwhile given the additional system complexity required to heat the MOF above ambient temperature.

The related MOFs Co₂(*m*-dobdc), Co₂(dobdc), and Ni₂(dobdc) were also evaluated for their H₂ storage performance under various temperature swings, and the results are summarized in Table 2. As the best known adsorbent for cryogenic hydrogen storage, MOF-5, was also measured for comparison (Figure 3.S1) and the data agree well with a previous measurement performed at 25 °C.⁴³ From the results in Table 3.2, Ni₂(*m*-dobdc) is clearly the top-performing material for all of the considered temperature swings. This superiority arises from it having the highest capacity under all conditions, which is a consequence of the greater charge density at its open metal coordination sites compared to the other materials. Volumetrically, MOF-5 is inferior to the M₂(*m*-dobdc) and M₂(dobdc) adsorbents due to a lack of strong adsorption sites within its pores.

Table 3.2. A comparison of the volumetric usable capacities in g/L for selected temperature swings.

	Co ₂ (<i>m</i> -dobdc)	Ni ₂ (<i>m</i> -dobdc)	Co ₂ (dobdc)	Ni ₂ (dobdc)	MOF-5
25 °C, no swing	10.5	11.0	8.8	9.9	8.8
–75 °C, no swing	18.2	19.0	16.5	18.4	15.8
–40 to 25 °C	17.3	18.2	14.0	16.6	12.8
–75 to 25 °C	21.9	23.0	18.3	21.4	16.5
–75 to 100 °C	22.3	23.4	18.6	21.8	16.7

It is important to understand the benefits that an adsorbent can offer over compression of pure H₂. To that end, a comparison of volumetric H₂ storage capacities at all of the measured temperatures shows that Ni₂(*m*-dobdc) imparts a clear enhancement in capacity relative to the compressed gas (Figure 3.3). Furthermore, this advantage increases substantially with decreasing temperature. Even at 100 °C, the volumetric H₂ capacity of a crystal of Ni₂(*m*-dobdc) is 121% of the capacity of pure H₂. This advantage increases to 155% at 25 °C and 209% at –75 °C, highlighting the utility of Ni₂(*m*-dobdc) for increasing the density of hydrogen in a storage cylinder filled at 100 bar.

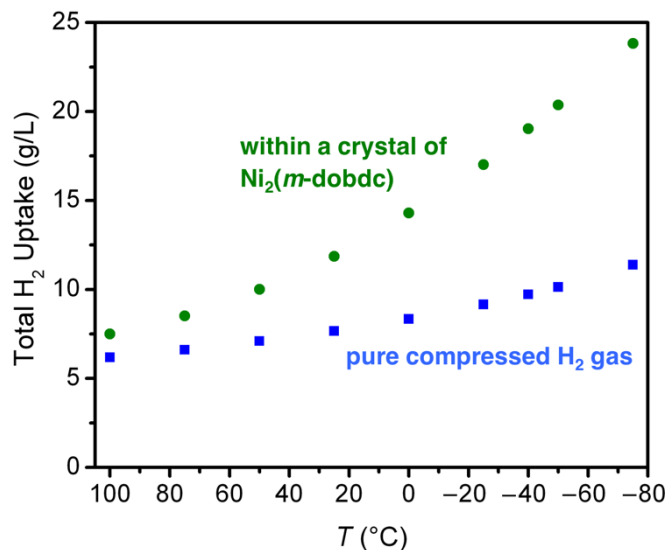


Figure 3.3. A comparison of the total volumetric capacities of Ni₂(m-dobdc) (green circles) and pure compressed H₂ (blue squares), both at 100 bar. Decreasing temperature leads to an increase in the advantage Ni₂(m-dobdc) has over pure H₂ in terms of total volumetric capacity.

3.3.3. Temperature-Programmed Desorption. Physisorptive storage of H₂ (such as in MOFs) has the advantage over chemisorptive storage (such as in metal hydrides) in that the gas is accessible without large energy inputs. As an illustration of this accessibility and the stronger binding in the M₂(m-dobdc) series, we carried out temperature-programmed desorption (TPD) experiments on samples of Ni₂(m-dobdc) and Ni₂(dobdc) loaded with H₂.

The results of the TPD measurements indicate that Ni₂(m-dobdc) binds H₂ more strongly, given the shift in the desorption profile of H₂ as compared with Ni₂(dobdc) (Figure 3.4). These desorption peaks, centered at -165 and -175 °C for Ni₂(m-dobdc) and Ni₂(dobdc), respectively, appear to indicate that both materials polarize H₂ strongly enough that it desorbs above liquid nitrogen temperature (-198 °C at the NREL altitude). Empirical differences in desorption temperature between materials typically arise due to differences in pore shape or size, which impact the diffusion of hydrogen through the pores. However, due to the similar pore shapes and sizes exhibited by these two MOFs, the higher desorption temperature for Ni₂(m-dobdc) is indicative of a stronger H₂ binding at the open Ni²⁺ sites.

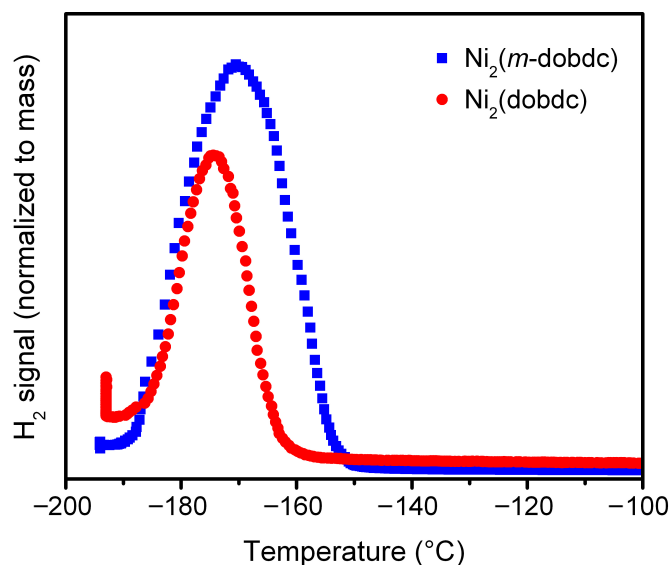


Figure 3.4. Temperature-programmed desorption of H_2 in $\text{Ni}_2(m\text{-dobdc})$ and $\text{Ni}_2(\text{dobdc})$. Note the difference in desorption temperature between $\text{Ni}_2(m\text{-dobdc})$ and $\text{Ni}_2(\text{dobdc})$.

3.3.4. In Situ Powder Neutron Diffraction. Powder neutron diffraction experiments were undertaken at high pressures in order to further understand hydrogen adsorption in the $\text{M}_2(m\text{-dobdc})$ frameworks. The measurements were performed on $\text{Co}_2(m\text{-dobdc})$, as its greater degree of crystallinity allowed for structure solutions of the D_2 -dosed samples and the refinement of the D_2 adsorption positions within the pores. While not a direct measure of the performance of $\text{Ni}_2(m\text{-dobdc})$, the similar structure and adsorption behavior of $\text{Co}_2(m\text{-dobdc})$ should provide a representative example of the $\text{Ni}_2(m\text{-dobdc})$ material. Additionally, D_2 and H_2 have previously been shown to behave nearly identically in powder neutron diffraction experiments.³⁹ Samples were measured at 198 K at pressures of 36, 54, and 79 bar, as well as at 77 K at a pressure of 78 bar in order to most closely simulate the adsorption isotherm conditions while retaining the ability to crystallographically locate each D_2 binding site within the pores.

At 77 K, the sample of $\text{Co}_2(m\text{-dobdc})$ loaded with D_2 at 78 bar revealed seven distinct adsorption sites (Figure 3.5). At site 1, the strongest adsorption site, the D_2 is bound to the open Co^{2+} coordination site with a $\text{Co}\cdots\text{D}_2(\text{centroid})$ separation of 2.25(7) Å. The D_2 at site 2 is directly adjacent, interacting with both the D_2 bound at site 1 as well as ligand O atoms from a hydroxide and a carboxylate. Site 3 occupies a position above the center of the aromatic ring of the $m\text{-dobdc}^{4-}$ linker, while site 4 lies adjacent to this. These first four adsorption sites were previously observed in neutron diffraction experiments carried out on $\text{Co}_2(m\text{-dobdc})$ at 4 K and pressures below 1 bar.³⁹ Adsorption sites 5-7, which only become occupied at the higher D_2 pressures measured here, could likely have been located in the previous study if higher dosings were used. Sites 5 and 6 lie at the center of the hexagonal channels of the framework, while site 7 resides 3.10(3) Å from the D_2 located at site 5 and primarily relies on $\text{D}_2\cdots\text{D}_2$ interactions for stabilization. At 77 K and 78 bar, sites 1-6 show full occupancy of D_2 and site 7 shows approximately half occupancy. Importantly, a comparison of the adsorption isotherm data collected at 198 K and the D_2 loadings observed by powder neutron diffraction at the same

temperature reveal a quantitative agreement between the two methods for measuring storage capacity (Figure 3.S4).

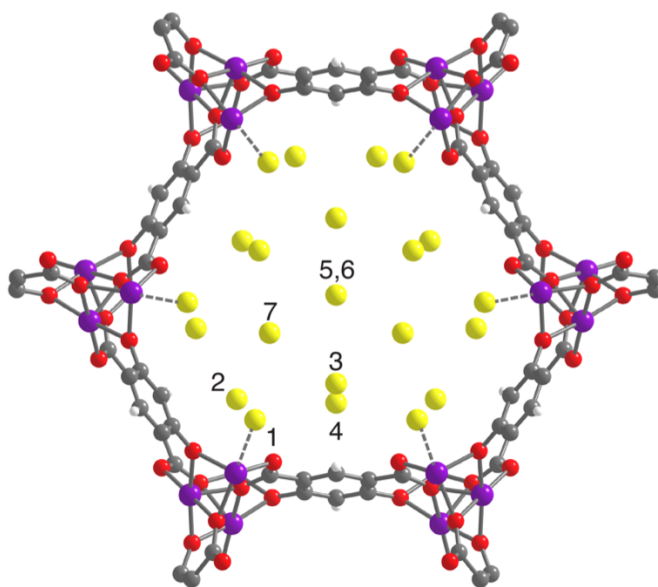


Figure 3.5. A single pore of $\text{Co}_2(m\text{-dobdc})$ showing the seven distinct D_2 binding sites as determined from neutron diffraction data. Purple, red, grey, white, and yellow spheres represent Co, O, C, H atoms and D_2 molecules, respectively.

Notably, the $\text{D}_2\cdots\text{D}_2$ distances measured for certain sites within the pores of $\text{Co}_2(m\text{-dobdc})$ are very short. For example, the distance between the D_2 molecules at sites 1 and 2 is only 2.86(3) Å. This is significantly shorter than the $\text{H}_2\cdots\text{H}_2$ separation of 3.21 Å in solid hydrogen,⁵² and is approaching the $\text{H}_2\cdots\text{H}_2$ distance of 2.656 Å in solid H_2 pressurized to 54 kbar at 300 K.⁵³ These comparisons to solid hydrogen powerfully illustrate the ability of materials in the $\text{M}_2(m\text{-dobdc})$ series to densify hydrogen within their pores. Other notably short $\text{D}_2\cdots\text{D}_2$ distances within $\text{Co}_2(m\text{-dobdc})$ can be seen in Table 3.3, further illustrating this principle.⁵⁴ Significantly, the high charge density on the metals not only strongly polarizes D_2 bound at the coordinatively-unsaturated Co^{2+} center, but additionally impacts D_2 bound in more weakly physisorbing secondary sites as well, leading to a high hydrogen packing density within the adsorbent.

Table 3.3. Selected $\text{D}_2\cdots\text{D}_2$ distances within $\text{Co}_2(m\text{-dobdc})$ as determined from powder neutron diffraction collected at 77 K and 78 bar. Numbers in parentheses indicate one standard deviation in the value.

$\text{D}_2\cdots\text{D}_2$ interaction	Distance (Å)
1 \cdots 2	2.86(3)
2 \cdots 2	3.08(3)
3 \cdots 4	3.12(5)
4 \cdots 5	3.41(3)
solid H_2 ⁵²	3.21

3.3.5. In Situ Infrared Spectroscopy. High-pressure H₂-dosed *in situ* infrared spectroscopy was used to further understand H₂ loading in Ni₂(*m*-dobdc). Spectra were collected in the pressure range 10–90 bar at multiple temperatures ranging from 198 K (Figure 3.6) to 298 K (Figures 3.S11-3.S19). Adsorbed H₂ in MOFs has been shown to exhibit a vibrational frequency that is lower than that of free gaseous H₂ (4161 cm⁻¹) and generally correlates with the H₂ binding energy at a given site.⁵⁵ In Figure 3.6, the peak at ~4035 cm⁻¹ corresponds to H₂ bound to the open Ni²⁺ sites in the framework, while the peak at ~4125 cm⁻¹ corresponds to H₂ adsorbed at more weakly interacting secondary sites within the pores. At lower pressures, the peak area of the Ni²⁺-bound H₂ is significantly larger than that of the peak area at the secondary sites, indicating a substantially higher H₂ binding enthalpy.

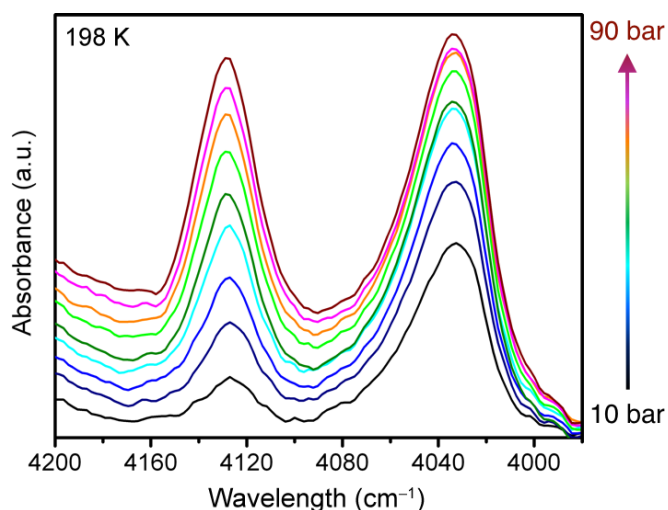


Figure 3.6. *In situ* H₂-dosed infrared spectroscopy of Ni₂(*m*-dobdc) at 198 K with H₂ pressure between 10 and 90 bar. Note that the spectra have been offset for clarity. The peak on the right corresponds to H₂ bound to the open Ni²⁺ site and the peak on the left corresponds to H₂ bound at secondary sites within the pores.

As the gas pressure is increased, the area of the secondary site peak grows with the corresponding increase in adsorbed H₂ within the pores. A commensurate increase is not seen for the Ni²⁺-bound H₂, as saturation of these sites prior to the occupation of secondary sites is likely. A comparison of the peak areas calculated from these spectra, which should be proportional to the H₂ loading, shows good agreement with the isotherm data when a single linear scaling factor (used to compare absolute adsorption from isotherms to the relative adsorption determined by infrared spectroscopy) is applied to the peaks areas at each temperature (Figures 3.S11-3.S19), especially at pressures below 60 bar. The small standard deviations for the observed scaling factors (<0.8 for all temperatures and <0.3 for 198 and 233 K) support the validity of this method (Table 3.S6).

Figure 7 displays infrared spectra collected for Ni₂(*m*-dobdc) at approximately equivalent H₂ loadings at various temperatures and pressures. The results illustrate how the loading of each of the two types of adsorption sites (Ni²⁺ centers at 4035 cm⁻¹ and more weakly physisorbing sites at 4125 cm⁻¹) changes as a function of temperature. At 273 K and 70 bar, the area under the peaks for each binding site are approximately equal, indicating an even distribution of bound H₂

between the open Ni^{2+} sites and other sites within the pores. As the temperature is decreased, the pressure drops as more H_2 adsorbs in the material, and the peak at 4035 cm^{-1} begins to grow while the peak at 4125 cm^{-1} shrinks, indicating a shift toward more adsorption at the open Ni^{2+} sites. At 198 K and 10 bar, most of the adsorbed H_2 is bound to the open metal sites. This confirmation of the temperature dependence of the binding site population, while expected, is quite interesting and illustrates the importance of operating conditions when considering the use of an adsorbent in a hydrogen storage system.

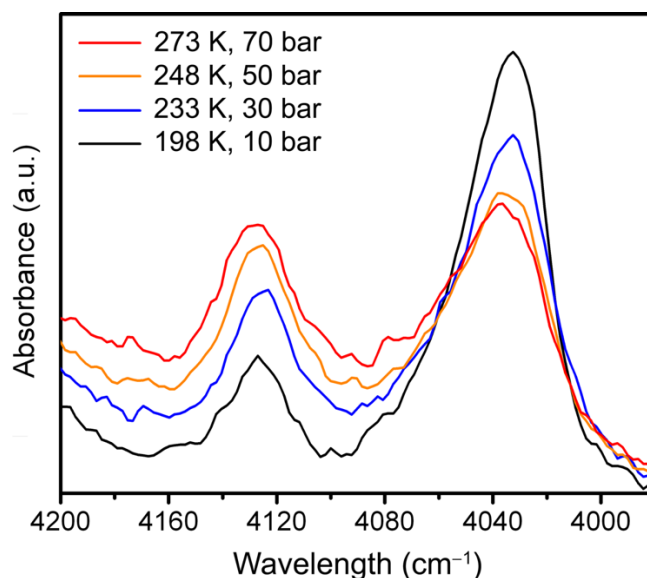


Figure 3.7. Comparison of infrared spectra with approximately constant adsorption of H_2 in $\text{Ni}_2(m\text{-dobdc})$ based on total peak area for each spectrum. Note the change in relative peak areas from approximately equal loading of open Ni^{2+} sites ($\sim 4035\text{ cm}^{-1}$) and other sites ($\sim 4125\text{ cm}^{-1}$) at 273 K and 70 bar to a much higher concentration of H_2 bound to the open Ni^{2+} sites at 198 K and 10 bar.

3.4. Outlook and Conclusions

Selected high-performance metal-organic frameworks were evaluated for their H_2 adsorption properties under conditions relevant to on-board storage in motor vehicles. Adsorption isotherms in the pressure range of 0–100 bar were measured for the materials $\text{Co}_2(m\text{-dobdc})$, $\text{Ni}_2(m\text{-dobdc})$, $\text{Co}_2(\text{dobdc})$, and $\text{Ni}_2(\text{dobdc})$, which contain a high density of coordinatively-unsaturated metal sites, as well as for MOF-5, which does not. $\text{Ni}_2(m\text{-dobdc})$ is the top-performing material with respect to the critical metric of usable volumetric H_2 capacity at pressures between 5 and 100 bar and near ambient temperatures. To our knowledge, this compound displays the highest physisorptive hydrogen storage capacity of any known adsorbent under these conditions. Its high capacity is attributable to the presence of highly polarizing Ni^{2+} adsorption sites, which lead to large binding enthalpies and a dense packing of H_2 within the material. This conclusion is supported by the results of temperature-programmed desorption, *in situ* powder neutron diffraction, and *in situ* infrared spectroscopy experiments performed under relevant conditions. The results provide benchmark data for comparison with future generations

of adsorbents designed for hydrogen storage. In particular, efforts are underway to create new metal-organic frameworks with low-coordiante metal cations capable of binding multiple H₂ molecules at enthalpies in the optimal range of –15 to –20 kJ/mol. Lastly, this study highlights the importance of adsorption conditions in the evaluation of materials and the superior performance of metal-organic frameworks containing open metal coordination sites for physisorptive H₂ storage.

3.5. Acknowledgements

Thanks to Tomče Runčevski, Jacob D. Tarver, Anthony Ayala, and Craig M. Brown for assistance with powder neutron diffraction data collection and analysis, Henry Z. H. Jiang and Stephen A. FitzGerald for assistance with infrared spectroscopy data collection and analysis, and Katherine E. Hurst, Philip A. Parilla, and Thomas Gennett for collection of high-pressure H₂ adsorption isotherms. Research support from the U.S. Department of Energy, Office of Energy Efficiency and Renewable Energy, Fuel Cell Technologies Office, under Contract No. DE-AC02-05CH11231 is gratefully acknowledged. Thanks to the NSF for providing graduate fellowship support for M.T.K., the U.S. Department of Energy, Office of Energy Efficiency and Renewable Energy, Fuel Cell Technologies Office, for support under Contract No. DE-AC36-08GO28308, and the NSF for support through Grant No. CHE-1111896. We also thank Rodolfo Torres-Gavosto for the improved H₂(*m*-dobdc) synthesis, Q. Barker-Plummer, D. Mukasa, J. Parker, and E. Rappeport for experimental assistance, and Dr. Katie R. Meihaus for editorial assistance.

3.6. References and Supplementary Data

1. Hoffmann, P. *Tomorrow's Energy: Hydrogen, Fuel Cells, and the Prospects for a Cleaner Planet*, The MIT Press, Cambridge, MA, 2012.
2. http://www.afdc.energy.gov/fuels/hydrogen_locations.html, (accessed April 23, 2017).
3. http://leginfo.legislature.ca.gov/faces/billNavClient.xhtml?bill_id=201320140AB8, (accessed April 25 2017).
4. Fuel Cell Technologies Market Report 2015, United States Department of Energy, Energy Efficiency & Renewable Energy, https://energy.gov/sites/prod/files/2016/10/f33/fcto_2015_market_report.pdf (accessed April 25, 2017).
5. H2USA, <http://www.h2usa.org/>; International Partnership for Hydrogen and Fuel Cells in the Economy, <http://www.iphe.net/>; California Fuel Cell Partnership, <http://cafcp.org/>; Low Carbon Vehicle Partnership, <http://www.lowcvp.org.uk/>; U. S. Drive Partnership, https://www.hydrogen.energy.gov/usdrive_partnership.html; Scandinavian Hydrogen Highway Partnership, <http://www.scandinavianhydrogen.org/shhp/vehicles/> (accessed April 25, 2017).
6. Schlapbach, L.; Züttel, A. *Nature*, **2001**, *414*, 353-358.
7. Midilli, A.; Ay, M.; Dincer, I.; Rosen, M. A.; *Renew. Sustainable Energy Rev.*, **2005**, *9*, 255-271.
8. Mazloomi, K.; Gomes, C. *Renew. Sustainable Energy Rev.*, **2012**, *16*, 3024-3033.

9. Arnold, G.; Eberle, U.; Hasenauer, D. *US Pat.*, US7517396 B2, **2009**.
10. Züttel, A. *Mater. Today*, **2003**, *6*, 24-33.
11. H35 (35 MPa/350 bar) vs. H70 (70 MPa/700 bar) Fueling Mirai Refueling Tips, https://ssl.toyota.com/mirai/Mirai_Fueling.pdf (accessed Jan. 2017).
12. Jepsen, L. H.; Ley, M. B.; Lee, Y.-S.; Cho, Y.-W.; Dornheim, M.; Jensen, J. O.; Filinchuk, Y.; Jørgensen, J. E.; Besenbacher, F.; Jensen, T. R.; *Mater. Today*, **2014**, *17*, 129-135.
13. Zhu, Q.-L.; Xu, Q. *Energy Environ. Sci.*, **2015**, *8*, 478-512.
14. He, T.; Pachfule, P.; Wu, H.; Xu, Q.; Chen, P. *Nat. Rev. Mater.*, **2016**, *1*, 16059.
15. Rusman, N. A. A.; Dahari, M. *Int. J. Hydrogen Energy*, **2016**, *41*, 12108-12126.
16. Dündar-Tekkaya E.; Yürüm, Y. *Int. J. Hydrogen Energy*, **2016**, *41*, 9789-9795.
17. Blankenship, T. S.; Mokaya, R. *Energy Environ. Sci.*, **2017**, *10*, 2552-2562.
18. Ahluwalia, R. K.; Peng, J. K. *Int. J. Hydrogen Energy*, **2009**, *34*, 5476-5487.
19. Petitpas, G.; Bernard, P.; Klebanoff, L. E.; Xiao, J.; Aceves, S. *Int. J. Hydrogen Energy*, **2014**, *39*, 10564-10584.
20. Rosi, N. L.; Eckert, J.; Eddaoudi, M.; Vodak, d. T.; Kim, J.; O'Keeffe, M.; Yaghi, O. M. *Science*, **2003**, *300*, 1127.
21. Farha, O. K.; Eryazici, I.; Jeong, N. C.; Hauser, B. G.; Wilmer, C. E.; Sarjeant, A. A.; Snurr, R. Q.; Nguyen, S. T.; Yazaydin, A. O.; Hupp, J. T. *J. Am. Chem. Soc.*, **2012**, *134*, 15016-15021.
22. Krause, S.; Bon, V.; Senkowska, I.; Stoeck, U.; Wallacher, D.; Töbrens, D. M.; Zander, S.; Pillai, R. S.; Maurin, G.; Coudert, F.-X.; Kaskel, S. *Nature*, **2016**, *532*, 348-352.
23. Yuan, S.; Chen, Y.-P.; Qin, J.-S.; Lu, W.; Zou, L.; Zhang, Q.; Wang, X.; Sun, X.; Zhou, H.-C. *J. Am. Chem. Soc.*, **2016**, *138*, 8912-8919.
24. Murray, L. J.; Dincă, M.; Long, J. R. *Chem. Soc. Rev.*, **2009**, *38*, 1294-1314.
25. Suh, M. P.; Park, H. J.; Prasad, T. K.; Lim, D.-W. *Chem. Rev.*, **2012**, *112*, 782-835.
26. Basdogan, Y.; Keskin, S. *CrystEngComm*, **2015**, *17*, 261-275.
27. Gómez-Gualdrón, D. A.; Colón, Y. J.; Zhang, X.; Wang, T. C.; Chen, Y.-S.; Hupp, J. T.; Yildirim, T.; Farha, O. K.; Zhang, J.; Snurr R. Q. *Energy Environ. Sci.*, **2016**, *9*, 3279-3289.
28. Rahali, S.; Belhocine, Y.; Seydou, M.; Maurel, F.; Tangour, B. *Int. J. Hydrogen Energy*, **2017**, *42*, 15271-15282.
29. Han, S. S.; Goddard III, W. A. *J. Am. Chem. Soc.* **2007**, *129*, 8422-8423.
30. Rao, D.; Lu, R.; Xiao, C.; Kan, E.; Deng, K. *Chem. Commun.*, **2011**, *47*, 7698-7700.
31. Meng, Z.; Lu, R.; Rao, D.; Kan, E.; Xiao, C.; Deng, K. *Int. J. Hydrogen Energy*, **2013**, *38*, 9811-9818.
32. Bhatia, S. K.; Myers, A. L. *Langmuir*, **2006**, *22*, 1688-1700.
33. DOE Technical Targets for Onboard Hydrogen Storage for Light-Duty Vehicles, <https://energy.gov/eere/fuelcells/doe-technical-targets-onboard-hydrogen-storage-light-duty-vehicles>, (accessed Jan. 2018).
34. Dincă, M.; Long, J. R. *Angew. Chem. Int. Ed.*, **2008**, *47*, 6766-6779.
35. Dincă, M.; Dailly, A.; Liu, Y.; Brown, C. M.; Neumann, D. A.; Long, J. R. *J. Am. Chem. Soc.*, **2006**, *128*, 16876-16883.
36. Vitillo, J. G.; Regli, L.; Chavan, S.; Ricchiardi, G.; Spoto, G.; Dietzel, P. D. C.; Bordiga, S.; Zecchina, A. *J. Am. Chem. Soc.*, **2008**, *130*, 8386-8396.

37. Zhou, W.; Wu, H.; Yildirim, T. *J. Am. Chem. Soc.*, **2008**, *130*, 15268-15269.
38. Oh, H.; Savchenko, I.; Mavrandonakis, A.; Heine, T.; Hirscher, M. *ACS Nano*, **2014**, *8*, 761-770.
39. Kapelewski, M. T.; Geier, S. J.; Hudson, M. R.; Stück, D.; Mason, J. A.; Nelson, J. N.; Xiao, D. J.; Hulvey, Z.; Gilmour, E.; FitzGerald, S. A.; Head-Gordon, M.; Brown, C. M.; Long, J. R. *J. Am. Chem. Soc.*, **2014**, *136*, 12119-12129.
40. Denysenko, D.; Grzywa, M.; Jelic, J.; Reuter, K.; Volkmer, D. *Angew. Chem. Int. Ed.*, **2014**, *53*, 5832-5836.
41. Weinrauch, I.; Savchenko, I.; Denysenko, D.; Souliou, S. M.; Kim, H.-H.; Tacon, M. L.; Daemen, L. L.; Cheng, Y.; Mavrandonakis, A.; Ramirez-Cuesta, A. J.; Volkmer, D.; Schütz, G.; Hirscher, M.; Heine, T. *Nature Commun.*, **2017**, *8*, 14496.
42. Mason, J. A.; Veenstra, M.; Long, J. R. *Chem. Sci.*, **2014**, *5*, 32-51.
43. Kaye, S. S.; Dailly, A.; Yaghi, O. M.; Long, J. R. *J. Am. Chem. Soc.*, **2007**, *129*, 14176-14177.
44. Hurst, K. E.; Heben, M. J.; Blackburn, J. L.; Gennett, T.; Dillon, A. C.; Parilla, P. A. *Rev. Sci. Instrum.*, **2013**, *84*, 025103.
45. FitzGerald, S. A.; Churchill, H. O. H.; Korngut, P. M.; Simmons, C. B.; Strangas, Y. E. *Rev. Sci. Instrum.*, **2006**, *77*, 093110.
46. Goldsmith, J.; Wong-Foy, A. G.; Cafarella, M. J.; Siegel, D. J. *Chem. Mater.*, **2013**, *25*, 3373-3382.
47. Gómez-Gualdrón, D. A.; Wang, T. C.; García-Holley, P.; Sawelewa, R. M.; Argueta, E.; Snurr, R. Q.; Hupp, K. T.; Yildirim, T.; Farha, O. K. *ACS Appl. Mater. Interfaces*, **2017**, *9*, 33419-33428.
48. Parilla, P. A.; Gross, K.; Hurst, K.; Gennett, T. *Appl. Phys. A*, **2016**, *122*, 42.
49. Mason, J. A.; Oktawiec, J.; Taylor, M. K.; Hudson, M. R.; Rodriguez, J. Bachman, J. E.; Gonzalez, M. I.; Cervellino, A.; Guagliardi, A.; Brown, C. M.; Llewellyn, P. L.; Masciocchi, N.; Long, J. R. *Nature*, **2015**, *527*, 357-361.
50. DeSantis, D.; Mason, J. A.; James, B. D.; Houchins, C.; Long, J. R.; Veenstra, M. *Energy Fuels*, **2017**, *31*, 2024-2032.
51. Parks, G.; Boyd, R.; Cornish, J.; Remick, R.; Popovich, N. *Hydrogen Station Compression, Storage, and Dispensing Technical Status and Costs*, NREL, Golden, CO, 2014 <http://www.nrel.gov/docs/fy14osti/58564.pdf>.
52. van Kranendonk, J.; Gush, H. P. *Phys. Lett.*, **1962**, *1*, 22-23.
53. Mao, H. K.; Jephcoat, A. P.; Hemley, R. J.; Finger, L. W.; Zha, C. S.; Hazen, R. M.; Cox, D. E. *Science*, **1988**, *239*, 1131-1134.
54. Liu, Y.; Kabbour, H.; Brown, C. M.; Neumann, D. A.; Ahn, C. C. *Langmuir*, **2008**, *24*, 4772-4777.
55. FitzGerald, S. A.; Burkholder, B.; Friedman, M.; Hopkins, J. B.; Pierce, C. J.; Schloss, J. M.; Thompson, B.; Rowsell, J. L. C. *J. Am. Chem. Soc.* **2011**, *133*, 20310-20318.

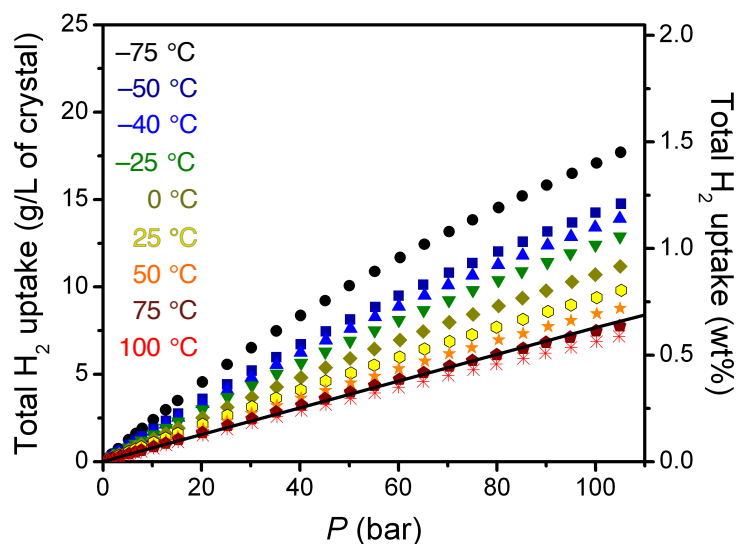


Figure 3.S1. Hydrogen adsorption isotherms for MOF-5 at -75 (black circles), -50 (navy squares), -40 (blue triangles), -25 (green upside-down triangles), 0 (gold diamonds), 25 (yellow hexagons), 50 (orange stars), 75 (dark red pentagons), and 100 °C (bright red crosses), measured between 0 and 100 bar and plotted in terms of total volumetric and gravimetric capacity. The black line represents the volumetric density of pure compressed H_2 at 25 °C.

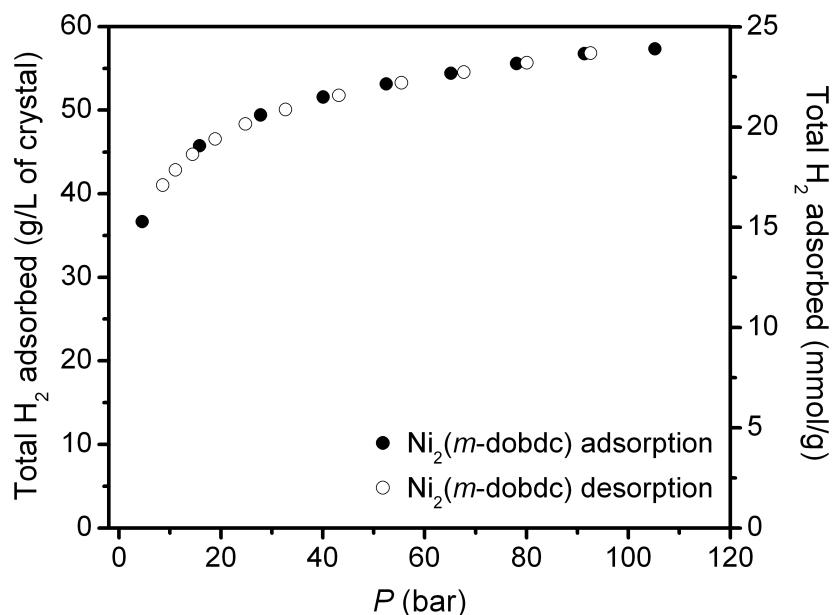


Figure 3.S2. Total H_2 adsorption in $Ni_2(m-dobdc)$ measured at 75.6 K (liquid nitrogen measurement made at the National Renewable Energy Laboratory, elevation 5768 feet (1758 m)). Filled circles represent adsorption and open circles represent desorption.

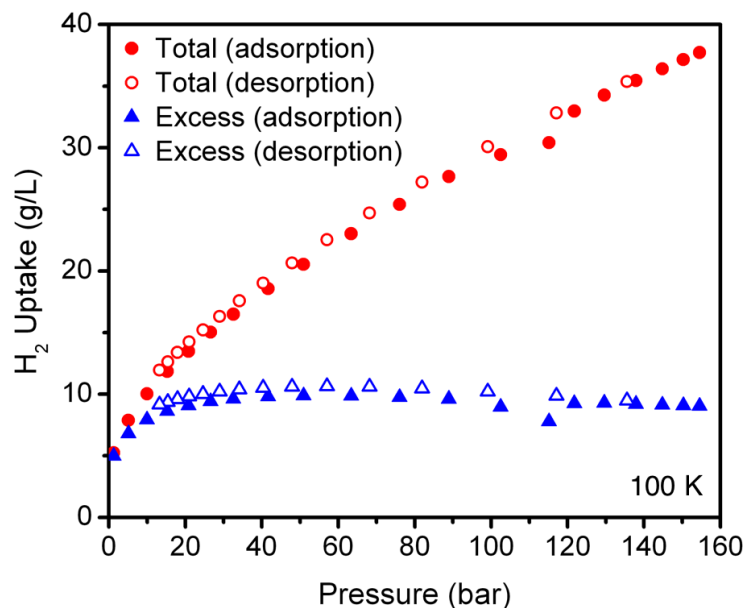


Figure 3.S3. Total and excess adsorption of $\text{Ni}_2(m\text{-dobdc})$ at 100 K as measured at NREL on 1.0117 g of $\text{Ni}_2(m\text{-dobdc})$ sample. Red circles represent total adsorption and blue triangles represent desorption, with filled and open symbols representing adsorption and desorption, respectively. The volumetric uptake here is calculated using the actual packing density of the sample, rather than the crystallographic density as used throughout most of this work.

Table 3.S1. Atomic parameters from Rietveld refinement of activated $\text{Co}_2(m\text{-dobdc})$ at 198 K [NCNR, BT1], $R3m$, $a = 25.8825(9) \text{ \AA}$, $c = 6.7838(4) \text{ \AA}$, $V = 3935.6(2) \text{ \AA}^3$. Goodness-of-fit parameters: $\chi^2 = 2.158$; $wRp = 3.22 \%$; $Rp = 2.57 \%$. Numbers in parentheses indicate 1 standard deviation in the value. Refined composition: $\text{Co}_2\text{C}_8\text{H}_2\text{O}_6$

Atom	X	Y	Z	Occupancy	$U_{\text{iso}} (\text{\AA}^2)$	Multiplicity
C1	0.6575(5)	0.8751(5)	0.092(1)	1	0.057(6)	18
C2	0.6675(7)	0.8333(4)	-0.005(2)	1	0.021(6)	9
C6	0.6412(5)	0.8666(4)	0.296(1)	1	0.020(4)	18
C11	0.6316(5)	0.9085(5)	0.408(1)	1	0.028(3)	18
Co	0.330(2)	0.372(1)	0.791(4)	1	0.006(6)	18
H7	0.673(1)	0.8364(5)	0.840(1)	1	0.03(1)	9
O9	0.6676(5)	0.9257(5)	-0.010(0)	1	0.005(3)	18
O12	0.6499(5)	0.9588(5)	0.338(2)	1	0.014(2)	18
O15	0.6095(5)	0.8945(6)	0.598(2)	1	0.014(2)	18
C2m	0.6289(8)	0.8145(4)	0.387(3)	1	0.029(5)	9
H7m	0.618(1)	0.8087(5)	0.540(4)	1	0.02(1)	9

Table 3.S2. Atomic parameters from Rietveld refinement of $\text{Co}_2(m\text{-dobdc})$ at 198 K dosed with 36 bar D_2 . [NCNR, BT1], $R3m$, $a = 25.8728(1) \text{ \AA}$, $c = 6.7926(6) \text{ \AA}$, $V = 3937.8(3) \text{ \AA}^3$. Goodness-of-fit parameters: $\chi^2 = 1.508$; wRp = 4.40 %; Rp = 3.71 %. Numbers in parentheses indicate 1 standard deviation in the value. Refined composition: $\text{Co}_2\text{C}_8\text{H}_2\text{O}_6(\text{D}_2)_{2.08}$

Atom	X	Y	Z	Occupancy	$U_{\text{iso}} (\text{\AA}^2)$	Multiplicity
C1	0.6580	0.8762	0.0995	1	0.051	18
C2	0.6588	0.8294	0.9995	1	0.021	9
C6	0.6377	0.8658	0.2962	1	0.023	18
C11	0.6270	0.9073	0.4089	1	0.029	18
Co	0.3335	0.3685	0.8103	1	0.006	18
H7	0.6670	0.8335	0.8408	1	0.001	9
O9	0.6695	0.9211	0.0044	1	0.002	18
O12	0.6449	0.9576	0.3445	1	0.017	18
O15	0.6152	0.8991	0.6050	1	0.017	18
C2m	0.6314	0.8158	0.3966	1	0.049	9
H7m	0.5224	0.4775	0.2183	1	0.083	9
D1	0.3550	0.4694	0.9278	1.28(3)	0.1013	18
D2	0.7744	0.5489	0.9964	0.80(0)	0.8	9
D3	0.052	-0.053	0.678	0.40(2)	0.8	18

Table 3.S3. Atomic parameters from Rietveld refinement of $\text{Co}_2(m\text{-dobdc})$ at 198 K dosed with 54 bar D_2 . [NCNR, BT1], $R3m$, $a = 25.872(1) \text{ \AA}$, $c = 6.7934(6) \text{ \AA}$, $V = 3937.9(3) \text{ \AA}^3$. Goodness-of-fit parameters: $\chi^2 = 1.948$; wRp = 3.80 %; Rp = 3.12 %. Numbers in parentheses indicate 1 standard deviation in the value. Refined composition: $\text{Co}_2\text{C}_8\text{H}_2\text{O}_6(\text{D}_2)_{2.27}$

Atom	X	Y	Z	Occupancy	$U_{\text{iso}} (\text{\AA}^2)$	Multiplicity
C1	0.6580	0.8762	0.0995	1	0.051	18
C2	0.6588	0.8294	0.9995	1	0.021	9
C6	0.6377	0.8658	0.2962	1	0.023	18
C11	0.6270	0.9073	0.4089	1	0.029	18
Co	0.3335	0.3685	0.8103	1	0.006	18
H7	0.6670	0.8335	0.8408	1	0.001	9
O9	0.6695	0.9211	0.0044	1	0.002	18
O12	0.6449	0.9576	0.3445	1	0.017	18
O15	0.6152	0.8991	0.6050	1	0.017	18
C2m	0.6314	0.8158	0.3966	1	0.049	9
H7m	0.5224	0.4775	0.2183	1	0.083	9
D1	0.3550	0.4694	0.9278	1.41(3)	0.1013	18
D2	0.7744	0.5489	0.9964	0.88(5)	0.8	9
D3	0.052	-0.053	0.678	0.42(2)	0.8	18

Table 3.S4. Atomic parameters from Rietveld refinement of Co₂(*m*-dobdc) at 198 K dosed with 79 bar D₂. [NCNR, BT1], *R3m*, *a* = 25.870(7) Å, *c* = 6.793(8) Å, *V* = 3937.8(7) Å³. Goodness-of-fit parameters: $\chi^2 = 1.786$; wRp = 3.56 %; Rp = 2.85 %. Refined composition: Co₂C₈H₂O₆(D₂)_{2.69}

Atom	X	Y	Z	Occupancy	U _{iso} (Å ²)	Multiplicity
C1	0.6580(4)	0.8762(8)	0.0995(0)	1	0.051(9)	18
C2	0.6588(8)	0.8294(9)	0.9995(2)	1	0.021(4)	9
C6	0.6377(9)	0.8658(5)	0.2962(4)	1	0.023(2)	18
C11	0.6270(1)	0.9073(6)	0.4089(2)	1	0.029(2)	18
Co	0.3335(1)	0.3685(8)	0.8103(6)	1	0.006(2)	18
H7	0.6670(2)	0.8335(2)	0.8408(0)	1	0.001(3)	9
O9	0.6695(0)	0.9211(4)	0.0044(3)	1	0.002(5)	18
O12	0.6449(1)	0.9576(6)	0.3445(5)	1	0.017(1)	18
O15	0.6152(9)	0.8991(2)	0.6050(8)	1	0.017(1)	18
C2m	0.6314(9)	0.8158(0)	0.3966(8)	1	0.049(9)	9
H7m	0.5224(4)	0.4775(6)	0.2183(9)	1	0.083(7)	9
D1	0.3550(7)	0.4694(8)	0.9278(2)	1.62(6)	0.1013	18
D2	0.7744(9)	0.5489(8)	0.9964(7)	1.01(9)	0.8	9
D3	0.052(3)	-0.053(3)	0.678(8)	0.56(1)	0.8	18

Table 3.S5. Atomic parameters from Rietveld refinement of Co₂(*m*-dobdc) at 77 K dosed with 78 bar D₂. [NCNR, BT1], *R3m*, *a* = 25.9276(21) Å, *c* = 6.8267(8) Å, *V* = 3974.4(8) Å³. Goodness-of-fit parameters: $\chi^2 = 1.648$; wRp = 3.30 %; Rp = 2.73 %. Refined composition: Co₂C₈H₂O₆(D₂)_{7.12}

Atom	X	Y	Z	Occupancy	U _{iso} (Å ²)	Multiplicity
C1	0.6551(11)	0.871(14)	0.843(4)	1	0.035(9)	18
C2	0.6753(17)	0.8377(8)	0.758(7)	1	0.056(13)	9
C6	0.6385(11)	0.8666(7)	0.049(4)	1	0.021(6)	18
C11	0.6330(9)	0.9109(8)	0.170(4)	1	0.015(6)	18
Co	0.3309(26)	0.3738(23)	0.558(8)	1	0.0017(2)	18
H7	0.6779(23)	0.8389(12)	0.590(10)	1	0.010(14)	9
O9	0.6704(14)	0.9222(15)	0.755(5)	1	0.056(11)	18
O12	0.6472(10)	0.9601(10)	0.091(4)	1	0.005(6)	18
O15	0.6126(13)	0.8964(15)	0.351(5)	1	0.026(7)	18
C2m	0.6315(16)	0.8158(8)	0.144(5)	1	0.009(7)	9
H7m	0.6171(22)	0.8085(11)	0.280(10)	1	0.02	9
D1	0.2054(8)	0.2182(9)	0.009(4)	1.9(1)	0.123(9)	18
D2	0.7733(10)	0.9461(10)	0.403(4)	1.9(1)	0.122(9)	18
D3	0.5764(10)	0.1528(20)	0.494(5)	2.1(1)	0.26(3)	9
D4	0.58715	0.17439	0.04181	2.1(1)	0.27(3)	9
D5	0.0	0.0	0.92706	2.1(1)	0.26(3)	3
D6	0.0	0.0	0.42637	1.8(2)	0.54(3)	3
D7	0.069	0.138	0.95	0.94(8)	0.10(3)	9

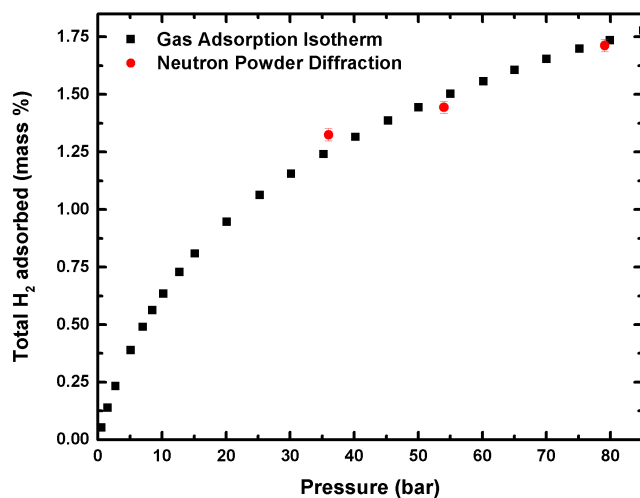


Figure 3.S4. Volumetric adsorption isotherm measured by adsorption isotherms for H₂ uptake at 198 K (black). Total H₂ uptake based on NPD data (red) show good agreement. Error bars indicate one standard deviation.

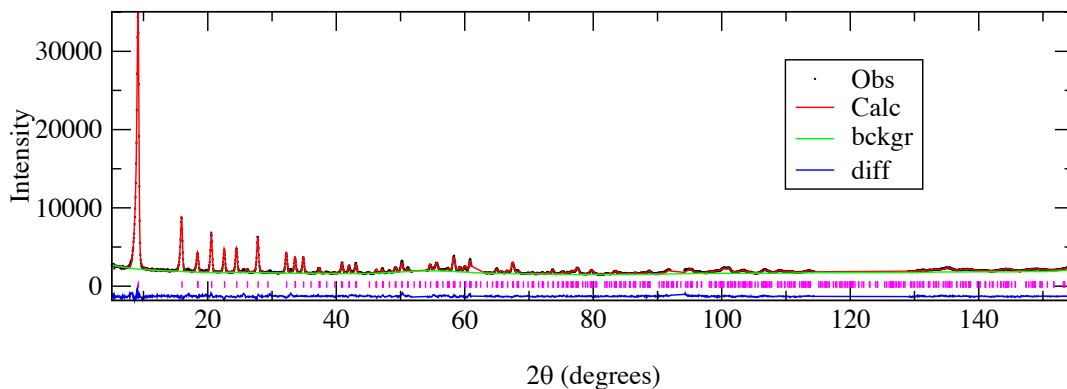


Figure 3.S5. Rietveld refinement of the experimental neutron diffraction pattern (198 K) of bare Co₂(*m*-dobdc). The calculated pattern (red trace) is in good agreement with the experimental data (hashes) as evidenced by the difference pattern (blue trace) between calculated and experimental data. Final Rietveld fit parameter was $\chi^2 = 1.967$.

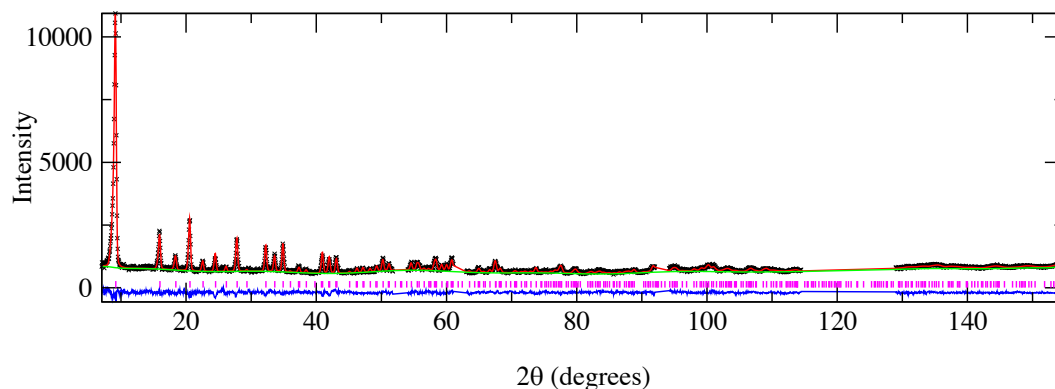


Figure 3.S6. Rietveld refinement of the experimental neutron diffraction pattern (198 K) of $\text{Co}_2(m\text{-dobdc})$ dosed with 36 bar D_2 . The calculated pattern (red trace) is in good agreement with the experimental data (hashes) as evidenced by the difference pattern (blue trace) between calculated and experimental data. Final Rietveld fit parameter was $\chi^2 = 1.509$.

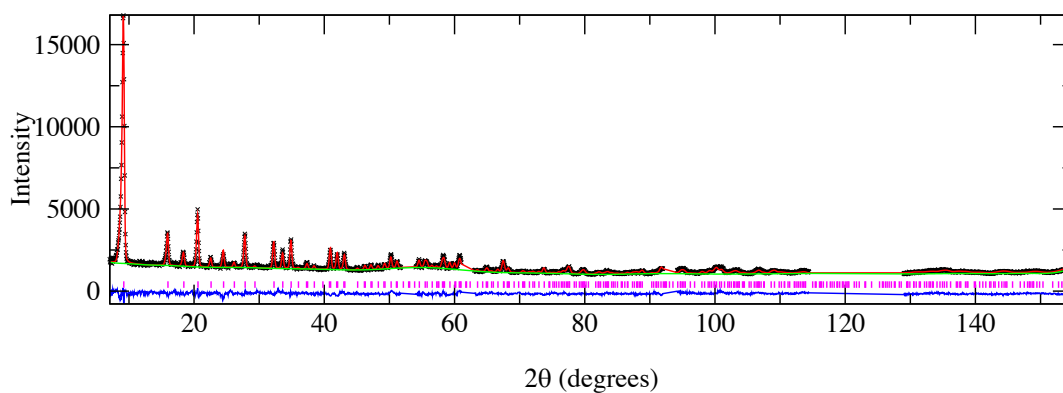


Figure 3.S7. Rietveld refinement of the experimental neutron diffraction pattern (198 K) of $\text{Co}_2(m\text{-dobdc})$ dosed with 54 bar D_2 . The calculated pattern (red trace) is in good agreement with the experimental data (hashes) as evidenced by the difference pattern (blue trace) between calculated and experimental data. Final Rietveld fit parameter was $\chi^2 = 1.948$.

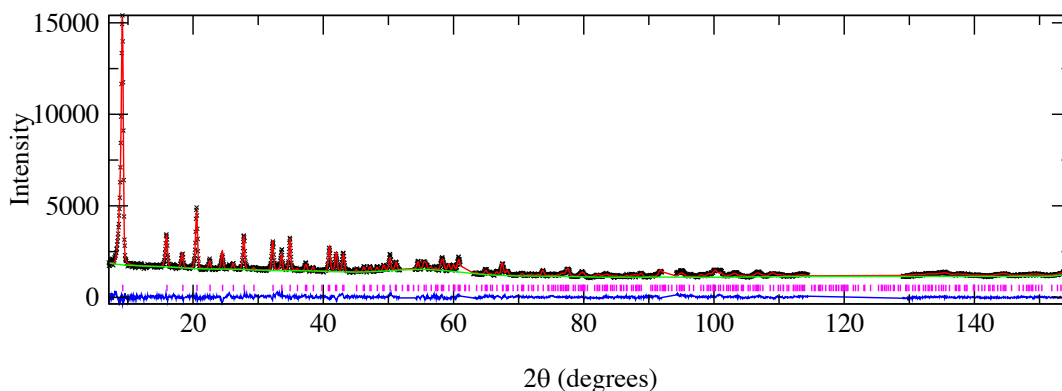


Figure 3.S8. Rietveld refinement of the experimental neutron diffraction pattern (198 K) of $\text{Co}_2(m\text{-dobdc})$ dosed with 79 bar D_2 . The calculated pattern (red trace) is in good agreement with the experimental data (hashes) as evidenced by the difference pattern (blue trace) between calculated and experimental data. Final Rietveld fit parameter was $\chi^2 = 1.786$.

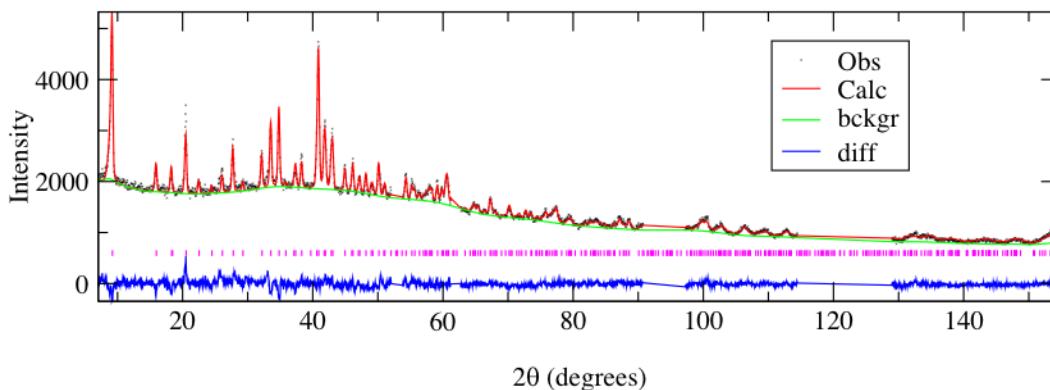


Figure 3.S9. Rietveld refinement of the experimental neutron diffraction pattern (77 K) of $\text{Co}_2(m\text{-dobdc})$ dosed with 78 bar D_2 . The calculated pattern (red trace) is in good agreement with the experimental data (hashes) as evidenced by the difference pattern (blue trace) between calculated and experimental data. Final Rietveld fit parameter was $\chi^2 = 1.648$.

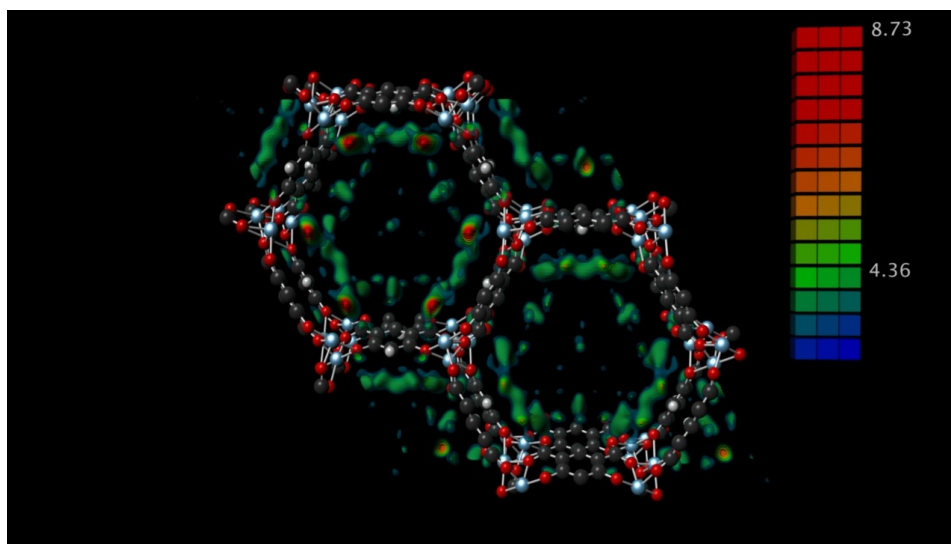


Figure 3.S10. Fourier difference map calculated for $\text{Co}_2(m\text{-dobdc})$ dosed at 79 bar D_2 at 198 K based on refinement of the bare sample reveals varying intensity in regions of missing nuclear scattering density. The intensity scale bar is in units of bound coherent scattering length (fm).

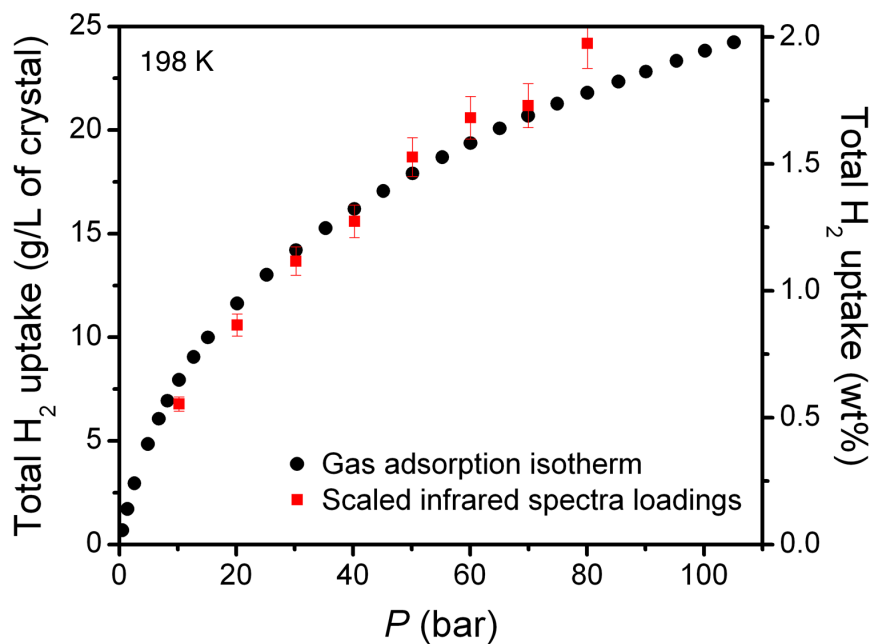


Figure 3.S11. A comparison of the 198 K H_2 adsorption isotherm in $\text{Ni}_2(m\text{-dobdc})$ with linearly scaled areas from the *in situ* infrared spectrum at 198 K (Figure 3.7).

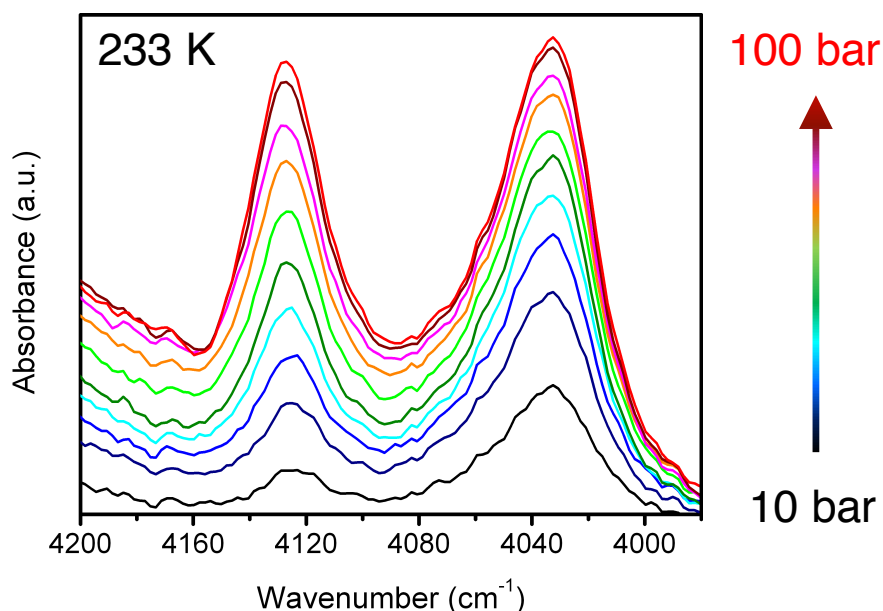


Figure 3.S12. Variable pressure *in situ* infrared spectra of Ni₂(*m*-dobdc) dosed with H₂ at 233 K. The peak on the right at ≈4030 cm⁻¹ corresponds to H₂ bound to the open metal coordination sites and the peak on the left at ≈4130 cm⁻¹ corresponds to H₂ bound to secondary binding sites.

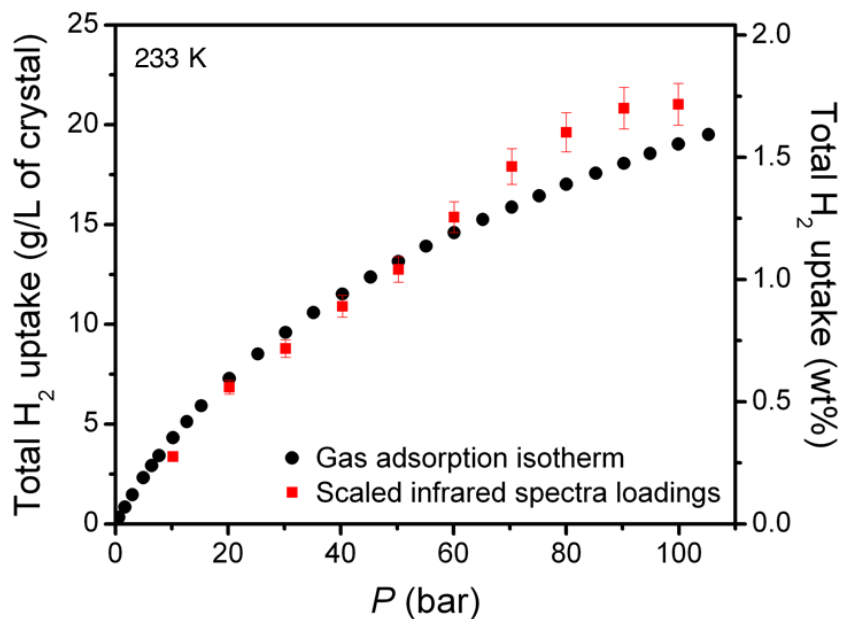


Figure 3.S13. A comparison of the 233 K H₂ adsorption isotherm in Ni₂(*m*-dobdc) with linearly scaled areas from the *in situ* infrared spectrum at 233 K.

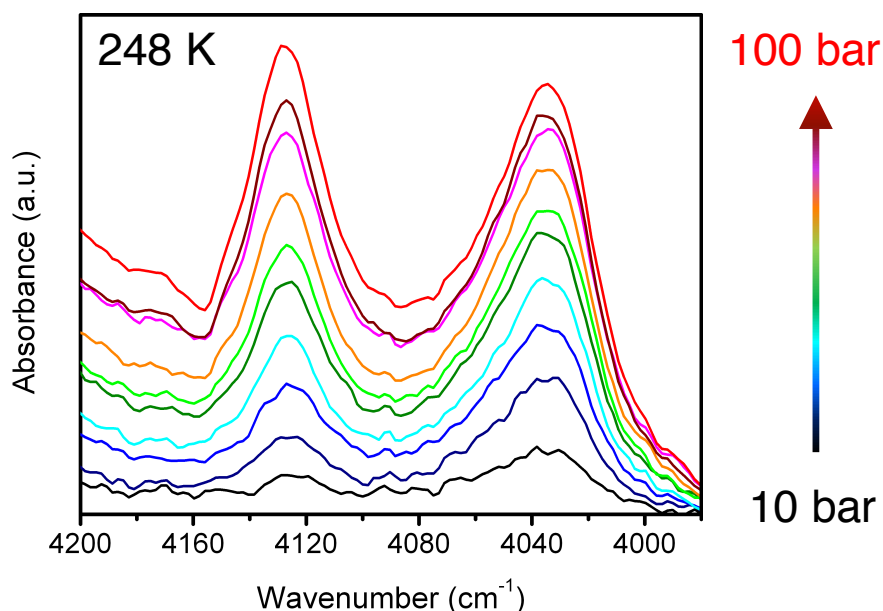


Figure 3.S14. Variable pressure *in situ* infrared spectra of $\text{Ni}_2(m\text{-dobdc})$ dosed with H_2 at 248 K. The peak on the right at $\approx 4030\text{ cm}^{-1}$ corresponds to H_2 bound to the open metal coordination sites and the peak on the left at $\approx 4130\text{ cm}^{-1}$ corresponds to H_2 bound to secondary binding sites.

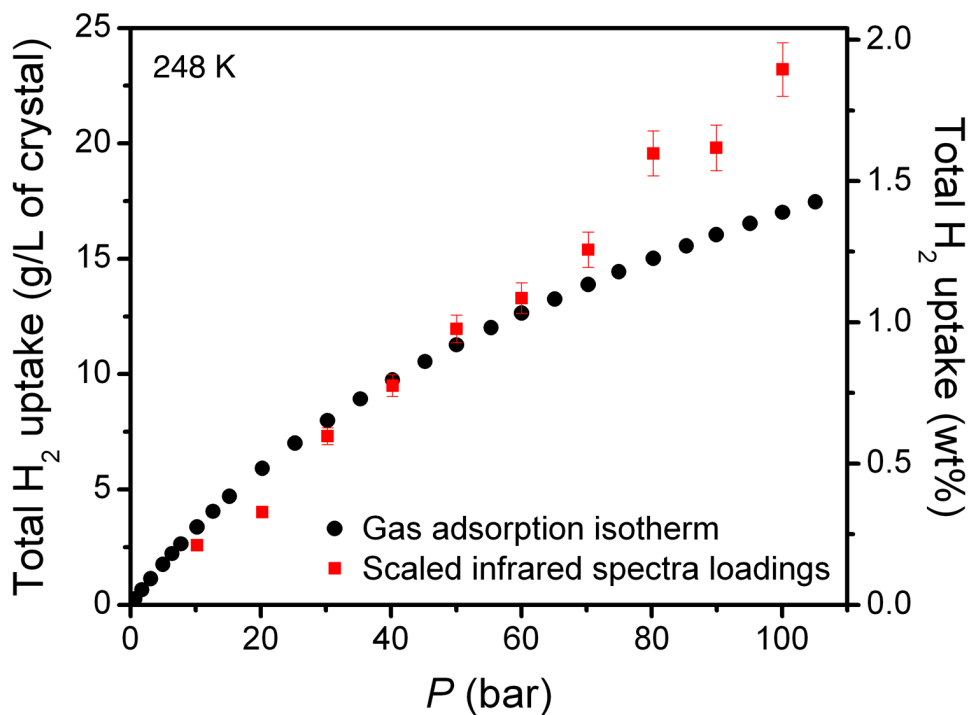


Figure 3.S15. A comparison of the 248 K H_2 adsorption isotherm in $\text{Ni}_2(m\text{-dobdc})$ with linearly scaled areas from the *in situ* infrared spectrum at 248 K.

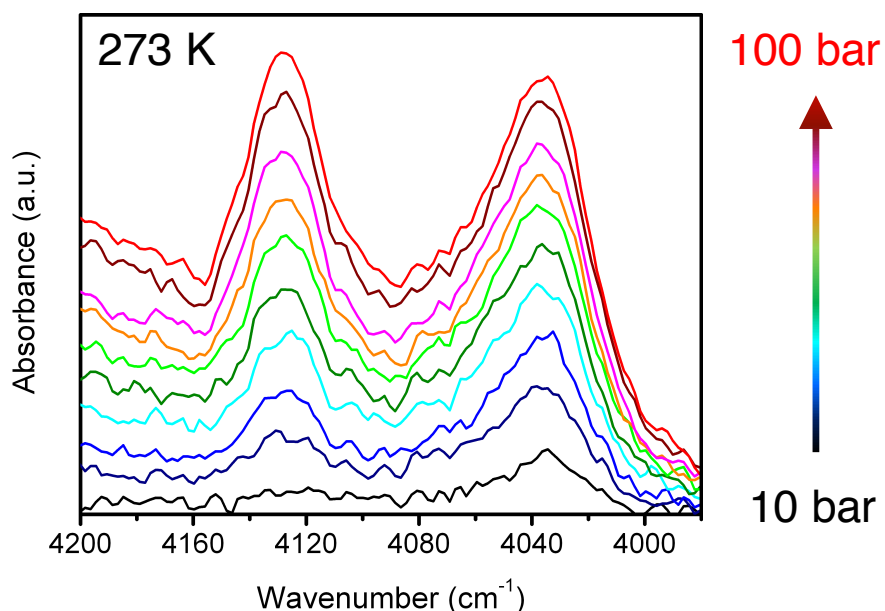


Figure 3.S16. Variable pressure *in situ* infrared spectra of $\text{Ni}_2(m\text{-dobdc})$ dosed with H_2 at 273 K. The peak on the right at $\approx 4030\text{ cm}^{-1}$ corresponds to H_2 bound to the open metal coordination sites and the peak on the left at $\approx 4130\text{ cm}^{-1}$ corresponds to H_2 bound to secondary binding sites.

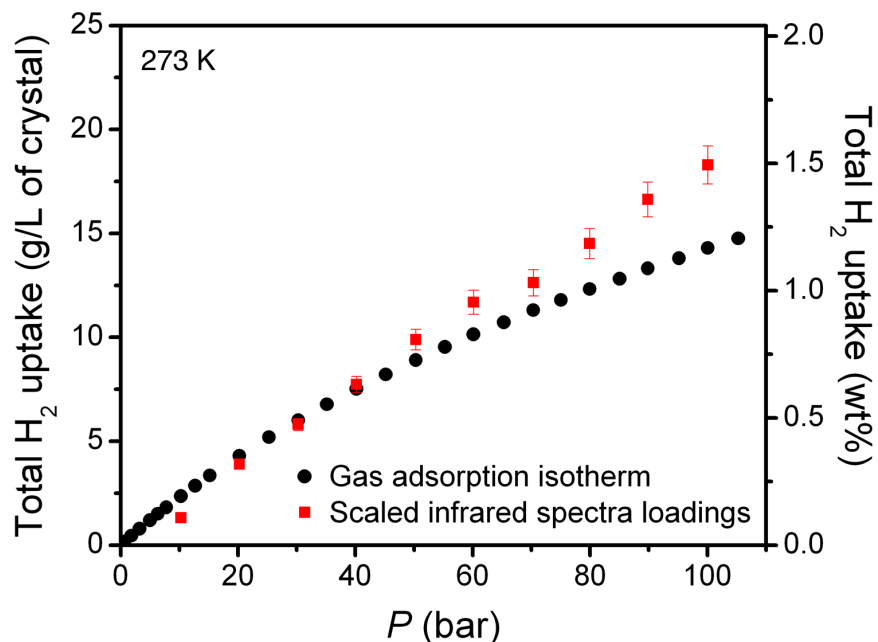


Figure 3.S17. A comparison of the 273 K H_2 adsorption isotherm in $\text{Ni}_2(m\text{-dobdc})$ with linearly scaled areas from the *in situ* infrared spectrum at 273 K.

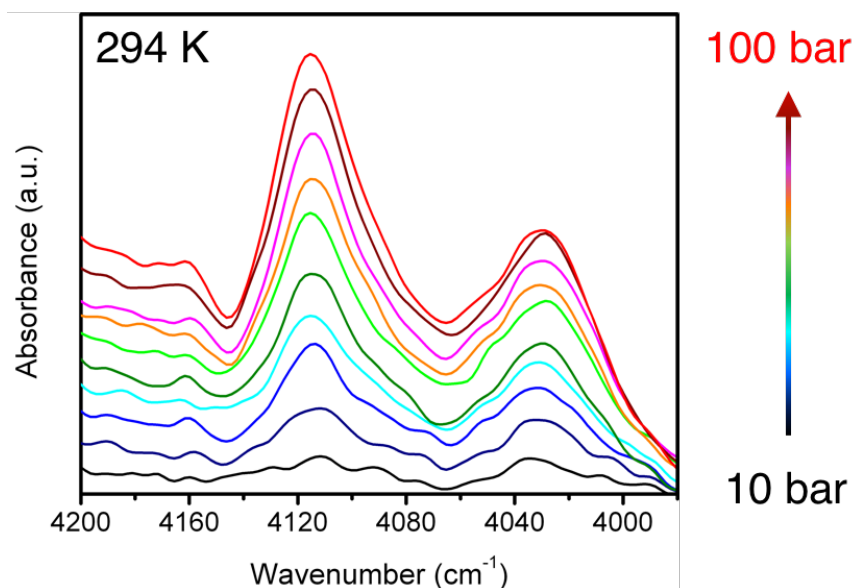


Figure 3.S18. Variable pressure *in situ* infrared spectra of $\text{Ni}_2(m\text{-dobdc})$ dosed with H_2 at 294 K. The peak on the right at $\approx 4030\text{ cm}^{-1}$ corresponds to H_2 bound to the open metal coordination sites and the peak on the left at $\approx 4110\text{ cm}^{-1}$ corresponds to H_2 bound to secondary binding sites. The large area under the secondary peaks relative to the primary peak and the peak shifts to lower energies relative to the spectra collected at all other temperatures are likely due to a contaminant at the open metal sites, perhaps water.

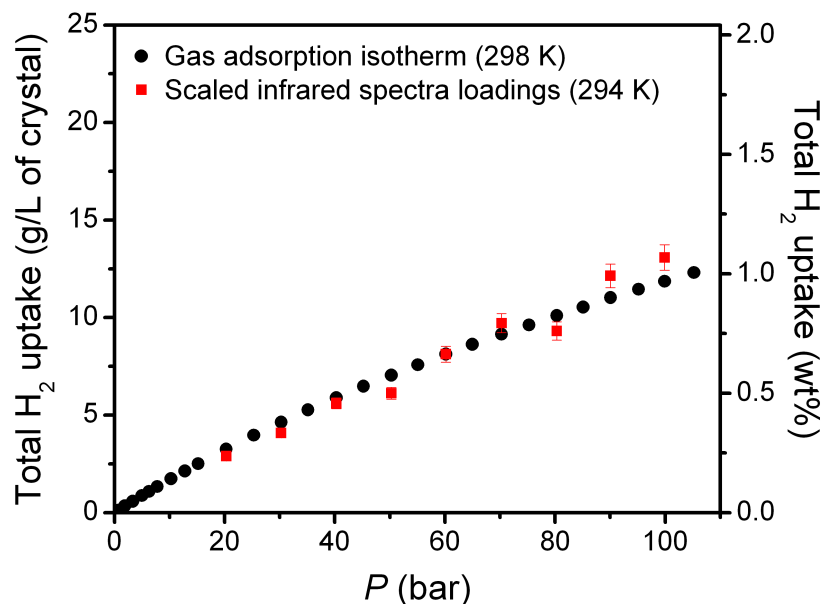


Figure 3.S19. A comparison of the 298 K H_2 adsorption isotherm in $\text{Ni}_2(m\text{-dobdc})$ with linearly scaled areas from the *in situ* infrared spectrum at 294 K.

Table 3.S6. A summary of the individual scaling factors calculated for each temperature at the comparable pressures to compare isotherm data with peak areas from infrared spectroscopy. Each scaling factor was calculated by dividing the isotherm uptake by the peak area. The average scaling factor is the single number used at each temperature to scale peak areas to their corresponding loadings for comparison with isotherms. The standard deviation (σ) for each temperature is the standard deviation of the population of individual scaling factors calculated at each pressure to ensure consistency at various pressures at a given temperature.

P (bar)	198 K	233 K	248 K	273 K	298 K
10	2.289	3.042	3.867	4.964	—
20	2.146	2.528	4.347	3.051	3.637
30	2.029	2.593	3.234	2.859	3.683
40	2.030	2.509	3.037	2.685	3.406
50	1.871	2.450	2.789	2.487	3.731
60	1.838	2.256	2.815	2.397	2.764
70	1.909	2.105	2.670	2.474	3.049
80	1.761	2.061	2.272	2.347	2.998
90	1.711	2.060	2.398	2.213	2.939
100	—	2.150	2.170	2.160	2.936
Average scaling factor	1.954	2.375	2.960	2.764	3.238
σ (Population)	0.176	0.296	0.662	0.779	0.354

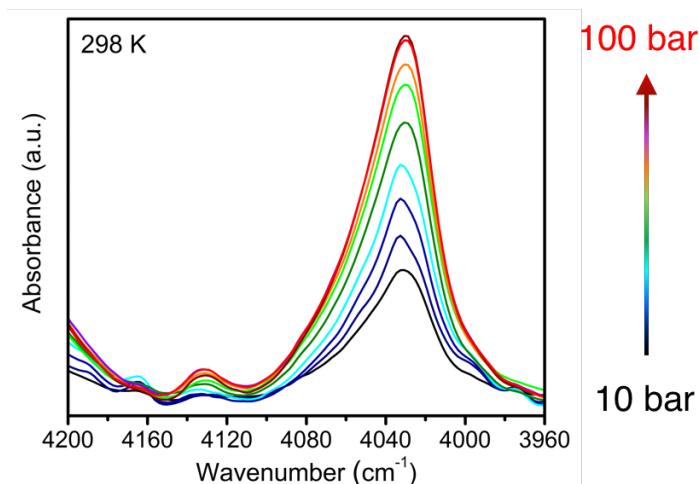


Figure 3.S20. Variable pressure *in situ* infrared spectra of $\text{Ni}_2(m\text{-dobdc})$ dosed with H_2 at 298 K at LBNL. This data was collected on a new DRIFTS instrument built at LBNL, the experimental details of which can be found below. It is notable that this spectrum shows little H_2 bound to the secondary binding sites ($\sim 4130\text{ cm}^{-1}$), indicating that the open metal coordination sites are not completely saturated at this temperature, even at 100 bar. This also confirms that the spectrum at 294 K in Figure S18 likely has water on the open coordination sites (leading to population of the secondary binding sites prior to saturation of the primary site).

Chapter 4: $M_2(m\text{-dobdc})$ ($M = \text{Mn, Fe, Co, Ni}$) Metal-Organic Frameworks as Highly Selective, High-Capacity Adsorbents for Olefin/Paraffin Separations

4.1. Introduction

Olefins, including ethylene and propylene, are high-value products obtained primarily from naphtha or ethane cracking and are ubiquitous feedstocks for the most commonly used polymers.¹ However, olefins are produced as a mixture with their saturated paraffinic counterparts. Separations of these olefin/paraffin mixtures are some of the most energy-intensive industrial processes and are currently dominated by cryogenic distillation technologies.^{1,2} The U.S. alone consumes over 120 TBtu/yr in carrying out olefin/paraffin separations.^{3,4} Non-thermally driven processes, such as adsorption, can dramatically reduce the cost and energy required to purify olefins.⁵ However, replacing distillation requires adsorbents with adequate performance characteristics, including selectivity, capacity, kinetics, and cost. While there have been significant research efforts directed towards designing materials with the requisite olefin/paraffin separation properties, usually operating via size-selective,^{6,7,8,9,10} chemisorptive,^{11,12,13,14,15,16,17} or physisorptive^{18,19,20,21,22} mechanisms, better performing materials are still needed.

Metal-organic frameworks are a class of porous crystalline materials with a high degree of structural tunability that have been demonstrated to be capable of facilitating gas separations through each of these three mechanisms.^{23,24,25,26} Due to the small and similar kinetic diameters of light olefins and paraffins, size-selective adsorbents typically display moderate selectivities alongside a very low working capacity and slow kinetics. These characteristics arise from the narrow pore sizes necessary to discriminate between small molecules. For example, NbOFFIVE-Ni, a metal-organic framework in which Ni^{2+} -pyrazine square grids are pillared by $[\text{NbOF}_5]^{2-}$ units to form 4.752(1) Å channels that accommodate propylene but reject propane, displays near perfect propylene/propane selectivity but is impaired by a very low (0.6 mmol/g) working capacity.¹⁰ Chemisorptive mechanisms, such as π -complexation with Ag(I) or Cu(I), appear promising due to the high binding enthalpy for olefins.²⁷ However, these high selectivities arise from metal-olefin interactions that are typically greater than 100 kJ/mol in strength, leading to irreversible binding under typical temperature swing or pressure swing adsorption conditions. By exchanging Ag(I) into the porous aromatic framework PAF-1- SO_3H ,²⁸ Li and coworkers showed high ethylene/ethane selectivity using the 106 kJ/mol binding affinity between the olefin and Ag(I); however, they could not demonstrate reversibility under process conditions.¹² Finally, adsorbents that display separation properties based on physisorptive mechanisms typically have faster cycling kinetics and better working capacities due to larger pore sizes and weaker binding affinities. However, due to the difficulty in discriminating between olefins and paraffins, adsorbents have not yet displayed sufficient selectivity to produce polymer grade (99.9% purity) olefins.²⁹

The metal-organic frameworks $M_2(p\text{-dobdc})$ ($M\text{-MOF-74}$; CPO-27- M ; $M = \text{Mg, Mn, Fe, Co, Ni, Zn}$; $p\text{-dobdc}^{4-} = 2,5\text{-dioxido-1,4-benzenedicarboxylate}$),^{30,31,32} which feature ~12 Å-wide hexagonal channels lined with a high concentration of exposed divalent cations, use coordinatively unsaturated M^{2+} sites to polarize and adsorb olefins preferentially over paraffins.^{18,19,33} Among these materials, $\text{Fe}_2(p\text{-dobdc})$ shows an ethylene/ethane selectivity of ~14 at 45 °C with an ethylene capacity of greater than 7 mmol/g, and $\text{Mn}_2(p\text{-dobdc})$ shows a

propylene/propane selectivity of ~ 16 with a propylene capacity of greater than 7.5 mmol/g. While these frameworks show reversible olefin adsorption with olefin capacities that are more than an order of magnitude higher than in size-selective adsorbents, improvements in selectivity are desired in order to boost olefin purity in the product stream. Such increases in selectivity would translate to olefin purities sufficient for downstream processes, such as polymerization.

We hypothesized that higher selectivities could be achieved in these physisorptive materials by altering the affinity of the metal site for adsorbed hydrocarbons. By employing a *meta*-substituted $H_4(m\text{-dobdc})$ ligand, a structural isomer $M_2(m\text{-dobdc})$ ($M = \text{Mg, Mn, Fe, Co, Ni}$; $m\text{-dobdc}^{4-} = 4,6\text{-dioxido-1,3-benzenedicarboxylate}$) can be formed. This metal–organic framework has been shown to have increased charge density at the metal sites, leading to enhanced H_2 binding enthalpies and greater H_2 storage capacities.³⁴ Further, this metal–organic framework is produced from low-cost raw materials, as its linker is derived from a reaction of CO_2 with the commodity chemical resorcinol, lending itself to large-scale industrial applications.³⁵ The present study aims to evaluate a series of $M_2(m\text{-dobdc})$ metal–organic frameworks for utility in olefin/paraffin separations using single-component equilibrium gas adsorption, multicomponent equilibrium gas adsorption, adsorption kinetics, transient breakthrough measurements, and *in-situ* single-crystal X-ray diffraction experiments. From this, we have found that the $M_2(m\text{-dobdc})$ frameworks exhibit superior performance to their *para*-functionalized counterparts ($M_2(p\text{-dobdc})$) and the highest selectivity values among materials that utilize a fast, reversible, physisorptive mechanism. Most notably, $Fe_2(m\text{-dobdc})$ shows an ethylene/ethane selectivity of ~ 25 and a propylene/propane selectivity of ~ 55 under relevant conditions, demonstrating that control over the electronic properties of the open metal sites can lead to improved performance. This is a generalizable concept, in that tuning the electronic environment around a given adsorption site in a given structure can greatly affect adsorption and separation properties. The combined features of these adsorbents including selectivity, capacity, kinetics, and cost, make the $M_2(m\text{-dobdc})$ compounds promising adsorbents for industrial olefin/paraffin separations, and these materials have the potential to offset significant energy consumption relative to the decades-old distillation technology that is employed today.

4.2. Experimental

4.2.1. Synthesis of $M_2(m\text{-dobdc})$ ($M = \text{Mn, Fe, Co, Ni}$). The $M_2(m\text{-dobdc})$ materials were synthesized according to modified versions of the large-scale literature procedures.³⁴ $MnCl_2$, $FeCl_2$, $CoCl_2$, and $NiCl_2$ were purchased from Sigma-Aldrich and used as received. Methanol was purchased from EMD Millipore Corporation as DriSolv grade, dried over 3 Å sieves, and sparged with Ar prior to use. Dimethylformamide (DMF) was purchased from EMD Millipore Corporation as OmniSolv grade, sparged with Ar, and dried with an alumina column prior to use.

4.2.1.1. $Co_2(m\text{-dobdc})$ and $Ni_2(m\text{-dobdc})$. A mixture of 310 mL of methanol and 310 mL of DMF was added to a 1-L three-neck round-bottom flask equipped with a reflux condenser and purged with N_2 while stirring for 1 h. The ligand $H_4(m\text{-dobdc})$ (2.00 g, 10.1 mmol) and $CoCl_2$ (3.27 g, 25.2 mmol) or $NiCl_2$ (3.27 g, 25.2 mmol) were added to the solvent under N_2 pressure and the reaction mixture was heated at 120 °C for 18 h while stirring vigorously. The mixture was cooled to ambient temperature and then filtered, yielding a microcrystalline powder. The resulting powder was collected by filtration, rinsed with DMF, and soaked in 20 mL of DMF at 120 °C for 24 h. The powder was collected by filtration, rinsed with methanol, and soaked in 20

mL of methanol at 60 °C for 12 h. The supernatant solution was decanted, and 10 mL of fresh methanol was added. This procedure was repeated four times, such that the total time washing with methanol was 2 days. This resulted in a ~54% yield Co₂(*m-dobdc*) and Ni₂(*m-dobdc*). The resulting powder was collected by filtration and heated at 180 °C under dynamic vacuum (< 0.01 mbar) for 24 h. The resulting activated powders were purple and brown for Co₂(*m-dobdc*) and Ni₂(*m-dobdc*), respectively.

4.2.1.2. Mn₂(*m-dobdc*) and Fe₂(*m-dobdc*). All manipulations involving the preparation and handling of Mn₂(*m-dobdc*) and Fe₂(*m-dobdc*) were performed under an N₂ atmosphere in a VAC Atmospheres glovebox or using standard Schlenk techniques. A solution of MCl₂ (2.5 equiv, 3.0 mmol) in 12 mL of methanol was added to a 200-mL Schlenk flask charged with a magnetic stir bar and a solution of H₄(*m-dobdc*) (240 mg, 1.0 equiv, 1.2 mmol) in 68 mL of DMF. The solution was stirred at 120 °C for 18 h. The resulting powder was collected by filtration, rinsed with DMF, and soaked in 20 mL of DMF at 120 °C for 24 h. The powder was collected by filtration, rinsed with methanol, and soaked in 20 mL of methanol at 60 °C for 12 h. The supernatant solution was decanted, and 10 mL of fresh methanol was added. This process was repeated four times, such that the total time washing with methanol was 2 days. This resulted in a ~75% yield for Mn₂(*m-dobdc*) and a ~85% yield for Fe₂(*m-dobdc*). The resulting powder was collected by filtration, and heated at 180 °C under dynamic vacuum (< 0.01 mbar) for 24 h. The resulting activated powders were light purple and light pink for Fe₂(*m-dobdc*) and Mn₂(*m-dobdc*), respectively.

4.2.2. Single-Component Gas Adsorption Measurements. Single-component gas adsorption experiments in the pressure range of 0-1.1 bar were conducted on a Micromeritics 3Flex instrument, which uses a volumetric method to determine the amount adsorbed under an equilibrated gas pressure. Activated samples were transferred under a dry N₂ atmosphere into pre-weighed sample tubes, and then capped with a Micromeritics TranSeal. Samples were then evacuated at 180 °C under a dynamic vacuum of < 10⁻⁵ bar, until the off-gas rate was less than 10⁻⁷ bar/s. The mass of the activated sample was then recorded, typically in the range of 50-150 mg. Prior to collecting each adsorption isotherm, the free-space of the sample was measured using UHP (99.999%) He. Gas adsorption isotherms of ethylene, ethane, propylene, and propane were measured at 25, 35, and 45 °C using a water bath to maintain a constant temperature. Samples were reactivated in between each isotherm measurement by heating at 180 °C under dynamic vacuum for 2 h. Oil-free vacuum pumps and oil-free pressure regulators were used for all measurements.

4.2.3. Isotherm Fitting, Ideal Adsorbed Solution Theory, and Differential Enthalpies. The single-component gas adsorption isotherms were fit using a dual-site Langmuir–Freundlich equation, given by

$$n = \frac{q_{\text{sat},a} b_a P^{\nu_a}}{1 + b_a P^{\nu_a}} + \frac{q_{\text{sat},b} b_b P^{\nu_b}}{1 + b_b P^{\nu_b}} \quad (1)$$

where n is the amount adsorbed in mmol/g, q_{sat} is the amount adsorbed when saturated with the gas in mmol/g, b is the Langmuir parameter in bar⁻¹, P is the gas pressure in bar, ν is the dimensionless Freundlich parameter, and subscripts a and b correspond to two different site identities. These parameters were determined using a least-squares method, and are given in

Supplementary Tables 1-4. Ideal Adsorbed Solution Theory (IAST) was used to determine adsorbent selectivities from single-component gas adsorption isotherms.^{36,37,38} This involves numerically solving for the spreading pressure and subsequently determining the composition of the adsorbed phase at a given gas phase composition. The selectivity is then given by

$$S = \frac{x_{\text{olefin}}/x_{\text{paraffin}}}{y_{\text{olefin}}/y_{\text{paraffin}}} \quad (2)$$

where S is the IAST selectivity, x is mole fraction in the adsorbed phase, and y is the mole fraction in the gas phase. Finally, the differential enthalpy was extracted from the temperature dependence of the isotherms using the Clausius–Clapeyron relationship.³⁹ The adsorption isotherm fits were numerically inverted and solved as $P(n)$. The differential enthalpy, h , can then be determined at a constant loading by

$$h = -R \frac{d(\ln P)}{d(1/T)} \quad (2)$$

where R is the ideal gas constant, P is the pressure at a given loading, and T is the temperature (298.15, 308.15, or 318.15 K) at which the isotherm data were collected.

4.2.4. Breakthrough Measurements. Breakthrough experiments were performed using a custom-built breakthrough apparatus, composed of primarily 1/8" copper tubing fitted with Swagelok fittings and valves to control the flow of the gas to either flow through the sample holder or bypass the sample holder and flow directly to a gas chromatograph used to monitor outflow composition. A premixed 1:1 ethane:ethylene or 1:1 propane:propylene cylinder was attached to the breakthrough manifold via an MRS mass flow controller to control gas flow from the cylinder. A helium (99.999%) cylinder used to dilute the hydrocarbon mixture was also attached to the manifold and controlled by an MRS mass flow controller. A coil of tubing was placed after the mass flow controllers to ensure mixing of the gases. The $\text{Co}_2(m\text{-dobdc})$ sample was pelletized and broken into pieces using a 20-40 mesh sieve. Then, 0.575 g of the sample was loaded into one vertical component (13.335 cm, inner diameter of 0.4572 cm) of a U-shaped sample holder comprised of 1/4" tubing and fitted with Swagelok VCR fittings with fritted (0.5 μm) gaskets to prevent the sample from moving. The U-shaped tubing was immersed in a sand-filled heating mantle and connected to the breakthrough manifold. The $\text{Co}_2(m\text{-dobdc})$ sample was activated in the sample holder by heating it in the sand bath at 180 °C under flowing He. The sample was then cooled to 45 °C for the breakthrough experiments. A total flow rate of 30 mL/min was employed, with each hydrocarbon mixture set to 2 mL/min and the He set to 28 mL/min. The uncertainty in the flow rate of the olefin/paraffin mixture is about 0.5 mL/min. The mixture was tested without flowing to the packed $\text{Co}_2(m\text{-dobdc})$ bed to ensure proper composition and separation using the GC monitoring the outflow. The mixture was then flowed through the packed bed of $\text{Co}_2(m\text{-dobdc})$ and the outflow was recorded by GC every 2.0 min for the ethane/ethylene mixture and every 3.5 min for the propane/propylene mixture. The outflow composition was analyzed by gas chromatography using an SRI Instruments 8610V GC equipped with a 6' HayeSep D column, which was kept at 90 °C. After both components for an experiment had broken through the packed $\text{Co}_2(m\text{-dobdc})$ bed, the flow was switched to He to

fully desorb both hydrocarbon components from the column. The data were recorded and analyzed using PeakSimple software.

4.2.5. Single-Crystal X-ray Diffraction Experiments. *In situ* X-ray diffraction measurements for both $\text{Co}_2(m\text{-dobdc})$ and $\text{Co}_2(p\text{-dobdc})$ were performed on single crystals in ethylene-dosed capillaries, which were prepared according to a previously reported procedure.⁴⁰ Briefly, a methanol-solvated crystal of either $\text{Co}_2(m\text{-dobdc})$ or $\text{Co}_2(p\text{-dobdc})$ was mounted onto a borosilicate glass fiber using a minimal amount of epoxy, ensuring accessibility of the crystal pores. The glass fiber was then inserted into a 1.0 mm borosilicate glass capillary, which was connected to a capillary-dosing assembly attached to a port on a Micromeritics 3Flex instrument. The sample was evacuated under reduced pressure at 180 °C for 24 h to remove all solvent from the crystal. The capillary was dosed with 300 mbar of ethylene, and then flame-sealed with a methane/oxygen torch.

X-ray diffraction data for all samples were collected at Beamline 11.3.1 at the Advanced Light Source at Lawrence Berkeley National Laboratory using synchrotron radiation ($\lambda = 0.8856$ Å for $\text{Co}_2(m\text{-dobdc})\cdot 2.0\text{C}_2\text{H}_4$ and $\lambda = 0.6888$ Å for $\text{Co}_2(p\text{-dobdc})\cdot 1.9\text{C}_2\text{H}_4$) and a Bruker PHOTON100 CMOS detector mounted on a D8 diffractometer. The samples were cooled to a 100 K using an Oxford Cryosystems cryostream for data collection. For $\text{Co}_2(p\text{-dobdc})\cdot 1.9\text{C}_2\text{H}_4$, the crystal was found to be an obverse/reverse twin based on analysis of the diffraction patterns, and CELL_NOW⁴¹ was used to determine the orientation matrices. Raw data for each structure (using both twin matrices for $\text{Co}_2(p\text{-dobdc})\cdot 1.9\text{C}_2\text{H}_4$) were integrated and corrected for Lorentz and polarization effects using the Bruker AXS SAINT⁴² software and corrected for absorption using SADABS for $\text{Co}_2(m\text{-dobdc})\cdot 2.0\text{C}_2\text{H}_4$ and TWINABS for $\text{Co}_2(p\text{-dobdc})\cdot 1.9\text{C}_2\text{H}_4$.⁴³ For $\text{Co}_2(p\text{-dobdc})\cdot 1.9\text{C}_2\text{H}_4$, TWINABS was used to produce a merged HKLF4 file for structure solution and initial refinement and an HKLF5 file for final structure refinement.

Structures were solved using either direct methods with SHELXS^{44,45} (for $\text{Co}_2(p\text{-dobdc})\cdot 1.9\text{C}_2\text{H}_4$) or intrinsic phasing methods for $\text{Co}_2(m\text{-dobdc})\cdot 2.0\text{C}_2\text{H}_4$ with SHELXT⁴⁶ and refined using SHELXL^{44,47} operated in the OLEX2 interface.⁴⁸ Thermal parameters were refined anisotropically for all non-hydrogen atoms. Disorder and thermal motion of the bound gas molecules required the use of displacement parameter and distance restraints. All framework H atoms were refined using the riding model. Hydrogen atoms on the coordinated ethylene molecules in $\text{Co}_2(m\text{-dobdc})\cdot 2.0\text{C}_2\text{H}_4$ could not be located in the electron density difference map and were omitted from the refinement, but not the formula. Hydrogen atoms on the coordinated ethylene molecules in $\text{Co}_2(p\text{-dobdc})\cdot 1.9\text{C}_2\text{H}_4$ were located in the electron density difference map, constrained to be coplanar with the ethylene carbon atoms, and restrained to have C–H distances based on those of free ethylene.

4.3. Results and Discussion

4.3.1. Structural Characterization of Ethylene-Dosed $\text{Co}_2(m\text{-dobdc})$ and $\text{Co}_2(p\text{-dobdc})$. *In-situ* single-crystal X-ray diffraction was employed as an initial means of comparing ethylene binding in the isomeric $\text{Co}_2(m\text{-dobdc})$ and $\text{Co}_2(p\text{-dobdc})$ frameworks. This technique requires large single crystals that can be manipulated and mounted, which restricts the method to the characterization of $\text{Co}_2(m\text{-dobdc})$ and $\text{Co}_2(p\text{-dobdc})$, the most crystalline of the $\text{M}_2(\text{dobdc})$ materials investigated here. However, relative differences between the two structures are expected to be similar in other variants. The structures of $\text{Co}_2(m\text{-dobdc})$ and $\text{Co}_2(p\text{-dobdc})$ under

~0.3 bar of ethylene at 100 K (Figure 4.1) confirm that ethylene primarily binds through a side-on interaction with the cobalt(II) sites in both materials. Unlike molecular Co–C₂H₄ complexes reported in the Cambridge Crystal Structure Database,⁴⁹ which feature low-spin cobalt(II) centers and Co–C distances in the range 1.965–2.087 Å, much longer Co···C distances are apparent in Co₂(*m*-dobdc)·2.0C₂H₄ (2.643(18) and 2.687(16) Å) and Co₂(*p*-dobdc)·1.9C₂H₄ (2.667(7) and 2.743(8) Å). These long distances indicate that the cobalt sites in both frameworks bind ethylene through much weaker reversible interactions compared to typical transition metal alkene complexes. Similar weak interactions have been reported for ethylene and propylene in Co₂(*p*-dobdc)¹⁹ and Fe₂(*p*-dobdc),¹⁸ and have been attributed to limited π backbonding from the high-spin metal(II) centers in these frameworks.

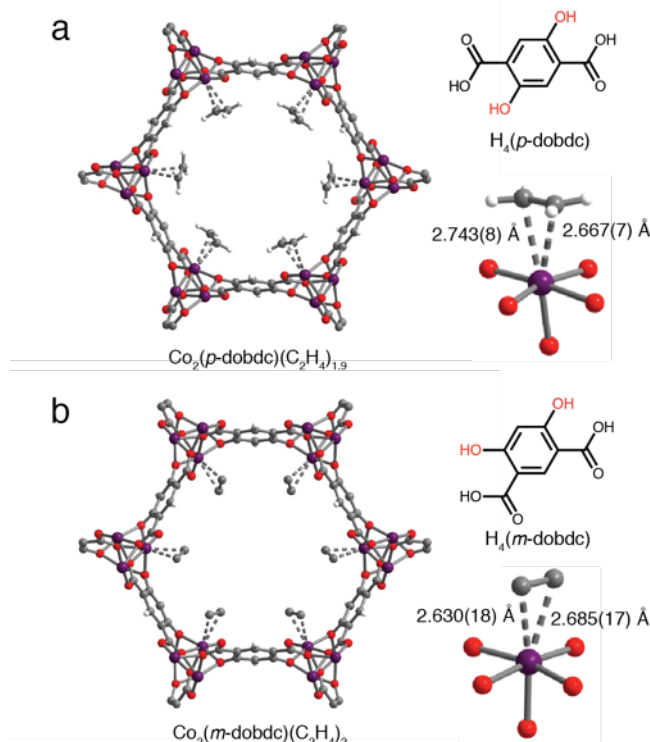


Figure 4.1. Comparison of the ligand structure, framework structures, and ethylene binding geometries for (a) Co₂(*p*-dobdc) and (b) Co₂(*m*-dobdc) under ~0.3 bar of ethylene at 100 K as determined from *in-situ* single-crystal X-ray diffraction experiments. Purple, red, gray, and white spheres represent Co, O, C, and H atoms, respectively.

The shorter Co···C distances in Co₂(*m*-dobdc)·2.0C₂H₄ compared to Co₂(*p*-dobdc)·1.9C₂H₄ likely result from stronger ethylene binding induced by the increased charge density at the cobalt(II) site in Co₂(*m*-dobdc). A similar effect was also observed for H₂ binding to Ni₂(*m*-dobdc), in structures obtained from *in-situ* neutron powder X-ray diffraction experiments, and this was attributed to a higher charge density at the metal site in the *meta*-substituted variant using density functional theory.³⁴ The stronger Co–C₂H₄ interactions inferred from shorter Co···C

distances in $\text{Co}_2(m\text{-dobdc}) \cdot 2.0\text{C}_2\text{H}_4$ are more generally expected to correspond to an increased olefin/paraffin selectivity in the $\text{M}_2(m\text{-dobdc})$ frameworks compared to the $\text{M}_2(p\text{-dobdc})$ isomers, as discussed below.

4.3.2. Gas Adsorption and Olefin/Paraffin Selectivity in $\text{M}_2(m\text{-dobdc})$ Frameworks. In rigid frameworks with well-defined gas adsorption sites, single-component gas adsorption isotherms reveal a wide range of information about the thermodynamics of gas molecules interacting within the system. Single-component ethylene, ethane, propylene, and propane isotherms were therefore measured at 25, 35, and 45 °C in $\text{M}_2(m\text{-dobdc})$ ($\text{M} = \text{Mn}, \text{Fe}, \text{Co}, \text{Ni}$) (Figures 4.2a and 4.2b). These isotherms display steep adsorption behavior at low pressures, corresponding to strong interactions with the frameworks. Among the four gases, propylene adsorbs the strongest, followed by ethylene, then propane, and lastly ethane for each variant. This qualitative comparison suggests that all of these materials selectively adsorb olefins over paraffins. Further, the high densities of coordinatively-unsaturated metal centers in these materials afford olefin saturation capacities in excess of 7 mmol/g. Note that the adsorption of one molecule per metal corresponds to a loading of 6.6, 6.5, 6.4 and 6.4 mmol/g for $\text{M} = \text{Mn}, \text{Fe}, \text{Co},$ and Ni , respectively.

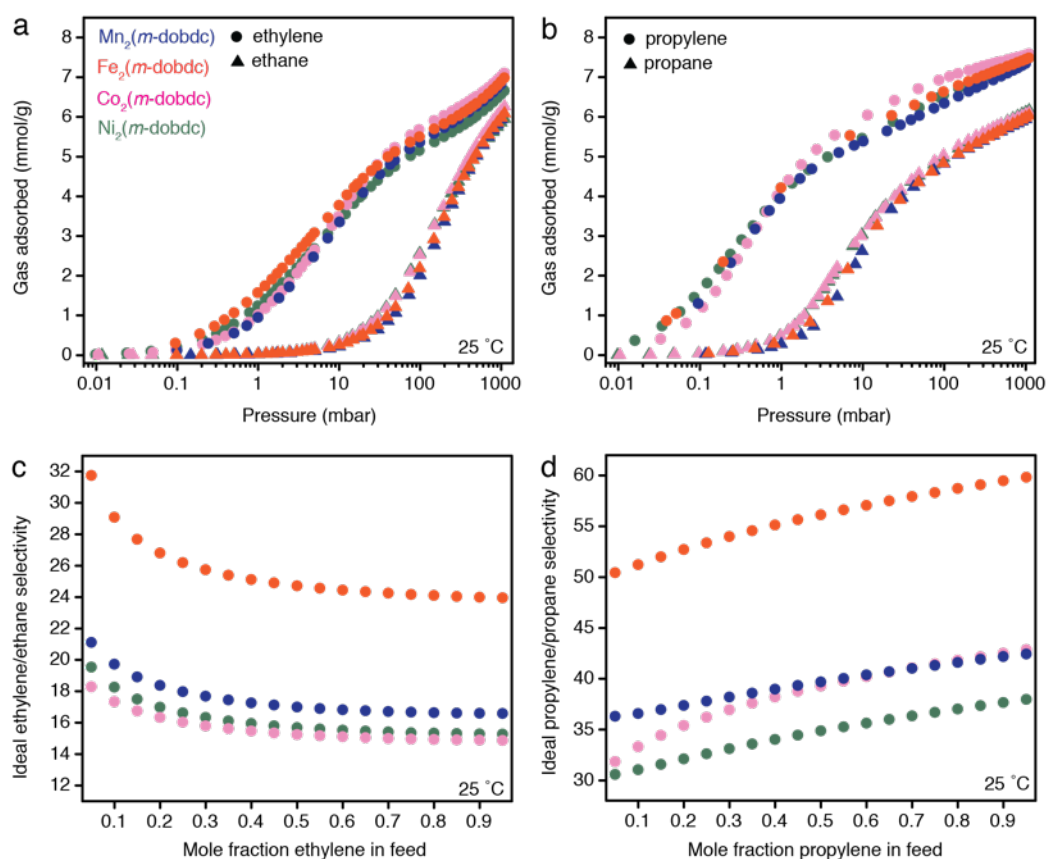


Figure 4.2. Single-component gas adsorption isotherms of (a) ethylene/ethane and (b) propylene/propane and their corresponding olefin/paraffin IAST selectivity for (c) ethylene/ethane and (d) propylene/propane at 25 °C in $\text{M}_2(m\text{-dobdc})$ ($\text{M} = \text{Mn}, \text{Fe}, \text{Co}, \text{Ni}$).

Single-component isotherms can be used to understand the expected equilibrium properties of multicomponent systems by applying IAST to predict the composition of the adsorbed phase in the presence of a gas mixture.³⁶ The IAST model is expected to work accurately for this system, given the relatively rigid nature of the framework and the absence of significant interactions between adsorbates bound to the metal sites at low gas loadings. The IAST selectivities were obtained from single-component dual-site Langmuir–Freundlich fits (Figures 4.2c and 4.2d). As this method extrapolates the isotherm of the less strongly bound gas (in this case ethane and propane), obtaining realistic results depends on restricting the saturation capacity for these isotherms to reasonable values (Tables 4.S1–4.S4). Otherwise, non-physical trends in the IAST selectivities can arise and severe overestimations of the values can result.⁹

After taking these procedures into consideration, we observe an ethylene/ethane IAST selectivity in $\text{Fe}_2(m\text{-dobdc})$ of over 25 under equimolar feed conditions at a total pressure of 1 bar and 25 °C, making it the most selective physisorptive material for the separation. This selectivity corresponds to a composition in the adsorbed phase of 96% ethylene in equilibrium with an equimolar gas phase. Within only two equilibrium stages, in which the ethylene adsorbed from an equimolar mixture at equilibrium is then desorbed and subsequently equilibrated with the adsorbent a second time, an ethylene purity of greater than 99.9% can be achieved. This is the minimum purity required for a polymerization feed, and can usually only be achieved through cryogenic methods.²⁹ Additionally, this separation is accomplished at near ambient temperatures, with further improvements in selectivity expected at reduced temperatures. Propylene/propane selectivity in $\text{Fe}_2(m\text{-dobdc})$ is greater than 55 under the same conditions, corresponding to 98% of the adsorbed phase composed of propylene in the first equilibrium stage. Variants including Mn, Co, and Ni also display high adsorption selectivities of greater than 15 for ethylene/ethane and greater than 30 for propylene/propane.

To verify the applicability of IAST in predicting behavior under real mixtures, multicomponent equilibrium adsorption measurements were conducted (Figure 4.S3). By dosing an ethylene/ethane mixture of known composition, determining the total amount of gas adsorbed at equilibrium, and measuring the equilibrium composition of the gas phase after adsorption using a mass spectrometer, the composition of the adsorbed phase can be determined. Indeed, samples of $\text{M}_2(m\text{-dobdc})$ ($\text{M} = \text{Fe}, \text{Co}, \text{Ni}$), when dosed with an equimolar mixture of ethylene and ethane, revealed significant enrichment of ethylene in the adsorbed phase. Additionally, equimolar ethylene/ethane breakthrough on $\text{Mn}_2(m\text{-dobdc})$ reveal its applicability under real gas conditions. Ethylene/ethane selectivities as determined from this method corroborate those calculated from IAST, with measured values of 25 ± 3 compared with 26, 14 ± 2 compared with 16, and 18 ± 2 compared with 16 for $\text{Fe}_2(m\text{-dobdc})$, $\text{Co}_2(m\text{-dobdc})$, and $\text{Ni}_2(m\text{-dobdc})$, respectively. This is not surprising, as the assumptions that are required for IAST to hold (the thermodynamic state of the adsorbent does not change upon gas adsorption, and adsorbate-adsorbate interactions are minimal, given they are isolated at discrete metal sites) are fulfilled in this system.

The IAST selectivities calculated at 45 °C for the $\text{M}_2(m\text{-dobdc})$ frameworks are significantly higher than for the corresponding $\text{M}_2(p\text{-dobdc})$ isomers (Figure 4.3). In the case of ethylene/ethane, the most selective in the *para* series, $\text{Fe}_2(p\text{-dobdc})$, shows similar selectivity to $\text{Ni}_2(m\text{-dobdc})$, the least selective of the *meta* series. Additionally, $\text{Ni}_2(m\text{-dobdc})$ and $\text{Co}_2(m\text{-dobdc})$ have more than double the selectivity of their *para*-substituted counterparts. These changes are even more pronounced for a propylene/propane separation. All variants in the $\text{M}_2(m\text{-dobdc})$ series are significantly more selective than in the $\text{M}_2(p\text{-dobdc})$ series, and $\text{Fe}_2(m\text{-dobdc})$

has nearly triple the selectivity of $\text{Fe}_2(p\text{-dobdc})$. Moreover, temperature-dependent IAST calculations predict more dramatic differences in selectivity at lower temperatures, under which differences in adsorption enthalpy play a larger role in determining adsorption equilibria.

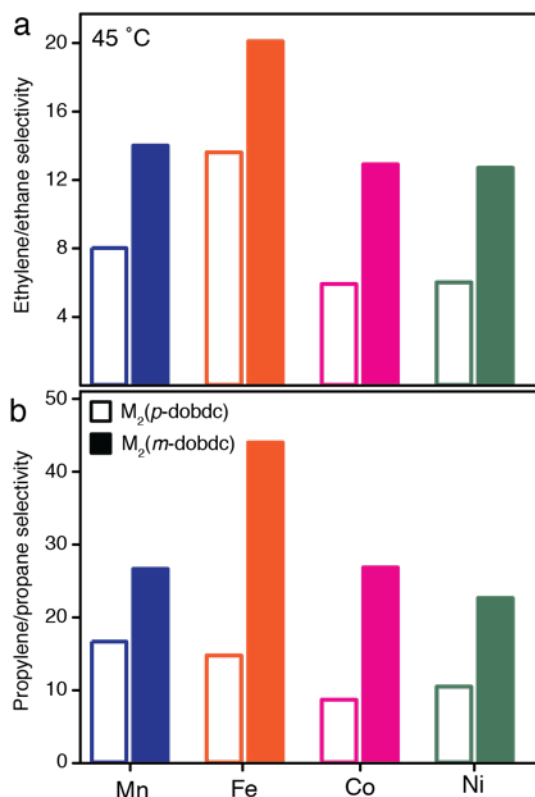


Figure 4.3. Comparison of the IAST selectivity under an equimolar feed at 45 °C between $M_2(p\text{-dobdc})$ and $M_2(m\text{-dobdc})$ ($M = \text{Mn}, \text{Fe}, \text{Co}, \text{Ni}$) for (a) ethylene/ethane and (b) propylene/propane separations.

As the increased charge density at the metal site changes the relative adsorption enthalpies, it was not surprising to see improvements in olefin/paraffin adsorption selectivity; however, the magnitude of these changes was unexpected. Using the single-component isotherm fits and the Clausius–Clapeyron relationship, differential enthalpies of ethylene, ethane, propylene, and propane were determined as a function of loading (Figure 4.4). For ethylene and propylene, initial adsorption enthalpies below ~1 mmol/g correspond to interactions between the gas and the metal site. The decrease in differential enthalpy for these species corresponds to saturation of the metal sites, and the enthalpies beyond this point result from subsequent binding sites. For ethane and propane, the initial adsorption at low loading also corresponds to interactions with the metal sites. However, increases in enthalpy are observed upon metal site saturation, due to more pronounced adsorbate–adsorbate interactions as the pore begins to fill with gas molecules.⁵⁰ This analysis reveals $\text{Fe}_2(m\text{-dobdc})$ to have the largest ethylene and propylene adsorption enthalpy relative to the other metal variants. At a loading of 1 mmol/g, where the differential enthalpies

primarily arise from the interaction between the adsorbate and the metal site, $\text{Fe}_2(m\text{-dobdc})$ shows ethylene adsorption of about -52 ± 0.1 kJ/mol and propylene adsorption of -65 ± 0.5 kJ/mol.

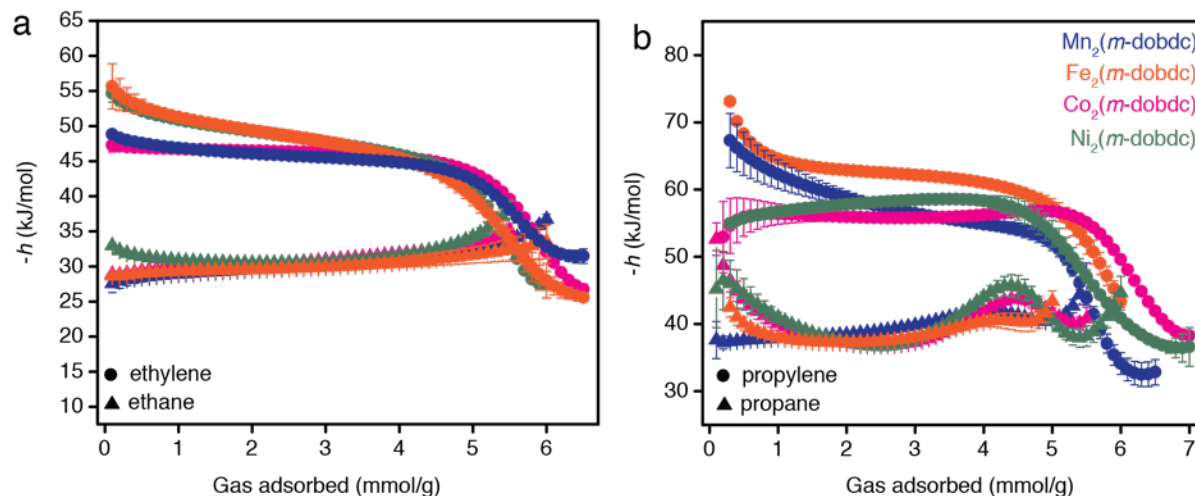


Figure 4.4. Differential enthalpies of adsorption for (a) ethylene and ethane and (b) propylene and propane in $\text{M}_2(m\text{-dobdc})$ (M = Mn, Fe, Co, Ni).

Ethylene adsorption enthalpy magnitudes follow the trend, $\text{Fe} \sim \text{Ni} \sim 52$ kJ/mol $>$ $\text{Mn} \sim \text{Co} \sim 47$ kJ/mol. Interestingly, these are not consistent with the trend in IAST selectivity. The explanation for this discrepancy lies in the ethane adsorption enthalpies. While $\text{Ni}_2(m\text{-dobdc})$ and $\text{Fe}_2(m\text{-dobdc})$ have similar ethylene adsorption enthalpies, the ethane adsorption enthalpy in $\text{Ni}_2(m\text{-dobdc})$ is ~ 5 kJ/mol greater than in $\text{Fe}_2(m\text{-dobdc})$. Selectivity is associated with the difference in adsorption enthalpy rather than the absolute enthalpy of the more strongly adsorbed component. This results in the $\text{Fe}_2(m\text{-dobdc})$ analog having the highest ethylene/ethane selectivity. Relatedly, $\text{Fe}_2(m\text{-dobdc})$ shows both the strongest propylene adsorption and also the highest difference in enthalpy between propylene and propane, leading to its high propylene/propane selectivity.

This metal-dependence can also be explained by a convolution of cation charge density and backbonding character. As the hard Ni^{2+} center polarizes olefins and paraffins strongly, both adsorbates show high adsorption enthalpies. Conversely, the softer Fe^{2+} cation does not polarize olefins or paraffins as strongly as Ni^{2+} , but can show enhanced backbonding interactions uniquely with olefins.

Along with olefin/paraffin selectivity, the kinetics of olefin adsorption is a crucial factor when evaluating adsorbents for industrial separations. To probe the kinetics of olefin adsorption, a transient volumetric measurement of ethylene uptake in $\text{Fe}_2(m\text{-dobdc})$ was conducted by dosing 1000 mbar of ethylene from a reservoir to the adsorbent and monitoring the pressure drop to an equilibrated pressure of 270 mbar. The resulting transient adsorption profile (Fig. 4.5) revealed rapid adsorption kinetics, reaching $> 90\%$ of equilibrium in less than 30 s, with complete adsorption observed in just 60 s. Thus, fast cycle times can be used in a pressure-swing adsorption process, minimizing the amount of adsorbent needed to process a given flow of gas.

This fast adsorption behavior distinctly contrasts with adsorbents that rely on a size-exclusion mechanism for separating gases, in which separation occurs far from equilibrium in a real process. These findings also emphasize the advantage of adsorbents displaying fast kinetics, as pure-component equilibrium adsorption measurements for these systems can accurately model the near-equilibrium operation of the process.

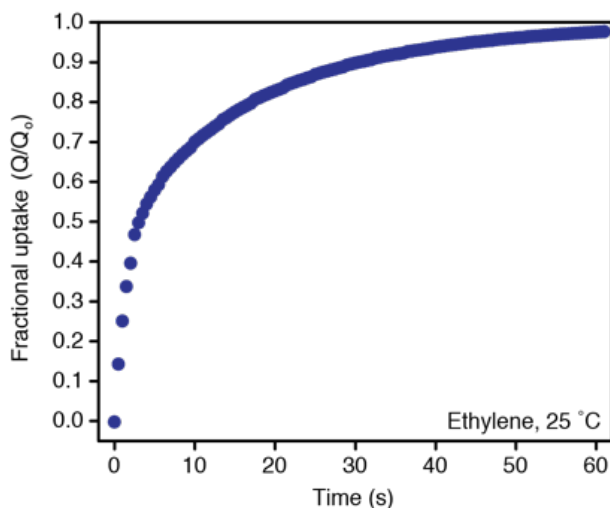


Figure 4.5. Transient adsorption measurement for ethylene in $\text{Fe}_2(m\text{-dobdc})$; the equilibrium pressure is ~ 300 mbar corresponding to an equilibrated loading (Q_{st}) of ~ 6 mmol/g.

4.3.3. Olefin/Paraffin Breakthrough Experiments. To test the applicability of the $\text{M}_2(m\text{-dobdc})$ adsorbents under more realistic process conditions, $\text{Co}_2(m\text{-dobdc})$ was tested in a breakthrough measurement. In a typical experiment, an ethylene/ethane or propylene/propane mixture was flowed through a fixed packed bed of adsorbent with He as the carrier gas. The relative time it takes for the olefin and paraffin to break through the bed indicates the ability of the adsorbent to discriminate between the two components (Figure. 6). Longer breakthrough times for the propylene/propane mixture relative to the ethylene/ethane mixture are likely due to uncertainties in the olefin/paraffin flow rate. Using an equimolar olefin/paraffin feed, it can be seen that the paraffin breaks through the bed first, followed by the olefin. The steep breakthrough of ethane, propane, ethylene, and propylene indicates that there is a clean separation of each species. After breakthrough of both components, when the bed is saturated with an equilibrium composition, the effluent composition returns to equimolar. A subsequent purge with He at ambient conditions regenerated the bed. Notably, residual paraffin in the bed shortly after switching to desorption was not observed, indicating that the adsorbed phase is highly enriched in olefin. This implies that during olefin separation, high purity ethylene or propylene can be produced, exceeding the purity requirement of 99.9%. Additionally, the rapid desorption of the olefin by merely purging with He indicates that the olefin is labile and regeneration of the bed can be accomplished without a temperature swing. This is significant, as flowing a purge gas or using a vacuum or pressure swing are desirable over a temperature swing process, which has longer cycle times due to the time-consuming heating and cooling steps.

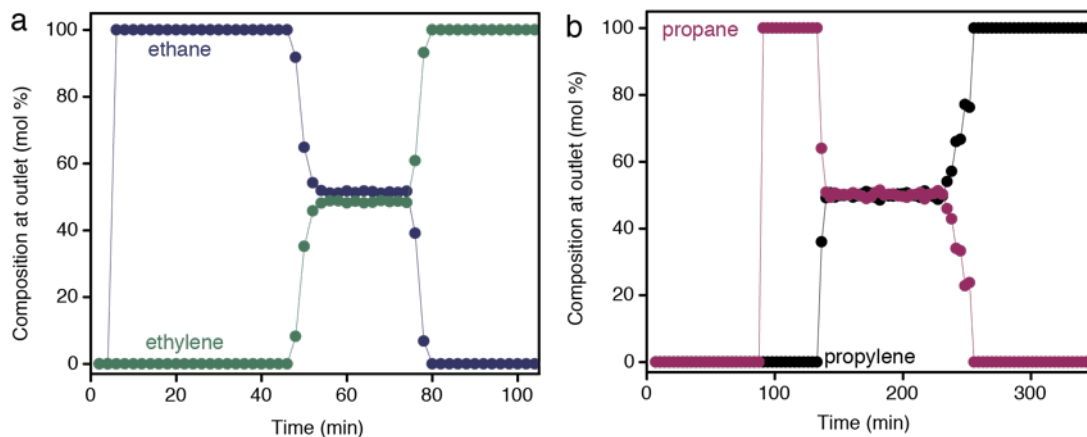


Figure 4.6. Transient breakthrough measurements of an equimolar mixture of (a) ethylene/ethane and (b) propylene/propane in $\text{Co}_2(m\text{-dobdc})$ at $45\text{ }^\circ\text{C}$. Breakthrough corresponds to the time when the olefin composition goes to approximately 50% of the total outflow from the packed bed. The subsequent uptick in olefin concentration corresponds to a change in the feed composition to 100% He to regenerate the bed.

4.4. Outlook and Conclusions

Olefin/paraffin separations account for an enormous amount of energy consumed in the industrial sector and represent a major opportunity for new adsorbents to replace cryogenic distillation. Competitive adsorbent-based technologies require materials with high selectivity and capacity, fast kinetics, labile desorption, and low production cost. We have demonstrated these key features in $\text{M}_2(m\text{-dobdc})$ ($\text{M} = \text{Mn}, \text{Fe}, \text{Co}, \text{Ni}$). Specifically, single-component adsorption isotherms combined with IAST reveal ethylene/ethane and propylene/propane selectivities at $25\text{ }^\circ\text{C}$ in excess of 25 and 55, respectively. These selectivities arise from differences in adsorption enthalpy between olefins and paraffins, in which olefins bind more strongly at the coordinatively-unsaturated metal sites present at high concentration in these materials. This separation mechanism does not rely on size-exclusion and thus retains the excellent adsorption kinetics necessary for fast cycling. Notably, stronger olefin adsorption arising from increased charge density at the metal site leads to much higher selectivity in the $\text{M}_2(m\text{-dobdc})$ frameworks relative to their structural isomers, $\text{M}_2(p\text{-dobdc})$. Finally, this separation capability was demonstrated in breakthrough measurements, in which high olefin purities under mild regeneration conditions were obtained. These unique properties make the $\text{M}_2(m\text{-dobdc})$ compounds the adsorbents of choice for industrial olefin/paraffin separations, and indicate a promising route to improving separation properties by tuning the electronic environment of the adsorption sites.

4.5. Acknowledgements

Thanks to Jonathan E. Bachman for help with all parts of this project, Douglas A. Reed for assistance with sample preparation and isotherm collection, and Miguel I. Gonzalez for

assistance with breakthrough data collection and collection and structure solution of the single-crystal X-ray diffraction structures. This research was supported through the Center for Gas Separations Relevant to Clean Energy Technologies, an Energy Frontier Research Center funded by the U.S. Department of Energy, Office of Science, Office of Basic Energy Sciences under Award DE-SC0001015. Single-crystal X-ray diffraction experiments were performed at Beamline 11.3.1 at the Advanced Light Source, a DoE Office of Science User Facility operated by Lawrence Berkeley National Laboratory under Contract No. DE-AC02-05CH11231.

4.6. References and Supplementary Data

1. Matar, S.; Hatch, L. F. *Chemistry of Petrochemical Processes*; Gulf Professional Publishing: MA, 2001.
2. Kohl, A. L.; Nielsen, R. B. *Gas Purification*; Gulf Publishing Company: TX, 1997.
3. U. S. Department of Energy. Materials for Separation Technology: Energy and Emission Reduction Opportunities. (2005).
4. Sholl, D. S.; Lively, R. P. *Nature* **2016**, *532*, 435-437.
5. Eldridge, R. B. *Ind. Eng. Chem. Res.* **1993**, *32*, 2208–2212.
6. Bai, P.; Jeon, M. Y.; Ren, L.; Knight, C.; Deem, M. W.; Tsapatsis, M.; Siepmann, J. I. *Nat. Commun.* **2015**, *6*, 5912
7. Rege, S. U.; Padin, J.; Yang, R. T. *AIChE Journal* **1998**, *44*, 799-809.
8. Ruthven, D. M.; Reyes, S. C. *Micropor. Mesopor. Mater.* **2007**, *104*, 59-66.
9. Yang, S.; Ramirez-Cuesta, A. J.; Newby, R.; Garcia-Sakai, V.; Manuel, P.; Callear, S. K.; Campbell, S. I.; Tang, C. C.; Schroder, M. *Nat. Chem.* **2015**, *7*, 121-129.
10. Cadiou, A.; Adil, K.; Bhatt, P. M.; Belmabkhout, Y.; Eddaoudi, M. *Science* **2016**, *353*, 137-140.
11. Yang, R. T.; Kikkinides, E. S. *AIChE Journal* **1995**, *41*, 509-517.
12. Li, B.; Zhang, Y.; Krishna, R.; Yao, K.; Han, Y.; Wui, Z.; Ma, D.; Shi, Z.; Pham, T.; Space, B.; Liu, J.; Thallapally, P. K.; Liu, J.; Chrzanowski, M.; Ma, S. *J. Am. Chem. Soc.* **2014**, *136*, 8654-8660.
13. Zhang, Y.; Li, B.; Krishna, R.; Wu, Z.; Ma, D.; Shi, Z.; Pham, T.; Forrest, K.; Space, B.; Ma, S. *Chem. Commun.* **2015**, *51*, 2714-2717.
14. Chang, G.; Huang, M.; Su, Y.; Xing, H.; Su, B.; Zhang, Z.; Yang, Q.; Yang, Y.; Ren, Q.; Bao, Z.; Chen, B. *Chem. Commun.* **2015**, *51*, 2859-2862.
15. Blas, F. J.; Vega, L. F.; Gubbins, K. E. *Fluid Phase Equilib.* **1998**, *150*, 117-124.
16. Aguado, S.; Bergeret, G.; Daniel, C.; Farrusseng, D. *J. Am. Chem. Soc.* **2012**, *134*, 14635-14637.
17. Yu, C.; Cowan, M. G.; Noble, R. D.; Zhang, W. *Chem. Commun.* **2014**, *50*, 5745-5747.
18. Bloch, E. D.; Queen, W. L.; Krishna, R.; Zadrozny, J. M.; Brown, C. M.; Long, J. R. *Science* **2012**, *335*, 1606-1610.
19. Geier, S. J.; Mason, J. A.; Bloch, E. D.; Queen, W. L.; Hudson, M. R.; Brown, C. M.; Long, J. R. *Chem. Sci.* **2013**, *4*, 2054-2061.
20. Da Silva, F. A.; Rodrigues, A. E. *AIChE Journal* **2001**, *47*, 341-357.
21. Bohme, U.; Barth, B.; Paula, C.; Kuhnt, A.; Schwieger, W.; Mundstock, A.; Caro, J.; Hartmann, M. *Langmuir* **2013**, *29*, 8592-8600.

22. Ferreira, A. F. P.; Santos, J.; Plaza, M.; Lamia, N.; Loureiro, J. M.; Rodrigues, A. E. *Chem. Eng. Journal* **2011**, *15*, 1-12.
23. Yaghi, O. M.; Li, H.; Eddaoudi, M.; O'Keefe, M. *Nature* **1999**, *402*, 276-279.
24. Zhou, H.-C.; Long, J. R.; Yaghi, O. M. *Chem. Rev.* **2012**, *112*, 673.
25. Herm, Z. R.; Bloch, E. D.; Long, J. R. *Chem. Mater.* **2014**, *26*, 323-338.
26. Li, J.-R.; Sculley, J.; Zhou, H.-C. *Chem. Rev.* **2012**, *112*, 869-932.
27. Yang, R. T. *Adsorbents: Fundamentals and Applications*; John Wiley & Sons, Inc.: NJ, 2003.
28. Ben, T.; Ren, H.; Ma, S.; Cao, D.; Lan, J.; Jing, X.; Wang, X.; Xu, J.; Deng, F.; Simmons, J. M.; Qui, S.; Zhu, G. *Angew. Chem.* **2009**, *121*, 9621-9624.
29. McKetta, J. J. *Encyclopedia of Chemical Processing and Design*; Marcel Dekker Inc.: NY, 1984.
30. Rosi, N. L.; Kim, J.; Eddaoudi, M.; Chen, B.; O'Keefe, M.; Yaghi, O. M. *J. Am. Chem. Soc.* **2005**, *127*, 1504-1518.
31. Caskey, S. R.; Wong-Foy, A. G.; Matzger, A. J. *J. Am. Chem. Soc.* **2008**, *130*, 10870-10871.
32. Bloch, E. D.; Murray, L. J.; Queen, W. L.; Chavan, S.; Maximoff, S. N.; Bigi, J. P.; Krishna, R.; Peterson, V. K.; Grandjean, F.; Long, G. J.; Smit, B.; Bordiga, S.; Brown, C. M.; Long, J. R. *J. Am. Chem. Soc.* **2011**, *133*, 14814-14922.
33. Bae, T.-S.; Lee, C. Y.; Kim, K. C.; Farha, O. M.; Nickias, P.; Hupp, J. T.; Nguyen, S. T.; Snurr, R. Q. *Angew. Chem. Int. Ed.* **2012**, *51*, 1857-1860.
34. Kapelewski, M. T.; Geier, S. J.; Hudson, M. R.; Stuck, D.; Mason, J. A.; Nelson, J. N.; Xiao, D. J.; Hulvey, Z.; Gilmour, E.; FitzGerald, S. A.; Head-Gordon, M.; Brown, C. M.; Long, J. R. *J. Am. Chem. Soc.* **2014**, *136*, 12119-12129.
35. DeSantis, D.; Mason, J. A.; James, B.; Long, J. R.; Veenstra, M. *Energy Fuels* **2017**, *31*, 2024-2032.
36. Myers, A. L.; Prausnitz, J. M. *AIChE Journal* **1965**, *11*, 121-127.
37. LeVan, M. D.; Vermeulen, T. *J. Phys. Chem.* **1981**, *85*, 3247-3250.
38. Richter, E.; Wilfried, S.; Myers, A. L. *Chem. Eng. Sci.* **1989**, *44*, 1609-1616.
39. Rudzinski, W.; Everett, D. H. *Adsorption of Gases on Heterogeneous Surfaces*; Academic Press, Inc: CA, 1992.
40. Gonzalez, M. I.; Mason, J. A.; Bloch, E. D.; Teat, S. J.; Gagnon, K. J.; Morrison, G. Y.; Queen, W. L.; Long, J. R. *Chem. Sci.* **2017**, *8*, 4387-4398.
41. Sheldrick, G. M. *CELL NOW V2008/2*; Bruker AXS Inc, 2008.
42. Bruker Analytical X-ray Systems, Inc. *SAINTE and APEX 2 Software for CCD Diffractometers*; Bruker Analytical X-ray Systems, Inc.: Madison, WI, USA, 2000.
43. Sheldrick, G. M. *TWINABS, Version 2012/1*; University of Göttingen, 2012.
44. Sheldrick, G. M. *Acta Crystallogr., A, Found. Crystallogr.* **2008**, *64* (Pt 1), 112-122.
45. Sheldrick, G. M. *SHELXS*; University of Göttingen, Germany, 2014.
46. Sheldrick, G. M. *Acta Crystallogr A Found Adv* **2015**, *71* (Pt 1), 3-8.
47. Sheldrick, G. M. *SHELXL*; University of Göttingen, Germany, 2014.
48. Dolomanov, O. V.; Bourhis, L. J.; Gildea, R. J.; Howard, J. A. K.; Puschmann, H. *Journal of Applied Crystallography* **2009**, *42* (2), 339-341.

49. Groom, C. R.; Bruno, I. J.; Lightfoot, M. P.; Ward, S. C. *Acta Crystallogr. Sect. B Struct. Crystallogr. Cryst. Chem.* **2016**, 72 (2), 171–179.
50. Suzuki, M. *Fundamentals of Adsorption*; Kodansha, Ltd: Tokyo, 1993.

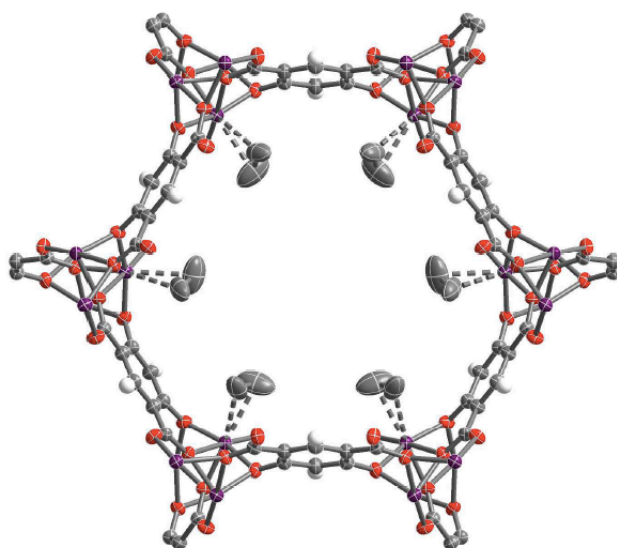


Figure 4.S1. Thermal ellipsoid plot of $\text{Co}_2(m\text{-dobdc})\cdot 2.0\text{C}_2\text{H}_4$ at 100 K drawn at 50% probability level as determined by single-crystal X-ray diffraction; purple, red, gray, and white ellipsoids represent Co, O, C, and H atoms, respectively.

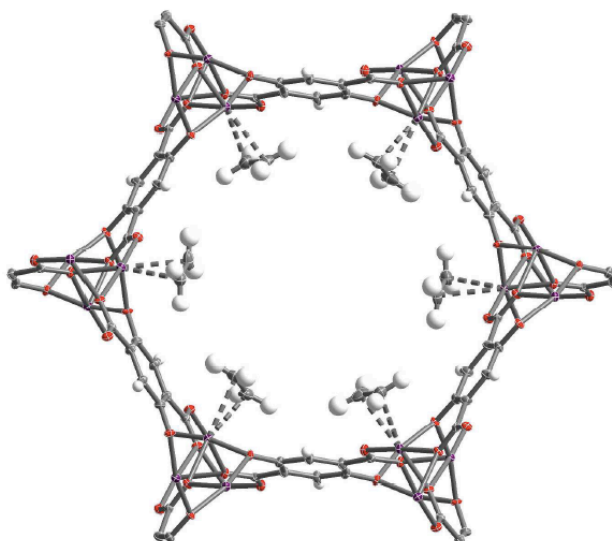


Figure 4.S2. Thermal ellipsoid plot of $\text{Co}_2(p\text{-dobdc})\cdot 1.89\text{C}_2\text{H}_4$ at 100 K drawn at 50% probability level as determined by single-crystal X-ray diffraction; purple, red, gray, and white ellipsoids represent Co, O, C, and H atoms, respectively.

Binary, equilibrium gas adsorption experiments were conducted based on methods reported in our previous works. Equilibrium gas adsorption of a binary mixture of ethylene and ethane were measured on a custom-built, high-throughput gas adsorption analyzer developed in collaboration with Wildcat Technologies. Activated samples were transferred under a dry nitrogen atmosphere into pre-weighed 4 ml vials, and sealed into a sample assembly. The sample assembly was affixed to the instrument, and samples were reactivated in-situ at 180 °C prior to measuring gas adsorption. Gas cylinders with verified compositions of $25.0 \pm 0.1\%$, $50.0 \pm 0.1\%$, and $75.0 \pm 0.1\%$ ethylene in ethane were supplied by Praxair Distribution. To determine the fraction $pC_2H_4/[pC_2H_4+pC_2H_6]$ in equilibrium with the adsorbed phase, a calibration curve using gases with known compositions was developed on a mass spectrometer (MKS Microvision 2).

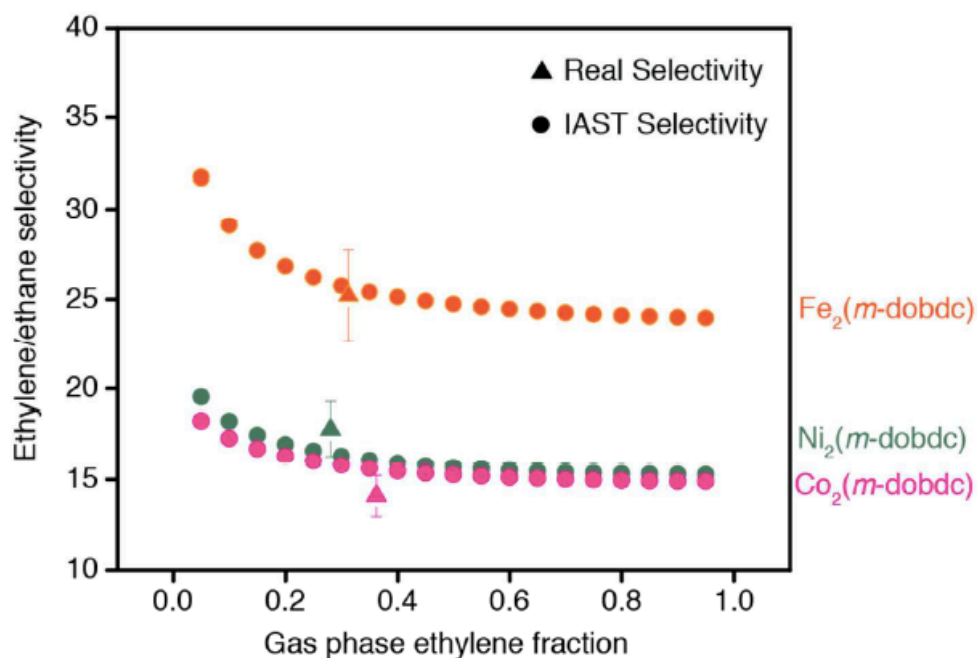


Figure 4.S3. Comparison of IAST selectivities as calculated from the single-component fits with measured selectivities using a binary ethylene/ethane mixture for $M_2(m\text{-dobdc})$ ($M = \text{Fe}, \text{Co}, \text{Ni}$) at 25 °C.

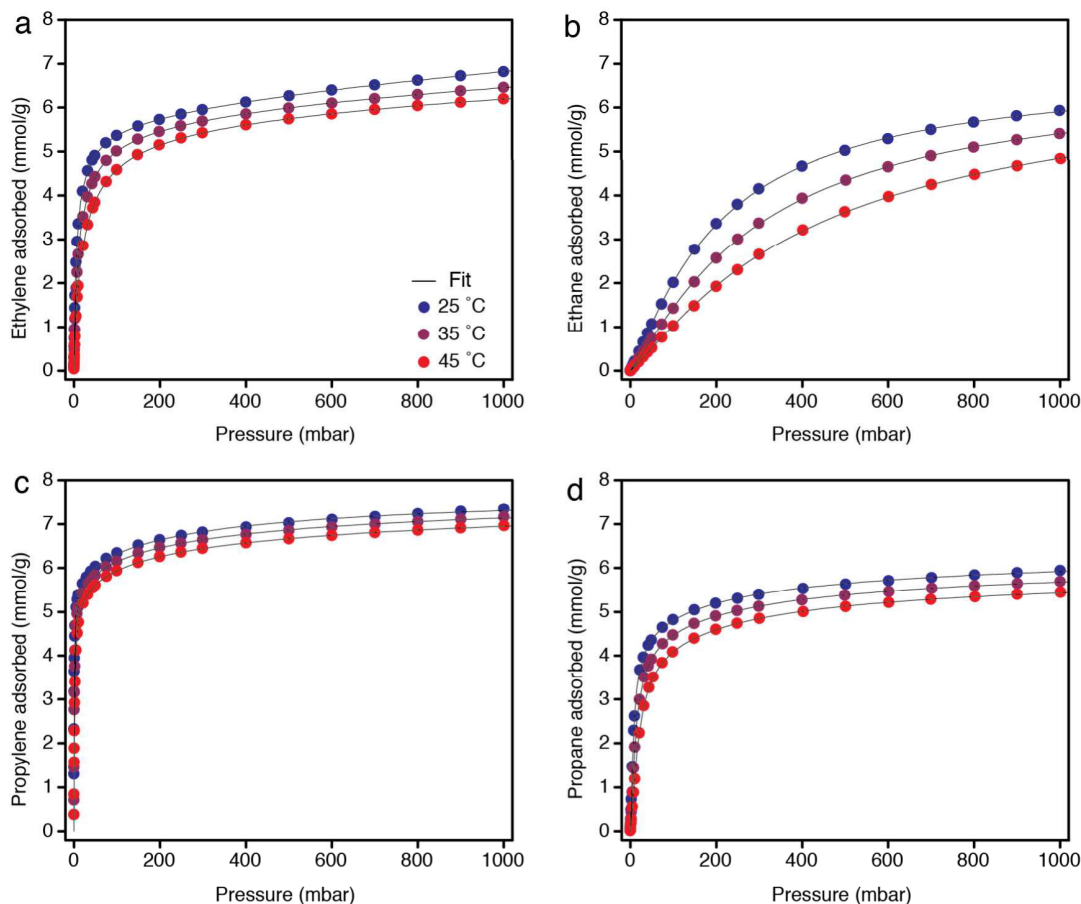


Figure 4.S4. Adsorption of (a) ethylene, (b) ethane, (c) propylene, and (d) propane in $\text{Mn}_2(m\text{-dobdc})$ at 25, 35, and 45 °C.

Table 4.S1. Dual-site Langmuir-Freundlich isotherm fitting parameters for ethylene, ethane, propylene, and propane at 25, 35, and 45 °C in $\text{Mn}_2(m\text{-dobdc})$.

	Ethylene			Ethane			Propylene			Propane		
	25	35	45	25	35	45	25	35	45	25	35	45
T (°C)	25	35	45	25	35	45	25	35	45	25	35	45
$q_{\text{sat},a}$ (mmol/g)	5.603	5.451	5.421	6.854	7.727	6.700	5.403	5.195	4.865	3.333	3.211	2.801
b_a (1/bar)	73.02	48.25	30.43	6.228	4.080	2.606	1109	1019	730.6	3165	1331	968.5
v_a	0.854	0.868	0.876	1.170	1.173	1.153	0.877	0.949	0.989	1.641	1.819	1.710
$q_{\text{sat},b}$ (mmol/g)	23.94	10.72	9.560	0	0	0	2.508	2.700	3.084	3.281	3.161	3.276
b_b (1/bar)	0.057	0.116	0.109	n/a	n/a	n/a	3.182	2.587	2.100	3.704	3.610	4.106
v_b	0.727	0.646	0.632	n/a	n/a	n/a	0.718	0.650	0.557	0.635	0.681	0.726

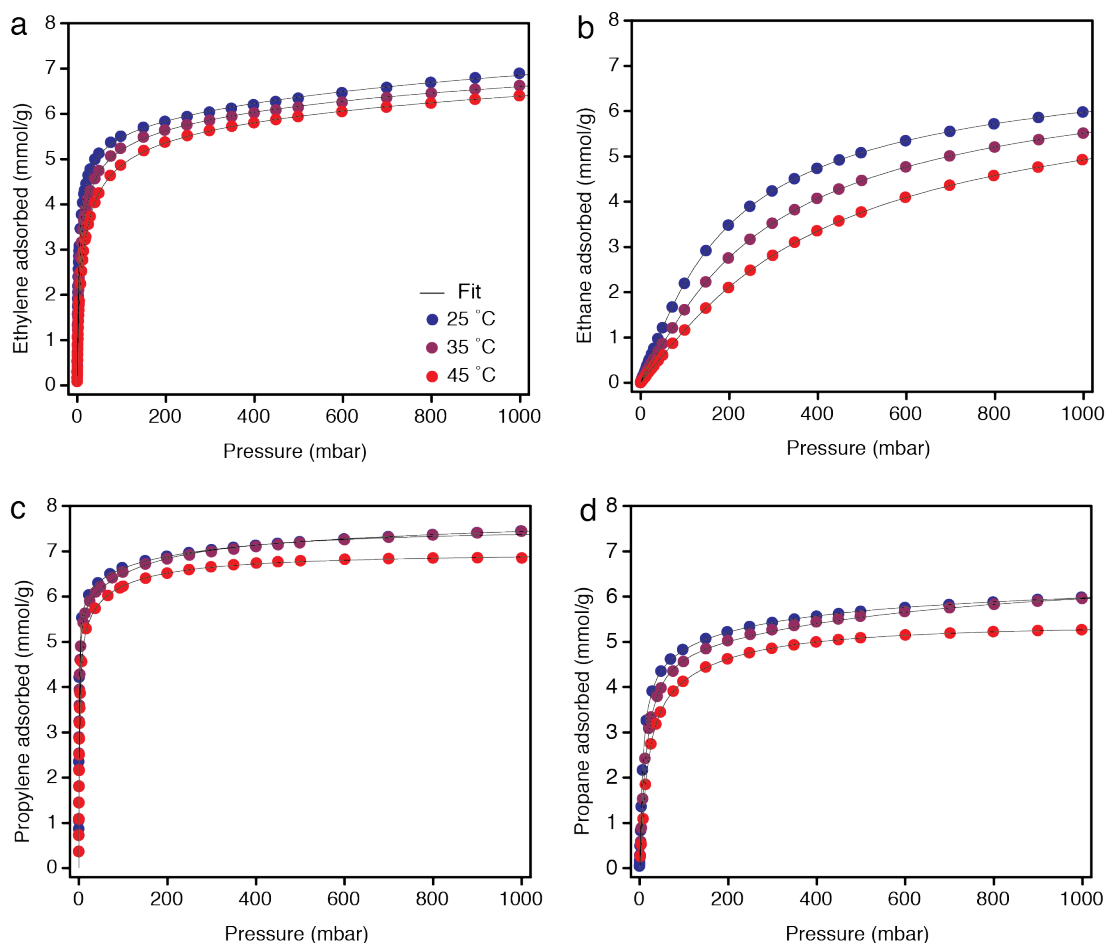


Figure 4.S5. Adsorption of (a) ethylene, (b) ethane, (c) propylene, and (d) propane in $\text{Fe}_2(m\text{-dobdc})$ at 25, 35, and 45 °C.

Table 4.S2. Dual-site Langmuir-Freundlich isotherm fitting parameters for ethylene, ethane, propylene, and propane at 25, 35, and 45 °C in $\text{Fe}_2(m\text{-dobdc})$.

T (°C)	Ethylene			Ethane			Propylene			Propane		
	25	35	45	25	35	45	25	35	45	25	35	45
$q_{\text{sat},a}$ (mmol/g)	5.657	5.288	5.479	4.907	4.250	3.485	4.623	6.093	5.546	3.155	5.026	3.975
b_a (1/bar)	59.52	48.99	28.01	9.727	6.895	4.924	2303	354.1	342.3	3.109	113.7	300.6
v_a	0.735	0.771	0.776	1.254	1.295	1.344	0.941	0.833	0.886	0.640	1.124	1.376
$q_{\text{sat},b}$ (mmol/g)	3.841	4.255	7.464	3.274	3.703	4.049	4.015	1.437	1.463	3.585	1.472	1.433
b_b (1/bar)	0.503	0.500	0.173	0.876	0.947	1.004	2.352	9.089	12.44	1094	1.929	9.997
v_b	0.790	0.593	0.576	0.700	0.761	0.818	0.366	1.214	0.993	1.395	1.453	1.341

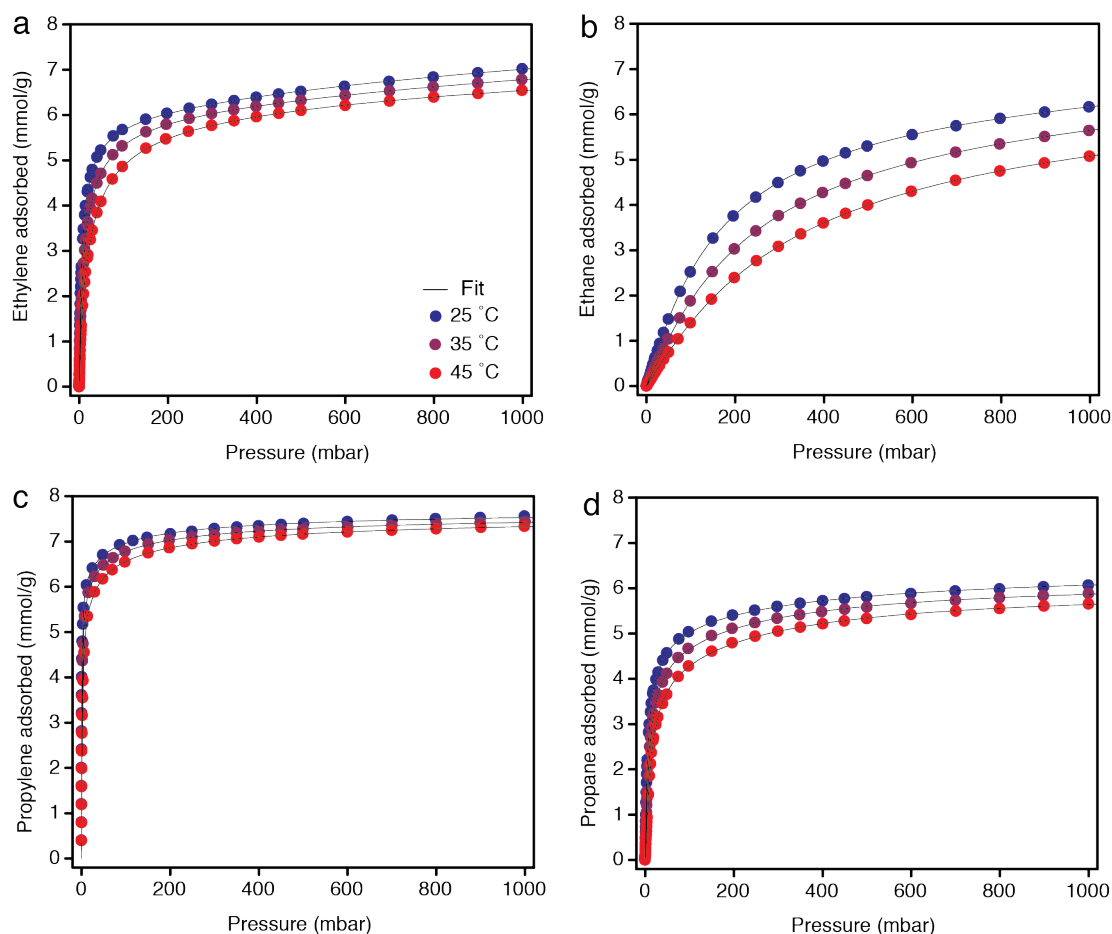


Figure 4.S6. Adsorption of (a) ethylene, (b) ethane, (c) propylene, and (d) propane in $\text{Co}_2(m\text{-dobdc})$ at 25, 35, and 45 °C.

Table 4.S3. Dual-site Langmuir-Freundlich isotherm fitting parameters for ethylene, ethane, propylene, and propane at 25, 35, and 45 °C in $\text{Co}_2(m\text{-dobdc})$.

	Ethylene			Ethane			Propylene			Propane		
	25	35	45	25	35	45	25	35	45	25	35	45
T (°C)	25	35	45	25	35	45	25	35	45	25	35	45
$q_{\text{sat,a}}$ (mmol/g)	5.968	5.983	5.850	5.756	3.409	0.178	5.611	5.061	4.282	4.410	4.260	3.893
b_a (1/bar)	79.89	45.60	29.82	8.88	0.362	82.65	2141	1804	1324	300	300	300
v_a	0.869	0.866	0.876	1.133	0.707	2.270	0.985	1.048	1.099	1.109	1.199	1.286
$q_{\text{sat,b}}$ (mmol/g)	4.917	9.454	3.615	3.724	5.561	6.697	2.169	2.673	3.451	2.192	1.996	2.128
b_b (1/bar)	0.293	0.108	0.321	0.362	5.767	2.725	7.674	7.618	7.616	3.234	4.679	4.767
v_b	0.838	0.760	0.719	0.684	1.130	1.033	0.645	0.607	0.570	0.760	1.019	1.061

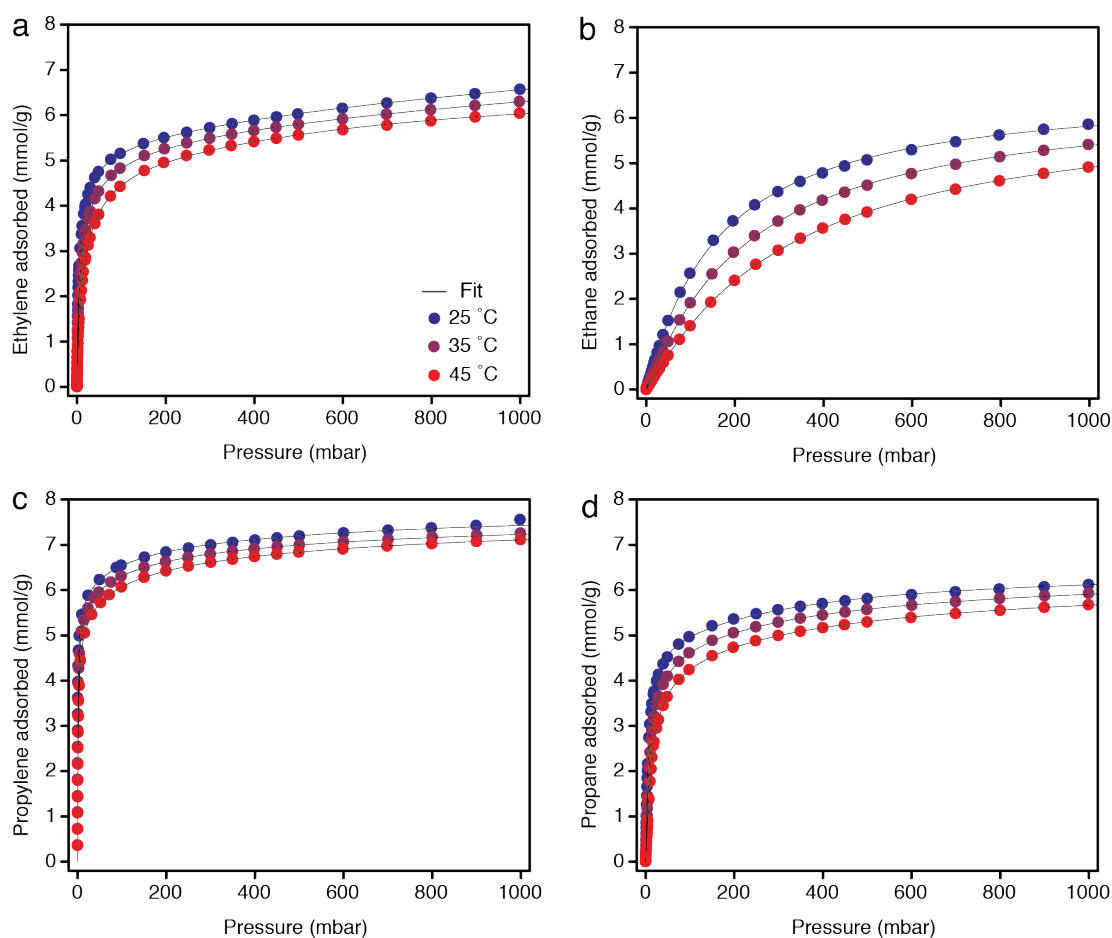


Figure 4.S7. Adsorption of (a) ethylene, (b) ethane, (c) propylene, and (d) propane in $\text{Ni}_2(m\text{-dobdc})$ at 25, 35, and 45 °C.

Table 4.S4. Dual-site Langmuir-Freundlich isotherm fitting parameters for ethylene, ethane, propylene, and propane at 25, 35, and 45 °C in $\text{Ni}_2(m\text{-dobdc})$.

T (°C)	Ethylene			Ethane			Propylene			Propane		
	25	35	45	25	35	45	25	35	45	25	35	45
$q_{\text{sat},a}$ (mmol/g)	5.496	5.304	5.631	6.666	6.510	6.321	4.634	4.065	4.462	4.959	3.470	3.024
b_a (1/bar)	52.14	38.07	21.79	6.824	4.804	3.460	2296	1802	523.4	216.6	702.1	685.1
v_a	0.755	0.777	0.776	1.046	1.063	1.075	0.927	0.978	0.909	1.074	1.347	1.461
$q_{\text{sat},b}$ (mmol/g)	5.558	6.990	1.003	0	0	0	3.590	4.018	3.589	1.473	3.276	3.576
b_b (1/bar)	0.267	0.192	1.784	n/a	n/a	n/a	3.511	3.711	2.847	3.963	2.934	2.843
v_b	0.866	0.727	1.774	n/a	n/a	n/a	0.485	0.457	0.511	1.278	0.681	0.677

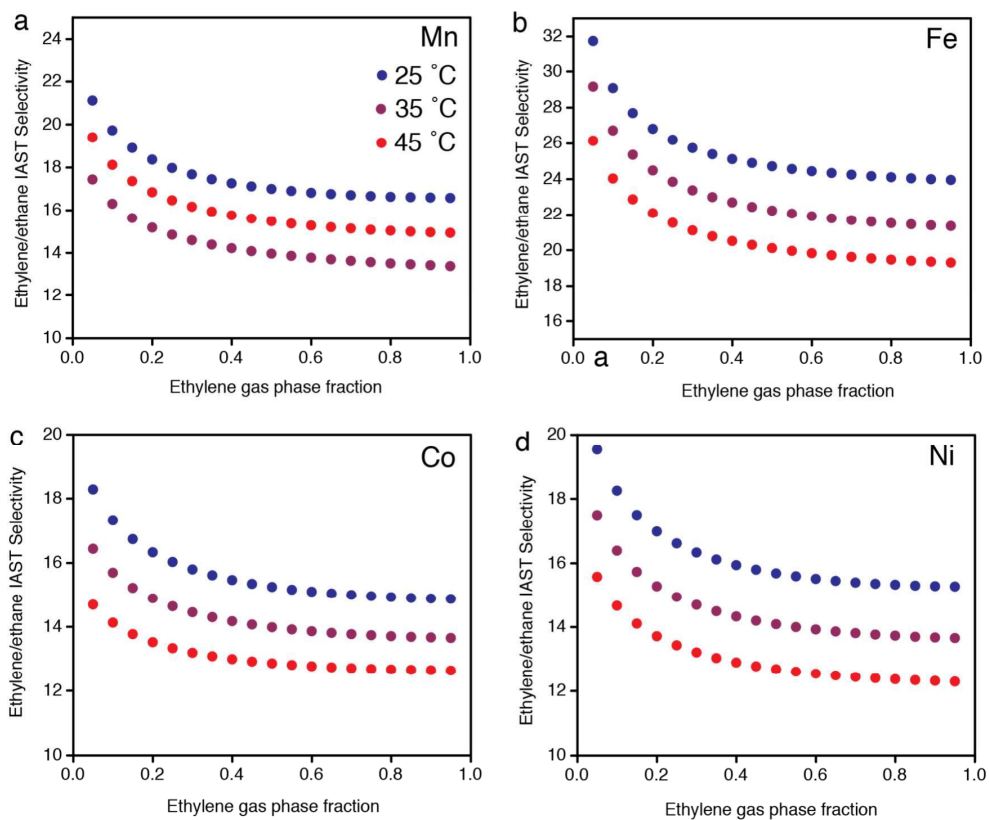


Figure 4.S8. Ethylene/ethane IAST selectivities for (a) $\text{Mn}_2(m\text{-dobdc})$, (b) $\text{Fe}_2(m\text{-dobdc})$, (c) $\text{Co}_2(m\text{-dobdc})$, (d) $\text{Ni}_2(m\text{-dobdc})$ at 25, 35, and 45 °C.

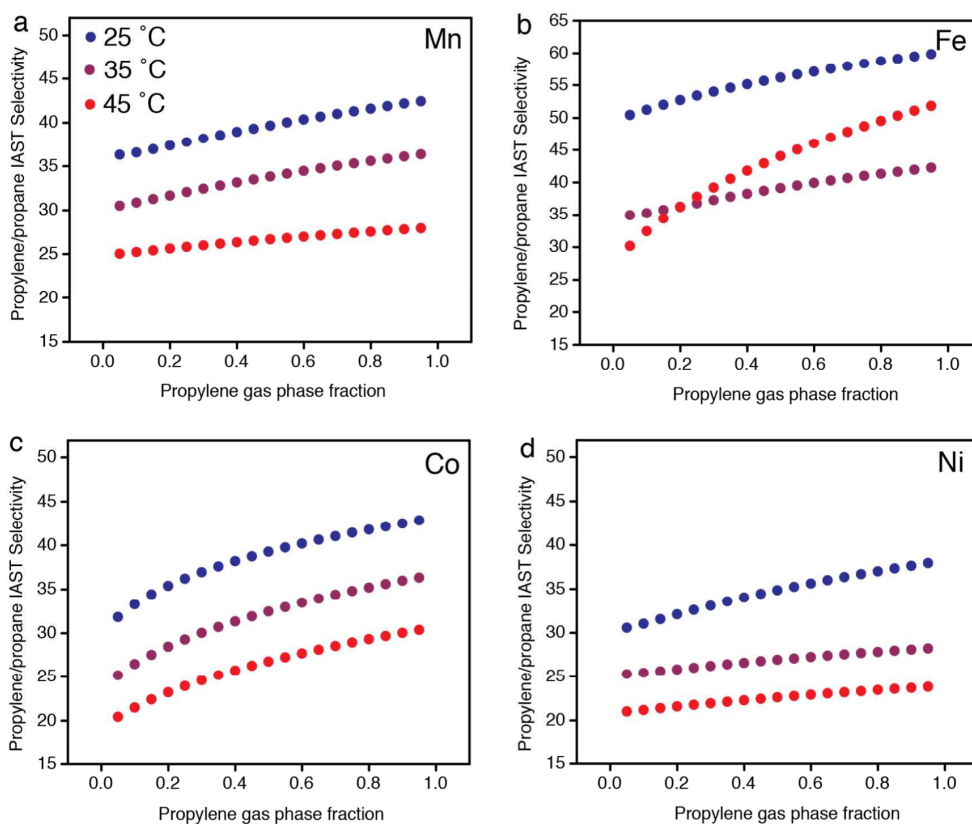


Figure 4.S9. Propylene/propane IAST selectivities for (a) $\text{Mn}_2(m\text{-dobdc})$, (b) $\text{Fe}_2(m\text{-dobdc})$, (c) $\text{Co}_2(m\text{-dobdc})$, (d) $\text{Ni}_2(m\text{-dobdc})$ at 25, 35, and 45 °C.

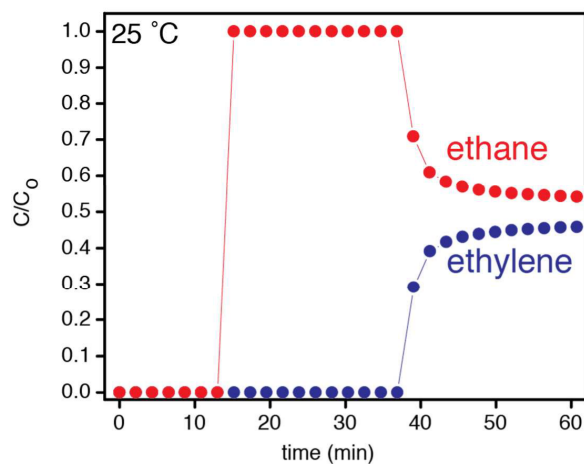


Figure 4.S10. Breakthrough of a binary ethylene/ethane mixture in $\text{Mn}_2(m\text{-dobdc})$. The method used for conducting breakthrough measurements on $\text{Co}_2(m\text{-dobdc})$ were repeated on 0.56 g of $\text{Mn}_2(m\text{-dobdc})$. Clean breakthrough of ethane with no observable ethylene indicates high adsorptive selectivity consistent with single-component equilibrium measurements.

Chapter 5: Separation of Xylene Isomers through Multiple Metal Site Interactions in Metal-Organic Frameworks

5.1 Introduction

Industrial chemical separations account for 22% of the global energy demand.¹ As a consequence, the development of more energy-efficient separations using adsorbent- or membrane-based technologies represents a key pursuit toward mitigating the continuous rise in worldwide energy consumption.² One of the most difficult industrial mixtures to partition consists of the C₈ isomers *o*-xylene, *m*-xylene, *p*-xylene, and ethylbenzene, which are primarily obtained from either reformates or pyrolysis gasoline.³ Both sources yield mixtures of the four isomers that do not match market demand. For example, of the 39.2 Mt of xylenes produced in 2008, 33.0 Mt was used as pure *p*-xylene, 3.6 Mt as *o*-xylene, 0.4 Mt as *m*-xylene, and the remainder was used directly without separation as mixed xylenes solvent.⁴ The large need for pure *p*-xylene stems from its use as a precursor to terephthalic acid, a major feedstock in the production of polyesters and polyamides.⁵ The second most valuable isomer, *o*-xylene, is mainly converted to phthalic anhydride, a precursor to plasticizers.⁶ Current processes do not isolate ethylbenzene from the C₈ mixture, as the isomer is produced more economically by the alkylation of benzene with ethylene.⁷ Optimizing output to meet economic demand requires separation of the desired isomers, mainly *p*-xylene and some *o*-xylene, followed by isomerization of the unwanted fraction back to the thermodynamic mixture.³

Table 5.1. Physical properties of the C₈ alkylaromatics^{3,8}.

C ₈ Isomer	Boiling point (°C)	Kinetic diameter (Å)	Dipole moment (× 10 ¹⁸ esu cm)	Polarizability (× 10 ⁻²⁵ cm ³)
<i>o</i> -xylene	144.4	6.8	0.649	141–149
<i>m</i> -xylene	139.1	6.8	0.36	142
<i>p</i> -xylene	138.4	5.8	0.1	137–149
ethylbenzene	136.2	5.8	0.59	142

The similar boiling points of the C₈ isomers makes distillative separation of all four nearly impossible, while their comparable sizes and polarizabilities limit the ability of adsorbents to distinguish between the different isomers (Table 5.1). Current state-of-the-art technology involves either crystallization (25% of production) or adsorption (75% of production) to effect separation. Industrial adsorption-based techniques for the production of pure *p*-xylene are carried out in the liquid phase with faujasite-type zeolites using simulated moving bed technology.⁵ Although difficult, *o*-xylene can be separated by fractional distillation, while the *m*-xylene and ethylbenzene are obtained through other adsorption- and complexation-based processes, such as the commonly used Parex process from Honeywell UOP.⁹ The isolation of all four isomers using a single process has yet to be implemented, prompting research efforts to pursue the development of more efficient technologies. Several studies have focused on improving

adsorptive separations with zeolites,¹⁰⁻¹⁴ while more recent work has highlighted membrane-based separations as competitive and less energy-intensive alternatives.^{10,15}

Metal-organic frameworks have previously been studied for the separation of hydrocarbon mixtures such as ethane/ethylene, propane/propylene, and C₆ alkane mixtures, among many others.¹⁶ In particular, some of these materials have been studied for the separation of xylene isomers based on size and shape selectivity.^{10,17-28} For example, the framework V(O)(bdc) (H₂bdc = 1,4-benzenedicarboxylic acid) or MIL-47 affords separation based on packing differences and adsorbate-adsorbate interactions upon adsorption,¹⁸ engendering many follow-up studies on both MIL-47^{19,20} and its structural analogs M(OH)(bdc) or MIL-53-M (M = Al, Fe).^{21,27,28} In addition, the flexible metal-organic framework Ce(Htcpb) (H₄tcpb = 1,2,4,5-tetrakis(4-carboxyphenyl)benzene) has been demonstrated to separate the four C₈ isomers effectively through shape-selective conformational changes in response to specific isomers.²⁶

Frameworks bearing coordinatively unsaturated metal centers have been extensively investigated as adsorbents for the separations of small gas molecules, due to the ability of their exposed metal sites to bind specific gases preferentially.^{16,29-40} Despite considerable work demonstrating the ability of these materials to separate gas mixtures that are generally difficult to purify, only a limited number of studies have explored their use in the separation of larger molecules such as the C₈ alkylaromatics.^{18,25} In one report, the metal-organic framework Ni₂(dobdc) was shown to separate two-component mixtures of *o*-xylene, *m*-xylene, and *p*-xylene although the exposed nickel(ii) coordination sites in this material were thought to play a minor role in the separation.²⁵ Here, we demonstrate through adsorption and breakthrough measurements coupled with structural characterization by single-crystal X-ray diffraction that the metal-organic frameworks Co₂(dobdc) and Co₂(*m*-dobdc) (Figure 5.1) facilitate the separation of the C₈ aromatics through subtle differences in the interaction of two coordinatively-unsaturated metal centers with each C₈ molecule. Furthermore, Co₂(dobdc) is found to undergo a structural distortion upon binding either *o*-xylene or ethylbenzene, which significantly increases its adsorption capacity for these isomers.

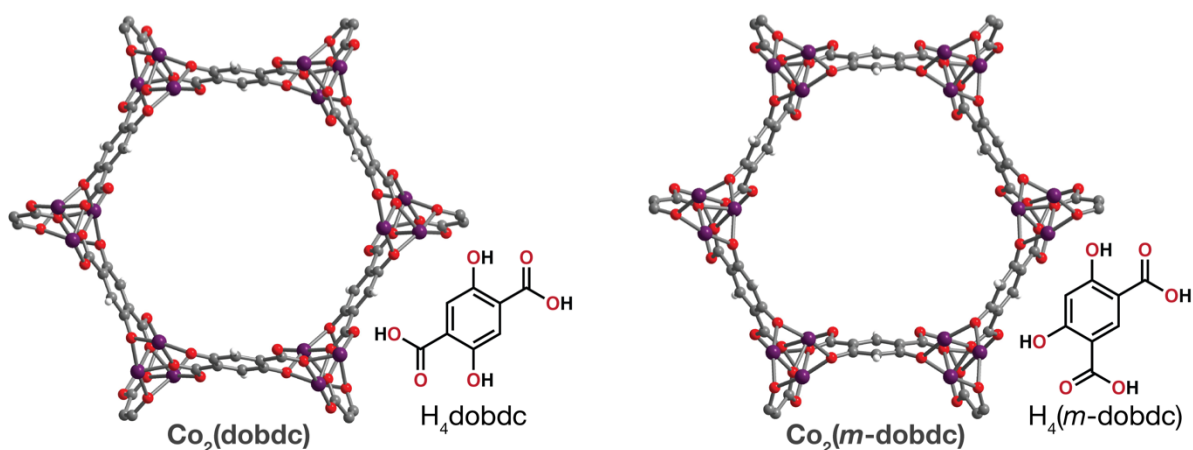


Figure 5.1. A portion of the crystal structures of Co₂(dobdc) and Co₂(*m*-dobdc) (dobdc⁴⁻ = 2,5-dioxido-1,4-benzenedicarboxylate; *m*-dobdc⁴⁻ = 4,6-dioxido-1,3-benzenedicarboxylate); purple, red, gray, and white spheres represent Co, O, C, and H atoms, respectively.

5.2. Experimental

5.2.1. Materials and Methods. *N,N*-dimethylformamide (DMF), tetrahydrofuran (THF), ethanol, and methanol were obtained from commercial sources and used without further purification. The solvent *n*-heptane, the internal standard *n*-undecane, and the C₈ isomers *o*-xylene, *m*-xylene, *p*-xylene, and ethylbenzene were purchased from commercial sources, dried over sodium (*n*-heptane) or 3 Å molecular sieves (undecane, *o*-xylene, *m*-xylene, *p*-xylene, and ethylbenzene), degassed *via* three successive freeze–pump–thaw cycles, and then stored over 3 Å molecular sieves in an N₂-filled glovebox. The compounds Co(NO₃)₂·6H₂O, Co(acetate)₂·4H₂O and 2,5-dihydroxy-1,4-benzenedicarboxylic acid (H₄dobdc) were purchased from commercial sources and used as received. The metal-organic framework Co₂(dobpdc) (dobpdc²⁻ = 4,4'-dioxidobiphenyl-3,3'-dicarboxylate), which is the expanded analogue of Co₂(dobdc) and the ligand 4,4'-dioxidobiphenyl-3,3'-dicarboxylic acid (H₄dobpdc) were synthesized according to a previously published procedures as detailed in the Supporting Information.⁴¹

5.2.2. Synthesis of H₄(*m*-dobdc). See Section 2.2.2.

5.2.3. Synthesis of Co₂(dobdc). The framework Co₂(dobdc) was synthesized using a slight modification to a previously published procedure.²⁹ A 1-L Pyrex jar was charged with H₄dobdc (2.23 g, 11.3 mmol), Co(NO₃)₂·6H₂O (10.9 g, 37.5 mmol), and a 1:1:1 (v/v/v) mixture of DMF/ethanol/water (900 mL), and then sealed with a PTFE-lined cap. The resulting mixture was sonicated until all reactants were fully dissolved to form a violet solution. The reaction mixture was then placed in an oven that was preheated to 100 °C and kept at this temperature for 24 h, yielding violet needle-shaped single crystals. The crystals were soaked three times in 1 L of DMF for 24 h at 120 °C, followed by soaking three times in 1 L of methanol at 60 °C. The crystals were then heated at 180 °C under dynamic vacuum for 24 h to give fully-desolvated Co₂(dobdc). Langmuir surface area (N₂, 77 K): 1410 m²/g.

The single crystals obtained from the large-scale synthesis of Co₂(dobdc) were all found to exhibit obverse/reverse twinning, which complicated analysis of the structures showing distortion of the lattice upon soaking with *o*-xylene or ethylbenzene. Non-twinned single-crystals were therefore synthesized using a slight modification to a previously published procedure.⁴² A solution of H₄dobdc (74.3 mg, 0.375 mmol) in 2.5 mL of THF was added to a solution of Co(acetate)₂·4H₂O (93.4 mg, 0.375 mmol) in 2.5 mL deionized water in a PTFE-lined Parr-reactor. The reactor was placed in an oven that was preheated to 110 °C and kept at this temperature for 5 days to give pink needle-shaped single crystals. The crystals were soaked three times in 20 mL of DMF for 24 h at 120 °C, followed by soaking three times in 20 mL of methanol at 60 °C. Fully-desolvated Co₂(dobdc) single crystals were obtained by heating at 180 °C under dynamic vacuum for 24 h.

5.2.4. Synthesis of Co₂(*m*-dobdc). The framework Co₂(*m*-dobdc) was synthesized according to literature procedures.⁴³ A 1 L three-neck round-bottom flask was charged with 310 mL of methanol and 310 mL of DMF and sparged with N₂ for 1 h while stirring. The solids H₄(*m*-dobdc) (2.00 g, 10.1 mmol) and CoCl₂ (3.27 g, 25.2 mmol) were added and the flask was equipped with a reflux condenser and sealed under N₂, forming a blue-pink suspension. The reaction mixture was then stirred at 120 °C for 18 h, yielding a pink microcrystalline solid that was isolated by filtration. The powder was soaked in 500 mL of DMF 500 mL at 60 °C for 24 h,

followed by soaking three times in 500 mL of methanol at 60 °C for 24 h. The resulting powder was collected by filtration and heated to 180 °C under dynamic vacuum for 24 h to give fully-desolvated Co₂(*m*-dobdc). Langmuir surface area (N₂, 77 K): 1500 m²/g.

Single crystals of Co₂(*m*-dobdc) were prepared by adapting the procedure used for the large-scale synthesis of Co₂(dobdc). A 100 mL Pyrex jar was charged with H₄(*m*-dobdc) (198 mg, 1.00 mmol), Co(NO)₂·6H₂O (970 mg, 3.33 mmol), and 80 mL of a 1:1:1 (v/v/v) mixture of DMF/ethanol/water, and then sealed with a PTFE-lined cap. The resulting mixture was sonicated until all reactants were fully dissolved to form a pink solution. The reaction mixture was then placed in an oven that was preheated to 100 °C and kept at this temperature for 24 h, yielding pink needle-shaped single crystals. The crystals were soaked three times in 100 mL of DMF at 120 °C for 24 h, followed by soaking three times in 100 mL of methanol at 60 °C. Fully desolvated Co₂(*m*-dobdc) single crystals were obtained by heating at 180 °C under dynamic vacuum for 24 h.

5.2.5. Single-Component Vapor-Phase Adsorption Experiments. Approximately 150 mg of each sample was loaded into a preweighed sample tube in an N₂-filled glovebox and the sample tubes were capped with a Transeal equipped with Kalrez O-rings. The samples were then transferred to a Micromeritics 2420 instrument degas manifold and heated at a rate of 0.2 °C/min to a temperature of 180 °C while each sample was under vacuum. When a degas rate of <1 μbar/min was achieved, each sample was considered to be activated. Following this procedure, the sample were transferred to a Micromeritics 3Flex gas adsorption analyzer equipped with a vapor dosing tube for single-component xylene adsorption measurements. Each sample tube was subsequently immersed in a temperature-controlled oil bath that surrounded most of the tube. Each xylene was stored over 4 Å molecular sieves prior to being placed in the vapor dosing tube, and was degassed on the instrument via three freeze–pump–thaw cycles. The vapor dosing tube was then heated to 35 °C with a heating mantle and kept at this temperature for the duration of the experiment. The manifold of the instrument itself was heated to 45 °C to prevent condensation of liquid xylenes. Experiments were conducted with the instrument in fixed pressure incremental dose mode in increments of 0.1 mmol/g. Importantly, to ensure full equilibration of each isomer with the metal–organic framework adsorbent, each dose was allowed to equilibrate until the change in pressure was below 0.01% of the average pressure measured over a 90-s interval.

5.2.6. Multi-Component Vapor-Phase Breakthrough Experiments. Breakthrough experiments were carried out using a custom-built breakthrough apparatus consisting of Swagelok fittings and copper tubing connecting an N₂ cylinder, several valves, a sample holder, and a bubbler to a Perkin Elmer Clarus 500 gas chromatograph (GC). A mixture of *o*-xylene, *m*-xylene, *p*-xylene, and ethylbenzene was loaded into a glass bubbler connected to the setup. Nitrogen (N₂, 99.999%) was flowed through the bubbler at a rate of 40 mL/min, which was controlled by a Parker Porter mass flow controller. Composition of the four components in the bubbler was adjusted until a 1:1:1:1 mixture was achieved in the vapor phase, as detected by the GC equipped with a Supelco SCOT Bentone 34/DNDP capillary column. Each sample was then loaded into one vertical portion of a U-shaped Swagelok assembly equipped with a fritted gasket to hold the sample in place, then connected to the apparatus and heated to 125 °C. The C₈ mixture from the bubbler was carried by this nitrogen flow through the sample and to the GC, which sampled the effluent gas every 5 min. Peak integration of each sampling event allowed for

the determination of the relative amounts of each component over time. Once all four of the C₈ isomers had broken through the column and the starting composition was detected, the flow was switched to pure N₂ and the temperature of the packed bed was increased to 225 °C at a rate of 1 °C/min, while continuing to monitor the eluent from the packed bed using the GC.

5.2.7. Multi-Component Liquid-Phase Adsorption Experiments. In an N₂-filled glovebox, equimolar stock solutions of *o*-xylene, *m*-xylene, *p*-xylene, and ethylbenzene (0.010–1.7 M for each isomer) in dry *n*-heptane were prepared with *n*-undecane (0.01 M) as an internal standard. For each concentration, a 250 μL aliquot of C₈ isomer solution was added to a pre-weighed (~20 mg in most cases) sample of Co₂(dobdc) in a 4-mL vial. Each sample vial was sealed with a PTFE-lined cap and kept at 33 °C for 24 h. The concentrations of both the stock solution and the solution over the Co₂(dobdc) were both analyzed by gas chromatography using an SRI instruments 8610V GC equipped with a Supelco SCOT Bentone 34/DNDP capillary column and a Cobra autosampler. The amount of each isomer adsorbed was then calculated from the difference between the initial and equilibrium concentrations of the isomer and the mass of the Co₂(dobdc) sample. Two-component selectivities, *S*, were calculated according to eq 1, where *q_i* and *q_j* represent the quantity adsorbed for components *i* and *j*, respectively, while *C_i* and *C_j* represent the equilibrium concentration for components *i* and *j*, respectively.

$$S = \frac{q_i/q_j}{c_i/c_j} \quad (1)$$

5.2.8. Single-Crystal X-ray Diffraction. In an N₂-filled glovebox, fully-desolvated single crystals of either Co₂(dobdc) or Co₂(*m*-dobdc) were soaked in ~3 mL of *o*-xylene, *m*-xylene, *p*-xylene, or ethylbenzene for at least 24 h at 33 °C in 4 mL vials sealed with PTFE-lined caps. Sample vials were kept sealed and taken out of the glove box prior to data collection. Immediately after opening the sample vial, crystals were coated with Paratone-N oil, mounted on MiTeGen loops, and then cooled to 100 K using an Oxford Cryostreams cryostream for data collection. X-ray diffraction data for all samples were collected at Beamline 11.3.1 at the Advanced Light Source at Lawrence Berkeley National Laboratory using synchrotron radiation ($\lambda = 0.8856 \text{ \AA}$ for Co₂(dobdc)·0.99(*o*-xylene), Co₂(dobdc)·0.36(ethylbenzene), Co₂(dobdc)·0.82(*p*-xylene), and Co₂(*m*-dobdc)(H₂O)_{0.61}·0.77(ethylbenzene); $\lambda = 0.7749 \text{ \AA}$ for Co₂(dobdc)·0.74(*m*-xylene) and Co₂(*m*-dobdc)·0.92(*o*-xylene)) with a Bruker D8 diffractometer equipped with a Bruker PHOTON100 CMOS detector.

Raw data were integrated and corrected for Lorentz and polarization effects using Bruker AXS SAINT⁴⁴ software and corrected for absorption using SADABS.⁴⁵ The structures were solved using direct methods with SHELXS^{46,47} or intrinsic phasing using SHELXT⁴⁸ and refined using SHELXL^{46,49} operated in the OLEX2 interface.⁵⁰ Thermal parameters were refined anisotropically for all non-hydrogen atoms. In all structures, disorder of the C₈ isomers required the use of displacement parameter and distance restraints. In some cases, the disorder was so severe that geometric constraints were necessary to model the aromatic ring of the C₈ isomers. All hydrogen atoms were refined using the riding model. In the presence of either *o*-xylene or ethylbenzene, Co₂(dobdc) undergoes a structural distortion that involves the elongation of three out of four hexagonal channels along the direction normal to two opposing walls of the pore. This distortion results in the formation of a supercell, characterized by the doubling of both the *a* and *b* axes of the undistorted structure. Refinement of the distorted structures (Co₂(dobdc)·0.99(*o*-xylene) and Co₂(dobdc)·0.36(ethylbenzene)) revealed significant residual

electron density at positions that match the structure of the undistorted framework (Figures S10 and S11), suggesting that a small fraction of these crystals remain undistorted. This likely arises from defects in the crystals where the cobalt(II) sites are inaccessible, which has been reported in the $M_2(\text{dobdc})$ series of metal–organic frameworks based on gas adsorption measurements.³⁴ A suitable structural model that accounts for this electron density could not be generated, leading to high *R*-factors for both structures.

5.2.9. Synthesis of 4,4'-dihydroxy-(1,1'-biphenyl)-3,3'-dicarboxylic acid ($H_4\text{dobpdc}$).

This compound was synthesized according to a previously reported procedure.¹

Briefly, 5-bromosalicylic acid (10.0 g, 46.1 mmol) was heated to reflux in methanol (300 mL) with sulfuric acid (10 mL) for 12 h and cooled to room temperature. The solvent was removed with a rotary evaporator, producing a white solid product (methyl 5-bromo-2-hydroxybenzoate).

A 500 mL three-neck round bottom flask was then charged with methyl 5-bromo-2-hydroxybenzoate (8.00 g, 34.6 mmol), bi(pinacolato)diboron (8.79 g, 34.6 mmol), potassium acetate (10.2 g, 104 mmol), bis(triphenylphosphine)-palladium dichloride (1.21 g, 1.73 mmol), and 1,4-dioxane (300 mL). The reaction mixture was sparged with argon for 1 h, heated at reflux under inert gas while stirring for 24 h, and cooled to ambient temperature. The solution was filtered and the filtrate was extracted with diethyl ether (3 × 150 mL). Organic extracts were combined, dried over MgSO_4 , and the solvent was removed on a rotary evaporator to yield and off-white crystalline powder (methyl 2-hydroxy-5-(4,4,5,5-tetramethyl-1,3,2-dioxaborolanyl)benzoate).

A 500 mL three-neck round-bottom flask was charged with methyl 5-bromo-2-hydroxybenzoate (5.00 g, 21.6 mmol), methyl 2-hydroxy-5-(4,4,5,5-tetramethyl-1,3,2-dioxaborolanyl)benzoate (6.62 g, 23.8 mmol), potassium carbonate (6.58 g, 47.6 mmol), lithium chloride (0.101 mg, 2.38 mmol), 1,4-dioxane (150 mL), and water (150 mL) and sparged with argon for 1.5 h. Tetrakis(triphenylphosphine)palladium (0.826 g, 0.714 mmol) was added to the reaction mixture while still under argon and the reaction mixture was heated to reflux under inert atmosphere for 24 h, cooled to ambient temperature, and then filtered. The filtrate was acidified to pH = 1 using 12 M HCl, causing a white precipitate to form. This precipitate was collected by filtration to yield a white powder, which is the $H_4(\text{dobpdc})$ product.

5.2.10. Synthesis of $\text{Co}_2(\text{dobpdc})$. This compound was synthesized according to a previously reported procedure.² Briefly, $H_4(\text{dobpdc})$ (41.1, 0.15 mmol), $\text{Co}(\text{NO}_3)_2 \cdot 6\text{H}_2\text{O}$ (109 mg, 0.375 mmol), and 15 mL of 1:1:1 water/DMF/ethanol were added to a 20 mL scintillation vial. The vial was sealed with a PTFE-lined cap, placed in a well plate, and heated to 393 K for 36 h. The reaction mixture was decanted and the remaining powder was soaked three times in DMF at 60 °C and then three times in methanol at 60 °C, each for 8 h. The pink solid was collected by filtration and desolvated by heating under dynamic vacuum (<10 μbar) at 523 K for 24 h, yielding the fully desolvated $\text{Co}_2(\text{dobpdc})$.

5.2.11. Powder X-ray Diffraction. In an N_2 -filled glovebox, single crystals of $\text{Co}_2(\text{dobdc})$ were ground into a microcrystalline powder and soaked for 24 h in 3 mL of *o*-xylene, *m*-xylene, *p*-xylene, or ethylbenzene. The soaked samples were then quickly filtered, taking care not to completely dry the powder, and loaded into 1.5 mm quartz capillaries that were flame-sealed. Powder X-ray diffraction data were collected on Beamline 17-BM-B at the Advanced Photon

Source (APS) at Argonne National Laboratory with a wavelength of 0.75009 Å. A standard peak search, followed by indexing via the Single Value Decomposition approach,³ as implemented in TOPAS-Academic,⁴ allowed the determination of approximate unit cell dimensions. Precise unit cell dimensions were determined by performing a structureless Le Bail refinement in TOPAS-Academic.

5.3. Results and Discussion

5.3.1. C₈ Isomer Adsorption Experiments. The isomeric metal–organic frameworks Co₂(dobdc) and Co₂(*m*-dobdc) both possess one-dimensional hexagonal channels lined with a high density of coordinatively unsaturated cobalt(II) centers.^{29,43} To determine the ability of these frameworks to distinguish the four C₈ isomers, single-component adsorption isotherms were collected at 150 °C. Comparison of the adsorption isotherms for Co₂(dobdc) (Figure 5.2a) reveals that the affinity of the framework for each isomer follows the trend *o*-xylene > ethylbenzene > *m*-xylene > *p*-xylene, suggesting that all four molecules can be separated by the framework. In contrast, the order of adsorption strength in Co₂(*m*-dobdc) is *o*-xylene > ethylbenzene ≈ *m*-xylene > *p*-xylene (Figure 5.2b), which indicates that the framework cannot discriminate between ethylbenzene and *m*-xylene despite having a structure similar to Co₂(dobdc). Previous work has shown that Ni₂(dobdc) exhibits the same trend in affinity for *o*-xylene, *m*-xylene, and *p*-xylene.²⁵ Both cobalt frameworks show saturation capacities that range from 3.1–3.6 mmol/g at ~7 mbar, which are much higher than those reported for the Ni variant (1.9–2.1 mmol/g), and correspond to the adsorption of one xylene molecule per two metal centers (3.2 mmol/g). Notably, Co₂(dobdc) and Co₂(*m*-dobdc) also display greater volumetric capacities (3.8–4.2 mmol/cm³) than those reported for the industrially relevant faujasite-type zeolites (2.4–2.8 mmol/cm³ of NaY).^{5,25,51,52} In general, the adsorption isotherms for the C₈ isomers in Co₂(dobdc) and Co₂(*m*-dobdc) show considerable uptake at low pressures (0.1 to 1 mbar) and relatively high temperature, indicating strong interactions between the framework and the alkylaromatics.

Additional single-component isotherms were collected at 140, 150, and 160 °C (Figures S18 and S19) for each C₈ isomer in both frameworks to determine differential enthalpies of adsorption. These were found to range from -63 ± 4 kJ/mol for ethylbenzene to -77 ± 6 kJ/mol for *o*-xylene in Co₂(dobdc), and from -67 ± 2 kJ/mol for *p*-xylene to -81 ± 1 kJ/mol for ethylbenzene in Co₂(*m*-dobdc) at about half saturation capacity (Figure S20). The large errors associated with the calculated enthalpies preclude meaningful comparisons between the different isomers for each framework, although these highly exothermic adsorption enthalpies are consistent with the steep adsorption isotherms and likely arise from a combination of multiple framework–guest interactions.

Multi-component vapor-phase breakthrough measurements were performed on Co₂(dobdc) and Co₂(*m*-dobdc) to evaluate their performance in separating an actual mixture of the four C₈ alkylaromatics. In these experiments, N₂ was bubbled through a mixture of *o*-xylene, *m*-xylene, *p*-xylene, and ethylbenzene to produce an equimolar vapor mixture that was subsequently flowed through approximately 1 g of each material at 125 °C. The components of the eluent from the sample columns were determined via gas chromatography and plotted as a function of normalized time (Figure 5.2c). Consistent with the order of adsorption strengths determined from the single-component adsorption isotherms, *p*-xylene breaks through the Co₂(dobdc) column first followed by *m*-xylene, ethylbenzene, and finally *o*-xylene. In contrast, as also predicted from the

single-component adsorption isotherms, the breakthrough profile of $\text{Co}_2(m\text{-dobdc})$ shows the elution of *p*-xylene first, followed by *m*-xylene and ethylbenzene simultaneously, and finally *o*-xylene (Figure 5.2d). Overall, these experiments establish that a four-component mixture of the C_8 isomers can be partitioned in $\text{Co}_2(\text{dobdc})$, whereas $\text{Co}_2(m\text{-dobdc})$ can separate all isomers except ethylbenzene and *m*-xylene.

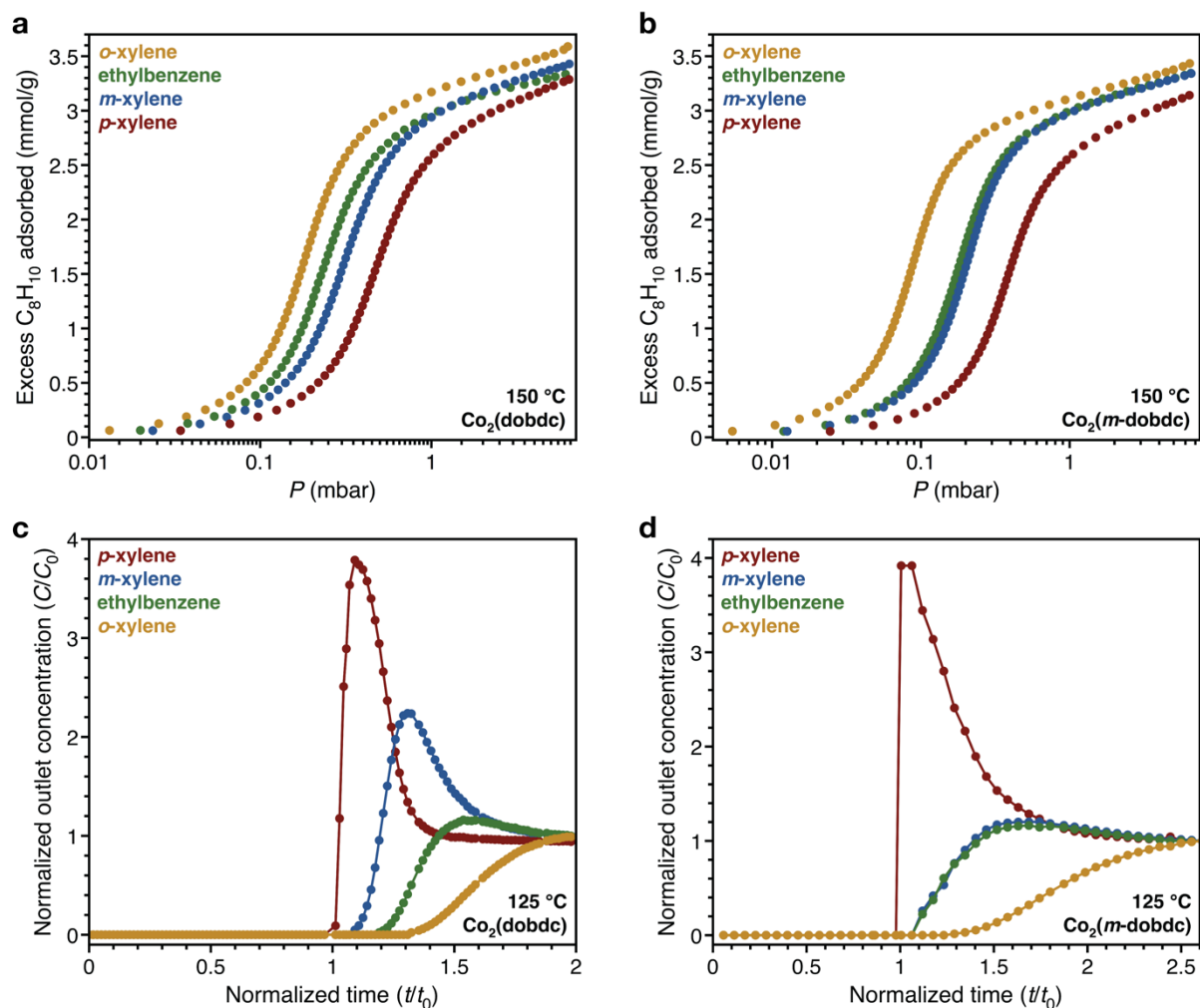


Figure 5.2. Single-component vapor-phase *o*-xylene (yellow), ethylbenzene (green), *m*-xylene (blue), and *p*-xylene (red) adsorption isotherms for $\text{Co}_2(\text{dobdc})$ (a) and $\text{Co}_2(m\text{-dobdc})$ (b) at 150°C . Multi-component vapor-phase breakthrough measurements for an equimolar mixture of *o*-xylene (yellow), ethylbenzene (green), *m*-xylene (blue), and *p*-xylene (red) vapor with $\text{Co}_2(\text{dobdc})$ (c) and $\text{Co}_2(m\text{-dobdc})$ (d) at 125°C . To facilitate comparisons between the two breakthrough experiments, time is normalized by assigning the time of *p*-xylene breakthrough as t_0 .

Although the breakthrough measurements clearly demonstrate separation of the four C₈ isomers in Co₂(dobdc), this experiment was conducted under adsorbate concentrations (~9–13 mbar partial pressure for each isomer) that are much lower than those typically employed in current adsorption-based processes, which operate in the liquid phase.⁵ As the selectivity of an adsorbent can show strong dependence on feed concentration,²⁰ Co₂(dobdc) was further evaluated through liquid-phase batch adsorption experiments at 33 °C using equimolar solutions of the four isomers (0.040–6.8 M total concentration) in *n*-heptane. The results of these measurements confirm that Co₂(dobdc) maintains its separation performance over a wide range of concentrations (Figure 5.3 and Figure 5.S22), even when approaching the concentrations in a pure xylenes mixture (~8 M total concentration). The selectivities calculated from these liquid-phase adsorption experiments (Table 5.2) agree well with the trends observed in both the single-component vapor-phase adsorption experiments and the multi-component breakthrough experiments. At the highest total concentration (6.8 M; 1.7 M in each isomer), Co₂(dobdc) is most selective for *o*-xylene over *p*-xylene (3.9 ± 0.5) and least selective for *o*-xylene over ethylbenzene (1.21 ± 0.02). Comparable values have been reported for two-component mixtures of *o*-xylene, *m*-xylene, and *p*-xylene in Ni₂(dobdc), although the reported capacities are much lower.²⁵

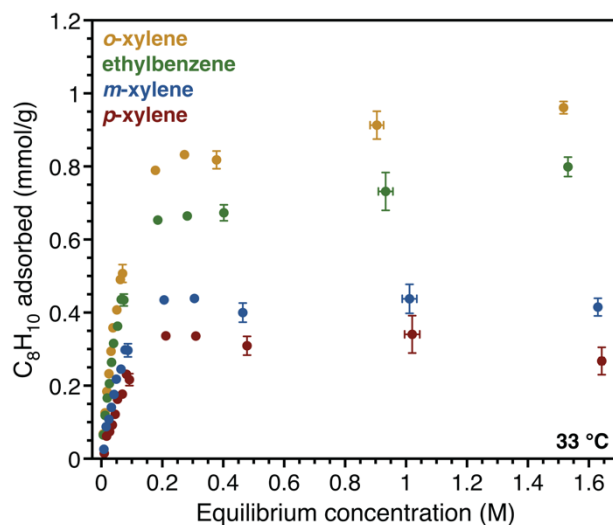


Figure 5.3. Multi-component liquid-phase *o*-xylene (yellow), ethylbenzene (green), *m*-xylene (blue), and *p*-xylene (red) adsorption measurements for Co₂(dobdc) at 33 °C using equimolar solutions of the four isomers in *n*-heptane. Data points with error bars (for measurements with initial C₈ isomer concentrations of 0.010, 0.050, 0.10, 0.50, 1.0, and 1.7 M) were determined from an average of three replications. The error bars for data points obtained from measurements with an initial concentration of 0.010 M are smaller than the markers.

Table 5.2. C₈ isomer selectivities for Co₂(dobdc) determined from a multi-component liquid-phase adsorption experiment with equimolar amounts of the C₈ isomers (1.7 M in each isomer; 6.8 M total concentration) in *n*-heptane at 33 °C.

C ₈ isomers	Selectivity
<i>o</i> -xylene/ <i>m</i> -xylene	2.5 ± 0.1
<i>o</i> -xylene/ <i>p</i> -xylene	3.9 ± 0.5
<i>o</i> -xylene/ethylbenzene	1.21 ± 0.02
ethylbenzene/ <i>m</i> -xylene	2.05 ± 0.05
ethylbenzene/ <i>p</i> -xylene	3.21 ± 0.4
<i>m</i> -xylene/ <i>p</i> -xylene	1.6 ± 0.2

The foregoing data suggest that Co₂(dobdc) could facilitate the separation of all four C₈ isomers in a single industrial adsorption process, which would be especially useful for removing ethylbenzene from C₈ mixtures. Although unable to separate all four isomers, Co₂(*m*-dobdc) could conceivably be applicable in current xylenes separation processes, wherein the *p*-xylene and *o*-xylene are obtained by separation and the mixture of *m*-xylene and ethylbenzene are regioisomerized to the equilibrium mixture. In addition, Co₂(*m*-dobdc) and its isostructural analogs with other metal cations also offer the advantage of combining high adsorption performance with low materials cost compared to that of other metal–organic frameworks.⁵³ The selectivity of both cobalt frameworks for the other isomers over *p*-xylene could even be used in the separation of these components from the 90+% *p*-xylene product mixtures of toluene disproportionation processes.⁵⁴

5.3.2. Structural Characterization of C₈ Isomer Adsorption. Single-crystal X-ray diffraction studies were performed to elucidate the structural features that underlie the ability of these frameworks to bind and differentiate the C₈ isomers. In general, structures were obtained from data collected at 100 K on single crystals that were soaked for ~24 h in an aliquot of each C₈ alkylaromatic. Contrary to the structural rigidity maintained by the M₂(dobdc) series of metal–organic frameworks upon adsorption of different small molecules,^{31-34,37,55-69} Co₂(dobdc) exhibits appreciable flexibility upon adsorption of the two strongest binding isomers, *o*-xylene and ethylbenzene. Upon binding either of these isomers, three out of every four pores in the framework elongate along the direction perpendicular to two opposing edges of the hexagonal channel (Figure 5.4). The arrangement of six deformed channels around a single undistorted channel maintains the $R\bar{3}$ symmetry of the lattice but lowers its translational symmetry, which manifests in the formation of a supercell with *a* and *b* edges that are double that of the undistorted framework. Notably, these experimental results corroborate computational work predicting similar adsorbate-induced lattice distortions in expanded variants of this framework.⁷⁰

Remarkably, each distorted pore in the *o*-xylene structure accommodates four xylene molecules for every three adsorbed in an undistorted channel, resulting in three distinct binding sites for *o*-xylene in the framework (Figure 5.4 and Figure 5.S3). Two cobalt(II) centers interact with a single *o*-xylene molecule at two of these sites, one located in a deformed channel and the other in an undistorted channel. In the third site, *o*-xylene binds to only a single cobalt(II) center through η^2 coordination of the aromatic ring. Only one binding site was resolved in the structure of ethylbenzene in Co₂(dobdc), which is located in the distorted pore of the framework (Figure 5.S5). In contrast, no framework distortion occurs when *m*-xylene or *p*-xylene bind to

Co₂(dobdc), and for these isomers only one xylene molecule is adsorbed for every two cobalt sites at full occupancy (Figure 5.S1 and 5.S2), consistent with the saturation capacities measured from the single-component adsorption isotherms.

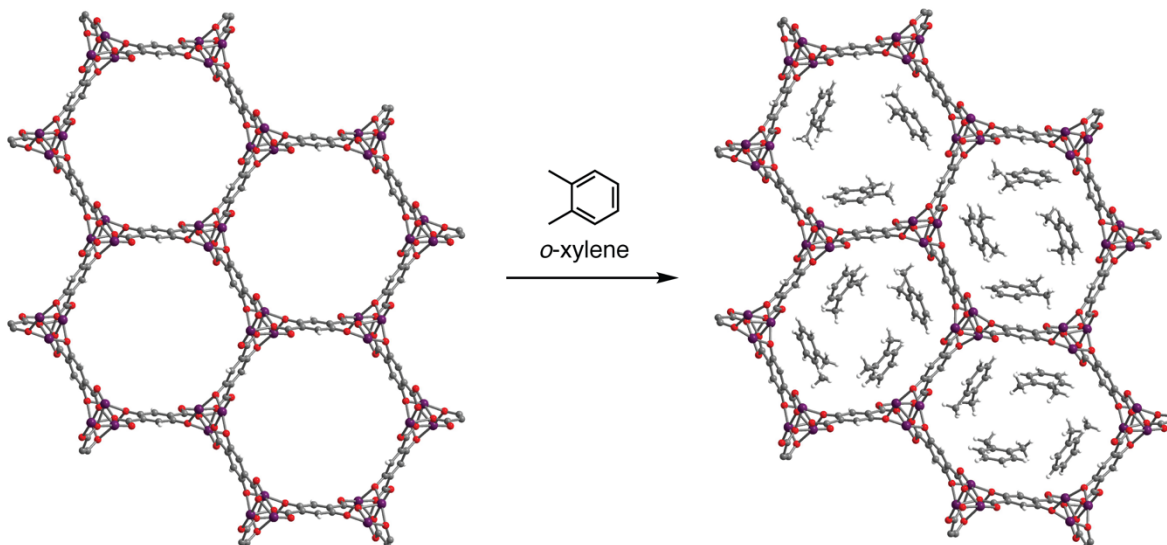


Figure 5.4. Structural distortion of Co₂(dobdc) upon adsorption of *o*-xylene as determined by single-crystal X-ray diffraction at 100 K. Three out of four channels distort to accommodate an additional equivalent of *o*-xylene. The *o*-xylene molecules in the undistorted pore were found to be disordered over two sets of locations due to the $\bar{3}$ symmetry of the framework, but only one set is shown here for clarity. Purple, red, gray, and white spheres represent Co, O, C, and H atoms, respectively.

In the *o*-xylene and ethylbenzene structures, the two cobalt centers interacting with a single molecule in the distorted channels are brought ~ 0.2 Å closer together than in the activated framework (7.854(2) Å with *o*-xylene and 7.897(3) Å with ethylbenzene compared to 8.0771(12) Å in the activated framework). This contraction facilitates a closer contact between the exposed cobalt sites and the adsorbate, resulting in greater stabilization of the adsorbed *o*-xylene or ethylbenzene molecules. As the framework distortion only occurs upon adsorption of the two strongest binding isomers, we can infer that this structural change requires sufficiently strong framework–guest interactions, while the tight packing of *o*-xylene molecules in the deformed channels suggests that guest–guest interactions also play a key role. Altogether, these structural results indicate that distortion of the framework is governed by an interplay between the energetic penalty incurred upon framework deformation and the thermodynamic stability gained through enhanced framework–guest interactions and the adsorption of additional molecules upon distortion.

To determine whether the structural distortion of Co₂(dobdc) occurs at temperatures relevant to those employed in evaluating C₈ isomer separations, we carried out variable-temperature powder X-ray diffraction studies on *o*-xylene- and ethylbenzene-soaked samples of the framework from 27–127 °C (Figures 5.S23 and 5.S24). These experiments revealed that the

distortion only happens at temperatures well below the those of the single-component adsorption isotherms (150 °C) and breakthrough measurements (125 °C). Specifically, *o*-xylene induces framework distortion at temperatures lower than or equal to 67 °C, while the ethylbenzene-soaked sample remained undistorted even as low as 27 °C. Moreover, diffraction experiments at 100 K on single crystals taken from the multi-component liquid-phase batch adsorption measurements showed no evidence of the distortion, indicating that the presence of the other isomers prevents *o*-xylene and ethylbenzene from distorting the framework. Thus, the observed separation performance of Co₂(dobdc) under the conditions of the breakthrough and liquid-phase adsorption experiments cannot be attributed to the flexibility of the framework. Comparing the *o*-xylene adsorption isotherms at 50 °C and 150 °C, however, demonstrates the distortion does impact the adsorption properties of the framework. Indeed, the saturation capacity at 150 °C corresponds to the loading of one *o*-xylene per two cobalt sites in the undistorted pore (3.2 mmol *o*-xylene), whereas the isotherm at 50 °C displays the anticipated 25% increase in capacity that accompanies the distortion (Figure 5.5).

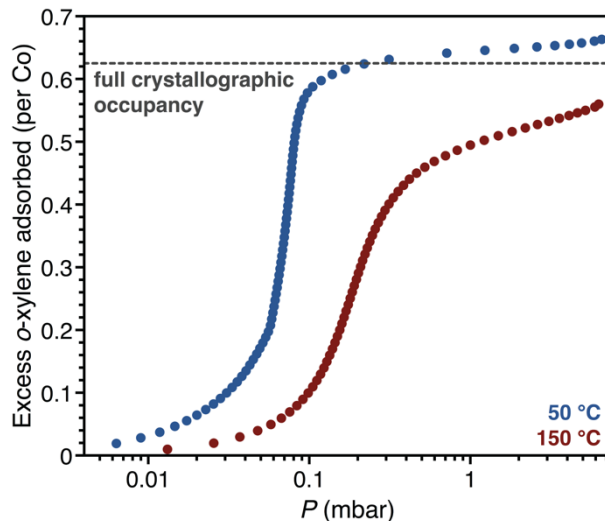


Figure 5.5. Comparison of the *o*-xylene adsorption isotherms for Co₂(dobdc) at 50 °C (blue) and 150 °C (red). The saturation capacity at 50 °C corresponds well with full crystallographic occupancy of all the *o*-xylene sites in the structure of *o*-xylene in Co₂(dobdc) at 100 K, whereas the capacity at 150 °C matches a loading of one *o*-xylene per two cobalt sites in an undistorted pore.

Comparison of the structures of the four isomers in Co₂(dobdc) at 100 K reveals that each isomer interacts with both the exposed cobalt(II) sites and the linker aromatic rings (Figure 5.6). All four isomers display comparable arene π - π interactions with the dobdc⁴⁻ linker, with centroid-to-centroid distances that range from 3.583(4) Å for *p*-xylene to 3.651(9) Å for *o*-xylene. The similarity of these distances and lack of an apparent trend with binding affinity suggest that π - π interactions do not contribute significantly to the xylene isomer selectivity. In contrast, clear differences can be identified in the interactions of each isomer with the exposed cobalt(II) sites of the framework. Significantly, *o*-xylene, ethylbenzene, and *m*-xylene are

capable of interacting with two cobalt(II) centers situated at opposite ends of a linker, whereas *p*-xylene, the weakest binding isomer, interacts with only a single metal site. Two of the binding sites for *o*-xylene feature the interaction of a methyl group and an aryl C–H group at the 1 and 4 positions of the *o*-xylene ring with two cobalt(II) centers on opposing sides of a dobdc^{4-} linker (Figure 5.6 and Figure 5.S3), with $\text{Co}\cdots\text{C}_{\text{methyl}}$ distances of 3.101(18) Å and 3.13(5) Å and $\text{Co}\cdots\text{C}_{\text{aryl}}$ distances of 2.789(19) Å and 2.9130(18) Å, respectively. These distances are much longer than those observed for agostic interaction in alkyl and aryl complexes,⁷¹⁻⁷⁷ indicating that the xylene molecule binds through weak non-covalent interactions that arise from polarization by the exposed partial positive charge on the cobalt centers. We note that although another binding mode was identified for *o*-xylene in the distorted structure of $\text{Co}_2(\text{dobdc})$ (Figure 5.S4), this site is less relevant as the distortion does not occur under the conditions of the multi-component separation.

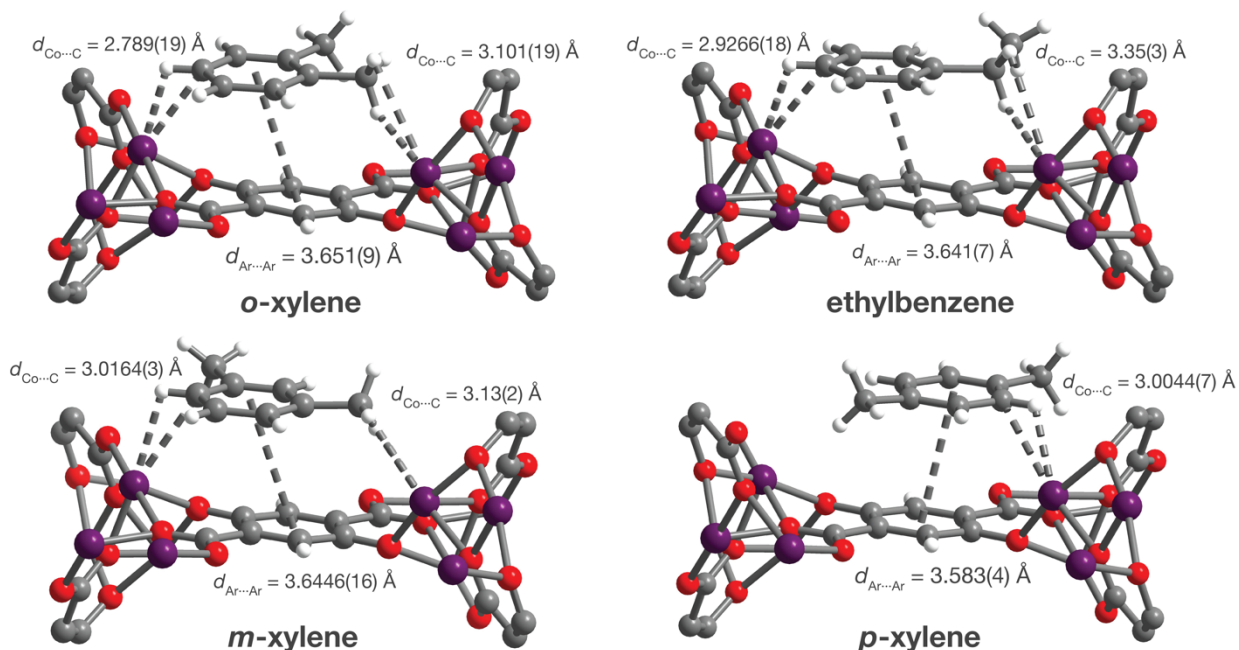


Figure 5.6. A portion of the structures of *o*-xylene, ethylbenzene, *m*-xylene, and *p*-xylene in $\text{Co}_2(\text{dobdc})$ at 100 K as determined through analysis of single-crystal X-ray diffraction data, showing the interactions of each isomer with two exposed cobalt(II) sites and the linker arene ring. The structures shown for *o*-xylene and ethylbenzene correspond to binding sites within the distorted hexagonal channels. Two additional binding sites were located for *o*-xylene (Figure S2). Purple, red, gray, and white spheres represent Co, O, C, and H atoms, respectively.

Ethylbenzene also interacts with two metal sites through a benzylic carbon and an opposing aryl C–H group. Both interactions are longer than those observed with *o*-xylene, in line with the lower affinity of $\text{Co}_2(\text{dobdc})$ for ethylbenzene (Figure 5.6). These comparatively weaker Co^{II} –ethylbenzene interactions likely result from the additional steric bulk of the ethyl group, which

prevents a closer approach of molecule to the cobalt sites and is evident in the much longer $\text{Co}\cdots\text{C}_{\text{benzyl}}$ distance (3.35(3) Å) of ethylbenzene compared to the $\text{Co}\cdots\text{C}_{\text{methyl}}$ distance of *o*-xylene (3.101(8) Å).

The second weakest adsorbing isomer, *m*-xylene, also binds to two cobalt(II) sites through opposing alkyl and aryl C–H groups. In comparison to *o*-xylene and ethylbenzene, *m*-xylene exhibits a longer $\text{Co}\cdots\text{C}_{\text{aryl}}$ distance of 3.0164(3) Å, which can be attributed to steric repulsion between the adjacent methyl group and a linker oxygen atom that is only 3.34(3) Å away. The longer $\text{Co}\cdots\text{C}_{\text{aryl}}$ distance suggests that a weaker Co^{II} –aryl interaction leads to the lower affinity of the framework for this isomer.

The 1,4 substitution of *p*-xylene causes it to be too long to adopt the same orientation as the other C_8 isomers, precluding its interaction with two metal sites. As a consequence, this isomer is only stabilized by the interaction of an aryl C–H group with a single cobalt(II) center and an arene π – π interaction with the linker. The absence of a second Co^{II} –*p*-xylene interaction results in this isomer binding the weakest to $\text{Co}_2(\text{dobdc})$. Single-component adsorption isotherms from an expanded analog of this material, $\text{Co}_2(\text{dobpdc})$ ($\text{dobpdc}^{4-} = 4,4'$ -dioxidobiphenyl-3,3'-dicarboxylate),⁴¹ corroborate that interaction with only a single metal site leads to weaker adsorption of the C_8 isomers, as the longer distances between the two cobalt(II) centers across each linker in this material prevent any of the four isomers from interacting with both cobalt sites (Figure 5.S21).

Interestingly, $\text{Co}_2(m\text{-dobdc})$ does not exhibit pore distortion upon binding any of the isomers at the investigated temperatures. The lack of any observed distortion likely arises from the closer distance between the cobalt(II) centers in $\text{Co}_2(m\text{-dobdc})$ (7.7923(15) Å) compared to $\text{Co}_2(\text{dobdc})$ (8.0771(12) Å). This difference of ~ 0.2 Å matches well with the observed change in $\text{Co}\cdots\text{Co}$ distance upon framework distortion in $\text{Co}_2(\text{dobdc})$ and likely precludes the need for a distortion to maximize the interaction between two metal sites and a single C_8 molecule in $\text{Co}_2(m\text{-dobdc})$. Furthermore, this difference in behavior between the isomeric frameworks highlights how subtle changes in the framework structure can affect its adsorption properties. As in $\text{Co}_2(\text{dobdc})$, *o*-xylene and ethylbenzene were also observed to bind to two cobalt(II) sites in $\text{Co}_2(m\text{-dobdc})$ through the interaction of an alkyl group and an aryl C–H group (Figure 5.7), resulting in three binding sites in each hexagonal channel related by three-fold symmetry (Figures S6 and 5.S7). The stronger binding isomer, *o*-xylene, displays a shorter $\text{Co}\cdots\text{C}_{\text{aryl}}$ distance of 2.7953(7) Å and a similar $\text{Co}\cdots\text{C}_{\text{alkyl}}$ distance of 2.89(3) Å compared to the respective distances of 3.09(3) Å and 2.81(4) Å for ethylbenzene, suggesting that $\text{Co}_2(m\text{-dobdc})$ also distinguishes between the two isomers through the strength of their interactions with two metal sites. Although sufficiently resolved structures of the other C_8 alkylaromatic molecules in $\text{Co}_2(m\text{-dobdc})$ could not be obtained due to severe disorder enforced by the mirror symmetry of the framework, the selectivity of $\text{Co}_2(m\text{-dobdc})$ for the different isomers is expected to be controlled by similar factors as those identified in $\text{Co}_2(\text{dobdc})$.

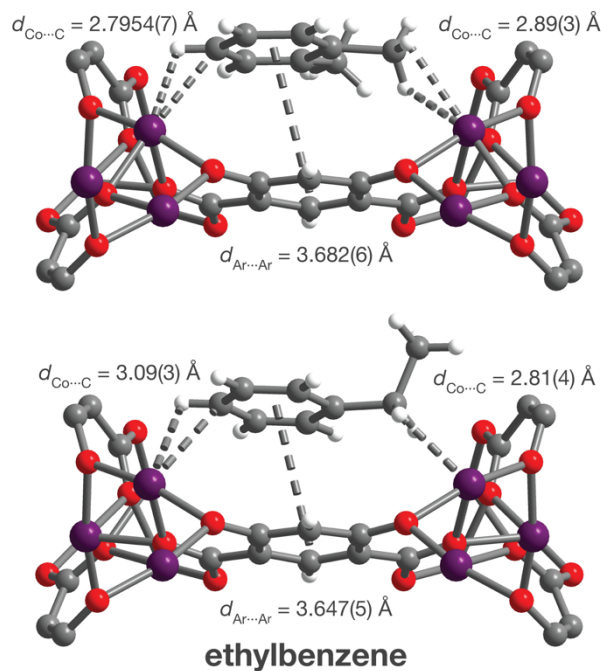


Figure 5.7. A portion of the structures of *o*-xylene and ethylbenzene in $\text{Co}_2(m\text{-dobdc})$ at 100 K as determined through analysis of single-crystal X-ray diffraction data, showing the interactions of each isomer with two exposed cobalt(II) sites and the linker arene ring. The C_8 isomers in both structures are disordered over two positions due to the mirror symmetry of the framework. Water was found to contaminate 30% of the cobalt(II) sites in the structure of ethylbenzene in $\text{Co}_2(m\text{-dobdc})$, but only ethylbenzene is shown here for clarity. Purple, red, gray, and white spheres represent Co, O, C, and H atoms, respectively.

5.4 Conclusions and Outlook

The foregoing results demonstrate that the C_8 alkylaromatics *o*-xylene, *m*-xylene, *p*-xylene, and ethylbenzene can be separated by the metal–organic frameworks $\text{Co}_2(\text{dobdc})$ and $\text{Co}_2(m\text{-dobdc})$ through the varied extent of interaction of each isomer with two adjacent coordinatively unsaturated cobalt(II) centers. Single-component adsorption isotherms, multi-component vapor-phase breakthrough measurements, and multi-component liquid-phase batch adsorption experiments show that $\text{Co}_2(\text{dobdc})$ effectively separates all four isomers and has the strongest affinity for *o*-xylene, followed by ethylbenzene, *m*-xylene, and *p*-xylene. In contrast, $\text{Co}_2(m\text{-dobdc})$ can only distinguish between three of the four isomers, due to its similar binding affinity for *m*-xylene and ethylbenzene.

Single-crystal X-ray diffraction experiments indicate that the strong adsorption of the C_8 alkylaromatics arise from their interactions with a linker aromatic ring and exposed cobalt(II) sites in both $\text{Co}_2(\text{dobdc})$ and $\text{Co}_2(m\text{-dobdc})$. In particular, a comparison of the structures of the four xylene isomers in $\text{Co}_2(\text{dobdc})$ shows that the framework distinguishes among the isomers due to nuanced differences in the interaction of *o*-xylene, ethylbenzene, and *m*-xylene with two

adjacent cobalt(II) centers and the inability of *p*-xylene to interact with a second metal site. Furthermore, the structures of *o*-xylene and ethylbenzene in Co₂(dobdc) reveal that the framework undergoes an unprecedented structural distortion upon binding of these isomers, allowing the accommodation of additional adsorbate molecules.

Altogether, these results highlight how leveraging the interaction of multiple coordinatively unsaturated metal centers with a single molecule may lead to the design of new adsorbents for the separation of hydrocarbons. In particular, altering the distance between the exposed metal sites in related materials could afford control over their selectivity for the different C₈ isomers and could potentially enable the separation of mixtures containing other adsorbates.

5.5. Acknowledgements

Thanks to Miguel I. Gonzalez for assistance with all parts of this chapter, Eric D. Bloch for initial research, Philip J. Milner for assistance with the liquid-phase experiments, Douglas A. Reed and Gokhan Barin for assistance with the gas-phase experiments, and Matthew R. Hudson, Jarad A. Mason, and Craig M. Brown for assistance with X-ray diffraction experiments. This work was supported through the Center for Gas Separations Relevant to Clean Energy Technologies, an Energy Frontier Research Center funded by the U.S. Department of Energy, Office of Science, Office of Basic Energy Sciences under Award DE-SC0001015. This research used resources of the Advanced Light Source, which is supported by the Director, Office of Science, Office of Basic Energy Sciences, of the U.S. Department of Energy under Contract No. DE-AC02-05CH11231, and the Advanced Photon Source, a DoE Office of Science User Facility operated by Argonne National Laboratory under Contract No. DE-AC02-06CH11357. We thank Greg Halder and the 17-BM-B staff for experimental assistance. Thanks to the National Science Foundation for graduate fellowship support. Thanks to Katie R. Meihaus for editorial assistance. Also thanks to Simon J. Teat and Rebecca L. Siegelman for helpful discussions.

5.6. References and Supplementary Data

1. *Materials for Separation Technologies. Energy and Emission Reduction Opportunities*; U.S. Department of Energy, 2005.
2. Sholl, D. S.; Lively, R. P. *Nature* 2016, 532 (7600), 435–437.
3. Fabri, J.; Graeser, U.; Simo, T. A. In *Ullman's Encyclopedia of Industrial Chemistry*; Wiley-VCH Verlag GmbH & Co. KGaA, 2000.
4. Denayer, J. F. M.; De Vos, D.; Leflaive, P. In *Metal-Organic Frameworks*; Farrusseng, D., Ed.; Applications from Catalysis to Gas Storage; Wiley-VCH Verlag GmbH & Co. KGaA: Weinheim, Germany, 2011; Vol. 83, pp 171–190.
5. Minceva, M.; Rodrigues, A. E. *AIChE J.* 2007, 53 (1), 138–149.
6. Pellegrino, J. L. *Energy and Environmental Profile of the Chemicals Industry*; U.S. Department of Energy, 2000.
7. Welch, V. A.; Fallon, K. J.; Gelbke, H.-P. *Ethylbenzene*; Wiley-VCH Verlag GmbH & Co. KGaA: Weinheim, Germany, 2000; Vol. 13, pp 451–414.
8. Li, J.-R.; Kuppler, R. J.; Zhou, H.-C. *Chem. Soc. Rev.* 2009, 38 (5), 1477–29.
9. Guo, G.-Q.; Chen, H.; Long, Y.-C. *Microporous Mesoporous Mater.* 2000, 39 (1-2), 149–161.

10. Yang, Y.; Bai, P.; Guo, X. *Ind. Eng. Chem. Res.* 2017.
11. Hulme, R.; Rosensweig, R. E.; Ruthven, D. M. *Ind. Eng. Chem. Res.* 1991, *30* (4), 752–760.
12. Yan, T. Y. *Ind. Eng. Chem. Res.* 1989, *28* (5), 572–576.
13. Ruthven, D. M.; Goddard, M. *Zeolites* 1986, *6* (4), 275–282.
14. Santacesaria, E.; Morbidelli, M.; Servida, A.; Storti, G.; Carra, S. *Ind. Eng. Chem. Process Des. Dev.* 1982, *21* (3), 446–451.
15. Koh, D.-Y.; McCool, B. A.; Deckman, H. W.; Lively, R. P. *Science* 2016, *353* (6301), 804–807.
16. Herm, Z. R.; Bloch, E. D.; Long, J. R. *Chem. Mater.* 2014, *26* (1), 323–338.
17. Van de Voorde, B.; Bueken, B.; Denayer, J.; De Vos, D. *Chem. Soc. Rev.* 2014, *43* (16), 5766–5788.
18. Alaerts, L.; Kirschhock, C. E. A.; Maes, M.; van der Veen, M. A.; Finsy, V.; Depla, A.; Martens, J. A.; Baron, G. V.; Jacobs, P. A.; Denayer, J. F. M.; De Vos, D. E. *Angew. Chem. Int. Ed.* 2007, *46* (23), 4293–4297.
19. Alaerts, L.; Maes, M.; Jacobs, P. A.; Denayer, J. F. M.; De Vos, D. E. *Phys. Chem. Chem. Phys.* 2008, *10* (20), 2979–2985.
20. Finsy, V.; Verelst, H.; Alaerts, L.; De Vos, D.; Jacobs, P. A.; Baron, G. V.; Denayer, J. F. M. *J. Am. Chem. Soc.* 2008, *130* (22), 7110–7118.
21. Alaerts, L.; Maes, M.; Giebeler, L.; Jacobs, P. A.; Martens, J. A.; Denayer, J. F. M.; Kirschhock, C. E. A.; De Vos, D. E. *J. Am. Chem. Soc.* 2008, *130* (43), 14170–14178.
22. Gu, Z.-Y.; Jiang, D.-Q.; Wang, H.-F.; Cui, X.-Y.; Yan, X.-P. *J. Phys. Chem. C* 2010, *114* (1), 311–316.
23. Bárçia, P. S.; Guimarães, D.; Mendes, P. A. P.; Silva, J. A. C.; Guillerm, V.; Chevreau, H.; Serre, C.; Rodrigues, A. E. *Microporous Mesoporous Mater.* 2011, *139* (1-3), 67–73.
24. Vermoortele, F.; Maes, M.; Moghadam, P. Z.; Lennox, M. J.; Ragon, F.; Boulhout, M.; Biswas, S.; Laurier, K. G. M.; Beurroies, I.; Denoyel, R.; Roeffaers, M.; Stock, N.; Düren, T.; Serre, C.; De Vos, D. E. *J. Am. Chem. Soc.* 2011, *133* (46), 18526–18529.
25. Peralta, D.; Barthelet, K.; Pérez-Pellitero, J.; Chizallet, C.; Chaplais, G.; Simon-Masseron, A.; Pirngruber, G. D. *J. Phys. Chem. C* 2012, *116* (41), 21844–21855.
26. Warren, J. E.; Perkins, C. G.; Jelfs, K. E.; Boldrin, P.; Chater, P. A.; Miller, G. J.; Manning, T. D.; Briggs, M. E.; Stylianou, K. C.; Claridge, J. B.; Rosseinsky, M. J. *Angew. Chem. Int. Ed.* 2014, *53* (18), 4592–4596.
27. Osta, El, R.; Carlin-Sinclair, A.; Guillou, N.; Walton, R. I.; Vermoortele, F.; Maes, M.; De Vos, D.; Millange, F. *Chem. Mater.* 2012, *24* (14), 2781–2791.
28. Agrawal, M.; Bhattacharyya, S.; Huang, Y.; Jayachandrababu, K. C.; Murdock, C. R.; Bentley, J. A.; Rivas-Cardona, A.; Mertens, M. M.; Walton, K. S.; Sholl, D. S.; Nair, S. J. *J. Phys. Chem. C* 2017.
29. Caskey, S. R.; Wong-Foy, A. G.; Matzger, A. J. *J. Am. Chem. Soc.* 2008, *130* (33), 10870–10871.
30. Dietzel, P. D. C.; Besikiotis, V.; Blom, R. *J. Mater. Chem.* 2009, *19* (39), 7362–7370.
31. Bloch, E. D.; Murray, L. J.; Queen, W. L.; Chavan, S.; Maximoff, S. N.; Bigi, J. P.; Krishna, R.; Peterson, V. K.; Grandjean, F.; Long, G. J.; Smit, B.; Bordiga, S.; Brown, C. M.; Long, J. R. *J. Am. Chem. Soc.* 2011, *133* (37), 14814–14822.
32. Bloch, E. D.; Queen, W. L.; Krishna, R.; Zadrozny, J. M.; Brown, C. M.; Long, J. R. *Science* 2012, *335* (6076), 1606–1610.

33. Bloch, E. D.; Hudson, M. R.; Mason, J. A.; Chavan, S.; Crocellà, V.; Howe, J. D.; Lee, K.; Dzubak, A. L.; Queen, W. L.; Zadrozny, J. M.; Geier, S. J.; Lin, L.-C.; Gagliardi, L.; Smit, B.; Neaton, J. B.; Bordiga, S.; Brown, C. M.; Long, J. R. *J. Am. Chem. Soc.* 2014, *136* (30), 10752–10761.
34. Queen, W. L.; Hudson, M. R.; Bloch, E. D.; Mason, J. A.; Gonzalez, M. I.; Lee, J. S.; Gygi, D.; Howe, J. D.; Lee, K.; Darwish, T. A.; James, M.; Peterson, V. K.; Teat, S. J.; Smit, B.; Neaton, J. B.; Long, J. R.; Brown, C. M. *Chem. Sci.* 2014, *5* (12), 4569–4581.
35. Xiao, D. J.; Gonzalez, M. I.; Darago, L. E.; Vogiatzis, K. D.; Haldoupis, E.; Gagliardi, L.; Long, J. R. *J. Am. Chem. Soc.* 2016, *138* (22), 7161–7170.
36. Reed, D. A.; Xiao, D. J.; Gonzalez, M. I.; Darago, L. E.; Herm, Z. R.; Grandjean, F.; Long, J. R. *J. Am. Chem. Soc.* 2016, *138* (17), 5594–5602.
37. Geier, S. J.; Mason, J. A.; Bloch, E. D.; Queen, W. L.; Hudson, M. R.; Brown, C. M.; Long, J. R. *Chem. Sci.* 2013, *4* (5), 2054–2061.
38. Bloch, E. D.; Queen, W. L.; Hudson, M. R.; Mason, J. A.; Xiao, D. J.; Murray, L. J.; Flacau, R.; Brown, C. M.; Long, J. R. *Angewandte Chemie* 2016, *128* (30), 8747–8751.
39. Murray, L. J.; Dincă, M.; Yano, J.; Chavan, S.; Bordiga, S.; Brown, C. M.; Long, J. R. *J. Am. Chem. Soc.* 2010, *132* (23), 7856–7857.
40. Sumida, K.; Rogow, D. L.; Mason, J. A.; McDonald, T. M.; Bloch, E. D.; Herm, Z. R.; Bae, T.-H.; Long, J. R. *Chem. Rev.* 2012, *112* (2), 724–781.
41. Gygi, D.; Bloch, E. D.; Mason, J. A.; Hudson, M. R.; Gonzalez, M. I.; Siegelman, R. L.; Darwish, T. A.; Queen, W. L.; Brown, C. M.; Long, J. R. *Chem. Mater.* 2016, *28* (4), 1128–1138.
42. Dietzel, P. D. C.; Morita, Y.; Blom, R.; Fjellvåg, H. *Angew. Chem. Int. Ed.* 2005, *44* (39), 6354–6358.
43. Kapelewski, M. T.; Geier, S. J.; Hudson, M. R.; Stück, D.; Mason, J. A.; Nelson, J. N.; Xiao, D. J.; Hulvey, Z.; Gilmour, E.; FitzGerald, S. A.; Head-Gordon, M.; Brown, C. M.; Long, J. R. *J. Am. Chem. Soc.* 2014, *136* (34), 12119–12129.
44. Bruker Analytical X-ray Systems, Inc. *SAINT and APEX 2 Software for CCD Diffractometers*; Bruker Analytical X-ray Systems, Inc.: Madison, WI, USA, 2000.
45. Sheldrick, G. M. *SADABS*; Bruker Analytical X-ray Systems, Inc.: Madison, WI, USA, 2014.
46. Sheldrick, G. M. *Acta Crystallogr., A, Found. Crystallogr.* 2008, *64* (Pt 1), 112–122.
47. Sheldrick, G. M. *SHELXS*; University of Göttingen, Germany, 2014.
48. Sheldrick, G. M. *Acta Crystallogr A Found Adv* 2015, *71* (Pt 1), 3–8.
49. Sheldrick, G. M. *SHELXL*; University of Göttingen, Germany: University of Göttingen, Germany, 2014.
50. Dolomanov, O. V.; Bourhis, L. J.; Gildea, R. J.; Howard, J. A. K.; Puschmann, H. *Journal of Applied Crystallography* 2009, *42* (2), 339–341.
51. Minceva, M.; Rodrigues, A. E. *Chemical Engineering Research and Design* 2004, *82* (5), 667–681.
52. Bellat, J.-P.; Simonot-Grange, M.-H.; Jullian, S. *Zeolites* 1995, *15* (2), 124–130.
53. DeSantis, D.; Mason, J. A.; James, B. D.; Houchins, C.; Long, J. R.; Veenstra, M. *Energy & Fuels* 2017, *31* (2), 2024–2032.
54. Perego, C.; Pollesel, P. In *Advances in Nanoporous Materials*; Ernst, S., Ed.; Advances in Nanoporous Materials; Elsevier, 2010; Vol. 1, pp 97–149.

55. Dietzel, P. D. C.; Georgiev, P. A.; Eckert, J.; Blom, R.; Strässle, T.; Unruh, T. *Chem. Commun.* 2010, 46 (27), 4962–4963.
56. Xiao, D. J.; Bloch, E. D.; Mason, J. A.; Queen, W. L.; Hudson, M. R.; Planas, N.; Borycz, J.; Dzubak, A. L.; Verma, P.; Lee, K.; Bonino, F.; Crocellà, V.; Yano, J.; Bordiga, S.; Truhlar, D. G.; Gagliardi, L.; Brown, C. M.; Long, J. R. *Nature Chemistry* 2014, 6 (7), 590–595.
57. McKinlay, A. C.; Xiao, B.; Wragg, D. S.; Wheatley, P. S.; Megson, I. L.; Morris, R. E. *J. Am. Chem. Soc.* 2008, 130 (31), 10440–10444.
58. Bloch, E. D.; Queen, W. L.; Chavan, S.; Wheatley, P. S.; Zadrozny, J. M.; Morris, R.; Brown, C. M.; Lamberti, C.; Bordiga, S.; Long, J. R. *J. Am. Chem. Soc.* 2015, 137 (10), 3466–3469.
59. Sumida, K.; Her, J.-H.; Dincă, M.; Murray, L. J.; Schloss, J. M.; Pierce, C. J.; Thompson, B. A.; FitzGerald, S. A.; Brown, C. M.; Long, J. R. *J. Phys. Chem. C* 2011, 115 (16), 8414–8421.
60. Queen, W. L.; Bloch, E. D.; Brown, C. M.; Hudson, M. R.; Mason, J. A.; Murray, L. J.; Ramirez-Cuesta, A. J.; Peterson, V. K.; Long, J. R. *Dalton Trans.* 2012, 41 (14), 4180–4188.
61. Lee, J. S.; Vlaisavljevich, B.; Britt, D. K.; Brown, C. M.; Haranczyk, M.; Neaton, J. B.; Smit, B.; Long, J. R.; Queen, W. L. *Adv. Mater.* 2015, 27 (38), 5785–5796.
62. Bloch, W. M.; Burgun, A.; Coghlan, C. J.; Lee, R.; Coote, M. L.; Doonan, C. J.; Sumbly, C. J. *Nature Chemistry* 2014, 6 (10), 906–912.
63. Furukawa, H.; Gándara, F.; Zhang, Y.-B.; Jiang, J.; Queen, W. L.; Hudson, M. R.; Yaghi, O. M. *J. Am. Chem. Soc.* 2014, 136 (11), 4369–4381.
64. Magdysyuk, O. V.; Adams, F.; Liermann, H.-P.; Spanopoulos, I.; Trikalitis, P. N.; Hirscher, M.; Morris, R. E.; Duncan, M. J.; McCormick, L. J.; Dinnebier, R. E. *Phys. Chem. Chem. Phys.* 2014, 16 (43), 23908–23914.
65. Ghose, S. K.; Li, Y.; Yakovenko, A.; Dooryhee, E.; Ehm, L.; Ecker, L. E.; Dippel, A.-C.; Halder, G. J.; Strachan, D. M.; Thallapally, P. K. *J. Phys. Chem. Lett.* 2015, 6 (10), 1790–1794.
66. Dietzel, P. D. C.; Johnsen, R. E.; Fjellvåg, H.; Bordiga, S.; Groppo, E.; Chavan, S.; Blom, R. *Chem. Commun.* 2008, No. 41, 5125–5127.
67. Liu, Y.; Kabbour, H.; Brown, C. M.; Neumann, D. A.; Ahn, C. C. *Langmuir* 2008, 24 (9), 4772–4777.
68. Gonzalez, M. I.; Mason, J. A.; Bloch, E. D.; Teat, S. J.; Gagnon, K. J.; Morrison, G. Y.; Queen, W. L.; Long, J. R. *Chem. Sci.* 2017, 8 (6), 4387–4398.
69. Rosnes, M. H.; Sheptyakov, D.; Franz, A.; Frontzek, M.; Dietzel, P. D. C.; Georgiev, P. A. *Phys. Chem. Chem. Phys.* 2017, 103, 2347.
70. Jawahery, S.; Simon, C. M.; Braun, E.; Witman, M.; Tiana, D.; Vlaisavljevich, B.; Smit, B. *Nat Commun* 2016, 8, 1–9.
71. Pike, S. D.; Thompson, A. L.; Algarra, A. G.; Apperley, D. C.; Macgregor, S. A.; Weller, A. S. *Science* 2012, 337 (6102), 1648–1651.
72. Pike, S. D.; Chadwick, F. M.; Rees, N. H.; Scott, M. P.; Weller, A. S.; Krämer, T.; Macgregor, S. A. *J. Am. Chem. Soc.* 2015, 137 (2), 820–833.
73. Chadwick, F. M.; Rees, N. H.; Weller, A. S.; Krämer, T.; Iannuzzi, M.; Macgregor, S. A. *Angew. Chem. Int. Ed.* 2016, 55 (11), 3677–3681.

74. Vigalok, A.; Uzan, O.; Shimon, L. J. W.; Ben-David, Y.; Martin, J. M. L.; Milstein, D. *J. Am. Chem. Soc.* 1998, *120* (48), 12539–12544.
75. Dani, P.; Karlen, T.; Gossage, R. A.; Smeets, W. J. J.; Spek, A. L.; Van Koten, G. *J. Am. Chem. Soc.* 1997, *119* (46), 11317–11318.
76. Gusev, D. G.; Madott, M.; Dolgushin, F. M.; Lyssenko, K. A.; Antipin, M. Y. *Organometallics* 2000, *19* (9), 1734–1739.
77. Stępień, M.; Latos-Grażyński, L.; Szterenber, L.; Panek, J.; Latajka, Z. *J. Am. Chem. Soc.* 2004, *126* (14), 4566–4580.

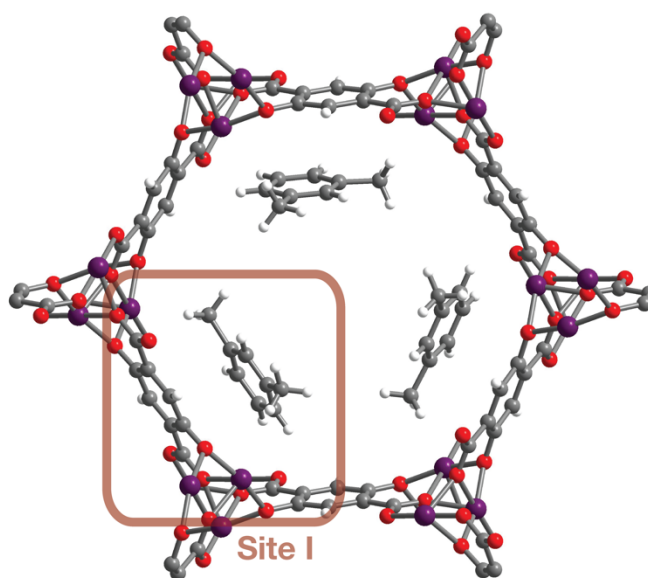


Figure 5.S1. A portion of the crystal structure of $\text{Co}_2(\text{dobdc})\cdot 0.74(m\text{-xylene})$ at 100 K as determined through analysis of single-crystal X-ray diffraction data. The chemical occupancy for m -xylene were refined to be 74% (37% site occupancy). The m -xylene molecules were found to be disordered over two sets of locations due to the $\bar{3}$ symmetry of the framework, but only one set is shown here for clarity. Purple, red, gray, and white spheres represent Co, O, C, and H atoms, respectively.

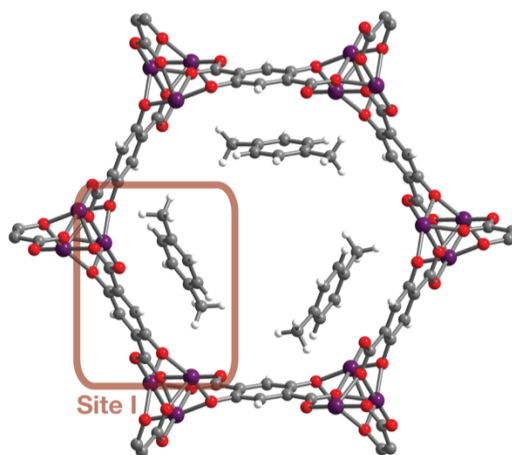


Figure 5.S2. A portion of the crystal structure of $\text{Co}_2(\text{dobdc}) \cdot 0.82(p\text{-xylene})$ at 100 K as determined through analysis of single-crystal X-ray diffraction data. The chemical occupancy for *p*-xylene were refined to be 82% (41% site occupancy). The *p*-xylene molecules were found to be disordered over two sets of locations due to the $\bar{3}$ symmetry of the framework, but only one set is shown here for clarity. Purple, red, gray, and white spheres represent Co, O, C, and H atoms, respectively.

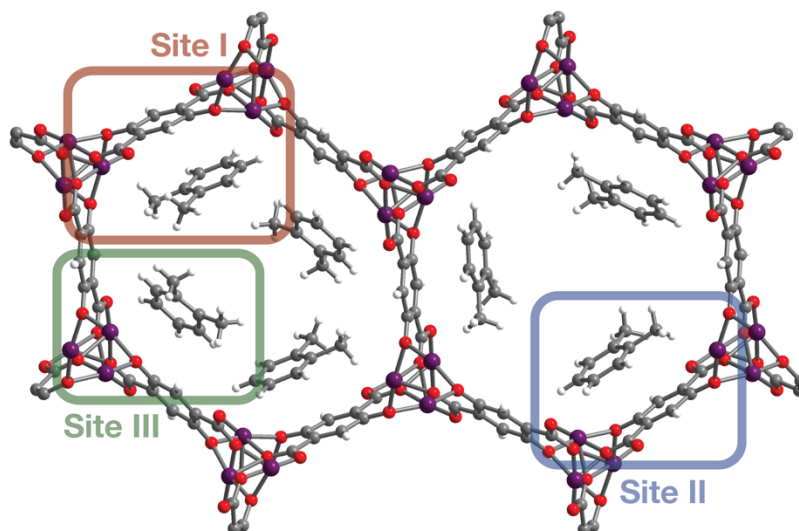


Figure 5.S3. A portion of the crystal structure of $\text{Co}_2(\text{dobdc}) \cdot 0.99(o\text{-xylene})$ at 100 K as determined through analysis of single-crystal X-ray diffraction data. In the structure, three out of four channels distort to accommodate an additional equivalent of *o*-xylene. The chemical occupancies for *o*-xylene were refined to be 89% for Site I, 78% for Site II, and 69% for Site III. The *o*-xylene molecules in the undistorted pore (Site II) were found to be disordered over two sets of locations due to the $\bar{3}$ symmetry of the framework, but only one set is shown here for clarity. Purple, red, gray, and white spheres represent Co, O, C, and H atoms, respectively.

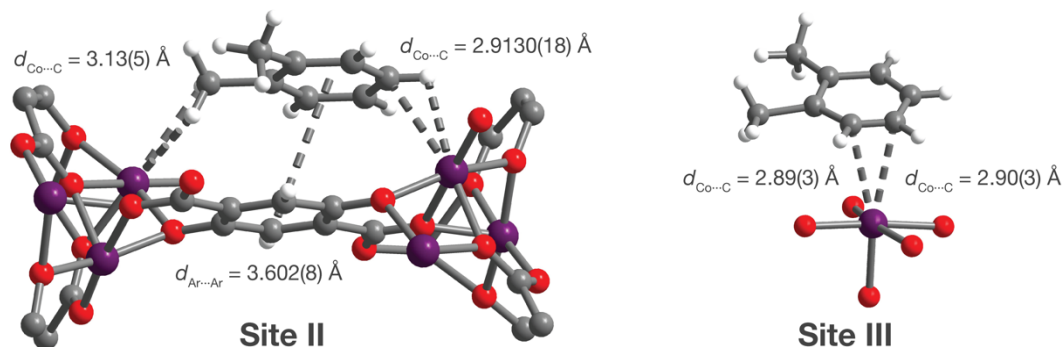


Figure 5.S4. Views of the single-crystal structure of *o*-xylene in $\text{Co}_2(\text{dobdc})$ at 100 K showing two additional binding sites for *o*-xylene. Site II shows the interaction of *o*-xylene with two exposed cobalt(ii) sites and the linker arene ring, whereas *o*-xylene at Site III interacts with only a single cobalt center. The *o*-xylene molecules in the undistorted pore (Site II) were found to be disordered over two sets of locations due to the $\bar{3}$ symmetry of the framework, but only one set is shown here for clarity. Purple, red, gray, and white spheres represent Co, O, C, and H atoms, respectively.

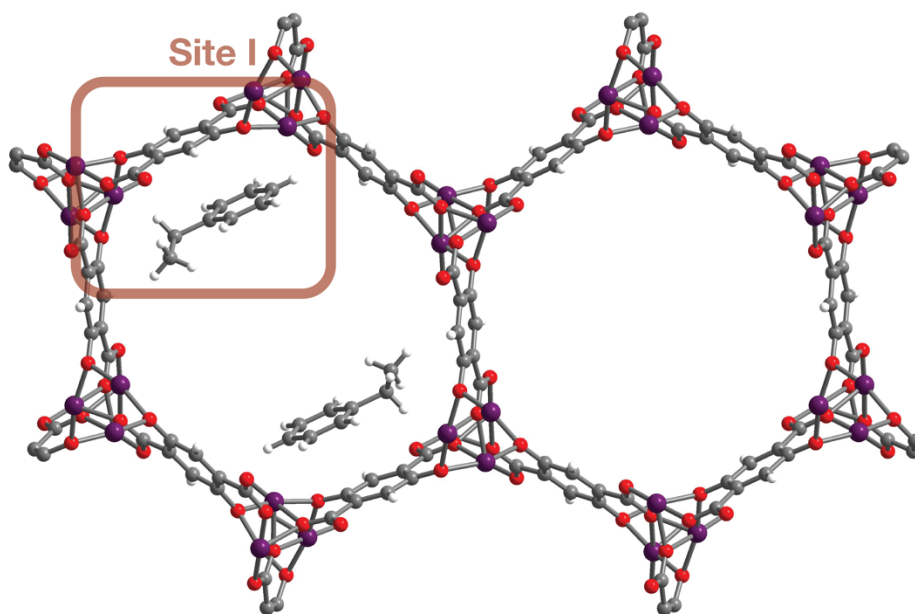


Figure 5.S5. A portion of the crystal structure of $\text{Co}_2(\text{dobdc}) \cdot 0.36(\text{ethylbenzene})$ at 100 K as determined through analysis of single-crystal X-ray diffraction data. In the structure, three out of four channels distort. The chemical occupancy for ethylbenzene were refined to be 71%. Purple, red, gray, and white spheres represent Co, O, C, and H atoms, respectively.

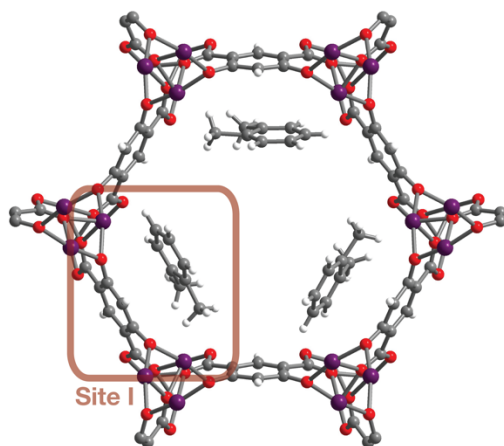


Figure 5.S6. A portion of the crystal structure of $\text{Co}_2(m\text{-dobdc})\cdot 0.92(o\text{-xylene})$ at 100 K as determined through analysis of single-crystal X-ray diffraction data. The chemical occupancy for *p*-xylene were refined to be 92% (46% site occupancy). The *o*-xylene molecules were found to be disordered over two positions due to the mirror symmetry of the framework, but only one orientation is shown here for clarity. Purple, red, gray, and white spheres represent Co, O, C, and H atoms, respectively.

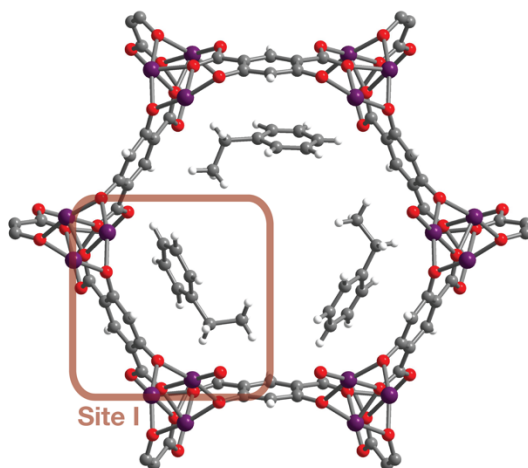


Figure 5.S7. A portion of the crystal structure of $\text{Co}_2(m\text{-dobdc})(\text{H}_2\text{O})_{0.61}\cdot 0.77(\text{ethylbenzene})$ at 100 K as determined through analysis of single-crystal X-ray diffraction data. The chemical occupancies for ethylbenzene were refined to be 77% (38.5% site occupancy). The ethylbenzene molecules were found to be disordered over two positions due to the mirror symmetry of the framework, but only one orientation is shown here for clarity. Water was found to contaminate 30% of the cobalt(II) sites in the structure of ethylbenzene in $\text{Co}_2(m\text{-dobdc})$, but only ethylbenzene is shown here for clarity. Purple, red, gray, and white spheres represent Co, O, C, and H atoms, respectively.

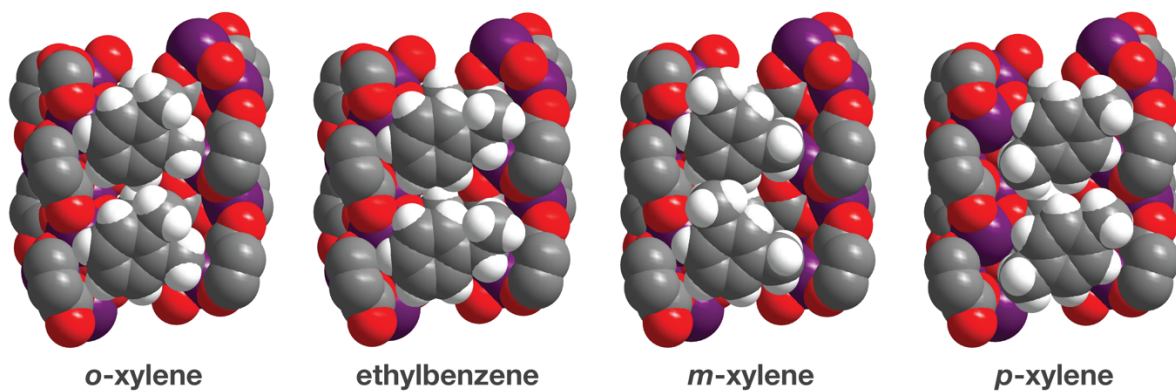


Figure 5.S8. Comparison of the space-filling models of the crystal structures of *o*-xylene, ethylbenzene, *m*-xylene, and *p*-xylene in Co₂(dobdc) at 100 K. The structures shown for *o*-xylene and ethylbenzene correspond to binding sites within the distorted hexagonal channels. Two additional binding sites were located for *o*-xylene. Purple, red, gray, and white spheres represent Co, O, C, and H atoms, respectively.

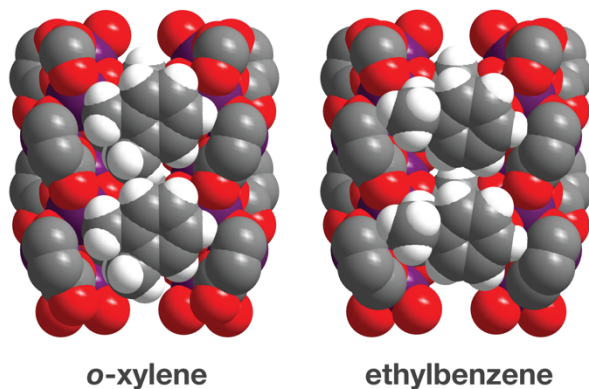


Figure 5.S9. Comparison of the space-filling models of the crystal structures of *o*-xylene and ethylbenzene in Co₂(*m*-dobdc) at 100 K. Purple, red, gray, and white spheres represent Co, O, C, and H atoms, respectively.

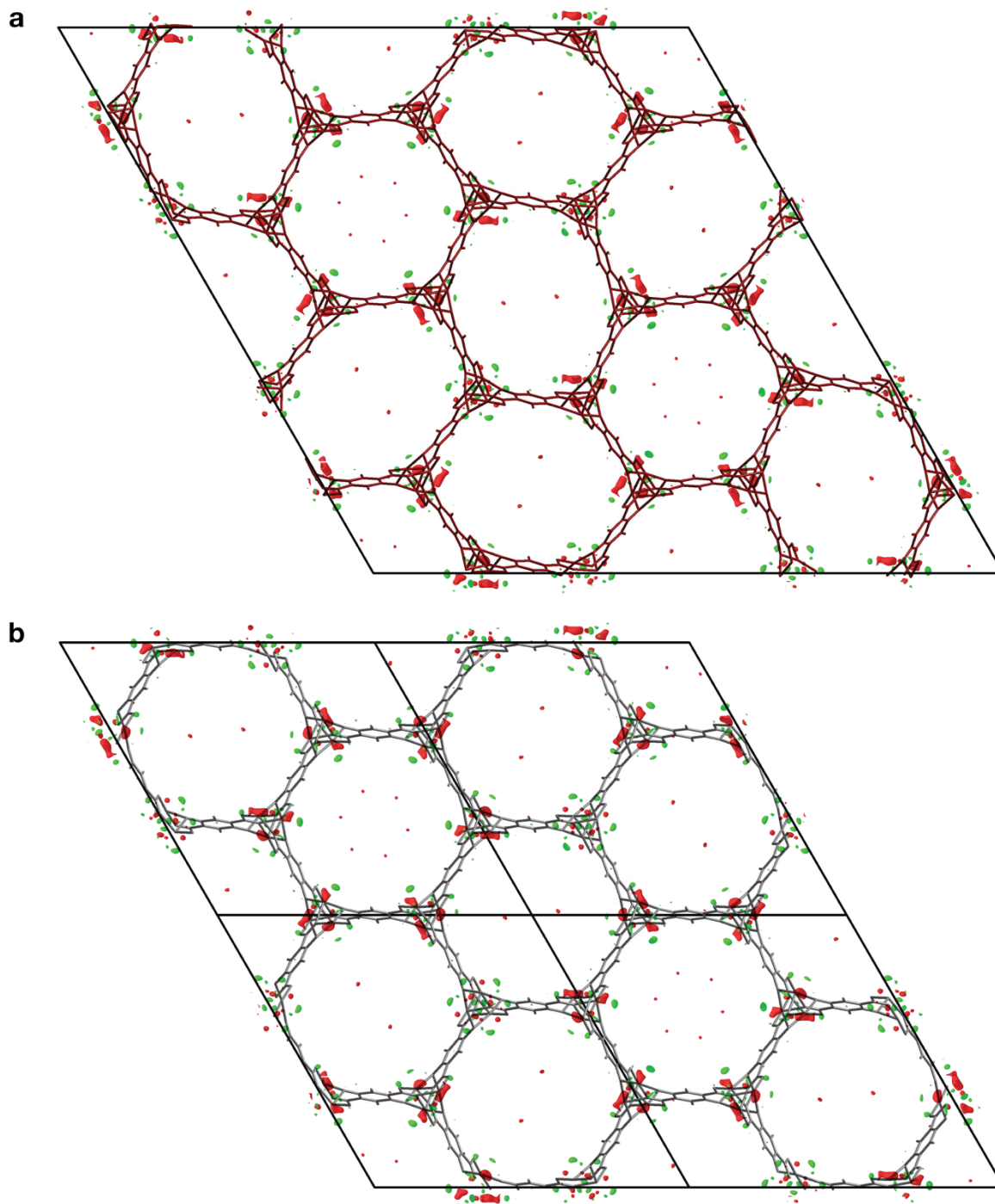


Figure 5.S10. Overlay of the electron-density difference map of the structure of $\text{Co}_2(\text{dobdc}) \cdot 0.99(o\text{-xylene})$ on the structural model for $\text{Co}_2(\text{dobdc}) \cdot 0.99(o\text{-xylene})$ (red) (a) and $\text{Co}_2(\text{dobdc})$ (gray) (b). Red surfaces correspond to regions of positive electron density, while green surfaces correspond to regions of negative electron density. Regions of electron density that are not accounted for by the model match the positions of the cobalt(ii) atoms in the structure of the undistorted $\text{Co}_2(\text{dobdc})$.

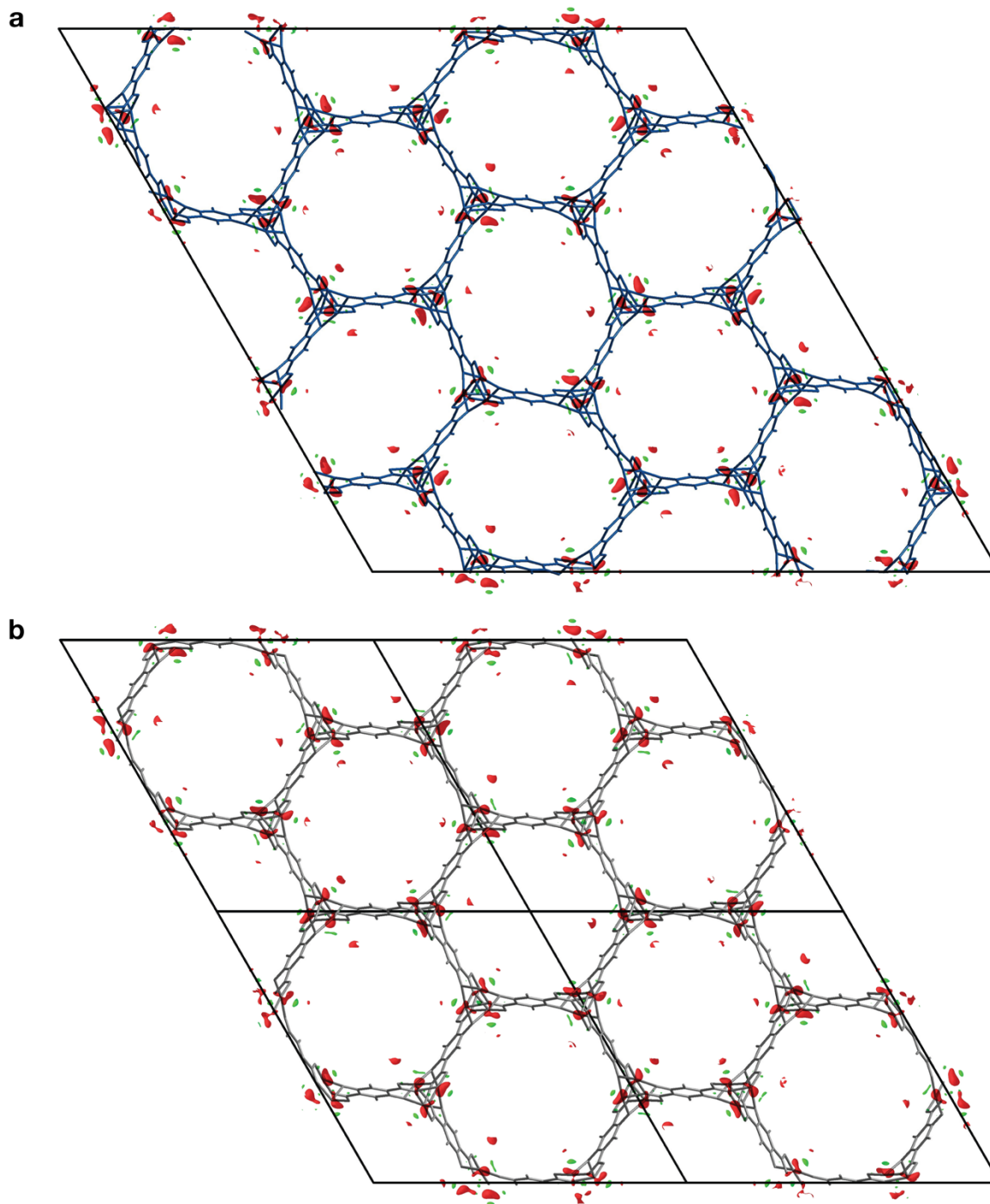


Figure 5.S11. Overlay of the electron-density difference map of the structure of $\text{Co}_2(\text{dobdc}) \cdot 0.36(\text{ethylbenzene})$ on the structural model for $\text{Co}_2(\text{dobdc}) \cdot 0.36(\text{ethylbenzene})$ (blue) (a) and $\text{Co}_2(\text{dobdc})$ (gray) (b). Red surfaces correspond to regions of positive electron density, while green surfaces correspond to regions of negative electron density. Regions of electron density that are not accounted for by the model match the positions of the cobalt(ii) atoms in the structure of the undistorted $\text{Co}_2(\text{dobdc})$.

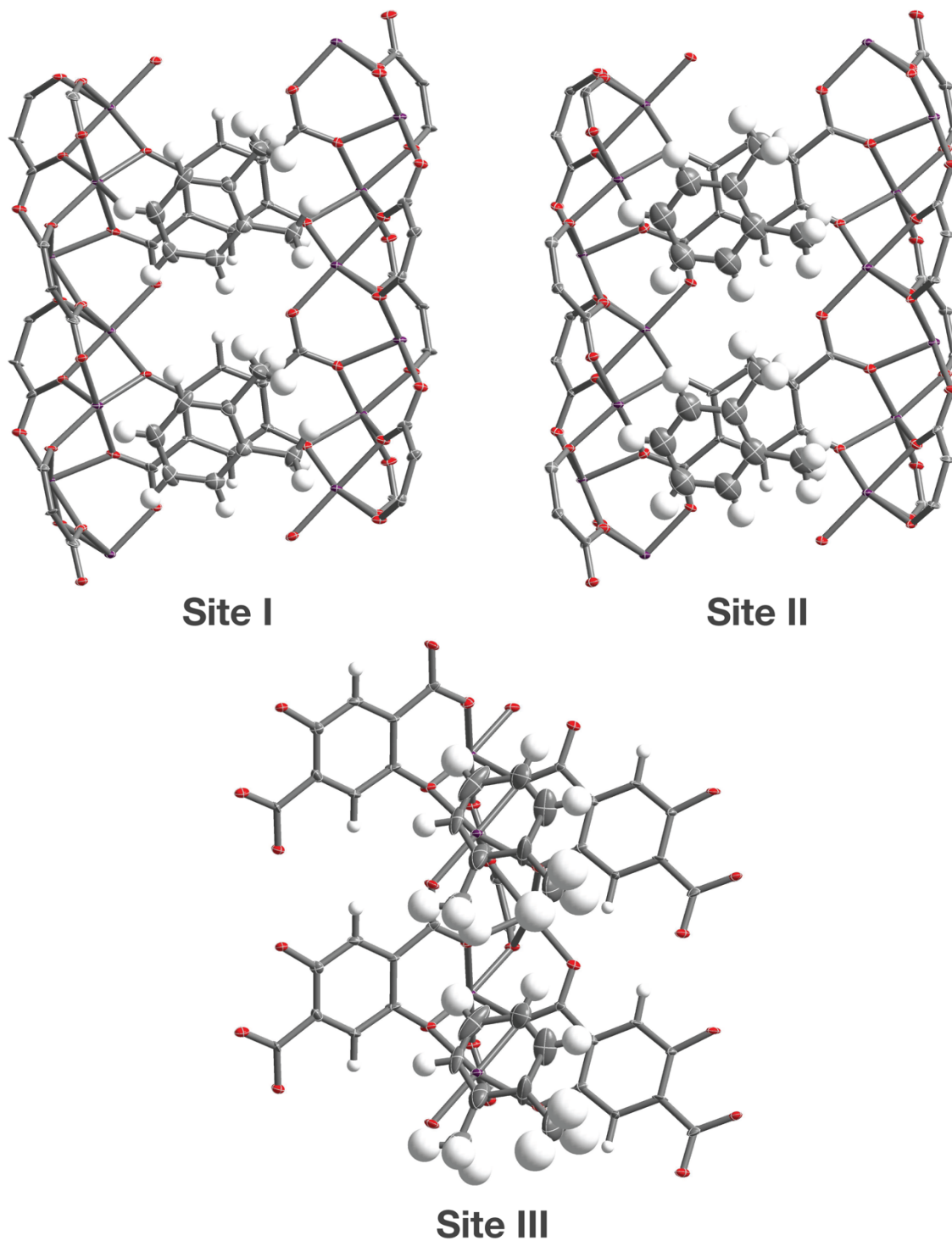


Figure 5.S12. Atomic displacement parameter plot for $\text{Co}_2(\text{dobdc})\cdot 0.99(o\text{-xylene})$ at 100 K drawn at 50% probability level as determined by single crystal X-ray diffraction; purple, red, gray and white ellipsoids represent Co, O, C, and H atoms, respectively.

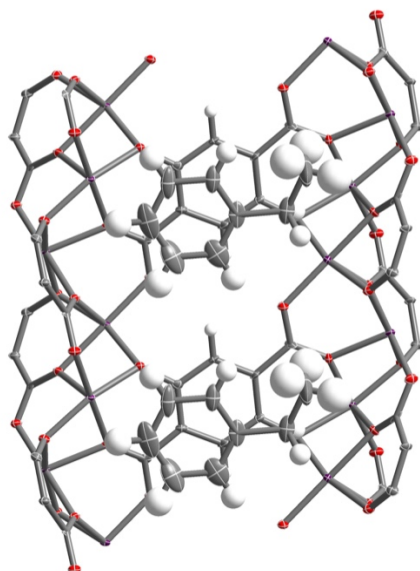


Figure 5.S13. Atomic displacement parameter plot for $\text{Co}_2(\text{dobdc})\cdot 0.36(\text{ethylbenzene})$ at 100 K drawn at 50% probability level as determined by single crystal X-ray diffraction; purple, red, gray and white ellipsoids represent Co, O, C, and H atoms, respectively.

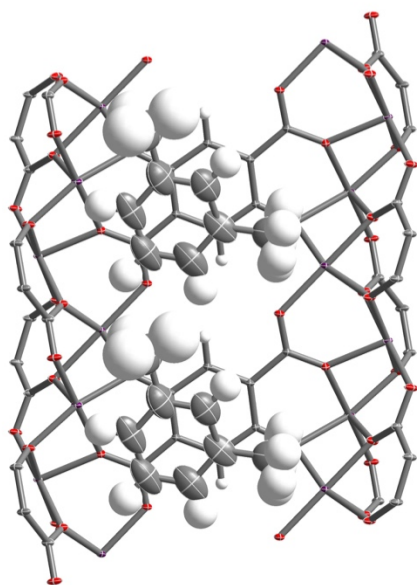


Figure 5.S14. Atomic displacement parameter plot for $\text{Co}_2(\text{dobdc})\cdot 0.74(m\text{-xylene})$ at 100 K drawn at 50% probability level as determined by single crystal X-ray diffraction; purple, red, gray and white ellipsoids represent Co, O, C, and H atoms, respectively.

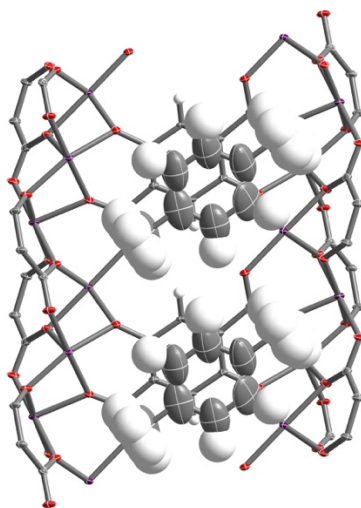


Figure 5.S15. Atomic displacement parameter plot for $\text{Co}_2(\text{dobdc}) \cdot 0.82(p\text{-xylene})$ at 100 K drawn at 50% probability level as determined by single crystal X-ray diffraction; purple, red, gray and white ellipsoids represent Co, O, C, and H atoms, respectively.

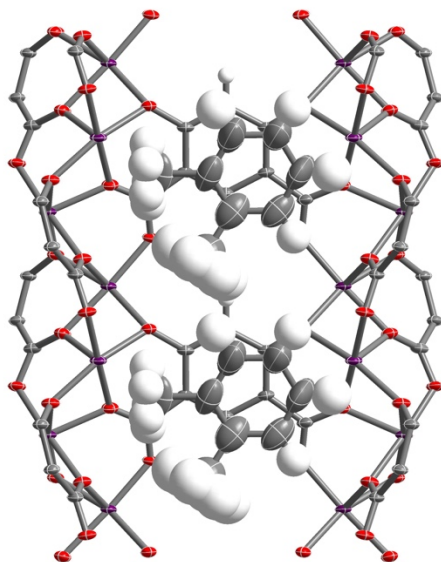


Figure 5.S16. Atomic displacement parameter plot for $\text{Co}_2(m\text{-dobdc}) \cdot 0.92(o\text{-xylene})$ at 100 K drawn at 50% probability level as determined by single crystal X-ray diffraction. The *o*-xylene molecules were found to be disordered over two positions due to the mirror symmetry of the framework, but only one orientation is shown here for clarity. Purple, red, gray and white ellipsoids represent Co, O, C, and H atoms, respectively.

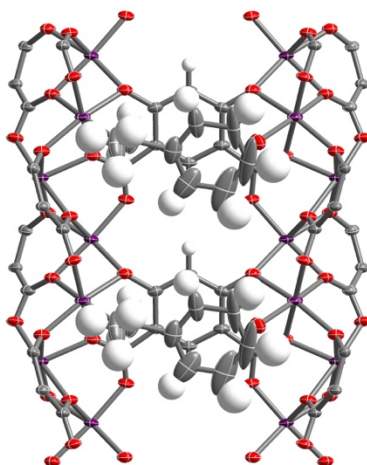


Figure 5.S17. Atomic displacement parameter plot for $\text{Co}_2(m\text{-dobdc})(\text{H}_2\text{O})_{0.61}\cdot 0.77(\text{ethylbenzene})$ at 100 K drawn at 50% probability level as determined by single crystal X-ray diffraction. The ethylbenzene molecules were found to be disordered over two positions due to the mirror symmetry of the framework, but only one orientation is shown here for clarity. Purple, red, gray and white ellipsoids represent Co, O, C, and H atoms, respectively.

Table 5.S1. Crystallographic Data

	Co ₂ (dobdc)-0.99 OX	Co ₂ (dobdc)-0.36 EB	Co ₂ (dobdc)-0.74 MX	Co ₂ (dobdc)-0.82 PX	Co ₂ (<i>m</i> - dobdc)-0.92OX	Co ₂ (<i>m</i> -dobdc) (H ₂ O) _{0.61} -0.77EB
Formula	C _{15.90} H _{11.88} Co ₂ O ₆	C _{10.84} H _{5.56} Co ₂ O ₆	C _{13.89} H _{9.36} Co ₂ O ₆	C _{14.53} H _{10.17} Co ₂ O ₆	C _{15.30} H _{11.23} Co ₂ O ₆	C _{14.15} H _{10.91} Co ₂ O _{6.61}
Temperature (K)	100(2)	100(2)	100(2)	100(2)	100(2)	100(2)
Crystal System	Trigonal	Trigonal	Trigonal	Trigonal	Trigonal	Trigonal
Space Group	$R\bar{3}$	$R\bar{3}$	$R\bar{3}$	$R\bar{3}$	<i>R3m</i>	<i>R3m</i>
<i>a</i> , <i>b</i> , <i>c</i> (Å)	51.6110(19), 51.6110(19), 6.8292(3)	51.7341(19), 51.7341(19), 6.8014(3)	25.8450(9), 25.8450(9), 6.8219(3)	25.9019(15), 25.9019(15), 6.8226(5)	25.812(3), 25.812(3), 6.8165(8)	25.8977(9), 25.8977(9), 6.7599(3)
<i>α</i> , <i>β</i> , <i>γ</i> (°)	90, 90, 120	90, 90, 120	90, 90, 120	90, 90, 120	90, 90, 120	90, 90, 120
<i>V</i> , (Å ³)	15753.8(14)	15764.6(14)	3946.3(3)	3964.1(5)	3933.1(11)	3926.4(3)
<i>Z</i>	36	36	9	9	9	9
Radiation, <i>λ</i> (Å)	Synchrotron, 0.8856	Synchrotron, 0.8856	Synchrotron, 0.7749	Synchrotron, 0.8856	Synchrotron, 0.7749	Synchrotron, 0.8856
2 <i>θ</i> Range for Data Collection (°)	5.204 to 75.960	5.192 to 75.880	5.954 to 87.922	6.790 to 64.562	5.962 to 65.120	6.792 to 68.968
Completeness to 2 <i>θ</i>	99.7% (2 <i>θ</i> = 64.194°)	99.8% (2 <i>θ</i> = 64.194°)	99.9% (2 <i>θ</i> = 55.412°)	99.9% (2 <i>θ</i> = 64.194°)	99.9% (2 <i>θ</i> = 55.412°)	99.8% (2 <i>θ</i> = 64.194°)
Data / Restraints / Parameters	9711 / 139 / 498	9751 / 69 / 350	5205 / 104 / 135	1623 / 115 / 133	2569 / 112 / 137	2004 / 54 / 146
Goodness of Fit on <i>F</i> ²	1.183	1.101	1.312	1.053	1.087	1.083
<i>R</i> ₁ ^{<i>a</i>} , <i>wR</i> ₂ ^{<i>b</i>} (<i>I</i> > 2 <i>σ</i> (<i>I</i>))	0.1481, 0.3584	0.1631, 0.4703	0.0492, 0.1271	0.0538, 0.1390	0.0412, 0.1064	0.0399, 0.1080
<i>R</i> ₁ ^{<i>a</i>} , <i>wR</i> ₂ ^{<i>b</i>} (all data)	0.1508, 0.3593	0.1743, 0.4748	0.0536, 0.1287	0.0749, 0.1516	0.0477, 0.1098	0.0440, 0.1099
Largest Diff. Peak and Hole (e Å ⁻³)	3.249 and -2.420	6.576 and -2.255	1.088 and -1.499	1.932 and -0.459	0.830 and -0.515	1.068 and -0.391

OX = *o*-xylene; EB = ethylbenzene; MX = *m*-xylene; PX = *p*-xylene. ^{*a*}*R*₁ = $\sum ||F_o| - |F_c|| / \sum |F_o|$. ^{*b*}*wR*₂ = $\{\sum [w(F_o^2 - F_c^2)^2] / \sum [w(F_o^2)^2]\}^{1/2}$.

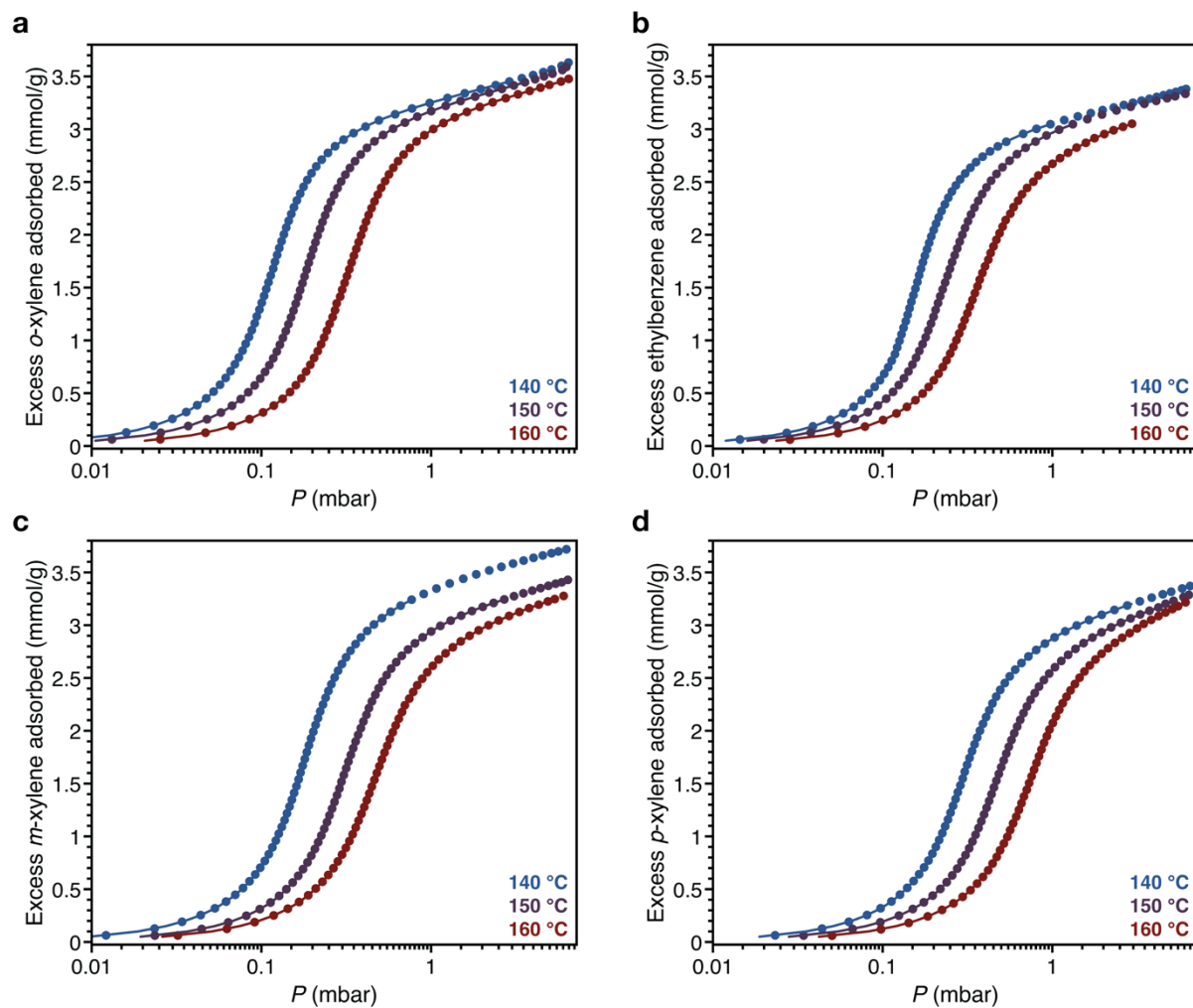


Figure 5.S18. Single-component vapor-phase *o*-xylene (a), ethylbenzene (b), *m*-xylene (c), and *p*-xylene (d) adsorption isotherms for $\text{Co}_2(\text{dobdc})$ at 140 °C (blue), 150 °C (violet), and 160 °C (red). Filled circles represent experimental data, while solid lines represent corresponding fits obtained by spline interpolation.

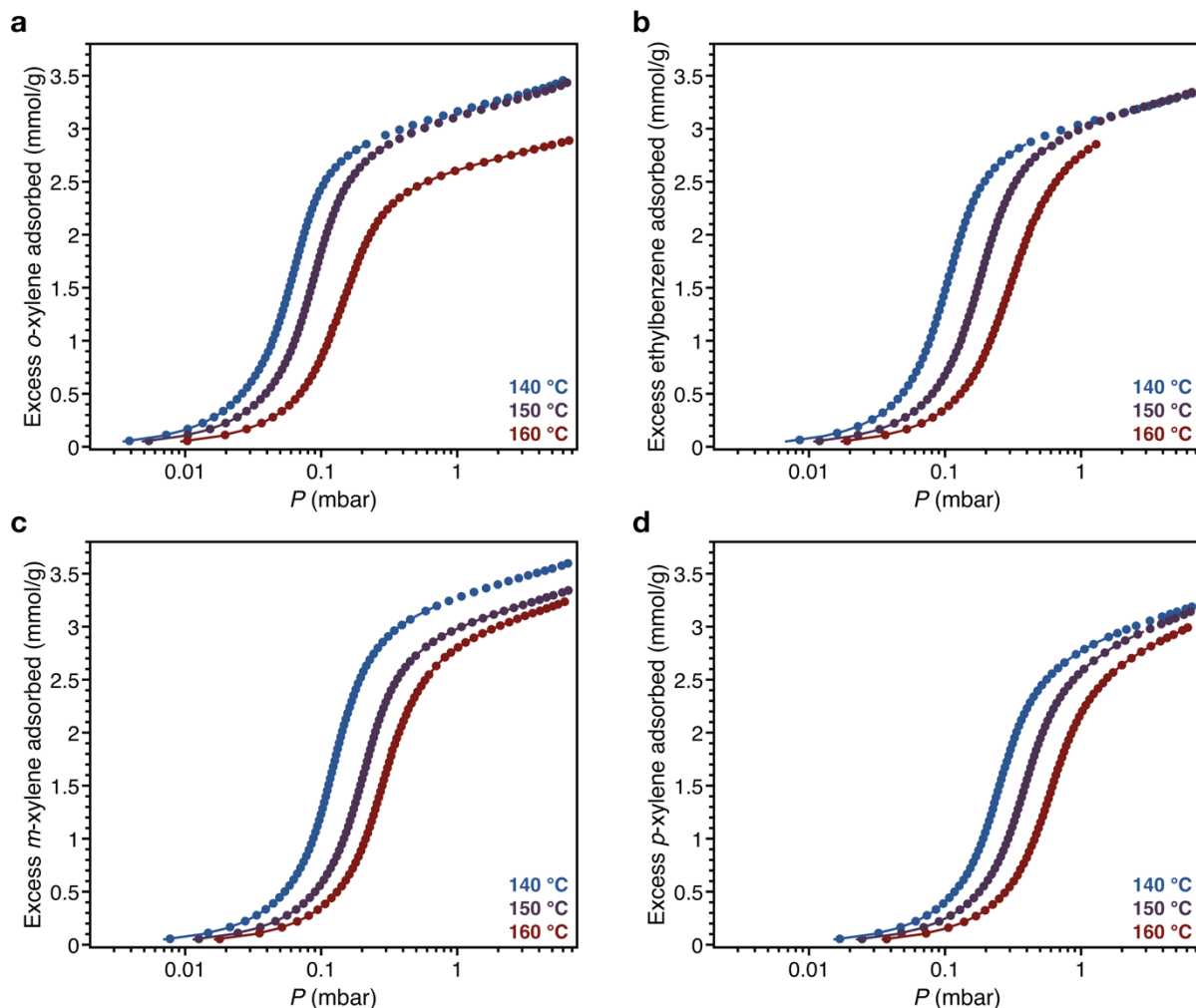


Figure 5.S19. Single-component vapor-phase *o*-xylene (a), ethylbenzene (b), *m*-xylene (c), and *p*-xylene (d) adsorption isotherms for $\text{Co}_2(\text{dobdc})$ at 140 °C (blue), 150 °C (violet), and 160 °C (red). Filled circles represent experimental data, while solid lines represent corresponding fits obtained by spline interpolation.

Differential Enthalpy of Adsorption Calculations. As suitable fits to the adsorption isotherm data could not be obtained with multi-site Langmuir equations, isotherms were fit independently by spline interpolation. Using the fits, the differential enthalpy of adsorption, Δh_{ads} , can be calculated as a function of the total amount of gas adsorbed, n , by using the the Clausius-Clapeyron equation (eq 1), where R is the gas constant in $\text{J/mol}\cdot\text{K}$, T is the temperature in K, n is the total amount adsorbed in mmol/g , and P is the pressure in bar.

$$\Delta h_{\text{ads}} = -RT^2 \left(\frac{\partial \ln P}{\partial T} \right)_n \quad (1)$$

The fits for each C_8 isomer (fit independently for each temperature) were used to obtain the exact pressures that correspond to specific loadings at different temperatures (140 °C, 150 °C, and 160 °C). This was done at loading intervals of 0.05 mmol/g . At each loading, the slope of the best-fit line to $\ln(P)$ versus $1/T$ was calculated to obtain the differential enthalpy.

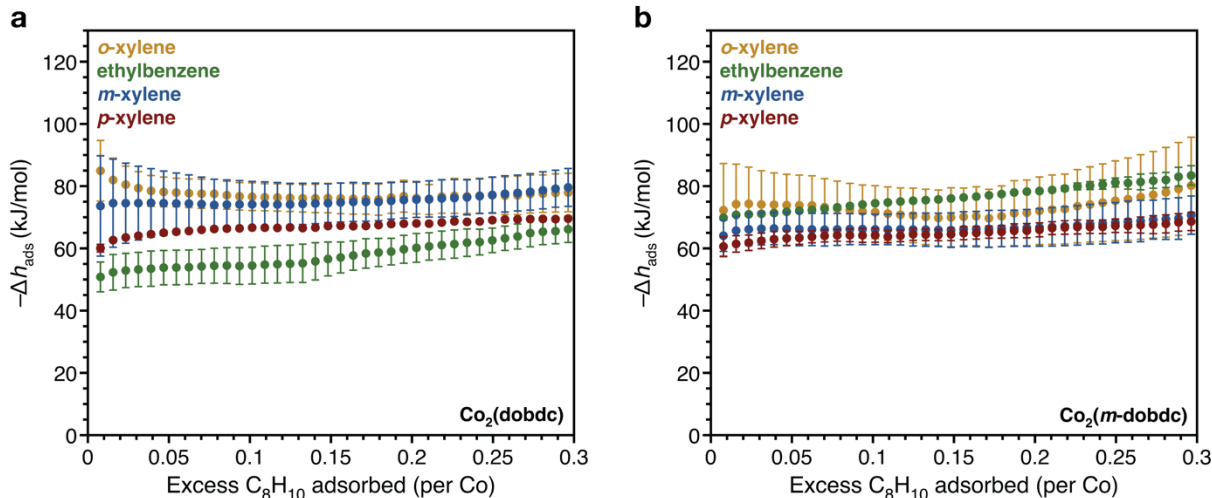


Figure 5.S20. Differential enthalpy of adsorption (Δh_{ads}) plots (calculated from fits to the adsorption isotherms generated by spline interpolation) *o*-xylene (orange), ethylbenzene (green), *m*-xylene (blue), and *p*-xylene (red) adsorption in $\text{Co}_2(\text{dobdc})$ (a) and $\text{Co}_2(\text{m-dobdc})$ (b).

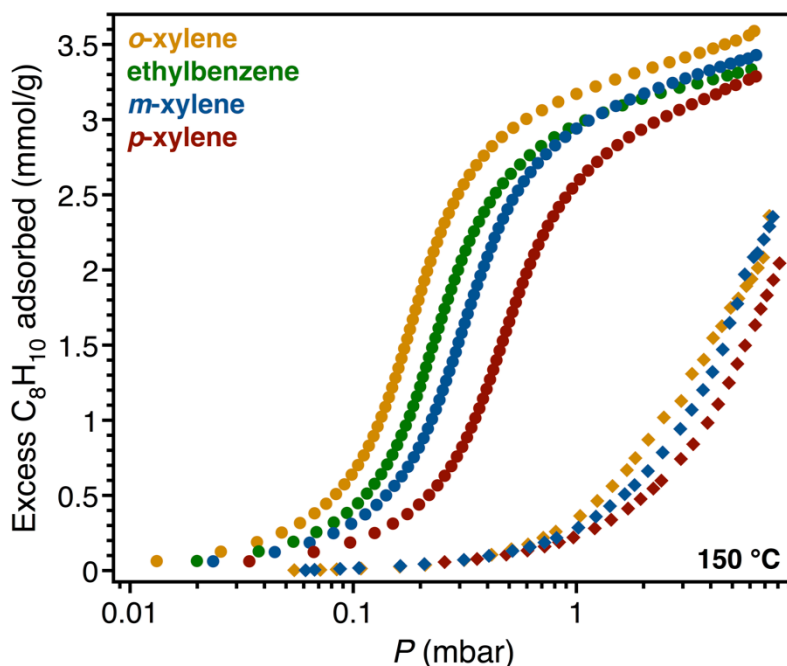


Figure 5.S21. Comparison of the single-component vapor-phase *o*-xylene (orange), ethylbenzene (green), *m*-xylene (blue), and *p*-xylene (red) adsorption isotherms for $\text{Co}_2(\text{dobdc})$ (filled circles) and $\text{Co}_2(\text{dobpdc})$ (filled diamonds) at $150\text{ }^\circ\text{C}$.

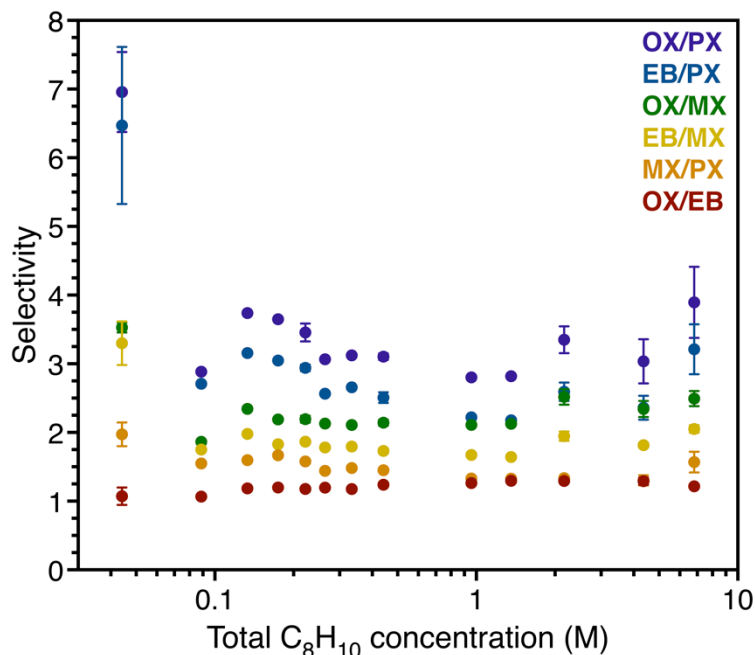


Figure 5.S22. Two-component selectivities for *o*-xylene/*p*-xylene (violet), ethylbenzene/*p*-xylene (blue), *o*-xylene/*m*-xylene (green), ethylbenzene/*m*-xylene (yellow), *m*-xylene/*p*-xylene (orange), and *o*-xylene/ethylbenzene (red) determined from a multi-component liquid-phase adsorption experiment with equimolar amounts of the C₈ isomers (0.1–1.7 M in each isomer; 0.4–6.8 M total concentration) in *n*-heptane at 33 °C. The selectivities are plotted over the initial total C₈ isomer concentration for each measurement. Data points with error bars (for measurements with initial total C₈ isomer concentrations of 0.044, 0.22, 0.44, 2.2, 4.4, and 6.8 M) were determined from an average of three replications.

Table 5.S2. Unit cell parameters for Co₂(dobdc) powder samples.

	Space Group	<i>T</i> (K)	<i>a</i> (Å)	<i>c</i> (Å)	<i>V</i> (Å ³)
<i>o</i> -xylene	$R\bar{3}$	300	51.713(1)	6.8842(3)	15943(1)
<i>o</i> -xylene	$R\bar{3}$	400	25.873(1)	6.8973(3)	3998.4(4)
<i>m</i> -xylene	$R\bar{3}$	300	25.8808(6)	6.8923(2)	3998.1(2)
<i>p</i> -xylene	$R\bar{3}$	300	25.8916(9)	6.8853(3)	3997.4(3)
ethylbenzene	$R\bar{3}$	300	25.9580(3)	6.9065(1)	4030.2(1)

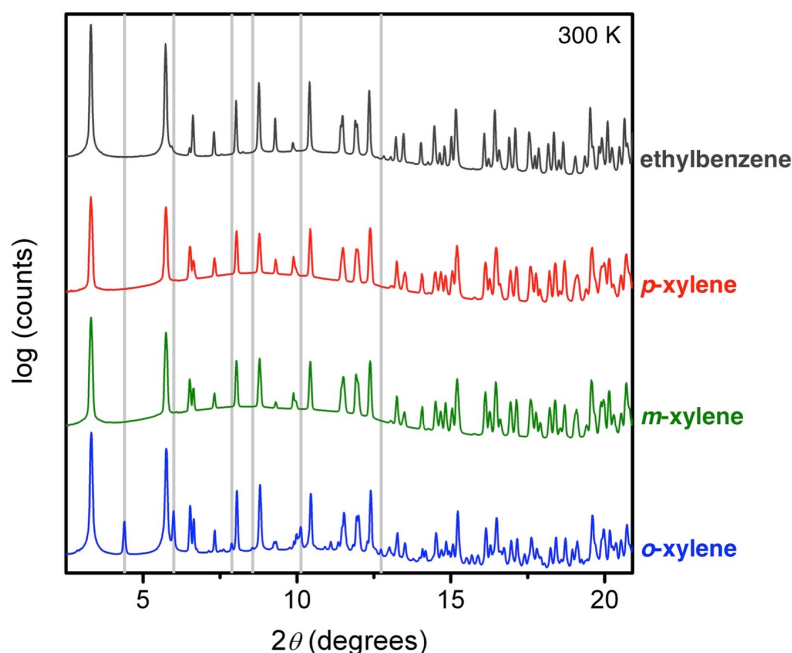


Figure 5.S23. Powder X-ray diffraction patterns ($\lambda = 0.75009 \text{ \AA}$) at 300 K for $\text{Co}_2(\text{dobdc})$ soaked in *o*-xylene (blue), *m*-xylene (green), *p*-xylene (red), and ethylbenzene (dark gray). Light gray lines indicate the positions of Bragg peaks that are only present in the distorted framework, where the dimensions of the *a* and *b* axes of the unit cell are doubled.

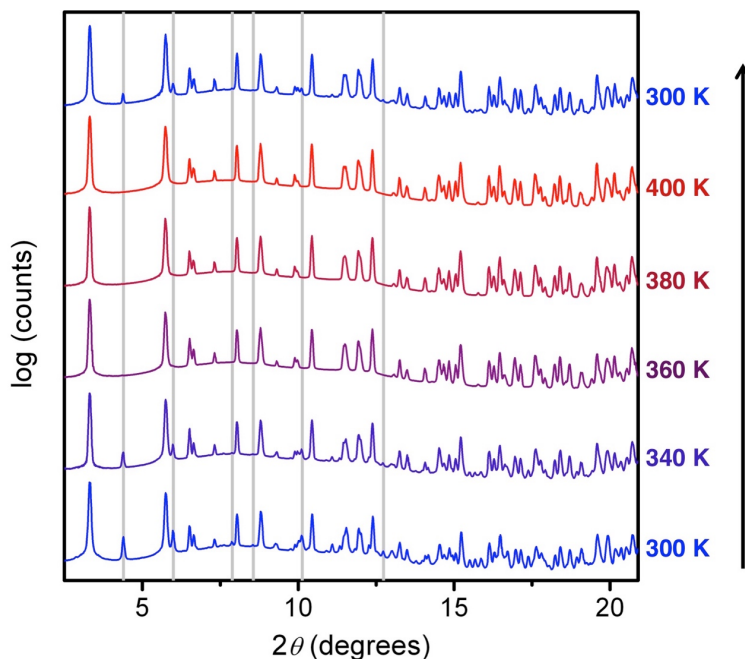


Figure 5.S24. Variable temperature powder X-ray diffraction patterns ($\lambda = 0.75009 \text{ \AA}$) for $\text{Co}_2(\text{dobdc})$ soaked in *o*-xylene from 300 K to 400 K. Light gray lines indicate the positions of Bragg peaks that are only present in the distorted framework, where the dimensions of the *a* and *b* axes of the unit cell are doubled.

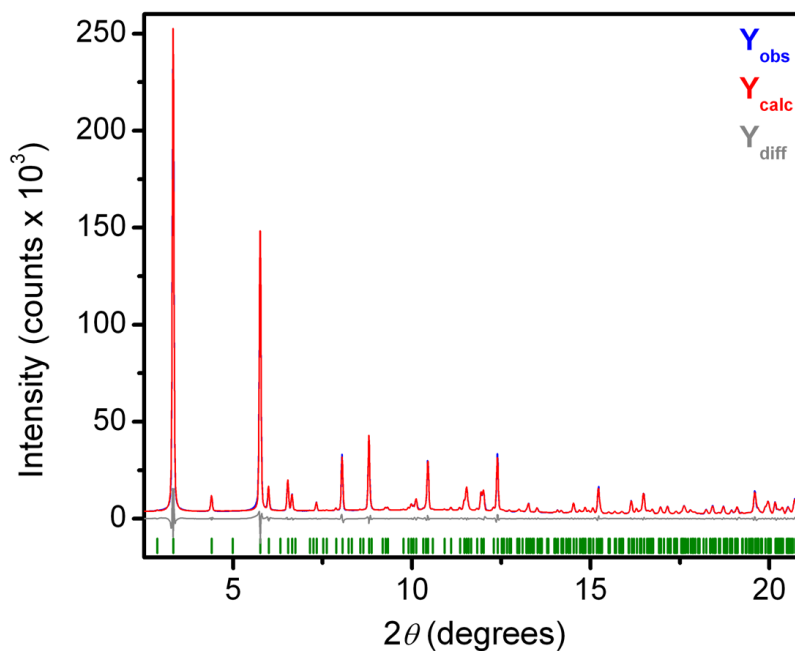


Figure 5.S25. Structureless Le Bail refinement for X-ray powder diffraction data at 300 K of $\text{Co}_2(\text{dobdc})$ soaked in *o*-xylene. Blue and red lines represent the observed and calculated diffraction patterns, respectively. The gray line represents the difference between observed and calculated patterns, and the green tick marks indicate calculated Bragg peak positions. $R_{\text{wp}} = 0.049$, $R_{\text{p}} = 0.035$, $\lambda = 0.75009 \text{ \AA}$.

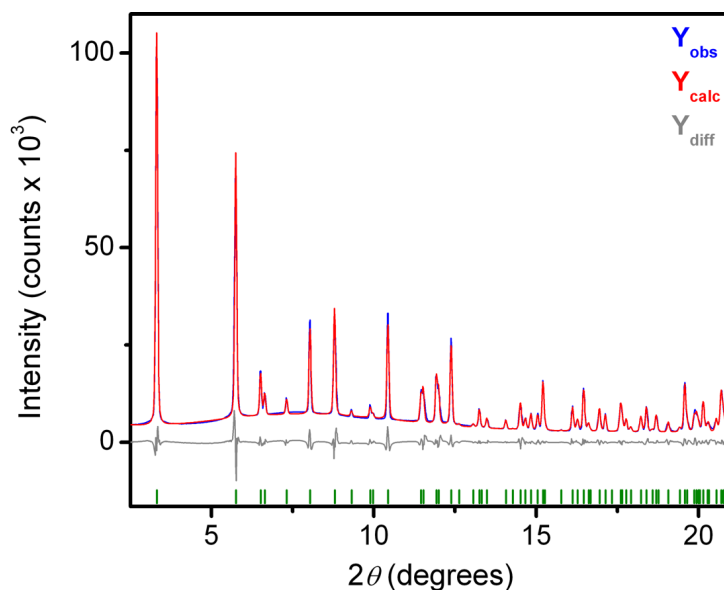


Figure 5.S26. Structureless Le Bail refinement for powder X-ray diffraction data at 400 K of $\text{Co}_2(\text{dobdc})$ soaked in *o*-xylene. Blue and red lines represent the observed and calculated diffraction patterns, respectively. The gray line represents the difference between observed and calculated patterns, and the green tick marks indicate calculated Bragg peak positions. $R_{\text{wp}} = 0.062$, $R_{\text{p}} = 0.045$, $\lambda = 0.75009 \text{ \AA}$.

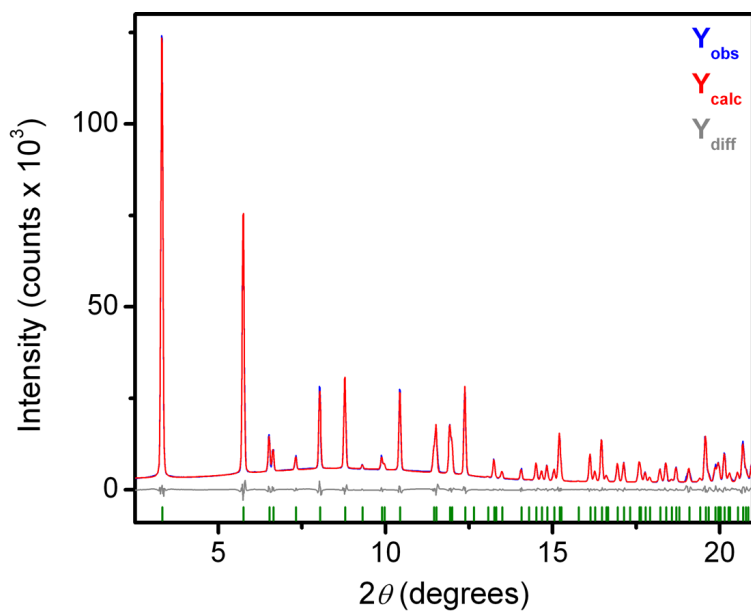


Figure 5.S27. Structureless Le Bail refinement for powder X-ray diffraction data at 300 K of $\text{Co}_2(\text{dobdc})$ soaked in *m*-xylene. Blue and red lines represent the observed and calculated diffraction patterns, respectively. The gray line represents the difference between observed and calculated patterns, and the green tick marks indicate calculated Bragg peak positions. $R_{\text{wp}} = 0.040$, $R_p = 0.028$, $\lambda = 0.75009 \text{ \AA}$.

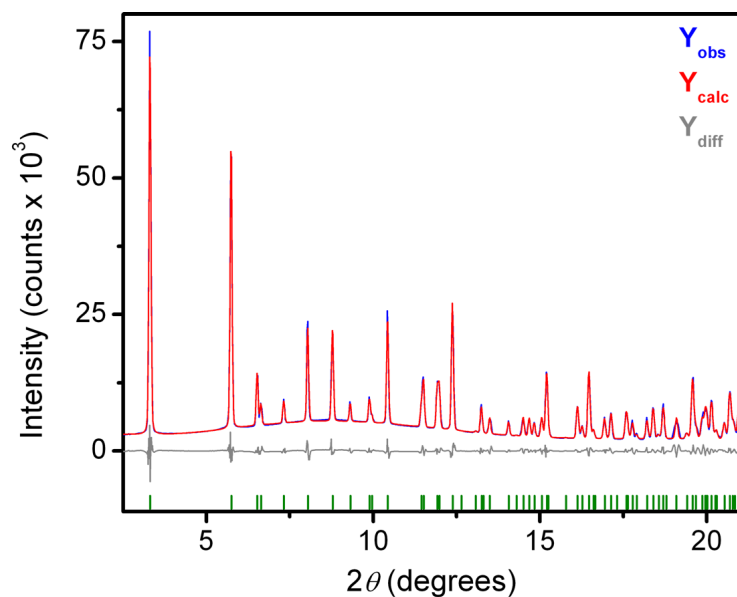


Figure 5.S28. Structureless Le Bail refinement for powder X-ray diffraction data at 300 K of $\text{Co}_2(\text{dobdc})$ soaked in *p*-xylene. Blue and red lines represent the observed and calculated diffraction patterns, respectively. The gray line represents the difference between observed and calculated patterns, and the green tick marks indicate calculated Bragg peak positions. $R_{\text{wp}} = 0.065$, $R_p = 0.045$, $\lambda = 0.75009 \text{ \AA}$.

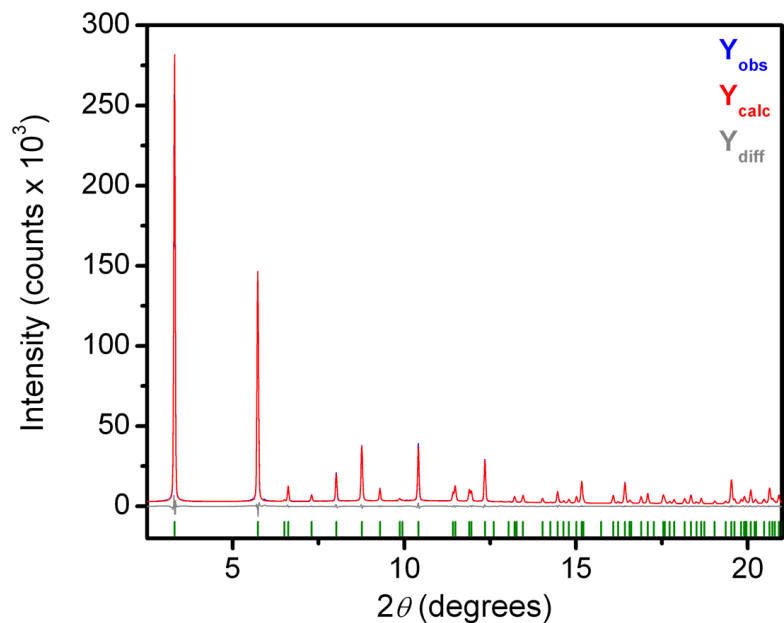


Figure 5.S29. Structureless Le Bail refinement for powder X-ray diffraction data at 300 K of $\text{Co}_2(\text{dobdc})$ soaked in ethylbenzene. Blue and red lines represent the observed and calculated diffraction patterns, respectively. The gray line represents the difference between observed and calculated patterns, and the green tick marks indicate calculated Bragg peak positions. $R_{\text{wp}} = 0.033$, $R_{\text{p}} = 0.025$, $\lambda = 0.75009 \text{ \AA}$.

Chapter 6: Acetylene/Ethylene Separation in the Metal-Organic Framework Cu[Ni(pdt)₂] *via* Binding in a Square Tetrapyrazine Cage

6.1. Introduction

Metal–organic frameworks (MOFs) are a class of porous materials comprised of inorganic units bridged by organic ligands. The high internal surface areas and degree of tunability in this structure class have led to interest in using them for a wide variety of applications including gas storage and gas separations. The separation of hydrocarbon mixtures relevant to the chemical industry, such as olefins and paraffins,¹ hexane isomers,² or xylene isomers³ have been of particular interest due to the potential energy savings non-thermally driven adsorptive-based separations could provide over currently-employed cryogenic distillation techniques.⁴

One particularly challenging separation is that of acetylene (C₂H₂) and ethylene (C₂H₄).^{5,6,7,8,9} Acetylene can poison ethylene polymerization catalysts, leading to the need for acetylene removal from ethylene streams. While acetylene is typically hydrogenated to produce ethylene in these streams, any over-hydrogenation from this reaction will reduce the amount of ethylene present. Adsorptive-based processes could potentially yield high selectivities for separating acetylene from ethylene without the need for hydrogenation. Furthermore, designing adsorbents that can perform this separation in a physisorptive manner is of fundamental interest owing to the difficulty in distinguishing between alkynes and alkenes *via* a physisorptive mechanism.

Relatedly, acetylene storage is quite dangerous and requires acetone as a stabilizing agent. MOFs offer a potential method for safely storing acetylene at high volumetric capacities by relying on the stabilizing host-guest interactions of acetylene binding in the pores.

A MOF with square channels, Cu[Ni(pdt)₂] (pdt²⁻ = pyrazine-2,3-dithiolate), is studied here for its use in separating acetylene and ethylene.¹⁰ This material is formed from a Ni(pdt)₂ metalloligand containing a square planar Ni(III) bound to two pdt²⁻ ligands that, in the presence of CuI, immediately precipitates the Cu[Ni(pdt)₂] MOF as a black solid. By taking advantage of the small square channels in this material and a unique interaction with the tetrapyrazine cages present in the pores, the difficult separation of acetylene and ethylene was completed.

6.2. Experimental

6.2.1. General procedures and measurements. The synthesis of Na₂[Ni(pdt)₂] was completed according to the literature procedure.¹⁰ Diffraction data were collected using a Bruker AXS D8 Advance diffractometer with the generator set at 40 kV and 40 mA; samples were loaded onto zero-background sample holders. Elemental analysis was obtained from the Microanalytical Laboratory at the University of California, Berkeley.

6.2.2. Synthesis of Cu[Ni(pdt)₂]. The synthesis of Cu[Ni(pdt)₂] was adapted from a previous report.¹⁰ A flask was charged with 270 mL acetonitrile and sparged with N₂ for 30 min. Na₂[Ni(pdt)₂] (0.630 g, 1.62 mmol) was added and the solution was stirred. A separate flask was charged with 75 mL of acetonitrile, sparged with N₂ for 30 min, and CuI (0.309 g, 1.62 mmol) was added. While under N₂, the CuI solution was then slowly added to the solution of Na₂[Ni(pdt)₂] via a syringe, rapidly precipitating Cu[Ni(pdt)₂] as a black solid. The resulting solid was filtered on 0.22 μm nylon filter paper in air and activated overnight at 90°C under high

vacuum on an ASAP 2420 instrument, yielding 0.453 g of the framework (68.8% yield). Elemental Analysis for Cu[Ni(pdt)₂]: calcd C 23.63%, H 0.99%, N 13.78%, S 31.54%; found: C 22.92%, H 1.05%, N 13.74%, S 30.43%.

6.2.3. Isotherm measurements. Approximately 100 mg of each sample was loaded into a preweighed sample tube in an N₂-filled glovebox and the sample tubes were capped with a Transeal. The samples were then transferred to a Micromeritics 2420 instrument degas manifold and heated at a rate of 0.5 °C/min to a temperature of 90 °C while under dynamic vacuum. When the degas rate was <1 μbar/min, each sample was considered to be activated. The mass of the sample was then recorded based on the mass of the evacuated tube prior to sample loading. The sample was then transferred to a Micromeritics 3Flex gas adsorption analyzer. Prior to collecting each isotherm, the free space of each sample was measured using UHP (99.999%) He. Gas adsorption isotherms of acetylene and ethylene were measured at 298, 308, and 318 K by immersing the sample in a bath of Dow Syltherm and the controlling the temperature using a water recirculator with copper coils immersed in the Dow Syltherm bath to maintain the desired temperature. The recirculator was set to the desired temperature. Samples were reactivated at 90 °C between each measurement under dynamic vacuum for at least 8 h. Oil-free pumps and pressure gauges were used for all measurements.

The single-component gas adsorption isotherms were fit using a tri-site Langmuir-Freundlich equation, fitting all three temperatures (298, 308, and 318 K) simultaneously. This is seen in equation 1; n is the amount adsorbed (mmol/g), q_{sat} is the saturation loading for site a , b , or c (mmol/g), b is the Langmuir parameter associated with either site a , b , or c (bar^{- v}), p is the pressure (bar), and v is the dimensionless Freundlich parameter for site a , b , or c . Subscripts indicate different sites (a , b , or c) for all variables. The value for b is calculated per equation 2.

$$n = \frac{q_{\text{sat},a} b_a p^{v_a}}{1 + b_a p^{v_a}} + \frac{q_{\text{sat},b} b_b p^{v_b}}{1 + b_b p^{v_b}} + \frac{q_{\text{sat},c} b_c p^{v_c}}{1 + b_c p^{v_c}} \quad (1)$$

$$b = b_0 e^{\frac{-E}{RT}} \quad (2)$$

The equation was fit using the Solver feature of Microsoft Excel. The quality of the fits was determined by comparing the residual sum of squares of the difference between the calculated and experimental uptake values at each pressure as well as by visual inspection. Wolfram Mathematica 11 was then used to create a series of data points corresponding to points on the fit curves at equivalent loadings for each temperature.

The Ideal Adsorbed Solution Theory (IAST) selectivities were then calculated using the data points from Mathematica for the 298, 308, and 318 K isotherms. This involves numerically solving for the spreading pressure and subsequently determining the composition of the adsorbed phase at a given gas phase composition. The selectivity is then given by

$$S = \frac{x_{\text{olefin}}/x_{\text{paraffin}}}{y_{\text{olefin}}/y_{\text{paraffin}}} \quad (3)$$

where S is the IAST selectivity, x is the mole fraction in the adsorbed phase, and y is the mole fraction in the gas phase. Finally, the differential enthalpy was extracted from the temperature dependence of the isotherms using the Clausius-Clapeyron relationship.¹¹

6.2.4. Powder X-ray Diffraction Measurements. Powder X-ray diffraction data for Cu[Ni(pdt)₂] was collected on Beamline 17-BM-B at the Advanced Photon Source at Argonne National Laboratory. Approximately 3 mg of fully desolvated framework was loaded into a 1.0 mm borosilicate capillary inside a N₂-filled glovebox. Each capillary was then attached to a custom designed gas-dosing cell equipped with a gas valve and transferred to the goniometer head. All adsorbed N₂ was then removed by evacuating *in situ* using a turbomolecular pump. An Oxford Cryosystems Cryostream 800 was used to hold the temperature of the sample at 25 °C. Scattered intensity was measured by a PerkinElmer a-Si flat panel detector.

Diffraction data was collected for the evacuated material, after which variable pressures of C₂H₂ and C₂H₄ gas was dosed using a custom-built gas dosing manifold. Each dose of gas was equilibrated on the sample for over half an hour, until no further change was observed in both the pressure above the sample and in the resulting diffraction patterns. The average wavelength of measurement was 0.45212 Å. In between dosing C₂H₂ and dosing C₂H₄, the sample was activated at 120 °C under vacuum for 1 hour to remove all traces of the previously dosed gas from the material. The re-evacuated sample had a diffraction pattern that was identical to the initial evacuated sample.

As was previously reported, the material Cu[Ni(pdt)₂] is isostructural to Cu[Cu(pdt)₂].¹⁰ As a result, the published structural model of Cu[Cu(pdt)₂] was used as a starting point for the Rietveld refinement of activated and gas-dosed Cu[Ni(pdt)₂]. Precise unit cell parameters of activated Cu[Ni(pdt)₂] were obtained by Pawley refinement as implemented in TOPAS-Academic 4.1, and were found to be consistent with a tetragonal lattice.¹² When progressing to Rietveld refinement, the thiolate-ligated Cu in the Cu[Cu(pdt)₂] was replaced by Ni, and C–N and C–C distances were restricted with “soft” constraints. H atoms were placed on calculated positions, with the aromatic C–H distance fixed at 1.09 Å. In the final stages of the refinement, all atomic positions (with the exception of special positions and the atomic positions of the H atoms) and thermal and unit cell parameters were fully refined with no constraints and convoluted with the sample and instrument parameters and Chebyshev background polynomials. The calculated diffraction pattern for the final structural model of Cu[Ni(pdt)₂] is in excellent agreement with the experimental diffraction pattern as seen in the plot of the Rietveld refinement in Figure 6.S5.

After determination of the activated structure of Cu[Ni(pdt)₂], the patterns of Cu[Ni(pdt)₂] after dosing 20, 92, 291, 591, and 1077 mbar of C₂H₂ were analyzed. All patterns showed peaks consistent with the P4₂/mm space group, but with changes in intensity indicative of gas molecules occupying the pores of the framework. Precise unit cell parameters of C₂H₂-dosed Cu[Ni(pdt)₂] were obtained by Pawley refinement. Using the refined structure of activated Cu[Ni(pdt)₂] as a starting model, a Fourier difference map was calculated after a Rietveld refinement of a pattern of Cu[Ni(pdt)₂] dosed with 291 mbar of C₂H₂. Excess electron density was observed along the c-axis, in a prolate shape reminiscent of an adsorbed acetylene molecule. When carbon atoms were placed within this shape and constrained to a bond length of 1.20 Å, the goodness-of-fit parameters showed a dramatic improvement.

In the initial stages of the refinement, C–C, and C–N bond distances were implemented with soft constraints, and H atoms were subsequently placed on calculated positions. In the final stages of the refinement, the C₂H₂ occupancy, all atomic positions (with the exception of those on special positions and all atomic positions for the H atoms) and thermal and unit cell parameters were fully refined with no constraints, convoluted with the sample and instrument

parameters and Chebyshev background polynomials. The calculated diffraction pattern for the final structural models of C₂H₂-dosed Cu[Ni(pdt)₂] are in excellent agreement with the experimental diffraction pattern (Rietveld plot in Figures 6.S6-S10).

Subsequently, the patterns of Cu[Ni(pdt)₂] after dosing 24, 88, 273, 589, and 985 mbar of C₂H₄ were analyzed. All patterns showed peaks consistent with the P4₂/mm space group, but with changes in intensity indicative of gas molecules occupying the pores of the framework. Precise unit cell parameters of C₂H₄-dosed Cu[Ni(pdt)₂] were first obtained by Pawley refinement. Then, using the refined structure of activated Cu[Ni(pdt)₂] as a starting model, a Fourier difference map was calculated after a Rietveld refinement of a pattern of Cu[Ni(pdt)₂] dosed with 273 mbar of C₂H₄. Excess electron density was observed along the c-axis, in a prolate shape reminiscent of an adsorbed ethylene molecule, similar in location to that observed for acetylene. When carbon atoms were placed within this shape and constrained to a bond length of 1.34 Å, the goodness-of-fit parameters showed a dramatic improvement.

In the initial stages of the refinement, C–C, and C–N bond distances were implemented with soft constraints, and H atoms were subsequently placed on calculated positions. Two sets of positions for H atoms on the ethylene molecule were assumed, to approximate the vibrational disorder of the adsorbed ethylene molecule. In the final stages of the refinement, the C₂H₄ occupancy, all atomic positions (with the exception of those on special positions and all atomic positions for the H atoms) and thermal and unit cell parameters were fully refined with no constraints, convoluted with the sample and instrument parameters and Chebyshev background polynomials. The calculated diffraction pattern for the final structural models of C₂H₄-dosed Cu[Ni(pdt)₂] are in excellent agreement with the experimental diffraction pattern (Rietveld plot in Figures 6.S11-S15 and crystallographic details in Table 6.S1).

6.2.5. *In situ* Infrared Spectroscopy Measurements. Infrared spectra were collected using a Bruker Vertex 70 spectrometer equipped with a glowbar source, KBr beamsplitter, and a liquid nitrogen cooled mercury-cadmium-telluride detector. A custom-built diffuse reflectance system equipped with an Oxford Instruments OptistatDry TLEX cryostat for temperature control and a sample cell which allows control of the atmosphere in the sample chamber through a manifold was used for all experiments. The sample cell atmosphere was controlled by a Micromeritics ASAP 2020Plus instrument connected to the manifold. In a typical experiment, a powder sample of activated framework (~5 mg) was ground with KBr, and transferred into the chamber. The sample was evacuated for 1 hr at 300 K prior to spectra collection. Dosing was performed through the ASAP 2020Plus instrument at the relevant temperatures while spectra were collected at a resolution of 4 cm⁻¹ at one-minute intervals until changes in pressure and spectral features were observed to cease.

6.3. Results and Discussion

Activation of the Cu[Ni(pdt)₂] material by heating to 90 °C under dynamic vacuum results in a material with a Langmuir surface area of 426 m²/g (Figure 6.1). Structure solution from powder X-ray diffraction data reveals that Cu[Ni(pdt)₂] is isostructural with the previously reported Cu[Cu(pdt)₂] (Figure 6.2), possessing square channels lined by square planar Ni²⁺ centers (Figure 6.3) and square cages formed by four pyrazine rings.

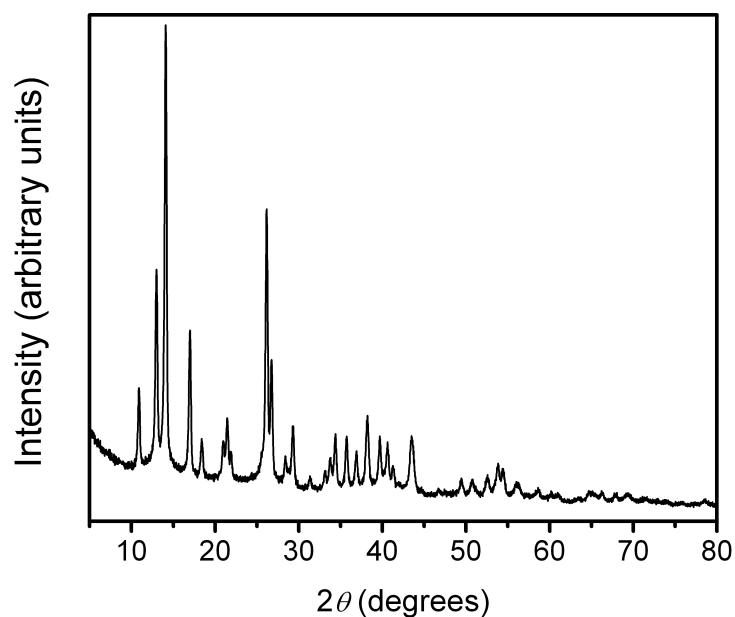


Figure 6.1. Powder X-ray diffraction pattern of Cu[Ni(pdt)₂].

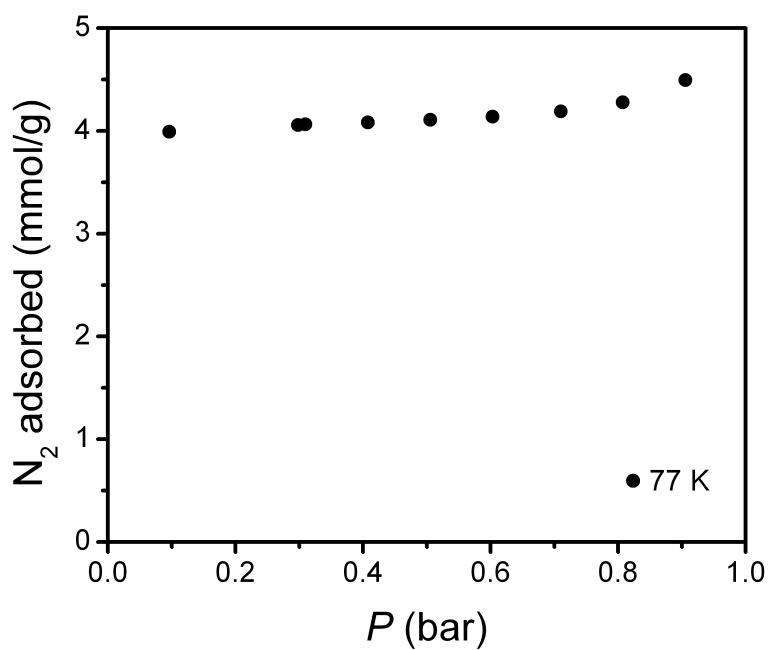


Figure 6.2. The 77 K N₂ adsorption isotherm collected for Cu[Ni(pdt)₂] and used to calculate the Langmuir surface area of 426 m²/g.

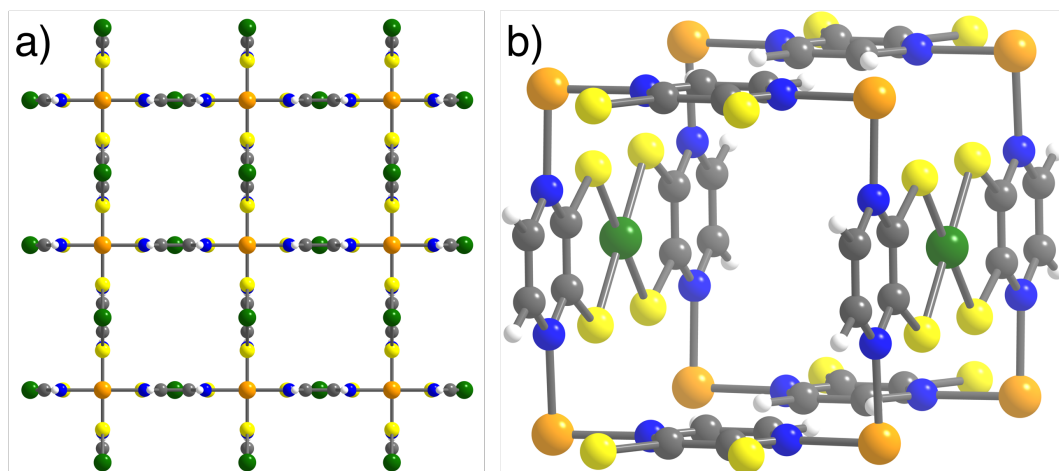


Figure 6.3. Structure of Cu[Ni(pdt)₂] as solved from powder X-ray diffraction a) down the *c*-axis and b) showing the connectivity of the main cage. White, gray, blue, yellow, green, and orange spheres represent H, C, N, S, Ni, and Cu atoms, respectively.

Since Cu[Ni(pdt)₂] has pore dimensions similar to the size of acetylene and ethylene, along with available Ni²⁺ sites lining the pores, it was thought that adsorptive-based separation of these two species could be completed in Cu[Ni(pdt)₂]. To that end, C₂H₂ and C₂H₄ adsorption isotherms were measured at 298, 308, and 318 K (Figure 6.4). Cu[Ni(pdt)₂] shows very strong acetylene adsorption, with an uptake of over 1 mmol/g at only 0.77 mbar pressure at 298 K. Acetylene and ethylene uptake at 298 K and a low pressure of 1 mbar are quite distinct, at 1.08 and 0.03 mmol/g, respectively.

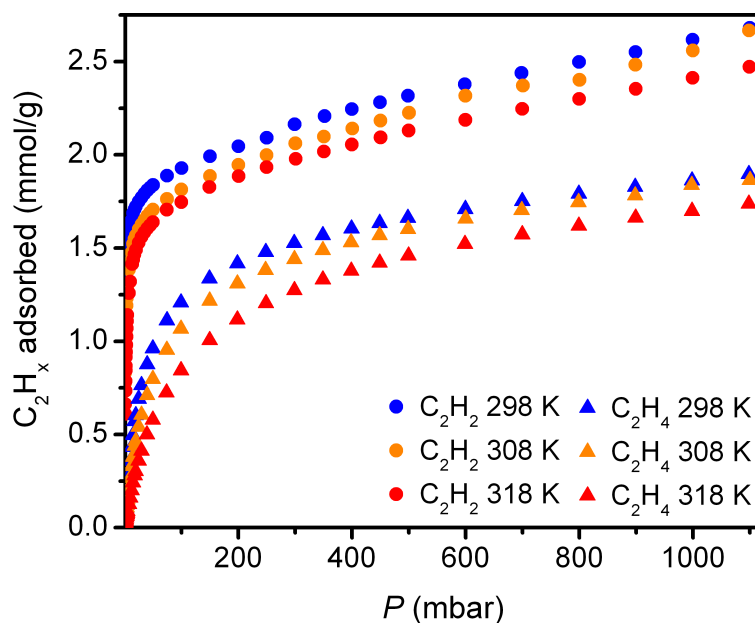


Figure 6.4. Acetylene (circles) and ethylene (triangles) isotherms at 298, 308, and 318 K.

This remarkable difference at low pressures suggests the use of Cu[Ni(pdt)₂] for separating trace amounts of acetylene from ethylene, at which <1% acetylene is present in the stream. From fitting a tri-site Langmuir-Freundlich equation to the single-component isotherms, ideal adsorbed solution theory (IAST) was used to predict multicomponent selectivities from the single-component adsorption isotherm data (Figure 6.5). The 298 K selectivity is as high as 44.6 at 5% acetylene; if this plot is extended to 1% acetylene in ethylene, the selectivity rises to 54.4, a record value for an adsorbent under these conditions.

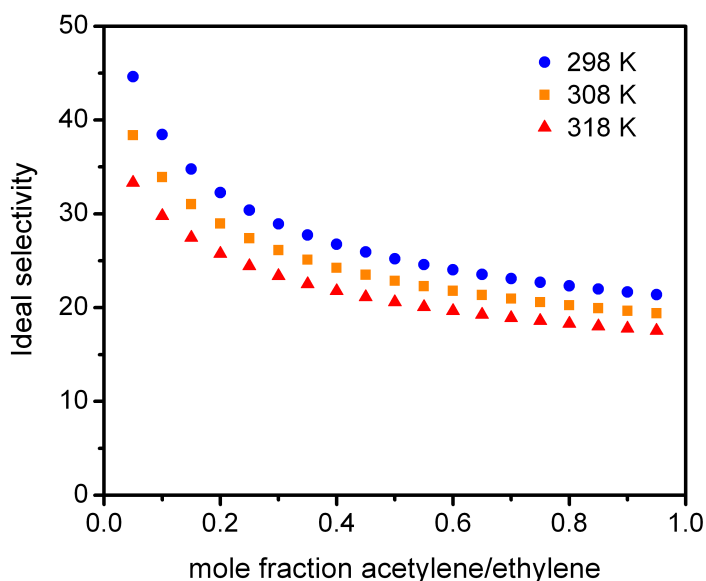


Figure 6.5. Ideal adsorbed solution theory (IAST) selectivities for acetylene/ethylene in Cu[Ni(pdt)₂].

To better understand the high selectivity for adsorbing acetylene over ethylene in Cu[Ni(pdt)₂], powder X-ray diffraction patterns of evacuated, acetylene-dosed, and ethylene-dosed Cu[Ni(pdt)₂] were collected. After structure solution, space filling models of the evacuated structure showed full accessibility of the channels (Figure 6.6a,b). Acetylene was identified to bind in the cage formed by four pyrazine rings at various pressures at 298 K (Figure 6.6c,d). The binding site was found to be fully occupied at a pressure of only 20 mbar. That this is the binding site is interesting, as the square planar Ni²⁺ sites lining the pores were expected to be the primary site of interaction due to the ability of open metal coordination sites in other metal-organic frameworks to bind small gas molecules more strongly than other surfaces within the pores.

Ethylene was found to bind in the same pyrazine cage. However, rather than having the nearly 100% occupancy at 20 mbar as the acetylene-dosed structure does, the occupancy of ethylene in the tetrapyrazine cage in the ethylene-dosed structure gradually increases as the pressure is increased, commensurate with the weaker binding of ethylene in this cage. The binding of these unsaturated hydrocarbons in this site is attributed to the pi-pi interactions available between the acetylene or ethylene and the pyrazine rings, which are oriented at 90° angles to one another and have a cage size that fits both acetylene and ethylene well enough to become the primary interaction site for both gases. Further supporting this hypothesis is that ethane was unable to be located in any discrete location in the channels of an ethane-dosed

sample of Cu[Ni(pdt)₂], indicating that the occupation of the pyrazine binding cage is unique to the unsaturated C₂ hydrocarbons. The immobilization of the pyrazine rings in this square cage allows for the donation of electron density from the pi orbitals in acetylene and ethylene into the pi cloud of the electron-deficient aromatic rings, highlighting the utility of MOFs in creating unique chemical environments that are relatively inaccessible in molecular chemistry.

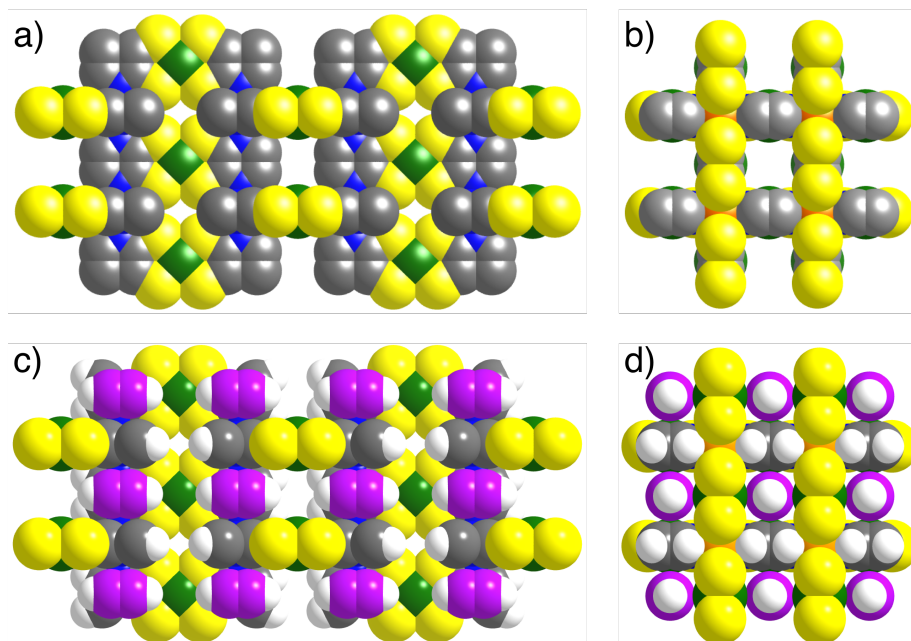


Figure 6.6. Crystal structures as determined from powder X-ray diffraction of evacuated Cu[Ni(pdt)₂] a) down the *b*-axis and b) down the *c*-axis and C₂H₂-dosed Cu[Ni(pdt)₂] c) down the *b*-axis and d) down the *c*-axis. White, gray, blue, yellow, green, and orange spheres represent H, C, N, S, Ni, and Cu atoms, while the pink spheres represent C atoms in acetylene.

Importantly, the difference in binding between these two molecules can be explained on the basis of this binding site. Since acetylene possesses electron density in two orthogonal pi bonds, it can interact with all four pyrazine rings, leading to the experimentally strong binding in Cu[Ni(pdt)₂]. In contrast, ethylene only has one pi bond and can thus interact with only two of the pyrazine rings in the cage, leading to a weaker interaction. Binding in this cage, rather than to an open metal site, is quite important to this separation. This becomes apparent in comparison with M₂(*m*-dobdc) (M = Co, Ni; *m*-dobdc⁴⁻ = 4,6-dioxido-1,3-benzenedicarboxylate), which has nearly no selectivity for binding acetylene over ethylene (Figure 6.7) despite having previously been shown to excel at olefin/paraffin separations.¹ This data agrees with previously reported IAST selectivities of <2.5 calculated for acetylene/ethylene separations in Fe₂(dobdc) (dobdc⁴⁻ = 2,5-dioxido-1,4-benzenedicarboxylate).¹³

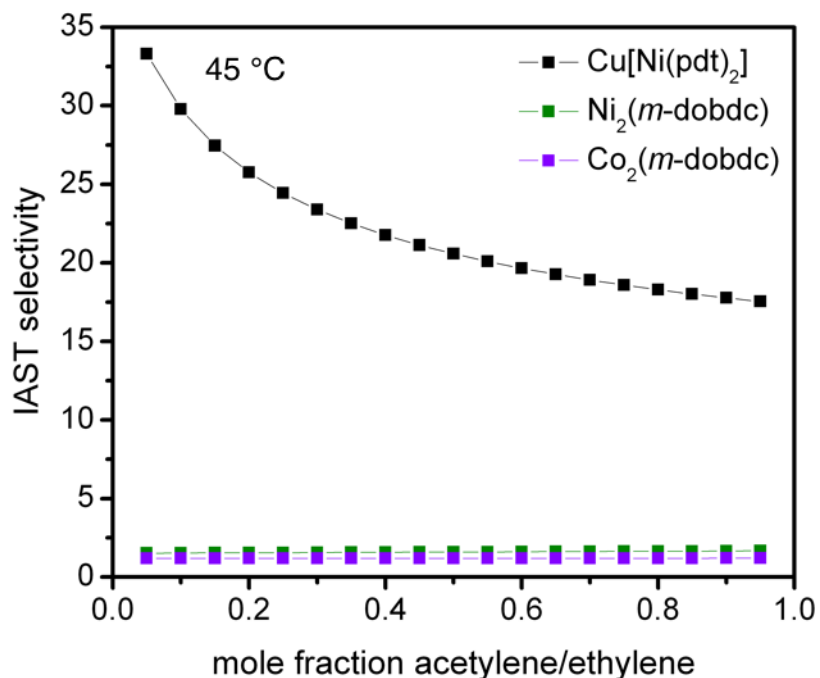


Figure 6.7. Comparison of the IAST selectivities for acetylene/ethylene separations at 45 °C between Cu[Ni(pdt)₂] and M₂(m-dobdc) (M²⁺ = Co, Ni).

This hypothesis was confirmed through the use of *in situ* gas-dosed infrared (IR) spectroscopy. Cu[Ni(pdt)₂] was loaded into a custom-built DRIFTS system in which a sample holder connected to an ASAP 2020 Plus gas sorption analyzer was placed in a cryostat for control of both temperature and pressure of gas while measuring the IR spectrum of the sample. Spectra were collected at various acetylene pressures, revealing that the typical acetylene IR-active C-H stretch at 3280 cm⁻¹ and C-H bend at 730 cm⁻¹ are visible (Figure 6.8). The stretch is shifted to a lower energy of 3240 cm⁻¹, which is typical of the interaction of the C-H bonds with surfaces within the pores of the MOF (Figure 6.9). The bend is shifted to slightly higher energy at 737 cm⁻¹, likely due to the constrained chemical environment of the acetylene (Figure 6.10). Notably, the Raman-active stretches typically seen in acetylene at 3374, 1974, and 612.8 cm⁻¹ are not visible (Table 1), indicating a perfectly symmetric environment that corroborates with the binding of acetylene in the symmetric pyrazine cage as seen in the structures solved from powder X-ray diffraction.

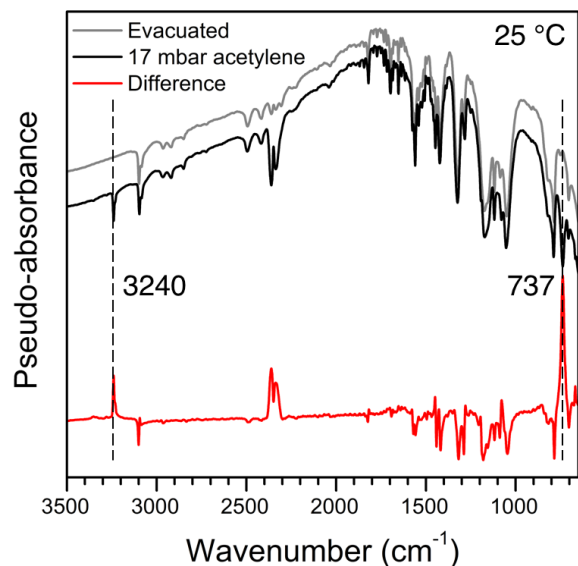


Figure 6.8. Overall infrared spectra of Cu[Ni(pdt)₂] evacuated (gray) and dosed to 17 mbar with C₂H₂ (black), with the difference shown at the bottom (red). The labeled peak in the difference spectrum at 3240 cm⁻¹ corresponds to the IR-active C–H stretch and the labeled peak at 737 cm⁻¹ corresponds to the IR-active C–H bend.

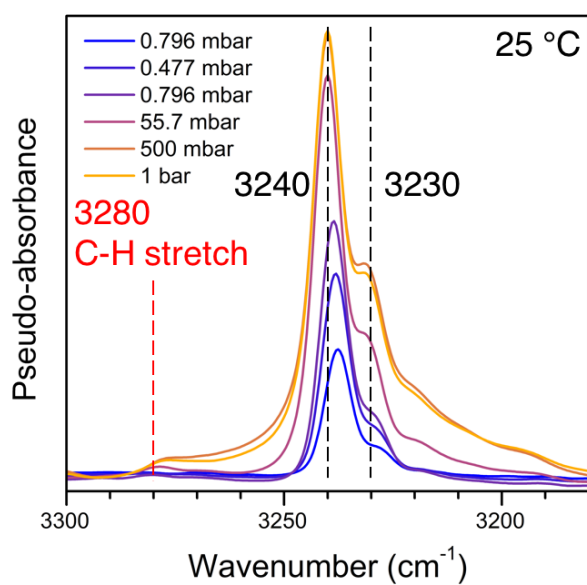


Figure 6.9. Variable pressure C₂H₂-dosed spectra of Cu[Ni(pdt)₂] at 25 °C. The C–H stretch is observed at 3240 and 3230 cm⁻¹, redshifted relative to the 3280 cm⁻¹ for free C₂H₂.

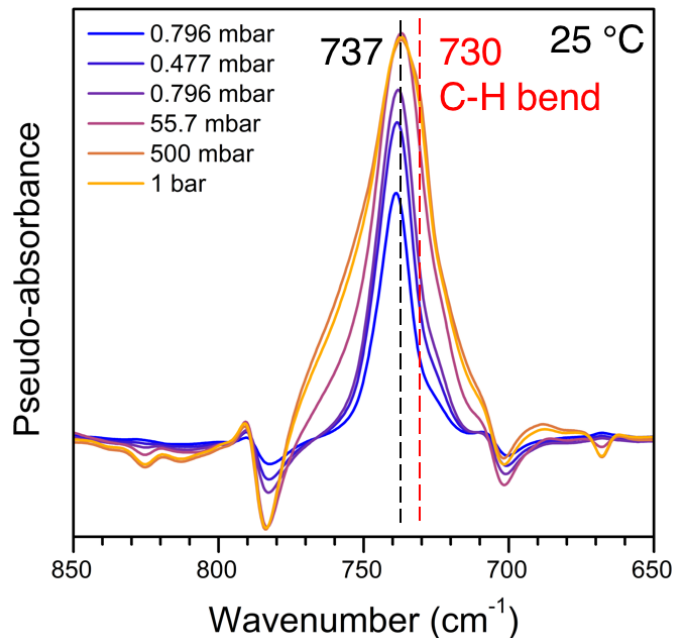


Figure 6.10. Variable pressure C_2H_2 -dosed spectra of $Cu[Ni(pdt)_2]$ at $25\text{ }^\circ\text{C}$. The C–H bend is observed at 737 cm^{-1} , blueshifted relative to the 730 cm^{-1} for free C_2H_2 .

Table 6.1. Summary of vibrational modes in C_2H_2 . *Modes marked with an asterisk are Raman active.¹⁴

Mode	$\nu\text{ (cm}^{-1}\text{)}$
C–H stretch*	3373.7
C–H stretch	3294.9
C–C stretch*	1973.8
C–H bend	730.3
C–H bend*	611.8

6.4. Outlook and Conclusions

In summary, the MOF $Cu[Ni(pdt)_2]$ was studied for its use in an adsorptive-based separation of acetylene and ethylene. Adsorption isotherms and calculated IAST selectivities indicated very strong binding of acetylene relative to ethylene, especially at low acetylene concentrations. Powder X-ray diffraction was used to determine that the tetrapyrazine cage was the primary binding site for both gases, indicating that acetylene binds more strongly due to the greater number of pi-pi interactions it can have with the tetrapyrazine cage. Infrared spectroscopy confirmed this symmetrical interaction. This highly unique mechanism for the challenging separation of acetylene and ethylene illustrates the opportunity that MOFs provide for adsorptive separations not possible in other classes of porous adsorbents.¹⁵

6.5. Acknowledgements

Thanks to Julia Oktawiec for powder X-ray diffraction data collection and structure solution, Henry Z. H. Jiang for *in situ* infrared spectroscopy data collection and analysis, Jonathan Melville for assistance with improving the synthesis of Cu[Ni(pdt)]₂, and Douglas A. Reed for assistance with isotherm collection. This work was supported as part of the Center for Gas Separations Relevant to Clean Energy Technologies, an Energy Frontier Research Center funded by the U.S. Department of Energy, Office of Science, Basic Energy Sciences under Award # DE-SC0001015. Thanks to the NSF for graduate fellowship support.

6.6. References and Supplementary Data

1. Bachman, J. E.; Kapelewski, M. T.; Reed, D. A.; Gonzalez, M. I.; Long, J. R. *J. Am. Chem. Soc.* **2017**, *139*, 15363.
2. Herm, Z. R.; Wiers, B. M.; Mason, J. a.; van Baten, J. M.; Hudson, M. R.; Zajdel, P.; Brown, C. M.; Masciocchi, N.; Krishna, R.; Long, J. R. *Science* **2013**, *340*, 6135.
3. Alaerts, L.; Kirschhock, C. E. A.; Maes, M.; van der Veen, M. A.; Finsy, V.; Depla, A.; Martens, J. A.; Baron, G. V.; Jacobs, P. A.; Denayer, J. F. M.; De Vos, D. E. *Angew. Chem. Int. Ed.* **2007**, *46*, 4293.
4. U.S. Department of Energy. Materials for Separation Technology: Energy and Emission Reduction Opportunities (2005).
5. Matsuda, R.; Kitaura, R.; Kitagawa, S.; Kubota, Y.; Belosludov, R. V.; Kobayashi, T. C.; Sakamoto, H.; Chiba, T.; Takata, M.; Kawazoe, Y.; Mita, Y. *Nature* **2005**, *436*, 238.
6. Zhang, J.-P.; Chen, X.-M. *J. Am. Chem. Soc.* **2009**, *131*, 5516.
7. Hu, T.-L.; Wang, H.; Li, B.; Krishna, R.; Wu, H.; Zhou, W.; Zhao, Y.; Han, Y.; Wang, X.; Zhu, W.; Yao, Z.; Xiang, S.; Chen, B. *Nat. Commun.* **2015**, *6*, 7328.
8. Yang, .; Ramirez-Cuesta, A. J.; Newby, R.; Garcia-Sakai, V.; Manuel, P.; Callear, S. K.; Campbell, S. I.; Tang, C. C.; Schröder, M. *Nat. Chem.* **2015**, *7*, 121.
9. Cui, X.; Chen, K.; Xing, H.; Yang, Q.; Krishna, R.; Bao, Z.; Wu, H.; Zhou, W.; Dong, X.; Han, Y.; Li, B.; Ren, Q.; Zaworotko, M. J.; Chen, B. *Science* **2016**, *353*, 141.
10. Kobayashi, Y.; Jacobs, B.; Allendorf, M. A.; Long, J. R. *Chem. Mater.* **2010**, *22*, 4120-4122.
11. Rudzinski, W.; Everett, D. H. *Adsorption of Gases on Heterogeneous Surfaces*; Academic Press, Inc.: CA, 1992.
12. Coelho, A. A. TOPAS-Academic, version 4.1 (Coelho Software, 2007).
13. Bloch, E. D.; Queen, W. L.; Krishna, R.; Zadrozny, J. M.; Brown, C. M.; Long, J. R. *Science* **2012**, *335*, 1606.
14. Shimanouchi, T. Tables of Molecular Vibrational Frequencies Consolidated Volume I, National Bureau of Standards, **1972**, 1-160.

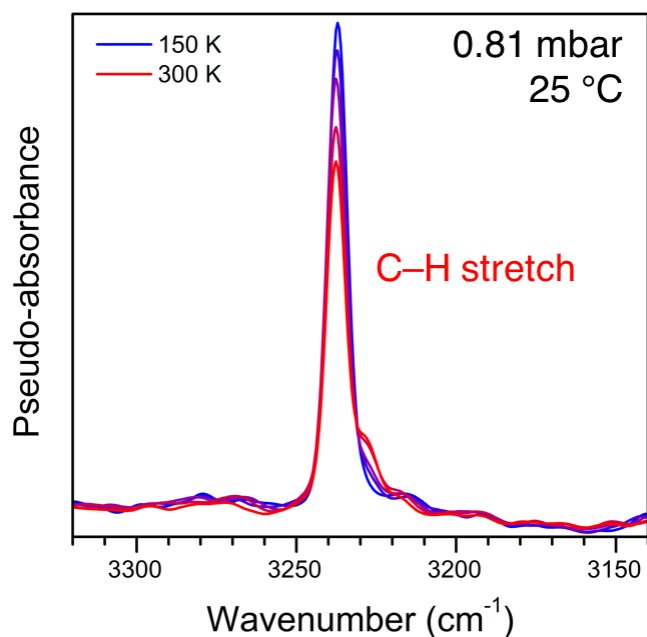


Figure 6.S1. Variable temperature C_2H_2 -dosed to 0.81 mbar in $Cu[Ni(pdt)_2]$ at 25 °C. The C–H stretch is observed at 3240 cm^{-1} and the peak shape is independent of temperature.

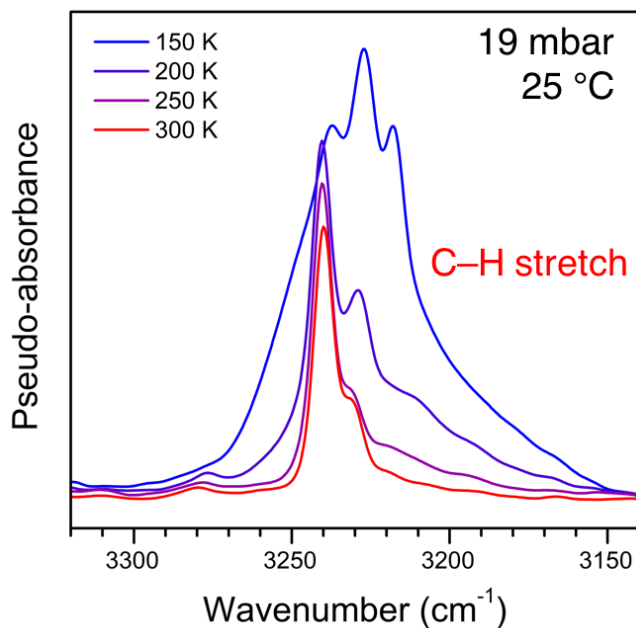


Figure 6.S2. Variable temperature C_2H_2 -dosed to 19 mbar in $Cu[Ni(pdt)_2]$ at 25 °C. The C–H stretch is observed at 3240 cm^{-1} and the peak shape now changes depending on the temperature. Compared to the lower loading in Figure 6.S1, these are spectra with more features, indicating a variety of C_2H_2 binding sites.

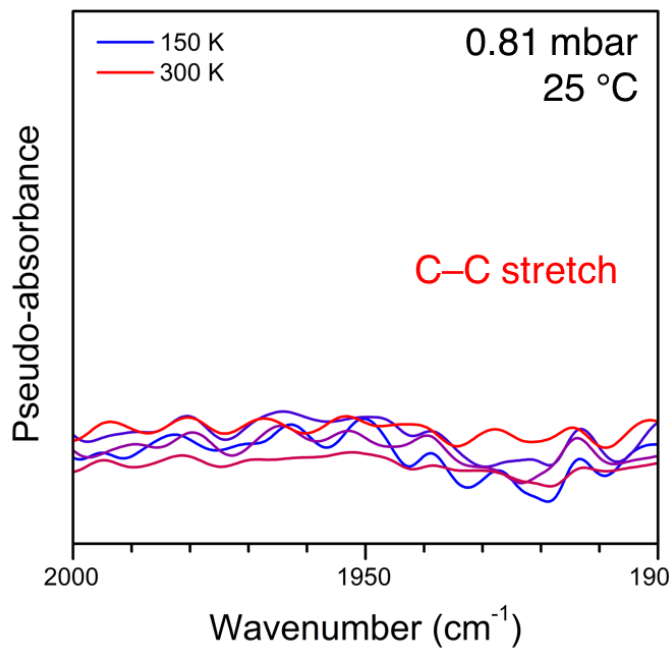


Figure 6.S3. Variable temperature C₂H₂-dosed to 0.81 mbar in Cu[Ni(pdt)₂] at 25 °C. The IR-inactive C–C stretch is not observed at this loading and temperature.

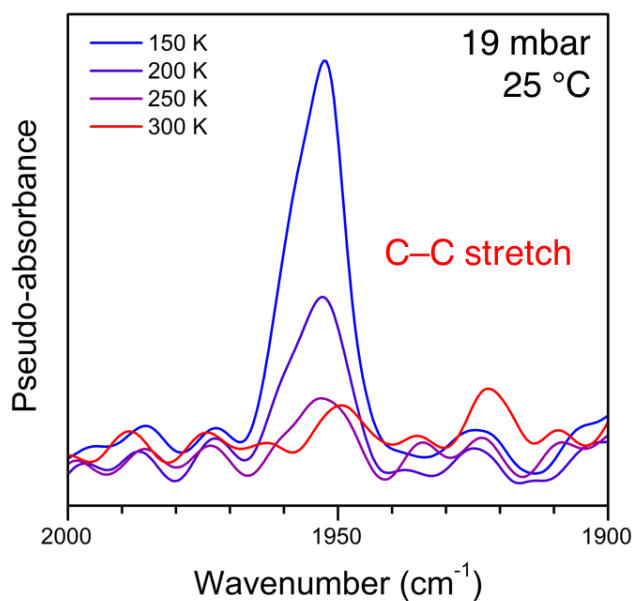


Figure 6.S4. Variable temperature C₂H₂-dosed to 0.81 mbar in Cu[Ni(pdt)₂] at 25 °C. The usually IR-inactive C–C stretch is now observed due to the higher loading, indicating an additional, asymmetric binding site for C₂H₂ in the pores outside of the tetrapyrazine cage.

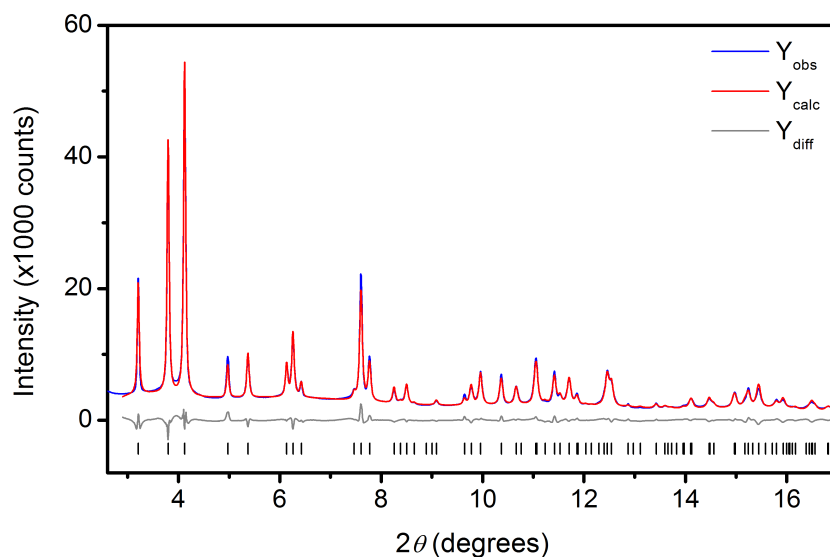


Figure 6.S5. Rietveld refinement of $\text{Cu}[\text{Ni}(\text{pdt})_2]$ dosed with 20 mbar C_2H_2 at 298 K from 2.6° to 17° . Blue and red lines represent the observed and calculated diffraction patterns, respectively. The gray line represents the difference between observed and calculated patterns, and the black tick marks indicate calculated Bragg peak positions. The inset shows the high angle region at a magnified scale. Figures-of-merit (as defined by TOPAS): $R_{\text{wp}} = 4.67\%$, $R_{\text{p}} = 3.52\%$, $R_{\text{exp}} = 1.57\%$, $R_{\text{Bragg}} = 2.50\%$, $\text{GoF} = 2.97$. The wavelength was 0.45212 \AA .

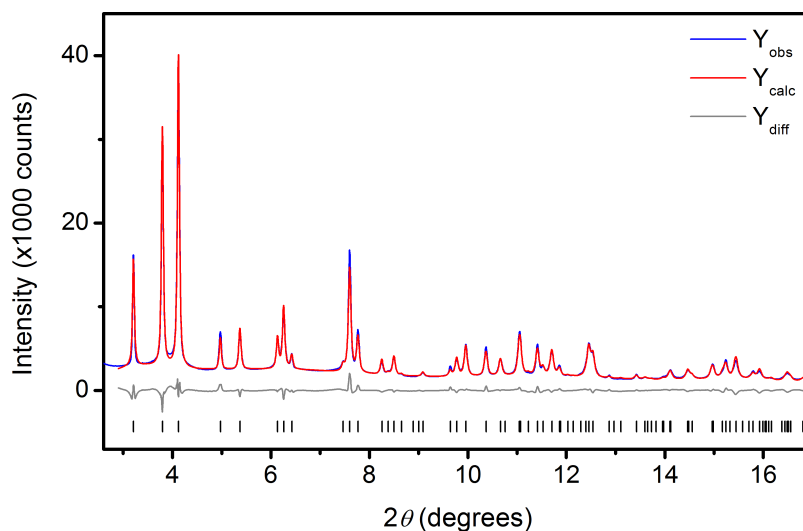


Figure 6.S6. Rietveld refinement of $\text{Cu}[\text{Ni}(\text{pdt})_2]$ dosed with 92 mbar C_2H_2 at 298 K from 2.6° to 17° . Blue and red lines represent the observed and calculated diffraction patterns, respectively. The gray line represents the difference between observed and calculated patterns, and the black tick marks indicate calculated Bragg peak positions. The inset shows the high angle region at a magnified scale. Figures-of-merit (as defined by TOPAS): $R_{\text{wp}} = 4.76\%$, $R_{\text{p}} = 3.60\%$, $R_{\text{exp}} = 1.83\%$, $R_{\text{Bragg}} = 2.79\%$, $\text{GoF} = 2.61$. The wavelength was 0.45212 \AA .

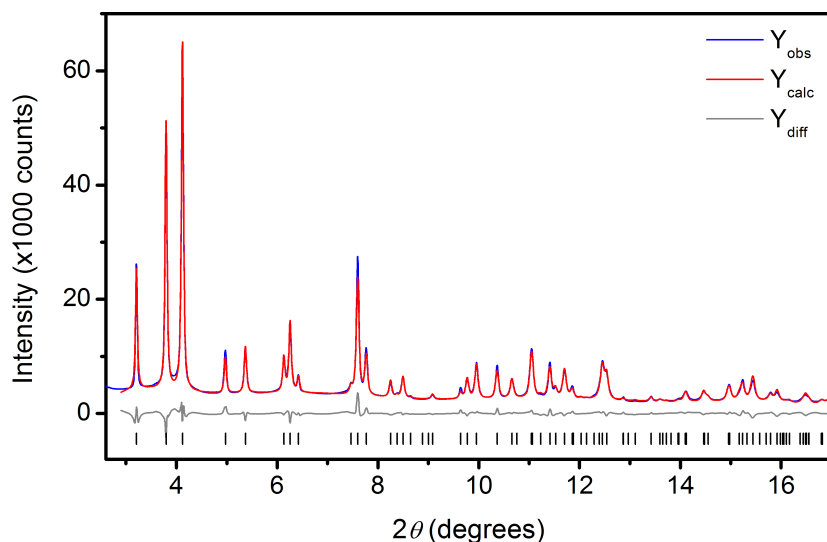


Figure 6.S7. Rietveld refinement of Cu[Ni(pdt)₂] dosed with 291 mbar C₂H₂ at 298 K from 2.6° to 17°. Blue and red lines represent the observed and calculated diffraction patterns, respectively. The gray line represents the difference between observed and calculated patterns, and the black tick marks indicate calculated Bragg peak positions. The inset shows the high angle region at a magnified scale. Figures-of-merit (as defined by TOPAS): $R_{wp} = 5.05\%$, $R_p = 3.83\%$, $R_{exp} = 1.47\%$, $R_{Bragg} = 2.94\%$, GoF = 3.44. The wavelength was 0.45212 Å.

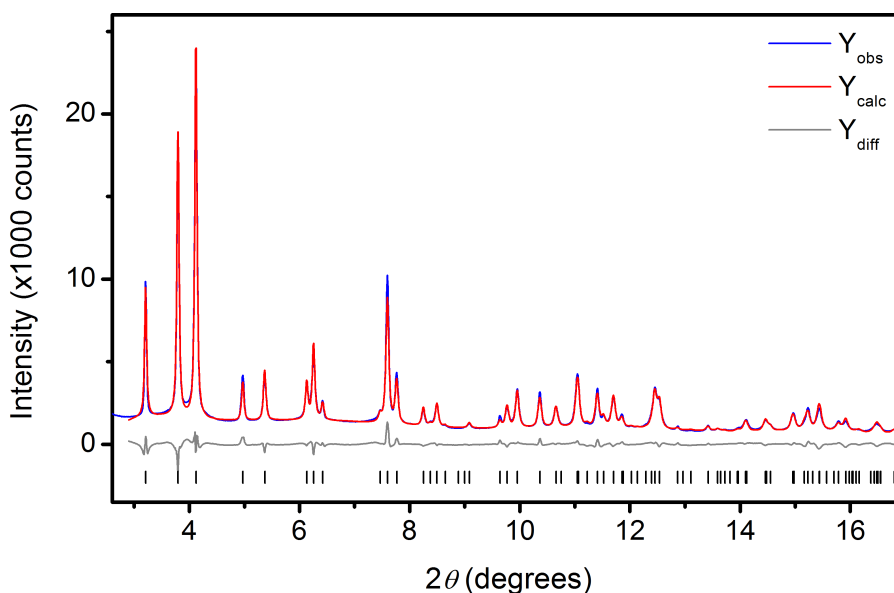


Figure 6.S8. Rietveld refinement of Cu[Ni(pdt)₂] dosed with 591 mbar C₂H₂ at 298 K from 2.6° to 17°. Blue and red lines represent the observed and calculated diffraction patterns, respectively. The gray line represents the difference between observed and calculated patterns, and the black tick marks indicate calculated Bragg peak positions. The inset shows the high angle region at a magnified scale. Figures-of-merit (as defined by TOPAS): $R_{wp} = 4.92\%$, $R_p = 3.83\%$, $R_{exp} = 2.38\%$, $R_{Bragg} = 2.91\%$, GoF = 2.07. The wavelength was 0.45212 Å.

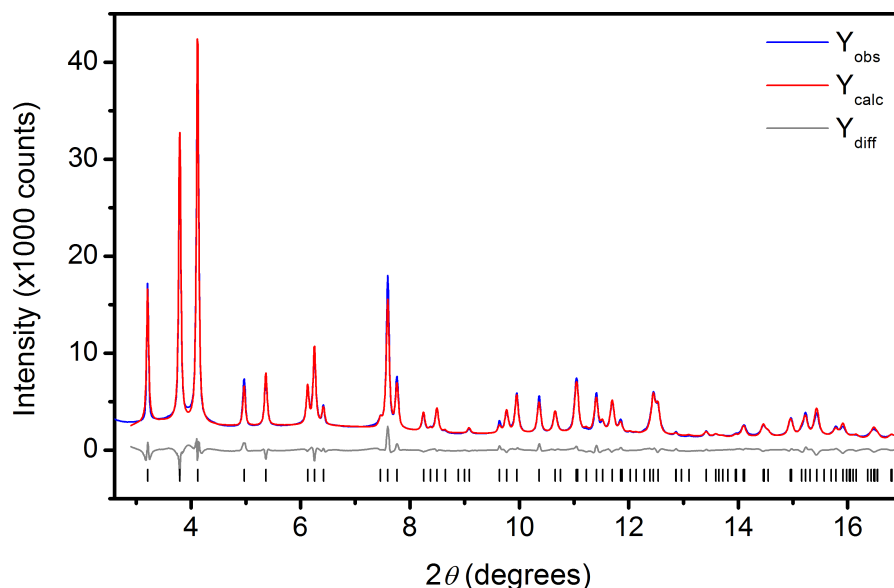


Figure 6.S9. Rietveld refinement of Cu[Ni(pdt)₂] dosed with 1077 mbar C₂H₂ at 298 K from 2.6° to 17°. Blue and red lines represent the observed and calculated diffraction patterns, respectively. The gray line represents the difference between observed and calculated patterns, and the black tick marks indicate calculated Bragg peak positions. The inset shows the high angle region at a magnified scale. Figures-of-merit (as defined by TOPAS): $R_{wp} = 4.92\%$, $R_p = 3.83\%$, $R_{exp} = 2.38\%$, $R_{Bragg} = 2.91\%$, $GoF = 2.07$. The wavelength was 0.45212 Å.

Table 6.S1. Experimental conditions, unit cell parameters, figures-of-merit, and C₂H₄ occupancy values as determined by Rietveld refinement of powder X-ray diffraction patterns of Cu[Ni(pdt)₂] dosed with increasing amounts of C₂H₄ gas.

	24 mbar C ₂ H ₄	88 mbar C ₂ H ₄	273 mbar C ₂ H ₄	589 mbar C ₂ H ₄	985 mbar C ₂ H ₄
λ (Å)	0.45212	0.45212	0.45212	0.45212	0.45212
Temp. (K)	298	298	298	298	298
Space Group	P42/mmc	P42/mmc	P42/mmc	P42/mmc	P42/mmc
a (Å)	6.8191(8)	6.8281(8)	6.8342(9)	6.8368(9)	6.8385(3)
c (Å)	16.1323(17)	16.1088(17)	16.0964(18)	16.0946(18)	16.0963(9)
V (Å ³)	750.16(19)	751.0(2)	751.8(2)	752.3(2)	752.76(8)
R_{wp}	6.31%	6.52%	6.84%	6.91%	7.06%
R_{exp}	1.91%	1.91%	1.91%	1.91%	1.91%
R_{Bragg}	3.89%	4.33%	4.72%	4.81%	5.01%
R_p	4.87%	5.04%	5.30%	5.29%	5.39%
GoF	3.30	3.40	3.57	3.62	3.70
C ₂ H ₄ occupancy	38.1(13)%	64.3(14)%	80.6(14)%	86.7(14)%	89.2(14)%

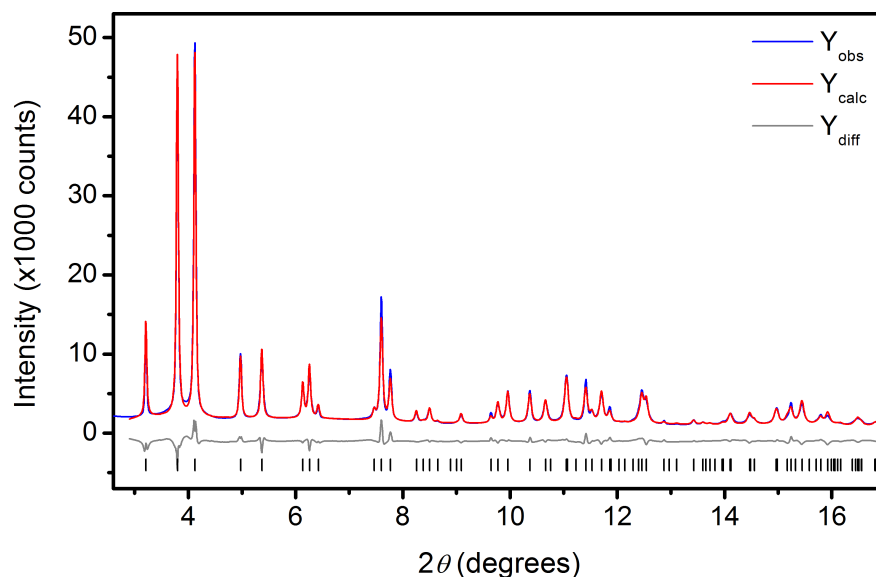


Figure 6.S10. Rietveld refinement of $\text{Cu}[\text{Ni}(\text{pdt})_2]$ dosed with 24 mbar C_2H_4 at 298 K from 2.6° to 17° . Blue and red lines represent the observed and calculated diffraction patterns, respectively. The gray line represents the difference between observed and calculated patterns, and the black tick marks indicate calculated Bragg peak positions. The inset shows the high angle region at a magnified scale. Figures-of-merit (as defined by TOPAS): $R_{\text{wp}} = 6.31\%$, $R_{\text{p}} = 4.87\%$, $R_{\text{exp}} = 1.91\%$, $R_{\text{Bragg}} = 3.89\%$, $\text{GoF} = 3.30$. The wavelength was 0.45212 \AA .

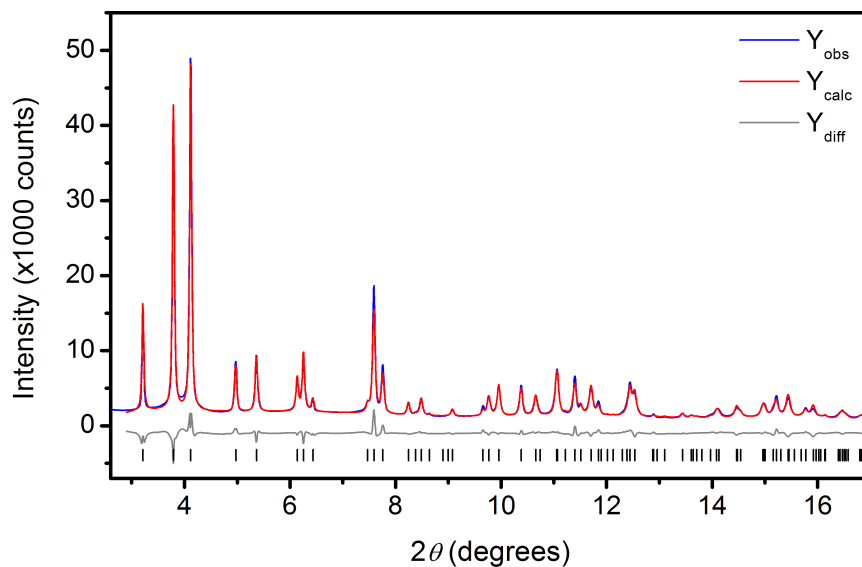


Figure 6.S11. Rietveld refinement of $\text{Cu}[\text{Ni}(\text{pdt})_2]$ dosed with 88 mbar C_2H_4 at 298 K from 2.6° to 17° . Blue and red lines represent the observed and calculated diffraction patterns, respectively. The gray line represents the difference between observed and calculated patterns, and the black tick marks indicate calculated Bragg peak positions. The inset shows the high angle region at a magnified scale. Figures-of-merit (as defined by TOPAS): $R_{\text{wp}} = 6.52\%$, $R_{\text{p}} = 5.04\%$, $R_{\text{exp}} = 1.91\%$, $R_{\text{Bragg}} = 4.33\%$, $\text{GoF} = 3.40$. The wavelength was 0.45212 \AA .

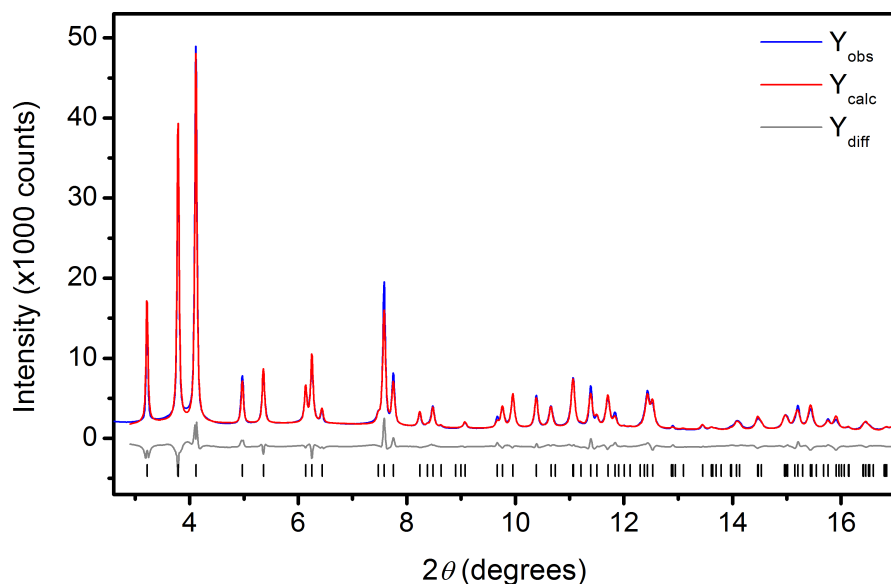


Figure 6.S12. Rietveld refinement of Cu[Ni(pdt)₂] dosed with 273 mbar C₂H₄ at 298 K from 2.6° to 17°. Blue and red lines represent the observed and calculated diffraction patterns, respectively. The gray line represents the difference between observed and calculated patterns, and the black tick marks indicate calculated Bragg peak positions. The inset shows the high angle region at a magnified scale. Figures-of-merit (as defined by TOPAS): $R_{wp} = 6.84\%$, $R_p = 5.30\%$, $R_{exp} = 1.91\%$, $R_{Bragg} = 2.94\%$, GoF = 3.57. The wavelength was 0.45212 Å.

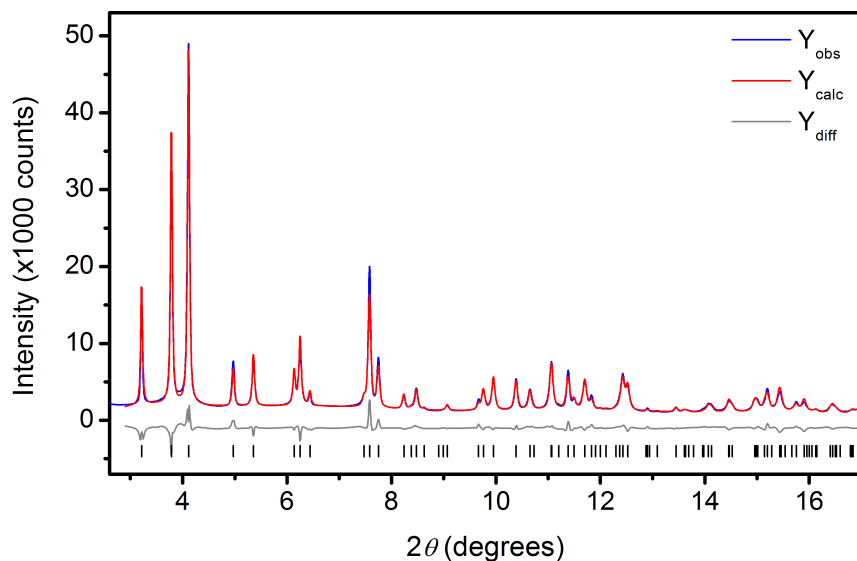


Figure 6.S13. Rietveld refinement of Cu[Ni(pdt)₂] dosed with 589 mbar C₂H₄ at 298 K from 2.6° to 17°. Blue and red lines represent the observed and calculated diffraction patterns, respectively. The gray line represents the difference between observed and calculated patterns, and the black tick marks indicate calculated Bragg peak positions. The inset shows the high angle region at a magnified scale. Figures-of-merit (as defined by TOPAS): $R_{wp} = 6.91\%$, $R_p = 5.29\%$, $R_{exp} = 2.38\%$, $R_{Bragg} = 4.81\%$, GoF = 3.62. The wavelength was 0.45212 Å.

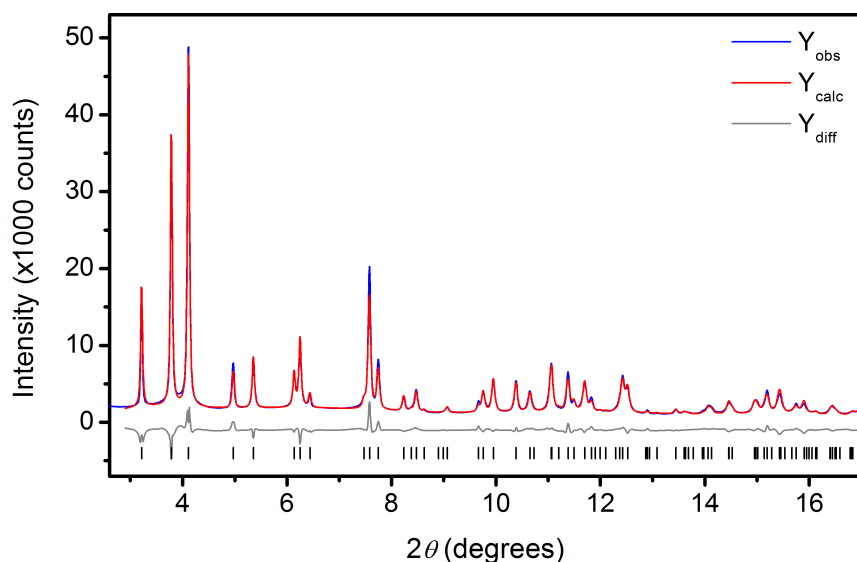


Figure 6.S14. Rietveld refinement of $\text{Cu}[\text{Ni}(\text{pdt})_2]$ dosed with 985 mbar C_2H_4 at 298 K from 2.6° to 17° . Blue and red lines represent the observed and calculated diffraction patterns, respectively. The gray line represents the difference between observed and calculated patterns, and the black tick marks indicate calculated Bragg peak positions. The inset shows the high angle region at a magnified scale. Figures-of-merit (as defined by TOPAS): $R_{\text{wp}} = 7.06\%$, $R_{\text{p}} = 5.39\%$, $R_{\text{exp}} = 1.91\%$, $R_{\text{Bragg}} = 5.01\%$, $\text{GoF} = 3.70$. The wavelength was 0.45212 \AA .